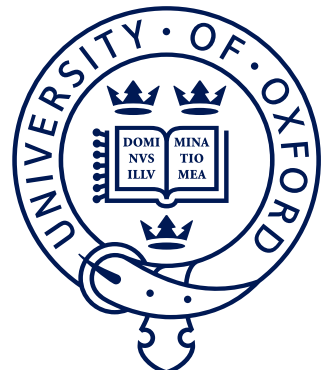


¹ **CP violation in $B^\pm \rightarrow Dh^\pm$ decays**
² **where $D \rightarrow K_S^0 h'^+ h'^-$**

³ *A measurement of the CKM angle γ at LHCb and understanding
⁴ the impact of neutral kaon CP violation*



⁶ Mikkel Bjørn
⁷ St. Anne's College
⁸ University of Oxford

⁹ A thesis submitted for the degree of
¹⁰ *Doctor of Philosophy*
¹¹ Trinity 2020

¹²

Acknowledgements

¹³ suitable thank you's

Abstract

14

¹⁵ World's best measurement of γ . Details to be added.

Contents

¹⁷	Preface	^{vii}
¹⁸	1 Introduction	¹
¹⁹	1.1 Structure of the thesis	¹
²⁰	2 Theoretical background	²
²¹	2.1 The C, P and T symmetries and their violation	²
²²	2.2 CP violation in the Standard Model	⁴
²³	2.2.1 The CKM matrix and the Unitarity Triangle	⁴
²⁴	2.2.2 Measuring γ in tree level decays	⁹
²⁵	2.3 Measuring γ using multi-body D final states	¹²
²⁶	2.3.1 Dalitz plots and the phase space of multi-body decays	¹²
²⁷	2.3.2 The GGSZ method to measure γ	¹⁴
²⁸	2.3.3 A model-independent approach	¹⁶
²⁹	2.3.4 Measuring strong-phase inputs at charm factories	¹⁸
³⁰	2.3.5 Global CP asymmetry and the relation to GLW and ADS measurements	²²
³¹	2.4 Strategy for the LHCb measurement	²⁶
³³	3 The LHCb experiment	²⁹
³⁴	3.1 Subdetectors	²⁹
³⁵	3.1.1 The VELO	²⁹
³⁶	3.1.2 Magnet and tracking stations	²⁹
³⁷	3.1.3 The RICH	²⁹
³⁸	3.1.4 Calorimeters	²⁹
³⁹	3.1.5 Muon detectors	²⁹
⁴⁰	3.2 Track reconstruction	²⁹
⁴¹	3.3 The LHCb triggering system	²⁹
⁴²	3.3.1 The level-0 hardware trigger	²⁹
⁴³	3.3.2 High-level triggers	²⁹
⁴⁴	3.3.3 Offline data filtering: the LHCb stripping	²⁹
⁴⁵	3.4 Simulation	²⁹

46	4 Neutral kaon CP violation and material	
47	interaction in BPGGSZ measurements	31
48	4.1 CP violation and material interaction of neutral kaons	31
49	4.1.1 A first look at the impact on γ measurements	35
50	4.2 Impact on BPGGSZ measurements of γ :	
51	principles	37
52	4.2.1 Modified symmetry relations	37
53	4.2.2 Relationship between the K_S^0 and K_L^0 amplitudes	38
54	4.2.3 Modification of the BPGGSZ yield equations	39
55	4.3 Impact on BPGGSZ measurements of γ :	
56	LHCb and Belle II measurements	42
57	4.3.1 Detector geometries	43
58	4.3.2 Kaon momentum distributions	44
59	4.3.3 Experimental time acceptance	45
60	4.3.4 Detector material budget	46
61	4.3.5 Calculation procedure	48
62	4.3.6 Results	49
63	4.3.7 Coupled $B^\pm \rightarrow DK^\pm$ and $B^\pm \rightarrow D\pi^\pm$ measurements	51
64	4.4 Concluding remarks	52
65	5 A BPGGSZ measurement of γ with $B^\pm \rightarrow Dh^\pm$ decays	54
66	5.1 Candidate reconstruction and selection	54
67	5.1.1 Initial requirements	55
68	5.1.2 Boosted decision tree	57
69	5.1.3 Particle-identification requirements	62
70	5.1.4 Final requirements	63
71	5.1.5 Selected candidates	63
72	5.2 Signal selection efficiencies	64
73	5.2.1 Efficiency of the PID requirements	67
74	5.2.2 Efficiency profile over the Dalitz plot	68
75	5.3 Background studies	70
76	5.3.1 Charmless decays	72
77	5.3.2 Background from four-body D decays	73
78	5.3.3 Semi-leptonic backgrounds	74
79	5.3.4 Cross-feed from other $D \rightarrow K_S^0 h^+ h^-$ decays	82
80	5.3.5 Swapped-track backgrounds	82
81	5.4 Signal and background mass shapes	83
82	5.4.1 Signal decays	85
83	5.4.2 Cross-feed between $B^\pm \rightarrow Dh^\pm$ channels	86

84	5.4.3	Partially reconstructed backgrounds	88
85	5.4.4	Combinatorial background	94
86	5.4.5	Fit results	94
87	5.5	Measurement of the CP-violation observables	97
88	5.5.1	Fit setup	98
89	5.5.2	Main results	101
90	5.5.3	Cross checks	105
91	5.6	Systematic uncertainties	112
92	5.6.1	Strong phase uncertainties	112
93	5.6.2	Efficiency-profile-related systematic uncertainties	113
94	5.6.3	Mass shapes	116
95	5.6.4	CP violation and material interaction of the K_S^0	124
96	5.6.5	Impact of D mixing	124
97	5.6.6	PID efficiencies	124
98	5.6.7	Dalitz-coordinate resolution	125
99	5.6.8	The fixed yield fractions	126
100	5.6.9	Systematic uncertainty due to backgrounds that are not modelled in fit	126
101	5.6.10	Bias correction	128
102	5.6.11	Charmless backgrounds	129
103	5.6.12	Summary of systematic uncertainties	129
104	5.7	Obtained constraints on γ	131
105	5.7.1	Statistical approach	131
106	5.7.2	Interpretation results	134
107	5.7.3	Compatibility with other measurements	136
109	6	Conclusions	140
110	Appendices		
111	A	Projections of main fit to data	142

Preface

112

113 The work presented in this thesis has been resulted in two papers, either under
114 review or published in the Journal of High Energy Physics. These are

115 [?] *Measurement of the CKM angle γ using $B^\pm \rightarrow [K_S^0 h^+ h^-]_D h^\pm$ decays,*

116 submitted to JHEP.

117 This paper describes a measurement of the CKM angle γ using pp collision
118 data taken with the LHCb experiment during the Run 1 of the LHC, in 2011
119 and 2012, and during the full Run 2, in 2015–2018. The measurement uses the
120 decay channels $B^\pm \rightarrow D h^\pm$ where $D \rightarrow K_S^0 h'^+ h'^-$, in which h and h' denotes
121 pions or kaons. It obtains a value of $\gamma = (? \pm ?)^\circ$, which constitutes the world’s
122 best single-measurement determination of γ . The work is the main focus of
123 this thesis and described in detail in Chapter 5.

124 [?] *CP violation and material interaction of neutral kaons in measurements*
125 *of the CKM angle γ using $B^\pm \rightarrow DK^\pm$ decays where $D \rightarrow K_S^0 \pi^+ \pi^-$* , JHEP
126 19 (2020) 106.

127 This paper describes a phenomenological study of the impact of neutral
128 kaon CP violation and material interaction on measurements of γ . With the
129 increased measurement precision to come in the near future, an understanding
130 of these effects is crucial, especially in the context of $B \rightarrow D\pi$ decays; however
131 no detailed study had been published at the start of this thesis. The study is
132 the subject of Chapter 4. Some text excerpts and figures from the paper have
133 been reproduced in the thesis.

134 All of the work described in this thesis is my own, except where clearly referenced
135 to others. Furthermore, I contributed significantly to an analysis of $B^\pm \rightarrow DK^\pm$
136 decays with LHCb data taken in 2015 and 2016, now published in

137 [?] *Measurement of the CKM angle γ using $B^\pm \rightarrow DK^\pm$ with $D \rightarrow K_S^0 \pi^+ \pi^-$*
138 *$K_S^0 K^+ K^-$ decays*, JHEP 08 (2018) 176.

139 I was responsible for the analysis of the signal channel, whereas the control channel
140 was analysed by Nathan Jurik. The measurement is superseded by that of Ref. [?]
141 and is not described in detail in the thesis.

1

¹⁴²

¹⁴³

Introduction

¹⁴⁴ All the big picture stuff: constraints on New Physics from high precision measurements, a small nod to matter-antimatter asymmetry questions etc.

¹⁴⁶ Do mention the Belle [?] and BaBar [?] combinations of γ measurements,
¹⁴⁷ including which decay channels they include (maybe).

¹⁴⁸ 1.1 Structure of the thesis

2

149

150

Theoretical background

151 This chapter lays out the theoretical framework of the thesis. Section 2.1 introduces
152 charge and parity symmetry violation in general, while Section 2.2 covers the
153 description in the Standard Model and the general theory behind charge-parity
154 symmetry violation measurements in charged B decays. Section 2.3 focuses on
155 the theory of measurements using $B^\pm \rightarrow Dh^\pm$ decays with multi-body D final
156 states, after which the specific analysis strategy for the measurement described
157 in the thesis is outlined out in Section 2.4.

158 2.1 The C, P and T symmetries and their vio- 159 lation

160 The concept of symmetry play a fundamental role in modern physics. By Noether's
161 theorem [?], the simple assumption of invariance of our physical laws under universal
162 temporal and spatial translations leads to the very non-trivial prediction of conserved
163 energy and momentum; within the field of particle physics, the interactions and
164 dynamics of the Standard Model (SM) follow completely simply from requiring
165 the fundamental particle fields to satisfy a local $U(1) \times SU(2) \times SU(3)$ gauge
166 symmetry [?]; and one of the short-comings of the SM, is that it fails to explain
167 the apparent *lack* of symmetry in our matter-dominated universe [?]. Indeed, it is
168 important to experimentally establish the symmetries of our world at a fundamental
169 level, and the degree to which they are broken.

170 Three discrete symmetries of importance are the symmetries under

I'll
adjust
this para-
graph
when
I've
written
the intro-
duction.

- 171 1. The charge operator C , which conjugates all internal quantum numbers of a
 172 quantum state and thus converts particles into their anti-particle counter parts.
 173 For example, C transforms the electric charge of a particle state $Q \rightarrow -Q$.
- 174 2. The parity operator P , which inverts the spatial dimensions of space time:
 175 $\vec{x} \rightarrow -\vec{x}$. As such, it transforms left-handed particle fields into right-handed
 176 particle fields and vice versa.
- 177 3. The time-inversion operator T , which inverts the temporal dimension of space
 178 time: $t \rightarrow -t$.

179 These are fundamentally related by the *CPT* theorem [?], which states that any
 180 Lorentz-invariant Quantum Field Theory (QFT) must be symmetric under the
 181 simultaneous application of *all* three operators. However, any one of the symmetries
 182 can be broken individually, and experiments have shown the physical laws of our
 183 world to violate each of the C , P , and T symmetries.

184 Such a symmetry-breaking effect was established for the first time in 1956, when
 185 Chien-Shiung Wu observed parity violation in weak decays of Co-60 nuclei [?], after
 186 carrying out an experiment that was proposed by Yang Chen-Ning and Tsung-Dao
 187 Lee [?]. While this experiment established the breaking of P symmetry, it left open
 188 the possibility that the physical laws are invariant under a combination of a charge-
 189 and parity inversion; that they are *CP* symmetric. However, this was disproved in
 190 1964 when Kronin and Fitch observed that long-lived kaons, which predominantly
 191 decay to the *CP*-odd 3π state, could also decay to the *CP*-even $\pi\pi$ states [?].

192 Since then *CP* violation has been found in the B^0 system by the BaBar and Belle
 193 collaborations [?, ?] during the early 2000's; the B factories, along with CDF, also saw
 194 evidence for *CP* violation in B^\pm decays [?, ?, ?, ?, ?, ?, ?] later confirmed by LHCb [?],
 195 and *CP* violation was measured for the B_s^0 meson by LHCb in 2013 [?]; within the
 196 last year and a half, the first observation of *CP*-violation in D^0 decays has also been
 197 made by the LHCb collaboration [?], and most recently evidence for *CP*-violation in
 198 the neutrino sector has been reported by the T2K collaboration [?]. The observed
 199 effects can be divided into distinct classes. The conceptually simplest case is

- 200 1. *CP-violation in decay*, where $|A/\bar{A}| \neq 1$ for some decay amplitude A , and the
 201 amplitude \bar{A} of the *CP*-conjugate decay. The result is different decay rates in
 202 two *CP*-conjugate decays

$$\Gamma(M \rightarrow f) \neq \Gamma(\bar{M} \rightarrow \bar{f}). \quad (2.1)$$

203 This type of *CP* violation was not seen until the late 1980ies [?, ?], more than
 204 20 years after the first observation of *CP* violation, and only finally established
 205 around the year 2000 [?, ?]. Also this discovery was made in $K \rightarrow \pi\pi$ decays.

206 CP -violation in decay is the only type possible for charged initial states, and
207 it is thus the main focus of the thesis. Two additional CP -violating effect are
208 possible for neutral initial states (a situation that will be the main focus of
209 Chapter 4). These effects are

210 2. *CP -violation in mixing*, which denotes the case where the mixing rates between
211 the M^0 and \bar{M}^0 states differ

$$\Gamma(M^0 \rightarrow \bar{M}^0) \neq \Gamma(\bar{M}^0 \rightarrow M^0). \quad (2.2)$$

212 The CP violation first observed by Kronin and Fitch in the neutral kaon
213 sector [?] is (dominantly) of this type.

214 3. *CP -violation in interference between mixing and decay*, which can be present
215 for a neutral initial states M^0 decaying into a final state f common to both
216 M^0 and \bar{M}^0 . The decay rate includes an interference term between two
217 amplitudes: the amplitude for a direct $M^0 \rightarrow f$ decay and the amplitude
218 for a decay after mixing: $M^0 \rightarrow \bar{M}^0 \rightarrow f$. Even in the absence of the two
219 aforementioned effects, the rates $\Gamma(M^0 \rightarrow f)$ and $\Gamma(\bar{M}^0 \rightarrow \bar{f})$ can differ due
220 to the interference term. Such CP asymmetries have been measured in eg.
221 $B^0 \rightarrow J/\psi K$ by LHCb and the B factories, and in $B_s^0 \rightarrow J/\psi \phi$ decays by the
222 LHC and Tevatron experiments [?].

223 CP violation measurements thus have a long, rich, and still-developing history.

224 2.2 **CP violation in the Standard Model**

225 All existing measurements of CP violation in the quark sector are naturally explained
226 in the SM; indeed, the need to explain the observation CP violation in neutral
227 kaons was a driving force in the development of the model in the first place, when
228 it lead Kobayashi and Maskawa to predict the existence of then-unknown particles
229 in 1973 [?] (now known to be the third generation quarks).

230 2.2.1 **The CKM matrix and the Unitarity Triangle**

231 The SM contains three generations of quarks, each consisting of an up-type quark (u ,
232 c , and t) and a down-type quark (d , s , and b). The charged weak interaction of the
233 W^\pm boson couples up and down-type quarks. The quark states that couple to the W
234 are not (a priori) identical to the mass eigenstates, and can be denoted (u' , c' , and t')
235 and (d' , s' , and b'). A basis for the quark states can be chosen such that the weakly

²³⁶ coupling up-quark states are identical to the propagating quark states, $u = u'$, but
²³⁷ then the down-type quark state are different: $d' \neq d$. The two bases of the down-type
²³⁸ quarks are related via the Cabibbo-Kobayashi-Maskawa (CKM) matrix [?, ?]¹

$$\begin{pmatrix} d' \\ s' \\ t' \end{pmatrix} = V \begin{pmatrix} d \\ s \\ t \end{pmatrix} = \begin{pmatrix} V_{ud} & V_{us} & V_{ub} \\ V_{cd} & V_{cs} & V_{cb} \\ V_{td} & V_{ts} & V_{tb} \end{pmatrix} \begin{pmatrix} d \\ s \\ t \end{pmatrix}. \quad (2.3)$$

²³⁹ Thus the Lagrangian terms representing the coupling of a W^\pm boson with a u -
²⁴⁰ and a d -type quark is

$$\mathcal{L}_{W^+} = -\frac{g}{\sqrt{2}} V_{ud} (\bar{u} \gamma^\mu W_\mu^+ d) \quad \mathcal{L}_{W^-} = -\frac{g}{\sqrt{2}} V_{ud}^* (\bar{d} \gamma^\mu W_\mu^- u) \quad (2.4)$$

²⁴¹ where g is the weak coupling constant, γ_u are the Dirac matrices, and u and d
²⁴² represent the left-handed components of the physical quark states.

²⁴³ The CKM matrix is a unitary complex 3×3 matrix, and hence has $3^2 = 9$
²⁴⁴ independent, real parameters. However, 5 of these can be absorbed into non-physical
²⁴⁵ phases of the quark states (both mass and weak eigenstates) and hence the matrix
²⁴⁶ has 4 real, physical parameters: 3 mixing angles and a single phase. Chau and
²⁴⁷ Keung [?] proposed the parameterisation

$$\begin{aligned} V &= \begin{pmatrix} 1 & 0 & 0 \\ 0 & c_{23} & s_{23} \\ 0 & -s_{23} & c_{23} \end{pmatrix} \begin{pmatrix} c_{13} & 0 & s_{13}e^{-i\delta_{CP}} \\ 0 & 1 & 0 \\ -s_{13}e^{-i\delta_{CP}} & 0 & c_{13} \end{pmatrix} \begin{pmatrix} c_{12} & s_{12} & 0 \\ -s_{12} & c_{12} & 1 \\ 0 & 0 & 1 \end{pmatrix} \\ &= \begin{pmatrix} c_{12}c_{13} & s_{12}c_{13} & s_{13}e^{-i\delta_{CP}} \\ -s_{12}c_{23} - c_{12}s_{23}s_{13}e^{i\delta_{CP}} & c_{12}c_{23} - s_{12}s_{23}s_{13}e^{i\delta_{CP}} & s_{23}c_{13} \\ s_{12}s_{23} - c_{12}c_{23}s_{13}e^{i\delta_{CP}} & -c_{12}s_{23} - s_{12}c_{23}s_{13}e^{i\delta_{CP}} & c_{23}c_{13} \end{pmatrix} \end{aligned} \quad (2.5)$$

²⁴⁸ which is the preferred standard by the PDG [?]. Here, $s_{ij} \equiv \sin \theta_{ij}$ and $c_{ij} \equiv \cos \theta_{ij}$
²⁴⁹ denote the sine and cosine of three rotation angles in quark space; $\theta_{12} = \theta_C$ being
²⁵⁰ the usual Cabibbo angle [?].

²⁵¹ The presence of the complex phase δ_{CP} in the Lagrangian term of the W coupling
²⁵² causes CP violation because, as evident from Eq. (2.4), if δ_{CP} enters the amplitude
²⁵³ for some decay mediated by a W boson, $A = |A|e^{i(\delta_0 + \delta_{CP})}$, then it will enter the
²⁵⁴ CP conjugate decay amplitude with the opposite sign: $\bar{A} = |A|e^{i(\delta_0 - \delta_{CP})}$. In these
²⁵⁵ expressions, δ_0 denotes a CP conserving phase that is not caused by complex terms
²⁵⁶ in the Lagrangian, but arises due to potential intermediate states in the decay

¹ A basis for the quarks can of course be chosen, such that neither the up-quarks or the down-quarks are expressed in their mass eigenstates. In that case the CKM matrix is recovered as $V = U_u^* U_d$, where $U_{u/d}$ is the unitary transformation matrices that brings the u/d quarks into their mass eigenstates.

amplitude.² Usually the underlying mechanism is due to QCD effects, and these CP conserving phases are therefore generally dubbed *strong* phases, as opposed to the CP violating *weak* phase of the W coupling [?]. This terminology will be applied throughout the thesis.

Experimentally, it has been observed that the CKM matrix elements of Eq. (2.5) satisfy $s_{13} \ll s_{23} \ll s_{12}$. This motivates an often used, alternative parameterisation of the matrix, where the elements are expressed as power series in a parameter λ that naturally incorporates this hierarchy: the Wolfenstein parameterisation [?].

The definitions

$$\begin{aligned} s_{12} &\equiv \lambda \\ s_{23} &\equiv \lambda^2 A \\ s_{13} &\equiv \lambda^3(\rho - i\eta) \end{aligned} \tag{2.6}$$

are made, after which the unitarity conditions (or Eq. 2.5) determine the remaining elements to any order in λ .³ To $\mathcal{O}(\lambda^5)$ the Wolfenstein parameterisation of the CKM matrix is [?, ?]

$$V = \begin{pmatrix} 1 - \frac{\lambda^2}{2} - \frac{\lambda^4}{8} & \lambda & A\lambda^3(\rho - i\eta) \\ -\lambda + \frac{\lambda^5}{2}A^2(1 - 2(\rho + i\eta)) & 1 - \frac{\lambda^2}{2} - \frac{\lambda^4}{8}(1 + 4A^2) & A\lambda^2 \\ A\lambda^3(1 - (\rho + i\eta)(1 - \frac{\lambda^2}{2})) & -A\lambda^2(1 - \frac{\lambda^2}{2}(1 - 2(\rho + i\eta))) & 1 - \frac{1}{2}A^2\lambda^4 \end{pmatrix}. \tag{2.7}$$

The unitarity condition $V^\dagger V = \mathbb{1}$ of the CKM matrix defines 9 relations between the CKM elements of the form

$$\sum_j V_{jq}^* V_{jq} = 1 \quad , \quad q \in \{d, s, b\} \quad \text{along the diagonal} \tag{2.8a}$$

$$\sum_j V_{jq}^* V_{jq'} = 0 \quad , \quad q, q' \in \{d, s, b\}, q \neq q' \quad \text{off-diagonal.} \tag{2.8b}$$

The off-diagonal conditions constrain three complex numbers to sum to zero, and can thus be visualised as triangles in the complex plane, the so-called unitarity triangles. Of these, the triangle corresponding to the (d, b) elements plays a special role, because all three sides are of the same order of magnitude, $\mathcal{O}(\lambda^3)$. When expressed in the form

$$\frac{V_{ud}^* V_{ub}}{V_{cd}^* V_{cb}} + \frac{V_{td}^* V_{tb}}{V_{cd}^* V_{cb}} + 1 = 0, \tag{2.9}$$

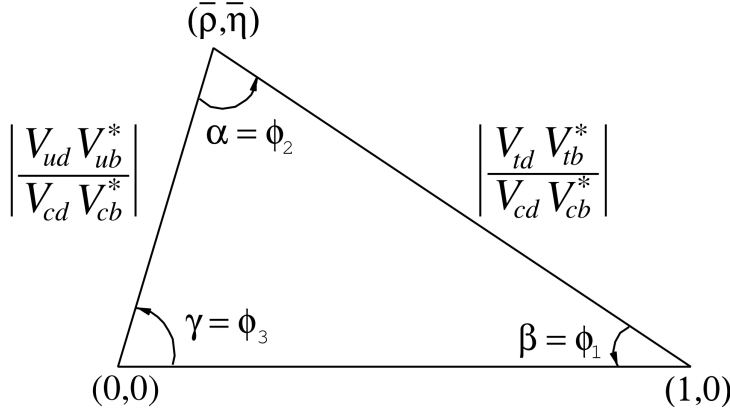


Figure 2.1: Definition of the lengths and sides of the Unitarity Triangle. Figure is taken from the *CKM Quark-Mixing Matrix* review of the PDG [?].

it is often referred to as the singular Unitarity Triangle, illustrated in Fig. 2.1 where the usual names for the three angles are also given.

Over-constraining the unitarity triangle by making separate measurements of all sides and angles, in as many different decay channels as possible, is an important, and non-trivial test of the SM. The current experimental constraints are in agreement with the SM predictions, as visualised in Fig. 2.2. The CKM angle

$$\gamma \equiv \arg(-V_{ud}V_{ub}^*/V_{cd}V_{cb}^*) = \arg(-V_{cb}V_{cd}^*/V_{ub}V_{ud}^*) \quad (2.10)$$

is unique among the CKM parameters, in that it can be measured in tree-level processes without significant theoretical uncertainty from lattice QCD calculations [?]. Because tree-level processes are less likely to be affected by Beyond-Standard-Model (BSM) effects, direct measurements of γ can be considered a SM benchmark, which can be compared to estimates based on measurements of other CKM elements that are measured in loop-level processes, and thus are more likely to be affected by BSM effects [?]. The current, worldwide combination of direct measurements, published by the CKMFitter group, is $\gamma = (72.1^{+5.4}_{-5.7})^\circ$, to be compared with the estimate from loop-level observables of $\gamma = (65.66^{+0.90}_{-2.65})^\circ$ [?]. Other world averages exist [?, ?], but the overall picture is the same: the ability to constrain BSM physics is currently limited by the uncertainty of the direct measurements. Hence further precision measurements of γ are highly motivated. Presently, the precision is driven by time-integrated measurements of direct CP -violation in $B^\pm \rightarrow DK^\pm$ decays;

Not sure if I should spend time explaining the non-gamma measurements entering?

²It is generally true that all phases of a single term in a given amplitude will be convention dependent, but that the phase differences between terms are not.

³Other variants of the Wolfenstein parameterisation do exist [?]. They all agree at the lowest orders of λ .

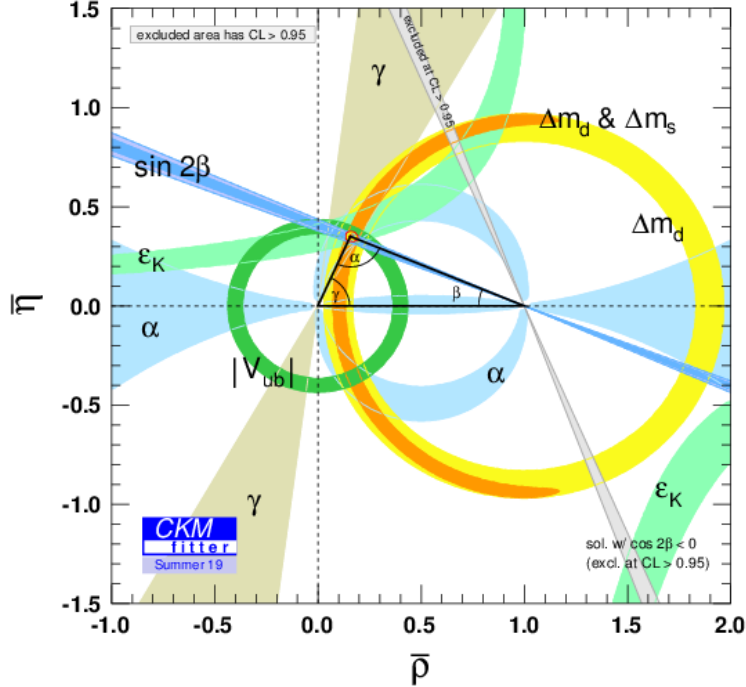


Figure 2.2: Current constraints on the Unitarity Triangle parameters as determined by the CKMFitter group for the EPS 2019 conference [?].

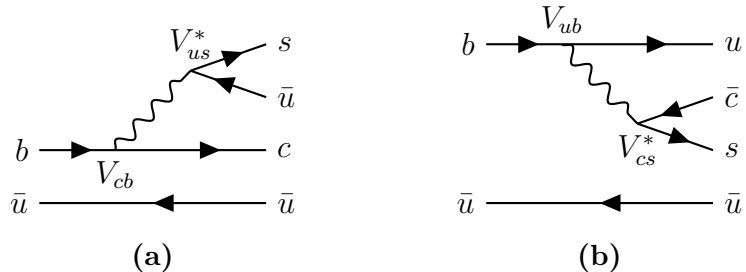


Figure 2.3: Tree level Feynman diagrams describing (a) $B^- \rightarrow D^0 K^-$ and (b) $B^- \rightarrow \bar{D}^0 K^-$ decays. The electro-weak phase difference between the two decays is $\Delta\phi = \arg(V_{cb}V_{us}^*/V_{ub}V_{cs}^*) \simeq \gamma$.

such a measurement is the topic of this thesis and the theory behind is treated in detail in the following section. It is also possible to measure γ in time-dependent mixing analyses of $B_s^0 \rightarrow D_s^\mp K^\pm$, $B^0 \rightarrow D^\mp \pi^\pm$ and related decays, by measuring CP violation in interference between mixing and decay. These modes are expected to provide competitive measurements in the future [?, ?].

301 2.2.2 Measuring γ in tree level decays

302 The phase γ can be measured in tree-level processes with interference between
 303 $b \rightarrow c\bar{s}u$ and $b \rightarrow \bar{c}s u$ transitions. The canonical example, also the subject
 304 of this thesis, is based on measurements sensitive to interference between the
 305 $B^\pm \rightarrow D^0 K^\pm$ and $B^\pm \rightarrow \bar{D}^0 K^\pm$ decay amplitudes. As illustrated in Fig. 2.3 for
 306 the case of B^- decays, the electro-weak phase difference between the two decays
 307 is $\Delta\phi = \arg(V_{cb}V_{us}^*/V_{ub}V_{cs}^*)$. While $\Delta\phi$ is not identical to the definition of γ in
 308 Eq. (2.10), the ratio of the involved CKM matrix elements is [?]

$$\begin{aligned} -\frac{V_{cd}^*/V_{ud}^*}{V_{us}^*/V_{cs}^*} &= -\frac{-\lambda[1 - \frac{\lambda^4}{2}A^2(1 - 2(\rho - i\eta))](1 - \frac{\lambda^2}{2} - \frac{\lambda^4}{8}(1 + 4A^2))}{\lambda(1 - \frac{\lambda^2}{2} - \frac{\lambda^4}{4})} \\ &= 1 - \lambda^4 A^2(1 - 2(\rho - i\eta)) + \mathcal{O}(\lambda^5). \end{aligned} \quad (2.11)$$

309 The ratio equals unity to $\mathcal{O}(\lambda^4) \simeq 2.6 \times 10^{-3}$, and thus $\Delta\phi \simeq \gamma$ is a good
 310 approximation within current experimental uncertainties. For the remainder of this
 311 thesis the approximation will be used without further comment. The diagrams in
 312 Fig. 2.3 describe the leading order contributions to the two amplitudes

$$\begin{aligned} A[B^- \rightarrow D^0 K^-] &\equiv A_B \\ A[B^- \rightarrow \bar{D}^0 K^-] &\equiv \bar{A}_B \equiv r_B A_B e^{i(\delta_B - \gamma)}, \end{aligned} \quad (2.12a)$$

313 where the last equality introduces two new parameters: the amplitude magnitude
 314 ratio $r_B \equiv |\bar{A}_B|/|A_B|$, and δ_B , the strong-phase difference between the decay
 315 amplitudes. Since all CP -violation is attributed to the electro-weak phase in the
 316 SM, the CP -conjugate decay amplitudes are [?]

$$\begin{aligned} A[B^+ \rightarrow \bar{D}^0 K^+] &= A_B \\ A[B^+ \rightarrow D^0 K^+] &= \bar{A}_B = r_B A_B e^{i(\delta_B + \gamma)}. \end{aligned} \quad (2.12b)$$

317 In an experimental setting, the D^0 and \bar{D}^0 mesons are reconstructed in some
 318 final state, f or its CP -conjugate \bar{f} . In analogy with the B^\pm decays, the D
 319 decay amplitude can be related⁴

$$\begin{aligned} A[D^0 \rightarrow f] &= A[\bar{D}^0 \rightarrow \bar{f}] = A_D \\ A[\bar{D}^0 \rightarrow f] &= A[D^0 \rightarrow \bar{f}] = r_D A_D e^{i\delta_D}. \end{aligned} \quad (2.13)$$

320 where the assumption has been made that CP violation in the D decays is negligible,
 321 and δ_D denotes a CP -conserving strong-phase difference. While CP -violation in

⁴In this notation δ_D is thus phase of the suppressed D -decay amplitude minus the phase of the favoured D -decay amplitude. This is the opposite convention to that used in the LHCb measurements with the ADS technique, but aligns with the notation used in the literature on γ measurements in $D \rightarrow K_S^0 \pi^+ \pi^-$ decays.

³²² D decays has recently been measured [?], the size of the effect is small and it is
³²³ considered negligible in this thesis. Based on Eqs. 2.12 and (2.13), the decay rates
³²⁴ of B^+ and B^- mesons into the possible final states can be seen to satisfy

$$\Gamma(B^- \rightarrow D(\rightarrow f)K^-) \propto 1 + r_D^2 r_B^2 + 2r_B r_D \cos [\delta_B + \delta_D - \gamma], \quad (2.14a)$$

$$\Gamma(B^+ \rightarrow D(\rightarrow \bar{f})K^+) \propto 1 + r_D^2 r_B^2 + 2r_B r_D \cos [\delta_B + \delta_D + \gamma], \quad (2.14b)$$

$$\Gamma(B^- \rightarrow D(\rightarrow \bar{f})K^-) \propto r_D^2 + r_B^2 + 2r_B r_D \cos [\delta_B - \delta_D - \gamma], \quad (2.14c)$$

$$\Gamma(B^+ \rightarrow D(\rightarrow f)K^+) \propto r_D^2 + r_B^2 + 2r_B r_D \cos [\delta_B - \delta_D + \gamma]. \quad (2.14d)$$

³²⁵ The processes in Eqs. (2.14a) and (2.14b) are CP -conjugate and it is clear how, in the
³²⁶ general case where $\delta_B + \delta_D \neq 0$, a non-zero value of γ leads to CP violation in the form
³²⁷ of differing decay rates. The same is true for the processes in Eqs. (2.14c) and (2.14d).
³²⁸ Depending on the choice of D final state, these expressions can be used to relate
³²⁹ γ to various observables that are experimentally accessible. This thesis concerns
³³⁰ the choice $f = K_S^0 \pi^+ \pi^-$ or $f = K_S^0 K^+ K^-$, where the terms related to the D decay
³³¹ all have a non-trivial variation over the phase space of the decay. However, it is
³³² useful to first analyse the simpler case where f is a two-body state.

³³³ The simplest case is when f is chosen to be a CP eigenstate, so that $f = \pm \bar{f}$
³³⁴ and the rate equations of (2.14a)–(2.14d) simplify, because $r_D = 1$ and $\delta_D \in \{0, \pi\}$.
³³⁵ Measurements of γ in such decay modes are denoted GLW measurements, after
³³⁶ Gronau, London, and Wyler who described the approach in the early 90ies [?, ?].
³³⁷ Experimentally it is preferable to measure yield ratios rather than absolute rates,
³³⁸ and the observables of interest are thus the CP asymmetry

$$\begin{aligned} A_{CP=\pm 1} &= \frac{\Gamma[B^- \rightarrow D_{CP} K^-] - \Gamma[B^+ \rightarrow D_{CP} K^+]}{\Gamma[B^- \rightarrow D_{CP} K^-] + \Gamma[B^+ \rightarrow D_{CP} K^+]} \\ &= \frac{\pm r_B \sin \delta_B \sin \gamma}{1 + r_B^2 \pm 2r_B \cos \delta_B \cos \gamma}, \end{aligned} \quad (2.15a)$$

³³⁹ as well as the ratio

$$\begin{aligned} R_{CP=\pm 1} &= 2 \frac{\Gamma[B^- \rightarrow D_{CP} K^-] + \Gamma[B^+ \rightarrow D_{CP} K^+]}{\Gamma[B^- \rightarrow D^0 K^-] + \Gamma[B^+ \rightarrow \bar{D}^0 K^+]} \\ &= 1 + r_B^2 \pm 2r_B \cos \delta_B \cos \gamma. \end{aligned} \quad (2.15b)$$

³⁴⁰ In practice, A_{CP} and R_{CP} are obtained from measured yield ratios that are corrected
³⁴¹ with appropriate branching fractions. A measurement of A_{CP} and R_{CP} alone is not
³⁴² sufficient to determine the underlying physics parameters (γ, r_B, δ_B) , and this is
³⁴³ not solely due to the number of parameters exceeding the number of constraints:
³⁴⁴ the equations also allow for multiple, ambiguous solutions for (γ, δ_B) . One way
³⁴⁵ to break the ambiguity, first noted in the original paper [?], is to make further

346 measurements in additional B decays. These can be described with the formalism
347 described above, but will not share the same ambiguous solutions because (r_B, δ_B)
348 are unique to a given B decay. Another method is to analyse D decay final states
349 that are not CP eigenstates.

350 A few years later, Atwood, Dunietz, and Sonis analysed an alternative choice of
351 D final states: a simultaneous analysis of a Cabibbo-favoured (CF) decay $D^0 \rightarrow f$
352 and the doubly-Cabibbo-suppressed (DCS) decay $D^0 \rightarrow \bar{f}$ into the CP conjugate
353 final state [?, ?]. Their suggested method is named the ADS method after the
354 authors. The classical example is to take $f = K^- \pi^+$ and $\bar{f} = \pi^- K^+$. The relative
355 suppression means that the r_D of Eq. (2.14) is small, typically of the same order of
356 magnitude as r_B , and thus the CP asymmetry of the suppressed decay is $\mathcal{O}(1)$:

$$\begin{aligned} A_{ADS(\bar{f})} &= \frac{\Gamma[B^- \rightarrow D(\rightarrow \bar{f})K^-] - \Gamma[B^+ \rightarrow D(\rightarrow f)K^+]}{\Gamma[B^- \rightarrow D(\rightarrow \bar{f})K^-] + \Gamma[B^+ \rightarrow D(\rightarrow f)K^+]} \\ &= \frac{r_D r_B \sin(\delta_B - \delta_D) \sin \gamma}{r_D^2 + r_B^2 + 2r_D r_B \cos(\delta_B - \delta_D) \cos \gamma}. \end{aligned} \quad (2.16a)$$

357 The large CP asymmetry is a prime feature of the ADS method. However, also the
358 suppressed-to-favoured yield ratio is sensitive to the physics parameters of interest:

$$\begin{aligned} R_{ADS(\bar{f})} &= \frac{\Gamma[B^- \rightarrow D(\rightarrow \bar{f})K^-] + \Gamma[B^+ \rightarrow D(\rightarrow f)K^+]}{\Gamma[B^- \rightarrow D(\rightarrow f)K^-] + \Gamma[B^+ \rightarrow D(\rightarrow \bar{f})K^+]} \\ &= \frac{r_B^2 + r_D^2 + 2r_D r_B \cos(\delta_B - \delta_D) \cos \gamma}{1 + r_D^2 r_B^2 + 2r_D r_B \cos(\delta_B + \delta_D) \cos \gamma}. \end{aligned} \quad (2.16b)$$

359 The interpretation of A_{ADS} and R_{ADS} in terms of (γ, r_B, δ_B) requires knowledge of
360 the r_D and δ_D parameters, but these can be measured independently. In general,
361 the constraints from a single set of ADS observables suffer the same ambiguities as
362 in the GLW case. However, unlike the GLW case, each D decay mode provides an
363 independent set of constraints, because the parameters related to the D decay vary.

364 The discussion of this section has centred on the classical case of $B^\pm \rightarrow DK^\pm$
365 decays with a two-body D final state. With minor modifications the techniques
366 have been used to make measurements of γ in B^0 decays [?], with B decay final
367 states including excited D mesons [?], excited kaons [?], or pions [?]. The decay
368 $B^\pm \rightarrow D\pi^\pm$ also is also CP -violating, although the effect is much smaller than
369 in the $B^\pm \rightarrow DK^\pm$ decay, because it is expected that $r_B^{D\pi^\pm} \simeq 0.005$ [?], whereas
370 $r_B^{DK^\pm} \simeq 0.1$. Furthermore, it is possible to use multi-body D final states. However,
371 in some cases, a better precision can then be obtained by exploiting phase-space
372 dependent decay rates. This is the topic of the next section.

373 2.3 Measuring γ using multi-body D final states

374 In multi-body D decays, the r_D and δ_D parameters of the fundamental rate equations
 375 in Eq. (2.14) vary over the phase space of the D decay. This section describes
 376 a model-independent approach to measure γ in $B \rightarrow D(\rightarrow K_S^0\pi^+\pi^-)h^\pm$ decays
 377 by exploiting this variation. The theory is identical for $D \rightarrow K_S^0K^+K^-$ decays,
 378 and similar ideas have been proposed for the $D \rightarrow K_S^0\pi^+\pi^-\pi^0$ [?] and $D \rightarrow$
 379 $2\pi^+2\pi^-$ modes [?]. First, however, the formalism for describing amplitudes of
 380 multi-body decays is briefly reviewed.

381 2.3.1 Dalitz plots and the phase space of multi-body decays

382 In general, the phase space of the n -body decay $P \rightarrow p_1 + p_2 + \dots + p_n$ consists of n
 383 four momenta, with a total of $4n$ components. The requirement that each of the final
 384 state particles is on-shell provides n constraints on these components, and energy-
 385 momentum conservation removes a further 4 degrees of freedom. If the original
 386 particle P is a scalar, the decay is isotropic, which removes an additional 3 degrees
 387 of freedom, leaving the total number of degrees of freedom at $3n - 7$. For the specific
 388 case of three-body decays, the available phase space can thus be parameterised with
 389 only two parameters. A practical and often used choice is the invariant masses

$$s_{12} = m^2(p_1 p_2) = (p_1^\mu + p_2^\mu)^2, \quad s_{13} = m^2(p_1 p_3) = (p_1^\mu + p_3^\mu)^2. \quad (2.17)$$

390 The choice of particle pairs is arbitrary, and the coordinates easily related

$$m_P^2 + m_{p_1}^2 + m_{p_2}^2 + m_{p_3}^2 = m^2(p_1 p_2) + m^2(p_1 p_3) + m^2(p_2 p_3). \quad (2.18)$$

391 A scatter plot of (s_{12}, s_{13}) values for a sample of particle decays is denoted a Dalitz
 392 plot [?]. It has the very useful feature that the presence of (narrow) resonances
 393 in the decay leads to visible bands in the scatter plot. Figure 2.4 illustrates how
 394 the limits of the Dalitz plot are defined by kinematic constraints, and shows an
 395 example of a Dalitz plot for $D \rightarrow K_S^0\pi^+\pi^-$ decays in which the $K^*(892)^\pm$ and $\rho(770)$
 396 resonances are clearly visible. The plot shows the sample of $B^+ \rightarrow D\pi^+$ decays
 397 used to make the measurement described in Chapter 5 and thus the D meson is in
 398 a superposition of D^0 and \bar{D}^0 states (as detailed in the following section).

399 In terms of the coordinates of Eq. (2.17) the differential decay rate is given by

$$d\Gamma = \frac{1}{32(2\pi)^3 m_P^3} |\mathcal{M}|^2 ds_{12} ds_{13}, \quad (2.19)$$

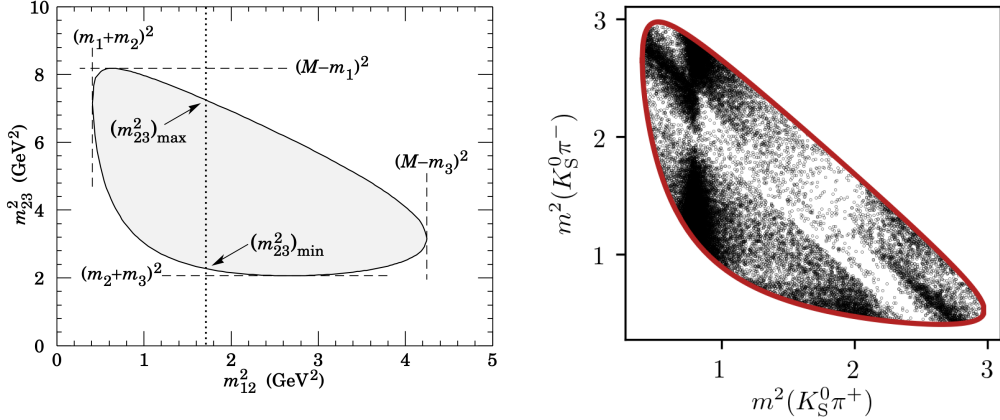


Figure 2.4: (Left) Schematic of a Dalitz plot and the limits of the kinematically allowed phase space limits. (Right) Example of a Dalitz plot for $D \rightarrow K_S^0 \pi^+ \pi^-$ decays where the D meson originates in a $B^+ \rightarrow D\pi^+$ decay; the decaying D meson is in a superposition of the D^0 and \bar{D}^0 states, but predominantly \bar{D}^0 -like.

where \mathcal{M} is the QFT matrix element, or total decay amplitude, corresponding to the decay. In general, it is not possible to calculate \mathcal{M} from first principles. Instead, a model is defined with an empirically well motivated form, in which a number of free parameters must be determined experimentally. The simplest case is that of an *isobar* model, where it is assumed that the full decay can be decomposed into consecutive two-body decays of the form $P \rightarrow R_{12}(\rightarrow p_1 + p_2)p_3$. Thus, \mathcal{M} is expressed as a non-resonant constant amplitude term, k_{NR} , plus a sum of resonance terms

$$\mathcal{M}(s_{12}, s_{13}) = k_{NR} + \sum_r k_r \mathcal{M}^r(s_{12}, s_{13}). \quad (2.20)$$

The exact form of the \mathcal{M}^r function depends on the resonance in question. An overview is given in the PDG review on resonances and references therein [?]. The isobar formalism breaks down when resonances in the decay are not well separated. In this case, models of the form in Eq. (4.27) can still be employed, if the contribution from overlapping resonances are collected in a single term. An example of such a model, is the amplitude model for $D^0 \rightarrow K_S^0 \pi^+ \pi^-$ decays developed by the Belle collaboration for a measurement of the CKM angle β in 2018 [?]. In this model, individual terms are included for $D^0 \rightarrow K^*(\rightarrow K_S^0 \pi^\pm)\pi^\mp$ decays, whereas the $\pi\pi$ and $K\pi$ S -wave contributions are modelled with the so-called K -matrix- and LASS formalisms [?, ?]. The amplitude and phase of \mathcal{M} as predicted by this model are shown in Fig. 2.5.

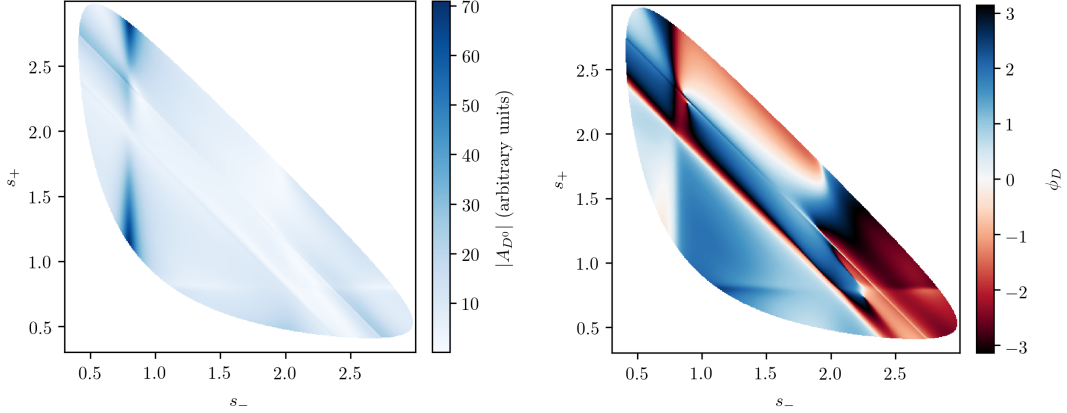


Figure 2.5: The (left) magnitude and (right) phase of the $D \rightarrow K_S^0 \pi^+ \pi^-$ amplitude in the Belle 2018 model [?].

2.3.2 The GGSZ method to measure γ

The non-trivial phase-space dependence of the $D \rightarrow K_S^0 \pi^+ \pi^-$ decay amplitude can be exploited to measure γ with $B^\pm \rightarrow DK^\pm$ or $B^\pm \rightarrow D\pi^\pm$ decays. This approach was proposed independently by Bondar [?], and by Giri, Grossman, Soffer, and Zupan [?] after whom it takes the commonly used acronym GGSZ. For this specific decay s_- and s_+ are used to describe the Dalitz coordinates $m^2(K_S^0 \pi^-)$ and $m^2(K_S^0 \pi^+)$, respectively, and the D decay amplitude is a function of these coordinates

$$A_S^{\bar{D}}(s_-, s_+) = A(\bar{D}^0 \rightarrow K_S^0 \pi^+ \pi^-). \quad (2.21)$$

To a good approximation the K_S^0 meson is a CP eigenstate, meaning that the $K_S^0 \pi^+ \pi^-$ state is self-conjugate. Assuming this approximation to be exact, and that CP violation in the D decay is negligible, the D decay amplitude satisfies the symmetry relation

$$A_S^{\bar{D}}(s_-, s_+) = A_S^D(s_+, s_-). \quad (2.22)$$

The impact of the K_S^0 meson *not* being an exact CP eigenstate is treated in detail in Chapter 4. In order to simplify equations, the short-hand notation

$$(s_{-+}) = (s_-, s_+), \quad (s_{+-}) = (s_+, s_-), \quad (2.23)$$

will be employed for the remainder of the thesis, so that the relation in Eq. (2.22) can be expressed as $A_S^{\bar{D}}(s_{-+}) = A_S^D(s_{+-})$. Thus, the rate equations of Eq. (2.14)

433 for the $D \rightarrow K_S^0\pi^+\pi^-$ decay mode are

$$\begin{aligned} d\Gamma^-(s_{-+}) &\propto |\mathcal{A}_S^-|^2 = |A_B|^2 |A_{K_S^0}|^2 \\ &\times [|A_S^D(s_{-+})|^2 + r_B^2 |A_S^D(s_{+-})|^2 + 2r_B |A_S^D(s_{-+})| |A_S^D(s_{+-})| \\ &\times (\cos[\delta_D(s_{-+})] \cos[\delta_B - \gamma] + \sin[\delta_D(s_{-+})] \sin[\delta_B - \gamma])], \end{aligned} \quad (2.24a)$$

$$\begin{aligned} d\Gamma^+(s_{-+}) &\propto |\mathcal{A}_S^+|^2 = |A_B|^2 |A_{K_S^0}|^2 \\ &\times [|A_S^D(s_{+-})|^2 + r_B^2 |A_S^D(s_{-+})|^2 + 2r_B |A_S^D(s_{-+})| |A_S^D(s_{+-})| \\ &\times (\cos[\delta_D(s_{-+})] \cos[\delta_B + \gamma] - \sin[\delta_D(s_{-+})] \sin[\delta_B + \gamma])]. \end{aligned} \quad (2.24b)$$

434 Here, $\delta_D(s_{-+}) = \phi_D(s_{-+}) - \phi_D(s_{+-}) = -\delta_D(s_{+-})$, where $\phi_D(s_{-+})$ denotes the
 435 complex phase of the $A_S^D(s_{-+})$ amplitude, and a standard trigonometric relation
 436 have been employed to factorise the terms depending on the complex phases of the B
 437 and D decays. It can be seen that in the case where $\gamma = 0$ the B^+ and B^- decay rates
 438 are symmetric if the Dalitz coordinates are exchanged: $\Gamma^+(s_-, s_+) = \Gamma^-(s_+, s_-)$.
 439 The presence of CP violation in the B decay breaks the symmetry. Therefore it is
 440 possible to measure γ (and the nuisance parameters r_B and δ_B) from the phase-space
 441 distribution of $B^\pm \rightarrow D(\rightarrow K_S^0\pi^+\pi^-)K^\pm$ decays, given knowledge of $A_S^D(s_{-+})$.

442 A series of measurements of γ have been made that use amplitude models of
 443 the D decay [?, ?, ?, ?, ?, ?, ?, ?, ?]. However, a model-independent approach has been
 444 proposed by Bondar and Poluektov [?, ?] that relies on binning phase-space, in
 445 which case the necessary information on the D decay amplitude can be summarised
 446 in a small set of coefficients that can be measured in a separate experiment. That is
 447 the approach followed in this thesis, and has been used previously by the Belle [?]
 448 and LHCb collaborations [?]. It is described in detail in the following section.

449 Such a model-independent approach is favourable for two reasons. Firstly,
 450 uncertainty estimates related to model inputs and the choice of parameterisation in
 451 an amplitude model are non-trivial, yet would become the leading systematic with
 452 the very high precision expected for γ measurements in the near future. Secondly,
 453 amplitude models are notoriously hard to reproduce, and in a high-precision era it
 454 is favourable that any experiment is easy to reinterpret in various extensions of the
 455 SM. This is a lot easier for an experiment that measures a small set of well-defined
 456 observables, than for an experiment that fits a complicated amplitude model.

457 An alternative model-independent approach has recently been proposed by
 458 Poluektov [?] where the externally measured input on the D -decay phase are Fourier
 459 expansion coefficients, and which therefore avoids binning phase space; this approach
 460 may have the potential to improve the obtainable precision in the future.

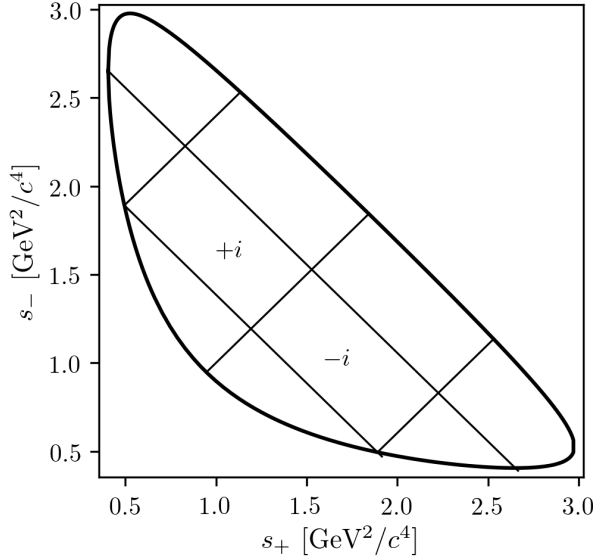


Figure 2.6: Illustration of the binning scheme used in GGSZ measurements: the bins are symmetric around the $m^2(K_S^0\pi^+) = m^2(K_S^0\pi^-)$ diagonal, and numbered so that opposite bins have the same number, but with opposite sign.

2.3.3 A model-independent approach

The phase-space distribution can be analysed in a model-independent way, if the D -decay phase space is split into regions, or bins, and the B decay yield in each bin determined experimentally. A measurement of γ using this approach is the main topic of the thesis. This section describes the fundamental principle, whereas the details pertaining to the exact experimental approach are delegated to Section 2.4.

The amplitude symmetry of Eq. (2.22) is exploited by defining $2N$ bins to be symmetric around the $s_- = s_+$ diagonal of the Dalitz plot, numbered $i = -N$ to N (omitting zero) such that if the point (s_-, s_+) is in bin i , then (s_+, s_-) is in bin $-i$, and by convention $i > 0$ for bins where $s_- > s_+$. The principle is illustrated in Fig. 2.6, but the binning schemes used in actual measurements are more complicated. The decay rates in Eq. (2.24) can be integrated over such bins, and give the bin yields

$$\begin{aligned} N_i^- &\propto h^- \left[K_i + r_B^2 K_{-i} + 2\sqrt{K_i K_{-i}} (c_i x_- + s_i y_-) \right], \\ N_i^+ &\propto h^+ \left[K_{-i} + r_B^2 K_i + 2\sqrt{K_i K_{-i}} (c_i x_+ - s_i y_+) \right], \end{aligned} \quad (2.25)$$

where the parameters describing the B decay have been expressed in terms of the observables

$$x_\pm = r_B \cos(\delta_B \pm \gamma), \quad y_\pm = r_B \sin(\delta_B \pm \gamma), \quad (2.26)$$

⁴⁷⁶ and a number of phase-space integrated quantities related to the D -decay have
⁴⁷⁷ been introduced. The K_i parameters denote fractional yield of a flavour-tagged
⁴⁷⁸ D^0 decaying into bin i , defined as

$$K_i = \frac{1}{N_K} \int_i ds^2 |A_S^D(s_{-+})|^2, \quad N_K = \int ds^2 |A_S^D(s_{-+})|^2, \quad (2.27)$$

⁴⁷⁹ where $\int_i ds^2$ denotes integration over bin i of the Dalitz plot. The c_i and s_i denote
⁴⁸⁰ the amplitude-weighted average of $\cos \delta_D(s_{-+})$ and $\sin \delta_D(s_{-+})$ over bin i

$$\begin{aligned} c_i &= \frac{\int_i ds^2 |A_S^D(s_{-+})| |A_S^D(s_{-+})| \cos[\delta_D(s_{-+})]}{\sqrt{\int_i ds^2 |A_S^D(s_{-+})|^2} \sqrt{\int_i ds^2 |A_S^D(s_{-+})|^2}}, \\ s_i &= \frac{\int_i ds^2 |A_S^D(s_{-+})| |A_S^D(s_{-+})| \sin[\delta_D(s_{-+})]}{\sqrt{\int_i ds^2 |A_S^D(s_{-+})|^2} \sqrt{\int_i ds^2 |A_S^D(s_{-+})|^2}}. \end{aligned} \quad (2.28)$$

⁴⁸¹ By the symmetry properties of $\delta_D(s_{-+})$ these parameters satisfy $c_i = c_{-i}$ and
⁴⁸² $s_i = -s_{-i}$. The normalisation constants h^+ and h^- are identical in the ideal case,
⁴⁸³ but it is convenient to define them separately for practical reasons: depending on
⁴⁸⁴ the experimental setup, there may be overall production and detection asymmetries
⁴⁸⁵ that affect the total signal yields. An experimental analysis can be made insensitive
⁴⁸⁶ to these effects because they can be absorbed into the normalisation constants, as
⁴⁸⁷ long as they are constant over the D -decay phase space. This comes at the cost
⁴⁸⁸ that the information on x_\pm and y_\pm from the overall CP asymmetry is lost, but
⁴⁸⁹ Section 2.3.5 will show the loss in precision to be minimal.

⁴⁹⁰ Thus, for a set of $2N$ bins, the bin yields of Eqs. (2.25) provide $4N$ constraints
⁴⁹¹ on a total of $4N + 6$ parameters: $(h^\pm, K_i, c_i, s_i, x_\pm, y_\pm)$. However, the K_i , c_i , and
⁴⁹² s_i parameters relate only to the D decay, and can thus, in principle, be measured
⁴⁹³ in independent experiments. With such external inputs, a measurement of the
⁴⁹⁴ $B^\pm \rightarrow D(\rightarrow K_S^0 \pi^+ \pi^-) K^\pm$ yields in a set of bins can be used to constrain x_\pm and
⁴⁹⁵ y_\pm , and thereby (γ, r_B, δ_B) . The measurement presented in this thesis determines
⁴⁹⁶ the K_i parameters directly, but uses externally measured values of c_i and s_i as
⁴⁹⁷ input, as measured in quantum correlated D decays by the CLEO [?] and BESIII [?]
⁴⁹⁸ collaborations. Because these measurements are the foundation of the approach,
⁴⁹⁹ they are described in some detail in the following section. In the future, it is possible
⁵⁰⁰ that the c_i and s_i parameters may be measured in quantum-correlated D decays
⁵⁰¹ in LHCb [?], and in charm-mixing measurements [?].

2.3.4 Measuring strong-phase inputs at charm factories

The strong-phase parameters c_i and s_i have been measured by the CLEO and BESIII collaborations, using quantum correlated $D^0\bar{D}^0$ pairs from decays of the $\psi(3770)$ resonance state, itself produced in e^+e^- collisions at the resonance energy. The $\psi(3770)$ has quantum-number $C = -1$, which is conserved in the strong decay into two D mesons, and thus the two D mesons are produced in an anti-symmetric wave function. By observing the decay of one D meson into a specific final state, say a CP eigenstate, the quantum state of the other D meson can be determined. The measurement is based on decays where both D decays are reconstructed, one in the $K_S^0\pi^+\pi^-$ final state, the other in one of several different tag categories. The main principles are outlined below, but most experimental considerations and implementation details are left out for the sake of brevity.

The simplest case is when one D meson decays into a final state that uniquely tags the flavour, such as $\bar{D}^0 \rightarrow K^+e^-\bar{\nu}_e$. In that case, the D meson decaying to $K_S^0\pi^+\pi^-$ is known to be in the D^0 state and the decay rate is simply determined by $A_S^D : \Gamma(s_{-+}) \propto |A_S^D(s_{-+})|^2$. This allows for a measurement of the K_i parameters.

If one D meson is reconstructed in a CP -even state, eg. K^+K^- , or a CP -odd state, eg. $K_S^0\pi^0$, the D meson decaying to $K_S^0\pi^+\pi^-$ is known to be in a state of opposite CP . Thus, for a tag-decay of $CP = \pm 1$ the decay rate has the form

$$\Gamma_{CP=\pm 1} \propto |A_S^D(s_{-+}) \mp A_S^D(s_{+-})|^2 \quad (2.29a)$$

and the bin yields will be given by

$$M_i^\pm \propto K_i + K_{-i} \mp 2\sqrt{K_i K_{-i}} c_i. \quad (2.29b)$$

Thus a simultaneous analysis of flavour and CP tagged decays allow for a determination of the K_i and c_i parameter sets.

Finally, the case where both D mesons, for now denoted D and D' , decay into the $K_S^0\pi\pi$ final state can be considered. The total amplitudes have contributions from the case where D is in the D^0 state and D' is in the \bar{D}^0 state, as well as the opposite flavour assignment. Thus the decay rate satisfies

$$\Gamma_{CP=\pm 1} \propto |A_S^D(s_{-+})A_S^{D'}(s'_{+-}) + A_S^D(s_{+-})A_S^{D'}(s'_{-+})|^2 \quad (2.30a)$$

where s_{-+} denotes the Dalitz-plot coordinates of the D meson, and s'_{-+} those of the D' meson. Defining M_{ij} to be the yield of decays where the D decay is in bin i and the D' in bin j , the bin yields satisfy

$$M_{ij} \propto K_i K_{-j} + K_j K_{-i} - 2\sqrt{K_i K_{-i} K_j K_{-j}} (c_i c_j + s_i s_j). \quad (2.30b)$$

531 Thus, analysing these decays in addition to the CP and flavour tagged decays provide
 532 information on all of K_i , c_i , and s_i . Note, however, that Eqs. (2.29) and (2.30) are
 533 invariant under the transformation $\delta_D \rightarrow -\delta_D$. In practice, the analysis is extended
 534 in a number of ways to enhance the statistics: using "flavour-tag" states that are not
 535 exact flavour tags, such as $K^-\pi^+$, using self-conjugate multi-body D -decay final
 536 states that are not exact CP eigenstates, such as $\pi^+\pi^-\pi^0$, and using the $K_L^0\pi^+\pi^-$
 537 final state as well. However, the main principles are the same as described above.

538 The measurements of c_i and s_i are made for a range of different binning schemes.
 539 It was noted already in Ref. [?] that a rectangular binning scheme, such as the
 540 example in Fig. 2.6, does not provide the optimal sensitivity to γ . A better sensitivity
 541 can be obtained if the bins are defined such that δ_D is approximately constant over
 542 a given bin, by defining bin i out of N via the condition

$$\text{bin}_i = \{(s_-, s_+) \mid 2\pi(i - 3/2)/N < \delta_D(s_-, s_+) < 2\pi \times (i - 1/2)/N\}. \quad (2.31)$$

543 In practice, the binning scheme is defined by splitting the D -decay phase-space
 544 into quadratic *micro bins* with a width of $0.0054 (\text{GeV}/c^2)^2$ and assigning a bin
 545 number to each micro bin via the condition in (2.31) as evaluated in an amplitude
 546 model of choice. The obtained binning scheme when using an amplitude model
 547 developed by the BaBar collaboration in 2008 [?] is shown in Fig. 2.7a. In Ref [?]
 548 it was also shown that the binning can be even further optimised for sensitivity.
 549 The suggested figure of merit is

$$Q^2 = \frac{\sum_i \left(\frac{1}{\sqrt{N_i^B}} \frac{dN_i^B}{dx} \right)^2 + \left(\frac{1}{\sqrt{N_i^B}} \frac{dN_i^B}{dy} \right)^2}{\int ds^2 \left[\left(\frac{1}{|\Gamma^B(s_-)|} \frac{d|\Gamma^B(s_-)|^2}{dx} \right)^2 + \left(\frac{1}{|\Gamma^B(s_-)|} \frac{d|\Gamma^B(s_-)|^2}{dy} \right)^2 \right]} \quad (2.32)$$

550 which quantifies the statistical sensitivity for a given binning, relative to the one
 551 achievable in an unbinned analysis. The CLEO collaboration defined an *optimal*
 552 binning scheme by an iterative procedure where, starting from the equal binning
 553 scheme, a micro-bin is randomly reassigned new bin numbers in each step, and a
 554 step accepted if Q^2 increases. The optimisation is done for the case where $x = y = 0$
 555 and thus Q^2 simplifies to $Q_{x=y=0}^2 = \sum_i N_i^{x=y=0} (c_i^2 + s_i^2) / N_{\text{total}}^{x=y=0}$. The resulting
 556 binning scheme is shown in Fig. 2.7b. An additional binning scheme is defined,
 557 denoted the *modified optimal* scheme and shown in Fig. 2.7c, where the Q^2 figure
 558 of merit is modified to take into account the presence of backgrounds [?]. The
 559 modified optimal binning scheme has proven beneficial to use in measurements with
 560 small signal yields [], but is not employed in the present thesis.

Where exactly is this phase sign known from?
Is the overall sign not arbitrary in amplitude models?

Table 2.1: The experimentally measured c_i and s_i values used in the thesis. The $D \rightarrow K_S^0\pi^+\pi^-$ values are the combined values from the BESIII and CLEO measurements published by BESIII [?]. The $D \rightarrow K_S^0K^+K^-$ values are measured by CLEO [?].

Optimal binning scheme: $D \rightarrow K_S^0\pi^+\pi^-$		
Bin i	c_i	s_i
1	-0.037 ± 0.049	0.829 ± 0.097
2	0.837 ± 0.067	0.286 ± 0.152
3	0.147 ± 0.066	0.786 ± 0.154
4	-0.905 ± 0.021	0.079 ± 0.059
5	-0.291 ± 0.041	-1.022 ± 0.062
6	0.272 ± 0.082	-0.977 ± 0.176
7	0.918 ± 0.017	-0.184 ± 0.065
8	0.773 ± 0.033	0.277 ± 0.118

2-bins binning scheme: $D \rightarrow K_S^0K^+K^-$		
Bin i	c_i	s_i
1	0.818 ± 0.107	-0.445 ± 0.215
2	-0.746 ± 0.083	-0.229 ± 0.220

Both the CLEO and BESIII collaborations have measured the values of c_i and s_i for the equal, optimal, and modified optimal binning schemes. The results are also shown in Fig. 2.7, where they are compared to the expectation from the latest amplitude model [?]. The measurements presented in this thesis are based on a combination of the BESIII and CLEO results for the optimal binning scheme, made by the BESIII collaboration [?] and tabulated in Table 2.1.

While the *definition* and *optimisation* of these binning schemes depend on knowledge of $A_S^D(s_-, s_+)$ via an amplitude model, it is important to note that no model information is needed when the binning schemes are used in the subsequent measurements of strong-phases⁵ or CP -observables. Therefore the measurements will not be biased by any modelling imperfections, although the obtained precision might be lower than expected.

The preceding discussion has been focusing on the $D \rightarrow K_S^0\pi^+\pi^-$ channel, however the $D \rightarrow K_S^0K^+K^-$ channel can be analysed completely analogously. The CLEO collaboration measure c_i and s_i values for this mode as well, in three binning schemes [?]. These are all equal-phase binning schemes, with 2, 3, and 4 bins,

⁵With the exception of minimal model-dependence introduced when the $K_L^0\pi^+\pi^-$ final state is employed to constrain the s_i parameters by the D -factories [?, ?], the impact of which is well under control.

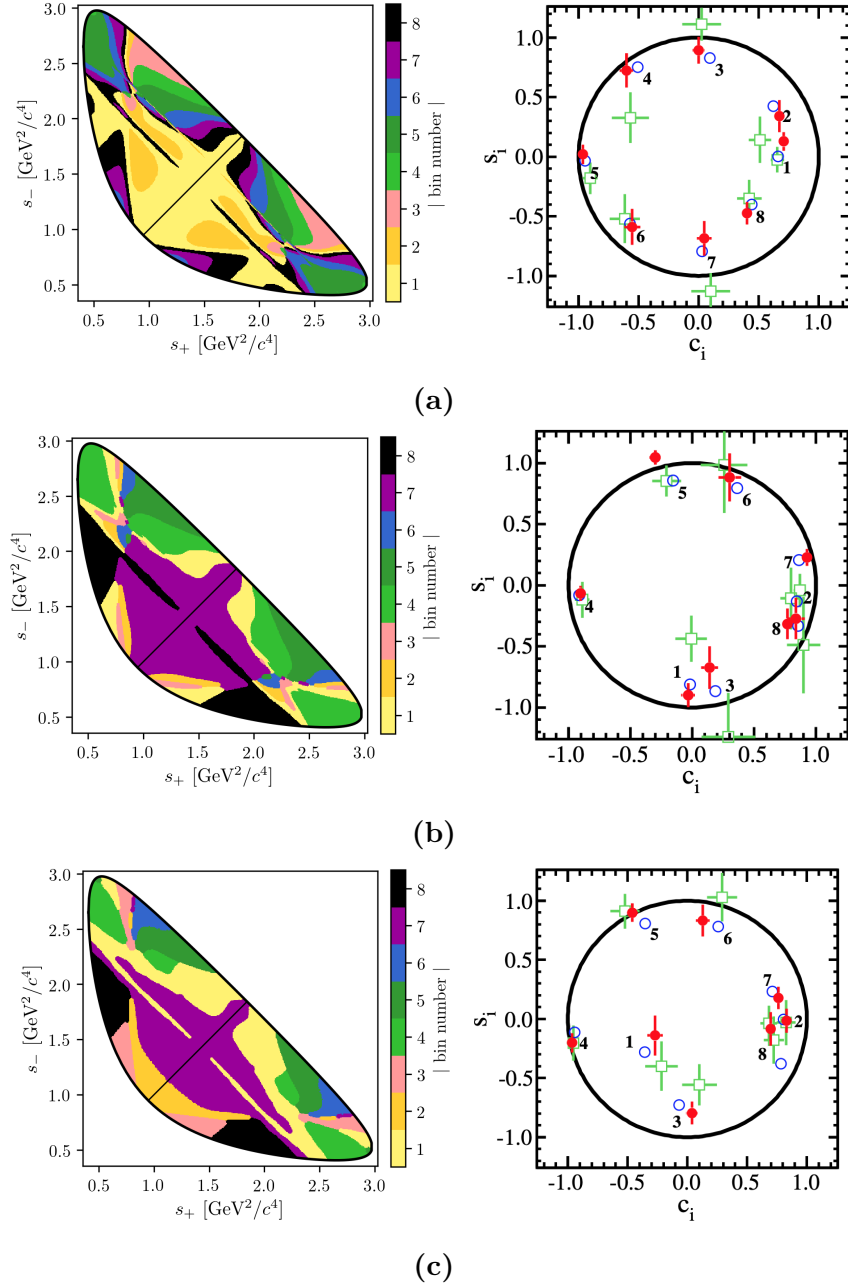


Figure 2.7: The (left) binning schemes and (right) measured values of (c_i, s_i) for (a) equal, (b) optimal, and (c) modified optimal binning schemes for $D \rightarrow K_S^0 \pi^+ \pi^-$ decays. The plots of the measured values are taken from Ref. [?] and show the results obtained by (red) BESIII, (green) CLEO, and (blue) the model expectation using the model from Ref. [?]. The measurement featured in this thesis used the optimal binning scheme.

respectively, shown in Fig. 2.8. The $D \rightarrow K_S^0 K^+ K^-$ decay amplitude is almost completely dominated by two $K^+ K^-$ resonances, the CP -odd $\phi(1020)$ and the CP -even $a_0(980)$, and this means that very little gain in sensitivity can be made by altering the equal-phase binning schemes. The measured c_i and s_i values are also shown in Fig. 2.8 and tabulated in Table 2.1 for the 2-bins scheme, which is used in this thesis. A BESIII measurement is in preparation, but has not been finished at the time of writing.

2.3.5 Global CP asymmetry and the relation to GLW and ADS measurements

The introduction of separate normalisation factors h^+ and h^- in Eq. (2.25) hides the fact that information on γ (in principle) can be obtained from the asymmetry in phase-space-integrated B^+ and B^- yields. In the ideal case where $h^- = h^+$ the total yield asymmetry is

$$\begin{aligned} A_{GGSZ} &= \frac{\sum_i N_- - N_i^+}{\sum_{i=-N}^N N_i^- + N_i^+} = \frac{\sum_{i=-N}^N \sqrt{K_i K_{-i}} c_i (x_- - x_+)}{1 + r_B^2 + 2 \sum_{i=-N}^N \sqrt{K_i K_{-i}} c_i (x_- + x_+)} \\ &= \frac{2 \sum_{i=1}^N \sqrt{K_i K_{-i}} c_i (x_- - x_+)}{1 + r_B^2 + 4 \sum_{i=1}^N \sqrt{K_i K_{-i}} c_i (x_- + x_+)}, \end{aligned} \quad (2.33)$$

where it has been exploited that $\sum_{i=-N}^N \sqrt{K_i K_{-i}} s_i = 0$ by definition. The size of the asymmetry is governed by the factor $\sum_{i=1}^N \sqrt{K_i K_{-i}} c_i$, which is small for $D \rightarrow K_S^0 \pi^+ \pi^-$ and $D \rightarrow K_S^0 K^+ K^-$ decays. The underlying reason is that $\delta_D(s_-, s_+)$ varies significantly across phase-space for these decays, as evident by the spread in the values of c_i in Table 2.1, which reduces the *average* of the asymmetry-generating $D^0 - \bar{D}^0$ interference term to being close to zero. The value of $\sum_{i=-N}^N \sqrt{K_i K_{-i}} c_i$ is closely related to the CP content of the final state in question: for a self-conjugate CP even (odd) final state

$$A_{D^0}(s_-, s_+) = {}^{(+)}_{(-)} A_{\bar{D}^0}(s_-, s_+) = {}^{(+)}_{(-)} A_{D^0}(s_+, s_-) \quad (2.34)$$

and thus $\sum_{i=1}^N \sqrt{K_i K_{-i}} c_i = {}^{(+)}_{(-)} 1$. This motivates the definition of the CP -even fraction of the decay

$$\mathcal{F}_+ \equiv \frac{1}{2} \left(1 + \sum_{i=1}^N \sqrt{K_i K_{-i}} c_i \right). \quad (2.35)$$

With \mathcal{F}_+ in hand, the asymmetry in Eq. (2.33) can be rewritten

$$A_{GGSZ} = \frac{(2\mathcal{F}_+ - 1)r_B \sin \delta_B \sin \gamma}{1 + r_B^2(2\mathcal{F}_+ - 1)2r_B \cos \delta_B \cos \gamma}, \quad (2.36)$$

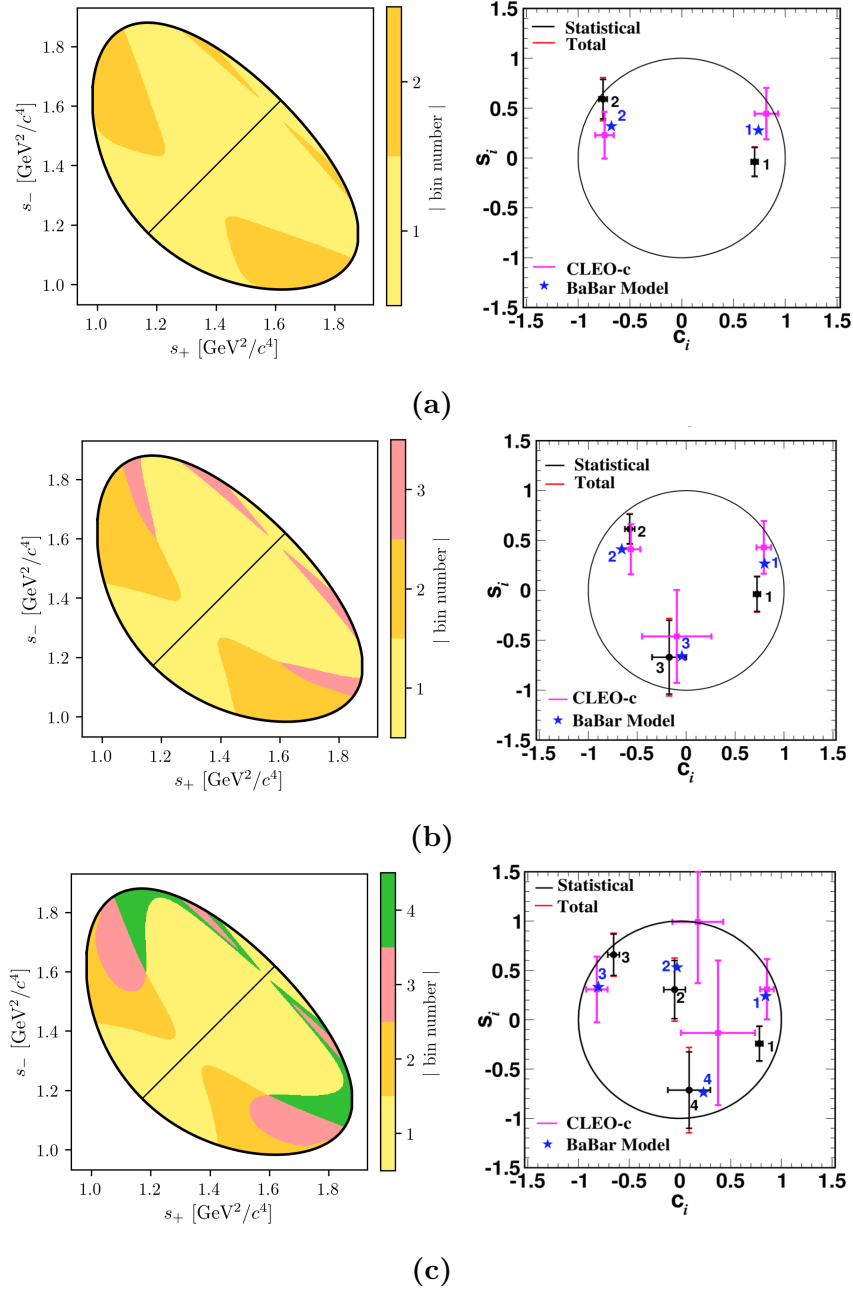


Figure 2.8: The (left) binning schemes and (right) measured values of (c_i, s_i) for the (a) 2-, (b) 3-, and (c) 4-bins binning schemes for $D \rightarrow K_S^0 K^+ K^-$ decays. The plots of the measured values are taken from Ref. [?] and show the (error bars) results obtained by (black) BESIII, (pink) CLEO, and (blue) the model expectation using the model from Ref. [?]. The measurement featured in this thesis uses the 2-bins scheme.

which is the usual form used in quasi-GLW measurements []; for $N = 1$ the definition in Eq. (2.35) is equivalent to \mathcal{F}_+ as defined in Ref. []. The value of \mathcal{F}_+ is independent of the number and shape of bins in a given binning scheme, as long as the bin definitions follow the symmetry principles outlined in Section 2.3.3. For $D \rightarrow K_S^0\pi^+\pi^-$ and $D \rightarrow K_S^0K^+K^-$ decays the values of \mathcal{F}_+ are

$$\begin{aligned}\mathcal{F}_+(K_S^0\pi^+\pi^-) &= X? \\ \mathcal{F}_+(K_S^0K^+K^-) &= X?\end{aligned}\tag{2.37}$$

as evaluated with the Belle 2018 model for $D \rightarrow K_S^0\pi^+\pi^-$ decays and the BaBar 2010 model for $D \rightarrow K_S^0K^+K^-$ decays. Since $r_B^{DK^\pm} \sim 0.1$ the predicted global asymmetries are thus approximately 1–2 %, which is not resolvable with the current experimental yields. As shown in Chapter 4, CP violation in the K_S^0 sector leads to asymmetries of a similar size, further complicating the use of global asymmetries to constrain x_\pm and y_\pm . Thus these modes are ill-suited for quasi-GLW measurements, and ignoring global asymmetries leads to a negligible loss of information on γ in a GGSZ measurement. The reverse is true for a well-suited quasi-GLW mode, such as $D \rightarrow \pi^+\pi^-\pi^0$: if \mathcal{F}_+ is close to either zero or unity, it means that (c_i, s_i) will be close to $(\pm 1, 0)$ in all bins for *any* given binning scheme, and the set of bins will provide almost identical constraints on x_\pm and y_\pm . Thus, the binning of phase space leads to no significant gain in precision compared to a global analysis.

Indeed, a crucial quality of the GGSZ method, is that exactly because each bin-pair provides independent constraints on x_\pm and y_\pm , the method provides a single solution for (γ, r_B, δ_B) that does not suffer the ambiguities of the ADS and GLW approaches. In order to illustrate this further, it is useful to make one more comparison of the model-independent GGSZ formalism to the ADS and GLW formalisms. If there was no CP symmetry the B^+ yield in bin $+i$ would equal the B^- yield in bin $-i$. Therefore the relevant CP asymmetry for a given Dalitz bin is

$$\begin{aligned}A_{GGSZ}^i &\equiv \frac{N_i^- - N_{-i}^+}{N_i^- + N_{-i}^+} \\ &= \frac{\sqrt{K_i K_{-i}}(c_i(x_- - x_+) + s_i(y_- - y_+))}{K_i + r_B^2 K_{-i} + 2\sqrt{K_i K_{-i}}(c_i(x_- + x_+) + s_i(y_- + y_+)})\end{aligned}\tag{2.38}$$

This expression is identical to the ADS asymmetry in Eq. (2.16a) if the effective D -decay parameters r_D^i and δ_D^i are defined via

$$\kappa_i \cos \delta_D^i \equiv c_i \quad , \quad \kappa_i \sin \delta_D^i \equiv s_i \quad , \quad r_D^i \equiv \sqrt{K_i/K_{-i}},\tag{2.39}$$

and a coherence factor, κ , is included in the interference terms of the ADS expression, as is standard for multi-body D decays []. These parameters allow us to classify

Table 2.2: Classification of the bins used in model-independent GGSZ measurements, in terms of whether the interplay between the D^0 and \bar{D}^0 amplitudes in the bin resemble typical GLW or ADS behaviour. The parameters are calculated using the 2018 Belle model [1] for $D \rightarrow K_S^0\pi^+\pi^-$ decays and the 2010 BaBar model [2] for $D \rightarrow K_S^0K^+K^-$ decays.

Optimal binning scheme: $D \rightarrow K_S^0\pi^+\pi^-$					
Bin i	\hat{r}_D	$\hat{\delta}_D$	\mathcal{F}_+	κ	Bin type
1	0.473	91.9°	48.97 %	0.81	Mixed
2	0.164	11.1°	63.38 %	0.85	ADS-like
3	0.157	79.4°	52.50 %	0.89	ADS-like
4	0.768	175.3°	5.85 %	0.92	GLW-odd-like
5	0.759	-99.9°	42.84 %	0.87	Mixed
6	0.223	-64.5°	57.92 %	0.87	ADS-like
7	0.651	-13.3°	89.44 %	0.89	GLW-even-like
8	1.745	21.0°	87.08 %	0.92	GLW-even-like

2-bins binning scheme: $D \rightarrow K_S^0K^+K^-$					
Bin i	\hat{r}_D	$\hat{\delta}_D$	\mathcal{F}_+	κ	Bin type
1	0.816	19.8°	86.14 %	0.78	GLW-even-like
2	0.775	154.5°	16.23 %	0.77	GLW-odd-like

629 a given pair of bins with number $\pm i$ as either *GLW-like*, if δ_D^i is close to 0 or π
 630 and r_D^i is close to unity, or *ADS-like* if $0 < r_D^i \ll 1$. The CP -even fraction of the
 631 D -decay can also be defined for a given bin-pair:

$$\mathcal{F}_+^i = \mathcal{F}_+^{-i} \equiv \frac{1}{2} \left(1 + 2c_i \frac{\sqrt{K_i K_{-i}}}{K_i + K_{-i}} \right) = \frac{1}{2} \left(1 + 2c_i \frac{r_D^i}{1 + r_D^{i/2}} \right). \quad (2.40)$$

632 A GLW-even-like bin pair will have $\mathcal{F}_+^i \simeq 1$ and a GLW-odd-like bin pair will
 633 have $\mathcal{F}_+^i \simeq 0$.

634 Table 2.2 summarises a classification of the bins for the optimal $D \rightarrow K_S^0\pi^+\pi^-$
 635 binning scheme and the 2-bins $D \rightarrow K_S^0K^+K^-$ binning scheme following these
 636 principles. Two bins are classified as *mixed* because r_D^i is not particularly small,
 637 but \mathcal{F}_+^i is close to 0.5. The fact that multiple bin types appear for both the
 638 $D \rightarrow K_S^0\pi^+\pi^-$ and $D \rightarrow K_S^0K^+K^-$ modes underline that each mode benefits from
 639 being analysed in the GGSZ formalism, and that the bins provide independent
 640 constraints, allowing for a non-ambiguous solution for (γ, r_B, δ_B) .

2.4 Strategy for the LHCb measurement

The main topic of the thesis is a model-independent GGSZ measurement using $B^\pm \rightarrow DK^\pm$ and $B^\pm \rightarrow D\pi^\pm$ decays, and the two D final states $K_S^0\pi^+\pi^-$ and $K_S^0K^+K^-$. The measurement uses the optimal binning scheme for the $D \rightarrow K_S^0\pi^+\pi^-$ mode, with the combined strong-phase inputs from the BESIII [?] and CLEO [?] collaborations published in Ref. [?]. For the $D \rightarrow K_S^0K^+K^-$ channel, the 2-bins scheme is used with the strong-phase parameters measured by the CLEO collaboration [?]. The details of the analysis are presented in Chapter (5), but the overall strategy and a few extensions of the formalism from the previous sections are given here.

Due to the geometry of the LHCb detector, the signal reconstruction efficiency for $B^\pm \rightarrow D(\rightarrow K_S^0h^+h^-)h'^\pm$ decays varies significantly across the D -decay phase space. Denoting the efficiency profile as $\eta(s_-, s_+)$, the yield equations of Eq. (2.25) are therefore modified slightly

$$\begin{aligned} N_i^- &= h^{B^-} \left[F_i + r_B^2 F_{-i} + 2\sqrt{F_i F_{-i}} (c'_i x_- + s'_i y_-) \right], \\ N_i^+ &= h^{B^+} \left[F_{-i} + r_B^2 F_i + 2\sqrt{F_i F_{-i}} (c'_i x_+ - s'_i y_+) \right], \end{aligned} \quad (2.41)$$

where the phase-space integrated quantities now include the efficiency profile

$$F_i = \frac{1}{N_F} \int ds^2 \eta(s_{-+}) |A_S^D(s_{-+})|^2, \quad N_F = \int ds^2 \eta(s_{-+}) |A_S^D(s_{-+})|^2, \quad (2.42)$$

$$c'_i = \frac{\int_i ds^2 \eta(s_{-+}) |A_S^D(s_{-+})| |A_S^D(s_{-+})| \cos[\delta_D(s_{-+})]}{\sqrt{\int_i ds^2 \eta(s_{-+}) |A_S^D(s_{-+})|^2} \sqrt{\int_i ds^2 \eta(s_{-+}) |A_S^D(s_{-+})|^2}}, \quad (2.43)$$

with an analogous definition of s'_i . At leading order, the strong-phase parameters are unaffected by the non-uniform efficiency, and, in addition, the bin definitions favour bins for which c_i and s_i take on similar values across each bin. Therefore, the c_i and s_i values reported by the charm factories are used directly in the measurement. The impact on the obtained central values is negligible, as described in detail in Section 5.6 where a systematic uncertainty is assigned.

The F_i are significantly different to the K_i due to the experimental acceptance profile in LHCb. Given external inputs for the strong-phase parameters, it is possible to fit the F_i parameters and x_\pm and y_\pm simultaneously in a fit to the LHCb $B^\pm \rightarrow DK^\pm$ data set, in which case the obtained F_i parameters incorporate the correct acceptance profile correction by construction. However, the obtainable precision for the CP observables measured by this procedure is suboptimal. As

an alternative, the first LHCb measurement [?] made a simultaneous analysis of $B^\pm \rightarrow DK^\pm$ and a much larger sample of $B^\pm \rightarrow D\pi^\pm$ decays; since the F_i parameters relate to the D decay, they can effectively be obtained in the $D\pi^\pm$ sample and shared between the two $B^\pm \rightarrow Dh^\pm$ channels. However, there is CP violation present in the $B^\pm \rightarrow D\pi^\pm$ decays, which led to a dominant systematic uncertainty. Later LHCb measurements [?, ?] instead relied on flavour tagged D mesons from $\bar{B}^0 \rightarrow D^{*+}(\rightarrow D^0\pi^+)\mu^-\bar{\nu}_\mu X$ decays to obtain F_i , where no CP violation is possible. However, due to necessarily different triggering paths and selections, the acceptance profile is not exactly identical between semi-leptonic decays and the $B^\pm \rightarrow Dh^\pm$ decays of interest. An efficiency correction based on simulation was therefore applied to obtain the correct F_i , and in this case, the uncertainty related to the correction constituted the largest systematic uncertainty on the measurement.

Both sources of systematic uncertainty can be avoided by making a simultaneous analysis of $B^\pm \rightarrow DK^\pm$ and $B^\pm \rightarrow D\pi^\pm$ decays, where CP -violating observables are measured in *both* channels and the F_i parameters are shared. Effectively, the F_i are determined in the high statistics $B^\pm \rightarrow D\pi^\pm$ channel, but with no systematic effect from CP -violation in that channel, since the CP -violation is incorporated in the yield description. At the start of the work that lead to this thesis, it was not clear to what degree the measured CP -violating observables in $B^\pm \rightarrow D\pi^\pm$ decays were affected by CP violation in the neutral kaon sector. The impact had been shown to scale as $\mathcal{O}(|\epsilon|/r_B)$ [?], which is negligible for the $B^\pm \rightarrow DK^\pm$ channel but suggests potentially large biases in the $B^\pm \rightarrow D\pi^\pm$ channel, where r_B is 20 times smaller. However, the dedicated analysis presented in Chapter 4 has proved the effect on GGSZ measurements to be in fact be *smaller* than $\mathcal{O}(|\epsilon|/r_B)$ and the simultaneous measurement is indeed viable.

The measurement is performed by making extended maximum-likelihood fits to the m_B spectra of $B \rightarrow D(\rightarrow K_S^0 h^+ h^-)h'^\pm$ candidates split by charge and Dalitz bin. The $B^\pm \rightarrow DK^\pm$ signal yields are parameterised using the expressions in Eq. (2.41) directly, thus obtaining values for x_\pm^{DK} and y_\pm^{DK} directly. The Cartesian CP -violating observables x_\pm and y_\pm are employed because they lead to better statistical behaviour than fits to data where the underlying parameters $(\gamma, r_B^{DK^\pm}, \delta_B^{DK^\pm})$ are determined [], at the cost of introducing a fourth degree of freedom. With the addition of the $B^\pm \rightarrow D\pi^\pm$ mode as a true signal channel, two new underlying parameters are introduced, $r_B^{D\pi^\pm}$ and $\delta_B^{D\pi^\pm}$. It is only necessary to introduce an additional two, not four, Cartesian parameters [?] by defining

$$\xi_{D\pi^\pm} = \left(\frac{r_B^{D\pi^\pm}}{r_B^{DK^\pm}} \right) \exp[i(\delta_B^{D\pi^\pm} - \delta_B^{DK^\pm})] \quad (2.44a)$$

704 and letting

$$x_\xi^{D\pi} = \text{Re}[\xi_{D\pi^\pm}] \quad y_\xi^{D\pi} = \text{Im}[\xi_{D\pi^\pm}]. \quad (2.44\text{b})$$

705 In terms of these parameters, the usual Cartesian x_\pm and y_\pm are given by

$$x_\pm^{D\pi} = x_\xi^{D\pi} x_\pm^{DK} - y_\xi^{D\pi} y_\pm^{DK}, \quad y_\pm^{D\pi} = x_\xi^{D\pi} y_\pm^{DK} + y_\xi^{D\pi} x_\pm^{DK}. \quad (2.45)$$

706 Using this expression, the $B^\pm \rightarrow D\pi^\pm$ yields can also be defined via Eq. (2.41) in the
707 maximum-likelihood fit. This allows for a stable fit for all six x and y parameters, as
708 well as the shared F_i , as described in much greater detail in Chapter 5. Note that ξ
709 does not depend on γ : all information on CP asymmetries in both the $B^\pm \rightarrow DK^\pm$
710 and $B^\pm \rightarrow D\pi^\pm$ channels is encoded in x_\pm^{DK} and y_\pm^{DK} .

711 The combined analysis of $B^\pm \rightarrow DK^\pm$ and $B^\pm \rightarrow D\pi^\pm$ decays presents a sig-
712 nificant step forward, because it solves the problem of obtaining F_i parameters
713 for the appropriate acceptance profile in a manner that avoids leading systematic
714 uncertainties, and almost all reliance on simulation. This is of great importance,
715 if the large data samples that will be collected by LHCb in the future are to be
716 exploited to their full potential.

3

717

718

The LHCb experiment

719 We have a detector? I thought ntuples were made of magic.

720 **3.1 Subdetectors**

721 **3.1.1 The VELO**

722 **3.1.2 Magnet and tracking stations**

723 **3.1.3 The RICH**

724 **3.1.4 Calorimeters**

725 **3.1.5 Muon detectors**

726 **3.2 Track reconstruction**

727 **3.3 The LHCb triggering system**

728 **3.3.1 The level-0 hardware trigger**

729 **3.3.2 High-level triggers**

730 **3.3.3 Offline data filtering: the LHCb stripping**

731 **3.4 Simulation**

732 A short description of truth matching: note that all simulation samples described

733 in the thesis have been truth matched appropriately.

⁷³⁴ Include a short description of RapidSim.

4

735

736

737

Neutral kaon CP violation and material interaction in BPGGSZ measurements

738 The presence of a K_S^0 meson in the $D \rightarrow K_S^0 h^+ h^-$ final states introduces a small
739 bias in BPGGSZ measurements due to CP -violation in the neutral kaon sector
740 and asymmetries caused by the interaction between the neutral kaons and detector
741 material. These fundamental physics effects are reviewed in Section 4.1, after which
742 the chapter presents a detailed analysis of the impact on the LHCb measurement
743 that is the subject of the thesis, as well as future γ measurements with the Belle II
744 experiment. Prior to this analysis, the only existing work on the effect on γ
745 measurements suggested a small effect in $B^\pm \rightarrow DK^\pm$ measurements but potentially
746 very significant effects in measurements based on $B^\pm \rightarrow D\pi^\pm$ decays [?]. However,
747 as described in Section 4.1.1, the analysis in Ref. [?] does not take into account
748 the fundamental aspect of the BPGGSZ method: that it relies on the phase-space
749 distribution of signal decays, not phase-space integrated asymmetries. Furthermore,
750 the study only considers the CP -violation effect, not material interaction. Therefore,
751 a more detailed study was necessary before the $B^\pm \rightarrow D\pi^\pm$ decay mode could
752 reliably be promoted to a signal channel.

753

754

4.1 CP violation and material interaction of neutral kaons

755

756

A brief review of the general phenomenology of mixing and CP violation in the neutral kaon system is useful, before analysing the impact on γ measurements.

757 The presentation in this section follows the PDG review of *CP violation in the
758 quark section [?]*. The general theory considers any pair of neutral mesons $|M^0\rangle$
759 and $|\bar{M}^0\rangle$ related by CP conjugation

$$CP|M^0\rangle = e^{i\phi_M}|\bar{M}^0\rangle \quad CP|\bar{M}^0\rangle = e^{-i\phi_M}|M^0\rangle, \quad (4.1a)$$

760 where ϕ_M is an arbitrary phase. In this thesis, the convention $\phi_M = 0$ is chosen
761 to equal zero, so that

$$CP|M^0\rangle = |\bar{M}^0\rangle \quad CP|\bar{M}^0\rangle = |M^0\rangle. \quad (4.1b)$$

762 A meson state that starts as a general superposition of $|M^0\rangle$ and $|\bar{M}^0\rangle$ states

$$\begin{aligned} \psi_M^0 &\equiv \psi_M(0) = a(0)|M^0\rangle + b(0)|\bar{M}^0\rangle \\ &\equiv \psi_{M^0}^0 + \psi_{\bar{M}^0}^0 \end{aligned} \quad (4.2)$$

763 will, over time, involve into a state that consists of a different superposition of
764 $|M^0\rangle$ and $|\bar{M}^0\rangle$, as well as components for all possible states the meson system
765 can decay into

$$\begin{aligned} \psi_M(t) &= a(t)|M^0\rangle + b(t)|\bar{M}^0\rangle + \sum c_i(t)f_i \\ &\equiv \psi_{M^0}(t) + \psi_{\bar{M}^0}(t) + \sum c_i(t)f_i. \end{aligned} \quad (4.3)$$

766 For time scales that are longer than the typical strong-interaction, the time evolution
767 of the M^0 - \bar{M}^0 superposition can be described by a 2×2 Hamiltonian

$$\frac{d}{dt} \begin{pmatrix} \psi_{M^0}(t) \\ \psi_{\bar{M}^0}(t) \end{pmatrix} = -i\mathcal{H}_0 \begin{pmatrix} \psi_{M^0}(t) \\ \psi_{\bar{M}^0}(t) \end{pmatrix} \quad (4.4)$$

768 that is *non-Hermitian* (to allow for decay) but can be parameterised in terms
769 of two Hermitian matrices \mathcal{M} and Γ_0

$$\mathcal{H}_0 = \mathcal{M} - \frac{i}{2}\Gamma_0. \quad (4.5)$$

770 The quantum states with well-defined (real) masses, m_j , and (real) decay widths,
771 Γ_j , are the two eigenstates of \mathcal{H}_0 with eigenvalues $\lambda_j = m_j - \frac{i}{2}\Gamma_j$. The eigenstates
772 (of course) evolve independently in time, so that

$$\psi_j(t) = e^{-i\lambda_j t}\psi_j^0 = e^{-im_j t - \frac{\Gamma_j}{2}t}\psi_j^0. \quad (4.6)$$

773 The eigenstates are denoted H and L according to the size of m_j , the real part
774 of the eigenvalues, such that $m_H > m_L$. Assuming that \mathcal{H}_0 conserves CPT the
775 eigenstates have the general form

$$\begin{aligned} |M_H\rangle &\equiv p|M^0\rangle - q|\bar{M}^0\rangle \\ |M_L\rangle &\equiv p|M^0\rangle + q|\bar{M}^0\rangle \end{aligned} \quad (4.7)$$

where p and q are complex numbers that satisfy $|q|^2 + |p|^2 = 1$. With the convention in Eq. (4.1b) it follows that if \mathcal{H}_0 also conserves CP , so that $|M_H\rangle$ and $|M_L\rangle$ are CP eigenstates, then $p = \pm q$, where the sign depends on which of the heavy and the light meson states is CP even, and which is CP odd.

The eigenstates of the Hamiltonian governing the neutral kaon system are almost, but not exactly, equal to the CP eigenstates

$$|K_1\rangle = \frac{|K^0\rangle + |\bar{K}^0\rangle}{\sqrt{2}} \quad |K_2\rangle = \frac{|K^0\rangle - |\bar{K}^0\rangle}{\sqrt{2}}, \quad (4.8)$$

which are CP even and odd, respectively. This approximate equality leads to the most prominent feature of the neutral kaon system: the two eigenstates of \mathcal{H}_0 have lifetimes that differ by orders of magnitude. This is best understood by assuming, for a moment, that the states in Eq. (4.8) *do* equal the eigenstates with definite life times. The K_1 state can decay in the CP even $\pi^+\pi^-$ and $\pi^0\pi^0$ modes, and does so almost 100% of the time; these decay modes are not available to the K_2 (in the absence of direct CP violation) which results in a much lower decay rate and much longer life time. Therefore, the eigenstates in the kaon system are labelled the *short-lived* kaon, K_S^0 , which is almost CP even, and the *long-lived* kaon, K_L^0 , which is almost CP odd. The life times are [?]

$$\tau_{K_S^0} = (8.954 \pm 0.004) \times 10^{-11} \text{s} \quad \tau_{K_L^0} = (5.116 \pm 0.021) \times 10^{-8} \text{s}. \quad (4.9)$$

Experimentally, it is found that the K_S^0 corresponds to the light eigenstate, but that the mass splitting [?]

$$\begin{aligned} \Delta m = m_{K_L^0} - m_{K_S^0} &= (0.5289 \pm 0.0009) \times 10^{10} \hbar s^{-1} \\ &\simeq 3.5 \times 10^{-6} \text{ eV} \end{aligned} \quad (4.10)$$

is tiny compared to the neutral kaon masses of $m_{K_S^0} = 497.6 \text{ MeV}/c^2$ [?].

However, the discovery of $K_L^0 \rightarrow \pi\pi$ decays by Kronin and Fitch in 1964 established that the K_S^0 and K_L^0 are *not* exactly equal to the CP eigenstates in Eq. (4.8), because the \mathcal{H}_0 relevant to the kaon system is CP -violating. The CP violation in the kaon sector is conventionally parameterised in terms of the complex parameters ϵ and ϵ' , in terms of which

$$\frac{A(K_L^0 \rightarrow \pi^+\pi^-)}{A(K_S^0 \rightarrow \pi^+\pi^-)} = \epsilon + \epsilon' \quad \frac{A(K_L^0 \rightarrow \pi^0\pi^0)}{A(K_S^0 \rightarrow \pi^0\pi^0)} = \epsilon - 2\epsilon'. \quad (4.11)$$

In these expressions ϵ denotes the contribution from CP violation in mixing and ϵ' the contribution due to direct CP violation in the decays. The ϵ parameter has been measured to be [?]

$$|\epsilon| = (2.228 \pm 0.011) \times 10^{-3}, \quad \arg \epsilon = (43.52 \pm 0.05)^\circ. \quad (4.12)$$

803 Direct CP violation is ignored for the remainder of the thesis, because ϵ' is measured
804 to be three orders of magnitude smaller than ϵ . In terms of the CP eigenstates
805 of Eq. (4.8), the mass eigenstates K_S^0 and K_L^0 are given by

$$\begin{aligned} |K_S^0\rangle &= \frac{|K_1\rangle + \epsilon|K_2\rangle}{\sqrt{1+|\epsilon|^2}} &= \frac{(1+\epsilon)|K^0\rangle + (1-\epsilon)|\bar{K}^0\rangle}{\sqrt{2(1+|\epsilon|^2)}} \\ |K_L^0\rangle &= \frac{|K_2\rangle + \epsilon|K_1\rangle}{\sqrt{1+|\epsilon|^2}} &= \frac{(1+\epsilon)|K^0\rangle - (1-\epsilon)|\bar{K}^0\rangle}{\sqrt{2(1+|\epsilon|^2)}}, \end{aligned} \quad (4.13)$$

806 corresponding to the definition $p = (1+\epsilon)/\sqrt{2(1+|\epsilon|^2)}$ and $q = (1-\epsilon)/\sqrt{2(1+|\epsilon|^2)}$
807 in Eq. (4.7).

808 In an experimental setting, the time evolution of a neutral kaon state is affected
809 by nuclear interactions with the detector. The interaction is governed by the strong
810 force, and therefore sensitive to the *flavour* of the kaon state; the interaction
811 strength is thus different for K^0 and \bar{K}^0 mesons. This difference introduces a
812 non-zero $K_S^0 \leftrightarrow K_L^0$ transition amplitude for neutral kaons traversing a detector
813 segment. This effect was predicted early in the history of kaon physics [?] and is
814 commonly denoted *kaon regeneration*. The effect can be described by including a
815 material-interaction term in the Hamiltonian that is diagonal in the $(|K^0\rangle, |\bar{K}^0\rangle)$
816 basis, so that the equation governing the time evolution is [?, ?]

$$\frac{d}{dt} \begin{pmatrix} \psi_{K^0}(t) \\ \psi_{\bar{K}^0}(t) \end{pmatrix} = -i \left[\mathcal{H}_0 + \begin{pmatrix} \chi & 0 \\ 0 & \bar{\chi} \end{pmatrix} \right] \begin{pmatrix} \psi_{K^0}(t) \\ \psi_{\bar{K}^0}(t) \end{pmatrix}. \quad (4.14)$$

817 The complex parameters χ and $\bar{\chi}$ describe the material interaction of the K^0
818 and \bar{K}^0 flavour eigenstates and are related to their scattering cross section, as
819 described further in Section 4.3.4. The solution of Eq. (4.14) for the time evolution
820 in the K_S^0 and K_L^0 states is [?]

$$\begin{aligned} \psi_S(t) &= e^{-i\Sigma t} \left(\psi_S^0 \cos \Omega t + \frac{i}{2\Omega} (\Delta\lambda\psi_S^0 - \Delta\chi\psi_L^0) \sin \Omega t \right), \\ \psi_L(t) &= e^{-i\Sigma t} \left(\psi_L^0 \cos \Omega t - \frac{i}{2\Omega} (\Delta\lambda\psi_L^0 + \Delta\chi\psi_S^0) \sin \Omega t \right), \end{aligned} \quad (4.15)$$

821 in terms of the parameters

$$\begin{aligned} \Delta\chi &= \chi - \bar{\chi}, \\ \Delta\lambda &= \lambda_L - \lambda_S = (m_L - m_S) - \frac{i}{2}(\Gamma_L - \Gamma_S), \\ \Sigma &= \frac{1}{2}(\lambda_S + \lambda_L + \chi + \bar{\chi}), \\ \Omega &= \frac{1}{2}\sqrt{\Delta\lambda^2 + \Delta\chi^2}. \end{aligned} \quad (4.16)$$

822 In the vacuum limit where $\chi = \bar{\chi} = 0$, the expressions in Eq. (4.6) and Eq. (4.15) are
823 equal.

4.1.1 A first look at the impact on γ measurements

The effects described above have an impact on measurements of CP asymmetries in modes with a neutral kaon in the final state. This was analysed for the first time in relation to γ measurements by Grossman and Savastio in 2014 [?]. The authors point out two sources of corrections to be included:

- the fact that K_S^0 is not an exact CP eigenstate can break potential symmetry relations employed in an analysis, and
- that when the neutral kaon is reconstructed in a $\pi\pi$ final state there will be contributions from both K_S^0 and K_L^0 decays.

The analysis in this chapter considers yet another effect, not treated by Grossman and Savastio, namely that

- material interaction can emulate the effect of neutral kaon CP violation, because it couples the almost- CP -even K_S^0 and the almost- CP -odd K_L^0 states.

Due to the presence of $K_L^0 \rightarrow \pi\pi$ decays, Grossman and Savastio point out that the relevant decay rates to consider in an experimental setting are of the form

$$d\Gamma(t) \propto |\psi_S(t) + \epsilon\psi_L(t)|^2. \quad (4.17)$$

The time dependence of the decay rates considered in Chapter 2 was left out because all terms shared a common time dependence. That is not the case in Eq. (4.17), due to the very different decay rates of the K_S^0 and K_L^0 components of the kaon state. As a consequence, the time-integrated yields have the form

$$N \propto \int dt \eta(t) |\psi_S(t) + \epsilon\psi_L(t)|^2, \quad (4.18)$$

where $\eta(t)$ is the time acceptance in a given experimental setting. Thus, the acceptance is crucial to model in order to correctly estimate the impact of kaon CP -violation effects on a given measurement.

Considering BPGBSZ measurements, the main effect of neutral kaon CP violation is a breakdown of the fundamental Dalitz-plot symmetry that is exploited in the derivation of the bin yield equations. Extending the amplitude definition of Eq. (2.21) to include K_L^0 decays

$$A_{S(L)}^{(\overline{D})}(s_-, s_+) = A((\overline{D})^0 \rightarrow K_{S(L)}^0 \pi^+ \pi^-), \quad (4.19)$$

the authors point out that CP -violation in the K_S^0 system means that the relation $A_S^{(\overline{D})}(s_{-+}) = A_S^D(s_{+-})$ is not exactly true; and in addition, there is now a

dependence on $A_L^D(s_{-+})$ which satisfies a different approximate symmetry, namely $A_L^{\bar{D}}(s_{-+}) \simeq -A_L^D(s_{+-})$. Grossman and Savastio describe these symmetry breaking effects in detail, but do not explicitly derive the corrections to the yield equations of Chapter 2, nor try to quantify the potential bias on γ in a measurement based on the binned yields. Instead, they derive expressions for the bias in a measurement obtained from phase-space integrated CP asymmetries. This is done for both GLW measurements that use $D \rightarrow K_S^0 X$ final states and for the $D \rightarrow K_S^0 h^+ h^-$ final states; however, for their quantitative estimate of $\Delta\gamma$ the authors make an approximation that corresponds to assuming that the $D \rightarrow K_S^0 h^+ h^-$ final state is a CP eigenstate, making the two results identical. The authors find that in this case, assuming a uniform experimental acceptance for all kaon decay times, the asymmetry has the form¹

$$A = \frac{2r_B \sin \gamma \sin \delta_B + 2\text{Re}[\epsilon]}{1 + r_B^2 - 2r_B \cos \gamma \cos \delta_B}, \quad (4.20)$$

If a measured value of A is interpreted to obtain γ without taking the ϵ term into account, it leads to a bias of

$$\Delta\gamma = -\frac{\text{Re}[\epsilon]}{r_B \cos \gamma \sin \delta_B} + O(|\epsilon|). \quad (4.21)$$

The scaling $\Delta\gamma \sim \mathcal{O}(r_B/|\epsilon|)$ is the main result of the analysis by Grossman and Savastio. For $B^\pm \rightarrow D K^\pm$ decays, where $r_B^{DK^\pm} \simeq 0.1$ this suggests a bias at the percent level, which is negligible compared to current experimental uncertainties. However, in the $B^\pm \rightarrow D \pi^\pm$ case, where $r_B^{D\pi^\pm} \simeq 0.005$ [?], their result suggests relative biases that are potentially of $\mathcal{O}(1)$.

The conclusions are lacking on two accounts, however. Firstly, as made clear in Section 2.3.5, the $K_S^0 \pi^+ \pi^-$ and $K_S^0 K^+ K^-$ states are *far from* CP eigenstates. From the asymmetry expression in that section, it is clear that the bias in a determination of γ based on phase-space asymmetries will in fact scale as

$$\Delta\gamma \sim \mathcal{O}\left(\frac{|\epsilon|}{(2\mathcal{F}_+ - 1)r_B}\right), \quad (4.22)$$

which suggests that Grossman and Savastio severely *underestimates* the potential impact. This is described in detail in Section 4.2.3. More importantly, the analysis of the phase-space integrated asymmetry is in fact *irrelevant* to BPGGSZ measurements as they are currently performed: as described in Section 2.3.5 the information from

¹In fact the expression in Eq. (4.20) is missing a term, as will be clear when an analogous expression is derived in detail in Section 4.2.3.

the global asymmetry is completely discarded. Therefore it is necessary to analyse the effects of kaon CP -violation on a full, binned analysis of $D \rightarrow K_S^0 h^+ h^-$ decays, which is done in detail in the following sections. While the aim is to extend the analysis if Grossman and Savastio, the treatment in the following sections is completely independent of that in Ref. [?].

4.2 Impact on BPGBSZ measurements of γ : principles

The analysis of the impact on BPGBSZ measurements is carried out in two stages. This section treats the leading order effects analytically, and derives the overall order of magnitude of the expected bias in a general setting. Then Section 4.3 presents a detailed numerical study of the expected effect in measurements with the LHCb and Belle II experiments specifically, because these will be crucial to constrain γ during the coming decade [?, ?].

4.2.1 Modified symmetry relations

In order to derive the corrections to the asymmetry relation $A_S^D(s_{-+}) \simeq A_S^{\bar{D}}(s_{+-})$, it is beneficial to express $A_{S(L)}^D$ in terms of the amplitudes

$$A_{1/2}^{\bar{D}} = A(\overline{D}^0 \rightarrow K_{1/2}^0 \pi^+ \pi^-), \quad (4.23)$$

because these amplitude satisfy the exact symmetries $A_1^D(s_{-+}) = A_1^{\bar{D}}(s_{+-})$ and $A_2^D(s_{-+}) = -A_2^{\bar{D}}(s_{+-})$. This approach is different to that of Grossman and Savastio, but the final results are equivalent. After the decay of a D^0 meson to a neutral kaon, the kaon state is

$$\begin{aligned} \psi^0 &= A_1^D |K_1\rangle + A_2^D |K_2\rangle \\ &= N \left[(A_1^D - \epsilon A_2^D) |K_S^0\rangle + (A_2^D - \epsilon A_1^D) |K_L^0\rangle \right], \end{aligned} \quad (4.24)$$

with the normalisation constant $N = \sqrt{1 + |\epsilon|^2}/(1 - \epsilon^2)$. Thus it can be seen that

$$\begin{aligned} A_S^D(s_{-+}) &= N \left[(A_1^D(s_{-+}) - \epsilon A_2^D(s_{-+})) \right], \\ A_L^D(s_{-+}) &= N \left[(A_2^D(s_{-+}) - \epsilon A_1^D(s_{-+})) \right], \end{aligned} \quad (4.25)$$

900 with an analogous expression for the \bar{D}^0 decay amplitudes. Therefore, the generalised
901 relations between the D^0 and \bar{D}^0 amplitudes are

$$\begin{aligned} A_S^{\bar{D}}(s_{+-}) &= N[A_1^{\bar{D}}(s_{+-}) - \epsilon A_2^{\bar{D}}(s_{+-})] \\ &= N[A_1^D(s_{-+}) + \epsilon A_2^D(s_{-+})] = A_S^D(s_{-+}) + 2N\epsilon A_2^D(s_{-+}), \\ A_L^{\bar{D}}(s_{+-}) &= N[A_2^{\bar{D}}(s_{+-}) - \epsilon A_1^{\bar{D}}(s_{+-})] \\ &= -N[A_2^D(s_{-+}) + \epsilon A_1^D(s_{-+})] = -A_L^D(s_{-+}) - 2N\epsilon A_1^D(s_{-+}). \end{aligned} \quad (4.26)$$

902 **4.2.2 Relationship between the K_S^0 and K_L^0 amplitudes**

903 The decay amplitude $A(D^0 \rightarrow K_S^0 \pi^+ \pi^-)$ has been carefully studied, and a number
904 of amplitude models have been published [?, ?, ?, ?, ?]. No models have been
905 published for $D^0 \rightarrow K_L^0 \pi^+ \pi^-$ decays. However, following an approach laid out by
906 the CLEO collaboration [?], the two amplitudes can be related. Again, this is
907 most easily done by relating the $A_1^D(s_{+-})$ and $A_2^D(s_{+-})$ amplitudes. In the isobar
908 formalism, the decay amplitude $A(D^0 \rightarrow K_1 \pi^+ \pi^-)$ is expressed as a non-resonant
909 constant amplitude plus a sum of resonances

$$A(D^0 \rightarrow K_1 \pi^+ \pi^-) = k_{NR} + \sum_{CF} k_i R^i(s_{K\pi^-}) + \sum_{DCS} k_j R^j(s_{K\pi^+}) + \sum_{R_{\pi\pi}} k_k R^k(s_{\pi^+\pi^-}). \quad (4.27)$$

910 The resonances are split into Cabibbo-favoured (CF) K^{*-} resonances, doubly
911 Cabibbo-suppressed (DCS) K^{*+} resonances and $\pi\pi$ resonances.² The CF resonances
912 couple to the \bar{K}^0 component of $K_1 (\propto K^0 + \bar{K}^0)$, and therefore the corresponding
913 k_i in the $K_2 (\propto K^0 - \bar{K}^0)$ amplitude will have a relative minus sign. The DCS
914 resonances couple to the K^0 component of K_1 , and so the corresponding k_j in the
915 K_2 amplitude will have a relative plus sign. For the $h^+ h^-$ resonances, there will be
916 a coupling to both the K^0 and \bar{K}^0 components, however the coupling to the K^0
917 component is expected to be suppressed with a Cabibbo suppression factor $r_k e^{i\delta_k}$,
918 where $r_k \simeq \tan^2 \theta_C \simeq 0.05$ is determined by the Cabibbo angle θ_C and δ_k can take
919 any value. Therefore, the k_k for these resonances have a relative $-(1 - 2r_k e^{i\delta_k})$
920 factor in the K_2 amplitude. The same effect leads to the differences in decay rates
921 between $D^0 \rightarrow K_S^0 \pi^0$ and $D^0 \rightarrow K_L^0 \pi^0$ decays [?, ?]. Thus, given a model of the

²In modern models, the $\pi\pi$ and $K\pi$ S -wave components are modelled via the K -matrix formalism and LASS parametrisations, respectively, instead of sums of individual resonances [?]. This does not alter the arguments below, as the R functions of Eq. (4.27) can equally well represent such terms.

922 form in Eq. (4.27), a model for the $A(D^0 \rightarrow K_2\pi^+\pi^-)$ amplitude will have the form

$$A(D^0 \rightarrow K_2\pi^+\pi^-) = k_{NR} + \sum_{CF} (-k_i) R^i(s_{K\pi^-}) + \sum_{DCS} (+k_j) R^j(s_{K\pi^+}) \\ + \sum_{R_{\pi\pi}} (-(1 - 2r_k e^{i\delta_k}) k_k) R^k(s_{\pi^+\pi^-}). \quad (4.28)$$

923 An important consequence of these substitution rules is that

$$A_2^D(s_{+-}) = -A_1^D(s_{+-}) + r_A \Delta A(s_{+-}), \quad (4.29)$$

924 where $r_A \simeq \tan^2 \theta_C$ and $\Delta A(s_{+-}) \sim A_1^D(s_{+-})$ are of the same order of magnitude
925 (at least when averaged over the bins used in γ measurements). This relation is
926 sufficient to make the qualitative arguments of this section, while the full set of
927 substitution rules above are used in the quantitative studies of Section 4.3.

928 4.2.3 Modification of the BPGBGSZ yield equations

929 With suitable models to calculate $A_{S(L)}^{\bar{D}}$ (or $A_{1/2}^{\bar{D}}$) and knowledge of $\Delta\chi$ for the
930 materials relevant to an experimental setting, the relations derived in the preceding
931 sections can be employed to calculate the expected phase-space bin yields, N_i^\pm ,
932 including the effects of kaon CP violation and material interaction. The decay
933 rates have additional terms compared to those in Eq. (2.24), because the K_L^0
934 contribution must be taken into account

$$d\Gamma(t, s_{+-}) \propto |\psi_S(t, s_{+-}) + \epsilon\psi_L(t, s_{+-})|^2, \quad (4.30)$$

935 where the time-dependence of $\psi_{S/L}(t, s_{+-})$ is governed by Eq. (4.15), and the phase-
936 space dependence is included in the state component, by defining $\psi_{S/L}^0$ in terms of
937 $A_{S(L)}^{\bar{D}}(s_{+-})$. For example, for the case of a $B^- \rightarrow DK^-$ decay, the definition is

$$\begin{aligned} \psi_{S/L}^{0,B^-}(s_{+-}) &= A_S^D(s_{+-}) + r_B e^{i(\delta_B - \gamma)} A_S^{\bar{D}}(s_{+-}) \\ &= A_1^D(s_{+-}) - \epsilon A_2^D(s_{+-}) + r_B e^{i(\delta_B - \gamma)} (A_1^{\bar{D}}(s_{+-}) - \epsilon A_2^{\bar{D}}(s_{+-})) \\ &= A_1^D(s_{+-}) - \epsilon A_2^D(s_{+-}) + r_B e^{i(\delta_B - \gamma)} (A_1^D(s_{+-}) + \epsilon A_2^D(s_{+-})). \end{aligned} \quad (4.31)$$

938 It is useful to look at the corrections to the BPGBGSZ yield expressions in Eq. (2.25)
939 to lowest order in ϵ and $r_\chi = \frac{1}{2} \frac{\Delta\chi}{\Delta\lambda}$, the dimensionless parameter governing material
940 interactions. For LHCb and Belle II the average $|r_\chi| \simeq 10^{-3}$, as detailed in the
941 Section 4.3. To first order in r_χ , the time-dependent kaon states within a material,
942 given in Eq. (4.15), simplify to [?]

$$\begin{aligned} \psi_S(t, s_{+-}) &= e^{-\frac{i}{2}(x+\bar{x})t} e^{-i\lambda_{St}} (\psi_S^0(s_{+-}) - r_\chi (1 - e^{-i\Delta\lambda t}) \psi_L^0(s_{+-})), \\ \psi_L(t, s_{+-}) &= e^{-\frac{i}{2}(x+\bar{x})t} e^{-i\lambda_{Lt}} (\psi_L^0(s_{+-}) + r_\chi (1 - e^{+i\Delta\lambda t}) \psi_S^0(s_{+-})). \end{aligned} \quad (4.32)$$

943 By inserting these expressions into Eq. (4.30) and employing the definition in
944 Eq. (4.31) (and a similar definition for B^+ decays), the binned yields can be
945 calculated by an integration over time and phase space. In the remainder of this
946 section, it is assumed that the experimental time acceptance is $\eta(t) = 1$ for all times
947 and that r_χ is constant at all times; more realistic assumptions are introduced in
948 Section 4.3. In this case, the binned yields are given by the expression

$$N_i^- = h_B^{-'} \left(\hat{K}_{+i} + r_B^2 \hat{K}_{-i} + 2\sqrt{\hat{K}_{+i} \hat{K}_{-i}} (x_- \hat{c}_i + y_- \hat{s}_i) + O(r\epsilon) \right), \\ N_i^+ = h_B^{+'} \left(\hat{K}_{-i} + r_B^2 \hat{K}_{+i} + 2\sqrt{\hat{K}_{+i} \hat{K}_{-i}} (x_+ \hat{c}_i - y_+ \hat{s}_i) + O(r\epsilon) \right), \quad (4.33)$$

949 where a number of new parameters have been defined, and where $O(r\epsilon)$ denotes terms
950 of $O(r_A\epsilon)$, $O(r_B\epsilon)$, $O(r_A r_\chi)$, and $O(r_B r_\chi)$. Since $r_B \sim r_A \sim 10^{-1}$ (in $B^\pm \rightarrow D K^\pm$
951 decays) and $r_\chi \sim \epsilon \sim 10^{-3}$, these terms are all of the same order of magnitude.

952 The new normalisation constants $h_B^{\pm'} = h_B^\pm (1 + |\epsilon + r_\chi|^2 \frac{\Gamma_S}{\Gamma_L} \mp \Delta h)$ are de-
953 fined in terms of

$$\Delta h = 2\text{Re}[\epsilon + r_\chi] - 4 \frac{\Gamma_S}{\Gamma_L + \Gamma_S} \frac{\text{Re}[\epsilon + r_\chi] + \mu \text{Im}[\epsilon + r_\chi]}{1 + \mu^2}, \quad \mu = 2 \frac{m_L - m_S}{\Gamma_L + \Gamma_S}. \quad (4.34)$$

954 The \hat{K}_i parameters are defined to be

$$\hat{K}_i = \frac{1}{1 + |\epsilon + r_\chi|^2 \frac{\Gamma_S}{\Gamma_L}} \left(K_i^{(1)} + |\epsilon + r_\chi|^2 \frac{\Gamma_S}{\Gamma_L} K_i^{(2)} \right), \quad (4.35)$$

955 in which the $K_i^{(1/2)}$ parameters are phase-space integrals, defined as in Eq. (2.27)
956 but for $A_{1/2}^D$. To lowest order, the \hat{K}_i correspond to the fractional D^0 decay yield
957 in each bin, as obtained in a measurement that averages D^0 and \bar{D}^0 decays, and
958 assumes the $A_S^D(s_{-+}) = A_S^D(s_{+-})$ symmetry to be exact:

$$K_i^{\text{meas}} \equiv \frac{N_i^D + N_{-i}^{\bar{D}}}{\sum_j N_j^D + N_{-j}^{\bar{D}}} = \hat{K}_i + \mathcal{O}(r\epsilon). \quad (4.36)$$

959 Here, N_i^D ($N_i^{\bar{D}}$) is the expected yield of flavour tagged D^0 (\bar{D}^0) mesons into bin
960 i of the D decay phase-space.

961 In similar fashion, the parameters (\hat{c}_i, \hat{s}_i) have been introduced to denote the
962 *measured* average strong-phases, which are expected to differ from (c_i, s_i) at $O(\epsilon)$,
963 since neutral kaon CP violation is not taken into account in the measurements
964 by CLEO. Thus, any corrections arising if (\hat{c}_i, \hat{s}_i) and (c_i, s_i) are substituted in
965 Eq. (4.33) will appear in the $O(r_B\epsilon)$ terms.

966 Two observations can be made from the expression in (4.33). The first is that
967 the phase-space *distribution* is only changed at $O(r\epsilon)$ compared to the expression in

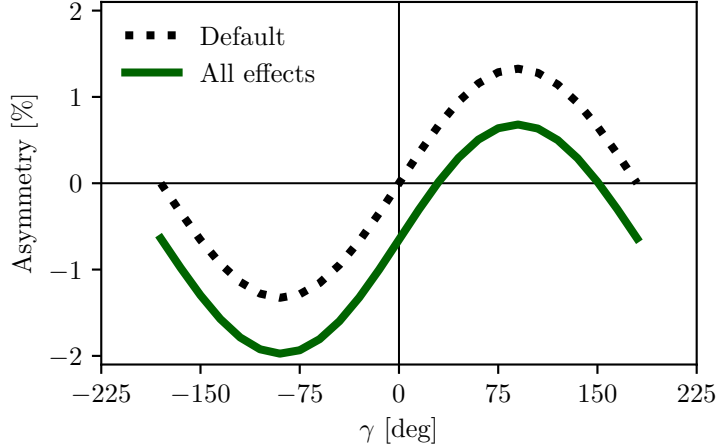


Figure 4.1: The asymmetry A_{total} as a function of γ calculated to $O(\epsilon)$ using Eq. (4.37). The calculation is made using for (black dotted line) the default case where $\Delta h = 0$ and (green) including neutral kaon CP -violation and material interaction with $r_\chi = \epsilon$.

Eq. (2.25), if the measured \hat{K}_i are used in the experimental analysis. This equally true whether the K_i are fitted in the signal channel along with x_\pm and y_\pm , as is the case in the measurement presented in the thesis, or if they are obtained in a control channel with flavour tagged D decays, according to Eq. (4.36). As the $D^0 - \bar{D}^0$ interference term that provides sensitivity to γ enters at order $O(r_B)$, the impact on γ measurements can be expected to be $\Delta\gamma/\gamma \sim O(r\epsilon/r_B)$. For $B \rightarrow DK$ analyses, where $r_B \simeq 0.1$, this is at the permille level, so the induced $\Delta\gamma$ bias can be expected to be smaller than 1° . Even in the case of $B^\pm \rightarrow D\pi^\pm$ decays, this suggests biases that are maximally a few percent. This is the main result of the chapter, because it means that the effect of neutral kaon CP violation and material interaction is small compared to the precision of the measurement that is the main subject of the thesis.

The second observation relates to potential future measurements of γ , which may also include sensitivity from the total, phase-space-integrated yield asymmetry

$$A_{\text{total}} = \frac{N^- - N^+}{N^- + N^+} = \frac{2(2\mathcal{F}_+ - 1)r_B \sin \delta_B \sin \gamma + \Delta h}{1 + r_B^2 + 2(2\mathcal{F}_+ - 1)r_B \cos \delta_B \cos \gamma} + O(r\epsilon), \quad (4.37)$$

where the definition of \mathcal{F}_+ from Section 2.3.5 has been employed. In the limit $r_B \rightarrow 0$ the expression agrees with the result for the analogous asymmetry in $D^\pm \rightarrow \pi^\pm K_S^0$ decays in Ref. [?], evaluated to $O(\epsilon)$ for an infinite and uniform time-acceptance. As hinted at above, the fact that $\mathcal{F}_+ \simeq 0.5$ means that the asymmetry due to γ being non-zero is not $\mathcal{O}(r_B)$, but of approximately the same order of magnitude as the asymmetry due to CP violation in the neutral kaon sector, governed by Δh . This is illustrated in Fig. 4.1, where the expression in Eq. (4.37) is plotted in the default

988 case where $\Delta h = 0$, using the model in Ref. [?] to calculate K_i and c_i , as well as
989 including neutral kaon CP violation and material interaction effects, calculated using
990 $r_\chi = \epsilon$, with ϵ taking the value in Eq. (4.12). The asymmetry changes significantly
991 when including the latter effects. Therefore, measurements based only on the global
992 asymmetry will suffer relative biases of tens of degrees, not a few degrees, if neutral
993 kaon CP violation and material interaction is not taken into account.

994 **4.3 Impact on BPGBSZ measurements of γ :**
995 **LHCb and Belle II measurements**

996 The previous section has established that the bias due to neutral kaon CP violation
997 and material interaction is at the sub-percent level for measurements based on
998 $B^\pm \rightarrow DK^\pm$ decays, and just a few percent in $B^\pm \rightarrow D\pi^\pm$ decays. Thus, the effects
999 only contribute a manageable systematic uncertainty in the measurement that is
1000 the subject of the thesis. However, the expected precision on γ measurements
1001 will increase significantly in the coming decade, as both the LHCb [?] and Belle
1002 II [?] collaborations expect to make BPGBSZ measurements that measure γ with
1003 a precision of 1–3°. Therefore a deeper understanding of the expected bias for
1004 these specific experiments is important.

1005 This section details a study, where the equations of the previous section are
1006 evaluated numerically to all orders, and care is taken to realistically model the
1007 experiment specific conditions. The scope of the original analysis, published in
1008 Ref. [?], was a stand-alone paper that covers both LHCb and Belle II, and which
1009 therefore does not rely on full detector simulation. Instead the following approaches
1010 are taken to model the necessary input

- 1011 • the experimental time-acceptance is modelled based on the detector geometry
1012 and typical neutral kaon momentum spectrum
- 1013 • the material interaction is included, using the material budget information
1014 available in the technical design reports on each experiment
- 1015 • both the time-acceptance and material interaction depends on the neutral
1016 kaon momentum, for which realistic distributions are estimated using the
1017 `RapidSim` simulation package [?].

1018 Each input is described in detail in the following sections. The study has been
1019 repeated to assign a systematic uncertainty to the LHCb measurement in Chapter 5,
1020 with slight adjustments to match the exact fit setup and with the inputs above
1021 extracted from full LHCb simulation. This is described further in Section 4.3.7.

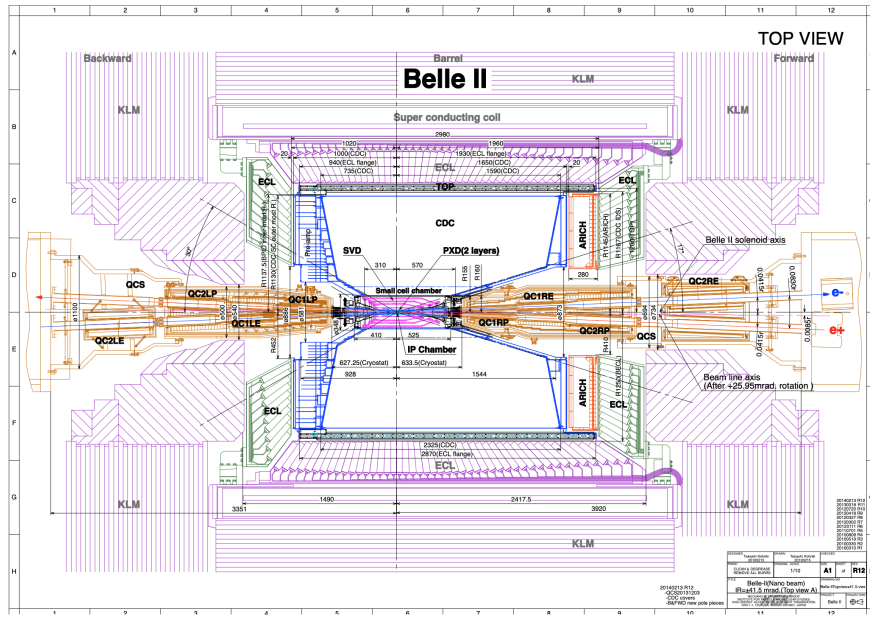


Figure 4.2: Schematic of the Belle II detector, reproduced from Ref. [?].

1022 4.3.1 Detector geometries

1023 The LHCb geometry and sub detectors are described in details in Chapter 3. In the
 1024 LHCb measurement discussed in Chapter 5, the K_S^0 mesons are reconstructed in
 1025 the $\pi^+\pi^-$ final state and two distinct categories of decay are considered, depending
 1026 on where in the detector the K_S^0 decay occurs. The categories have very different
 1027 decay-time acceptance, and therefore two scenarios are considered for LHCb: one
 1028 in which the decay products of the K_S^0 leave reconstructed tracks in both the silicon
 1029 vertex detector and downstream tracking detectors (denoted *long-long* or LL), and
 1030 one in which the decay products of the K_S^0 only leave tracks in the downstream
 1031 tracking detectors (denoted *down-down* or DD).

1032 The Belle II detector is a general purpose spectrometer, built to collect data
 1033 from asymmetric e^+e^- collisions made by the SuperKEKB accelerator in Japan [?].
 1034 A schematic of the detector is shown in Fig. 4.2. The relevant sub detectors for
 1035 the present study are the tracking detectors: a central silicon vertex detector,
 1036 comprised of a total of six layers within 140 mm of the beam, and a large volume
 1037 drift chamber with 56 wire layers, extending to a radius of 1130 mm [?]. A single
 1038 scenario is considered for Belle II, because essentially all the K_S^0 mesons produced
 1039 in signal decays in Belle II decay within the tracking volume, with more than 90 %
 1040 decaying in the vertex detector according to the studies described below. Thus,
 1041 three scenarios are considered in total: LL LHCb, DD LHCb, and Belle II.

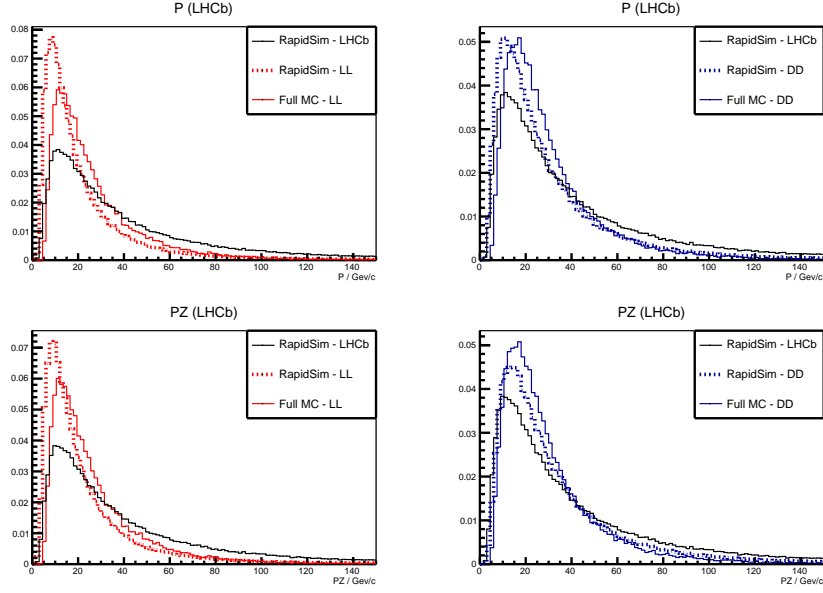


Figure 4.3: Momentum spectra for the K_S^0 meson in LHCb, as generated using **RapidSim** (black lines) directly, as well as reweighted to match decay time acceptance in the (red) LL and (blue) DD data categories of LHCb. The LHCb spectra are compared with the spectra in fully simulated signal decays, for both (dotted red lines) LL and (dotted blue lines) DD data categories.

1042 4.3.2 Kaon momentum distributions

1043 The neutral kaon momentum distributions are obtained using **RapidSim** [?], a simple
1044 tool to generate MC samples. **RapidSim** has an inbuilt capability to generate decays
1045 of B mesons with the kinematic distribution found in LHCb collisions and falling in
1046 the LHCb acceptance. However, the distributions need to be reweighted to take the
1047 kaon-decay-time acceptance into account. After being reweighted, the **RapidSim**
1048 momentum spectra are reasonably close to those found in full LHCb simulation
1049 samples of $B^\pm \rightarrow D(\rightarrow K_S^0\pi^+\pi^-)K^\pm$ decays, as seen in Fig. 4.3

1050 At Belle II, the signal B mesons stem from decays of $\Upsilon(4S)$ mesons produced in
1051 asymmetric electron-positron collisions. This leads to substantially different decay
1052 kinematics in comparison to those found at LHCb. The momentum distribution in
1053 Belle II is estimated by letting **RapidSim** decay B mesons with a momentum of 1.50
1054 GeV/ c along the z -axis using **RapidSim**, corresponding to the $\gamma\beta = 0.28$ boost of
1055 the centre-of-mass system in Belle II when operated at the $\Upsilon(4S)$ resonance [?]. A
1056 perfect 4π angular acceptance is assumed. It is not necessary to reweigh the Belle II
1057 momentum spectrum to account for the kaon-decay-time acceptance because all
1058 produced K_S^0 mesons decay in the tracking volume.

1059 The resulting momentum distributions for the three types of sample are shown in
1060 Fig. 4.4.

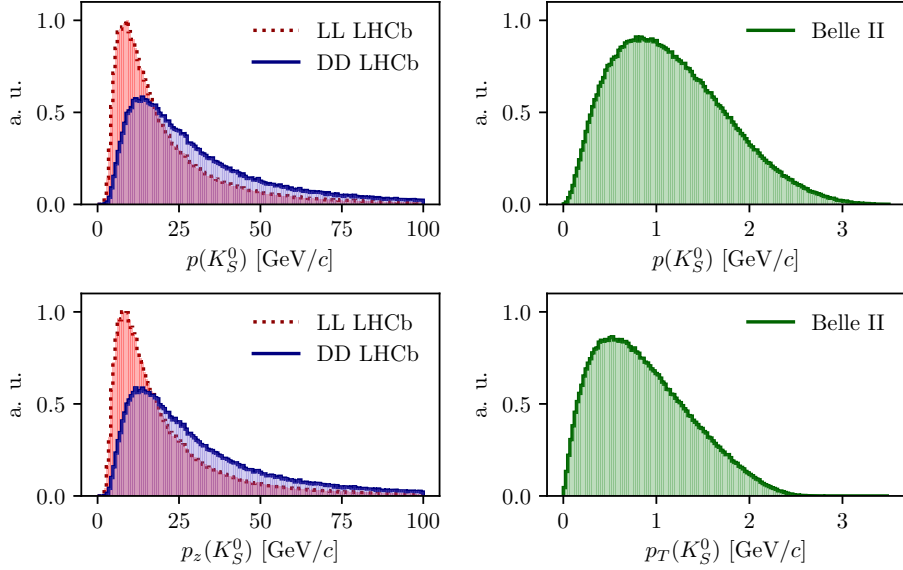


Figure 4.4: Momentum distributions for the LHCb (red dotted line) LL and (blue) DD categories, as well as (green) Belle II, obtained using `RapidSim`.

4.3.3 Experimental time acceptance

In order to model the experimental time acceptance, the time-dependent decay rates are only integrated over a finite time interval (τ_1, τ_2) . The intervals are defined for each of the three experimental categories, by requiring that a neutral kaon, if produced at $x = y = z = 0$ with momentum $p = (p_T, p_z)$, decays within the relevant part of the corresponding detector. For the LL LHCb category, it is required that the kaon decays before reaching $z_{max} = 280$ mm, corresponding to a decay where the decay products traverse at least 3 VELO segments (ignoring a number of widely spaced VELO segments placed at a distance of up to $z = 750$ mm from the interaction point) [?]. For the DD LHCb category a decay at $z \in [280, 2350]$ mm is required, corresponding to decay between the LL cut-off and the first downstream tracking station [?]. The time acceptance has a significant impact for the LHCb categories, where some 20 % of the kaons escape the tracking stations completely before decaying.

For Belle II, it is assumed that the K_S^0 reconstruction is similar to the Belle K_S^0 reconstruction, which is based on a neural network and reconstructs K_S^0 decays for which the decay product leave tracks in both the drift chamber and silicon vertex detectors, as well as decays that leave tracks in the drift chamber only [?, ?]. Therefore, the K_S^0 decay is required to be within $r_{max} = 1130$ mm of the beam axis, corresponding to a decay within the outer radius of the drift-chamber. In practice,

most of the kaons decay inside the silicon vertex detector, and requiring a decay before 1130 mm is essentially equivalent to having no time cut-off.

4.3.4 Detector material budget

The effect of the material interaction is governed by parameter $\Delta\chi$ of Eq. (4.16). The parameter varies along a given kaon path, as the kaon intersects detector components made of different materials. In these studies, the calculations are simplified by using a single average material parameter for each experimental scenario. The average material parameters can be estimated for a given experimental scenario by considering the type and length of material traversed by a kaon in the relevant sub-detector(s). The average value is estimated, by exploiting that $\Delta\chi$ is related to the forward scattering amplitude f (\bar{f}) of K^0 (\bar{K}^0) mesons in a given material [?, ?]

$$\Delta\chi = -\frac{2\pi\mathcal{N}}{m_K}(f - \bar{f}) = -\frac{2\pi(N_A\rho/A)}{m_K}(f - \bar{f}), \quad (4.38)$$

where $\mathcal{N} = N_A\rho/A$ is the scattering centre density of the material, m_K is the mass of the kaon state, A and ρ are the nucleon number and density of the material, and N_A is Avogadro's number. Measurements made for a range of nuclei [?] show that in the momentum range $p_K \in [20, 140] \text{ GeV}/c$

$$\left| \frac{f - \bar{f}}{p_K} \right| = 2.23 \frac{A^{0.758}}{p_K^{0.614}(\text{GeV}/c)} \text{ mb}, \quad \arg[f - \bar{f}] = -\frac{\pi}{2}(2 - 0.614), \quad (4.39)$$

where the phase of Δf is determined via a phase-power relation [?]. In the numerical studies presented here, Eq. (4.39) is also used for the low momentum neutral kaons in the Belle II calculations, as a more detailed modelling of the low momentum $\Delta\chi$ based on Ref. [?] is found to yield very similar results. The scattering centre density \mathcal{N} is approximated as being constant, equal to the average density along a neutral kaon path due to its intersection with different detector segments. This average is estimated using the simplifying assumption that the total detector material budget is due to silicon. In practice, $\mathcal{N} = N_A\rho/A$ is calculated using $A = 28$ and $\rho = f^{\text{Si}}\rho^{\text{Si}}$, where $f^{\text{Si}} < 1$ is the average fraction of a neutral kaon path length that is inside detector material, estimated via the known dimensions of the detector, the average nuclear interaction length seen by a track traversing it cf. the technical design reports [?, ?], and the nuclear interaction length of silicon $\lambda_I^{\text{Si}} = 465.2 \text{ mm}$ [?]. The average value of $r_\chi = \frac{1}{2}\frac{\Delta\chi}{\Delta\lambda}$, which governs the size of the matter regeneration effect, can be calculated for the three considered experimental scenarios and satisfy $|r_\chi^{\text{LL}}| = 2.7 \times 10^{-3}$, $|r_\chi^{\text{DD}}| = 2.2 \times 10^{-3}$, and $|r_\chi^{\text{Belle II}}| = 1.0 \times 10^{-3}$.

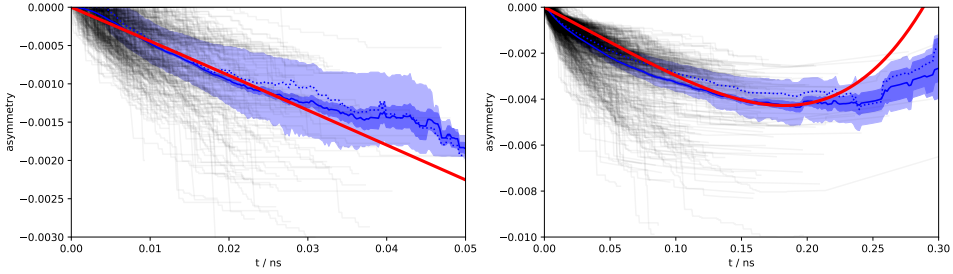


Figure 4.5: The asymmetry in Eq. (4.40) as a function of time for (left) LL and (right) DD K_S^0 tracks in a simulated LHCb sample. The black lines show individual tracks. The light blue area is the central 50 % quantile, the dark blue area is the 1σ uncertainty band on the mean. The red lines are calculated using the average $\Delta\chi$ values that are also used in the calculation of biases in BPGGSZ measurements.

The neutral kaon tracks in LHCb generally pass through somewhere between zero (for a significant amount of the LL tracks) and a hundred (for some DD tracks) distinct detector segments. Therefore it is worth examining the degree to which using a single average $\Delta\chi$ value, obtained following the procedure outlined above, provides a reasonable description of the average material interaction. This can be done using full LHCb simulation, where the kaon state for a simulated track can be evaluated at all times, by applying Eq. (4.15) iteratively for each detector segment the track traverses, using a $\Delta\chi$ value appropriate for that segment. This is done in Fig. 4.5 for a simple observable: the yield asymmetry

$$A_{K^0} = \frac{|\psi_K^0(t)|^2 - |\psi_{\bar{K}^0}(t)|^2}{|\psi_K^0(t)|^2 + |\psi_{\bar{K}^0}(t)|^2}, \quad (4.40)$$

where $\psi_K^0(t)$ ($\psi_{\bar{K}^0}(t)$) is the amplitude for an initial K^0 (\bar{K}^0) to decay to two pions at time t . In this calculation, it is assumed that $\epsilon = 0$ to isolate the material effect with no asymmetry contribution from the inherent CP -violation in the neutral kaon sector. While the track-by-track asymmetries are found to differ significantly depending on the exact detector segments a track intersects, the average asymmetry is seen to evolve smoothly as a function of decay time, and in reasonable agreement with the asymmetry value that is calculated using the average $\Delta\chi$ values estimated above.

The LHCb detector is undergoing a significant upgrade prior to the start of the LHC Run 3. However, the material budget and geometry of the relevant sub-detectors will be similar to the sub-detectors used during Run 1 and 2 [?, ?]. Hence the results of this study will be valid for measurements during the upgrade phases of LHCb, even though the detector parameters presented in this section relate to the original LHCb detector.

1133 4.3.5 Calculation procedure

1134 The main idea in the bias study is to calculate the BPGBSZ bin yields including
1135 the full effect of neutral kaon CP violation and material, fit them using the default
1136 equations of Chapter 2, and obtain the bias $\Delta\gamma = \gamma - \gamma^0$ due to the kaon effects not
1137 being considered in the parameter extraction. For the purpose of Ref. [?], a simple
1138 fit setup of a single $B^\pm \rightarrow Dh^\pm$ mode is investigated, where the K_i parameters are
1139 determined in a control channel with the relevant experimental acceptance. This
1140 setup is modified in the study used to assign a systematic uncertainty on the LHCb
1141 measurement of Chapter 5, as described in Section 4.3.7 below.

1142 In practice, the amplitude model for $D^0 \rightarrow K_S^0 \pi^+ \pi^-$ decays in Ref. [?] is taken
1143 to represent the $A_1(s_{+-})$ amplitude. Then $A_2(s_{+-})$ is obtained as described in
1144 Section 4.2.2. In terms of A_1 and A_2 , the amplitudes $A_{S(L)}^{(\bar{D})}(s_{+-})$ can be expressed
1145 and related via Eqs. (4.25) and (4.26), and the full signal decay amplitudes as a
1146 function of phase-space coordinates, time, and the material interaction parameter
1147 $\Delta\chi$ can be calculated for a given set of input parameters $(\gamma^0, r_B^0, \delta_B^0)$. The squared
1148 decay amplitudes are then integrated over phase space and the kaon decay times
1149 to obtain the binned signal yield.

1150 The signal yields depend on the momentum via the time-acceptance parameters
1151 τ_1 and τ_2 , and because the material interaction parameter $\Delta\chi$ is momentum
1152 dependent. Therefore, the yields are averaged over the K_S^0 momentum distributions
1153 of LHCb and Belle II.

1154 The parameters x_\pm and y_\pm are determined by a maximum likelihood fit to the
1155 calculated yields, after which the fit result and covariance matrix are interpreted in
1156 terms of the physics parameters (γ, r_B, δ_B) using another maximum likelihood
1157 fit [?]. In the fits, the K_i are obtained using the definition $K_i = K_i^{\text{meas}} =$
1158 $(N_i^D + N_{-i}^{\bar{D}})/(\sum_j N_j^D + N_{-j}^{\bar{D}})$, in terms of the expected yields N_i^D ($N_i^{\bar{D}}$) of a flavour-
1159 tagged D^0 (\bar{D}^0) decays in bin i of the D decay phase space, calculated as described
1160 above for $r_B^0 = 0$. This corresponds to experimentally measuring the K_i in a control
1161 channel, and takes the effect of neutral kaon CP violation and material interaction
1162 on K_i measurements into account, as well the experimental time acceptance. The
1163 (c_i, s_i) are calculated using $A_1(s_{+-})$ and the experimental time acceptance is taken
1164 into account in this calculation as well.

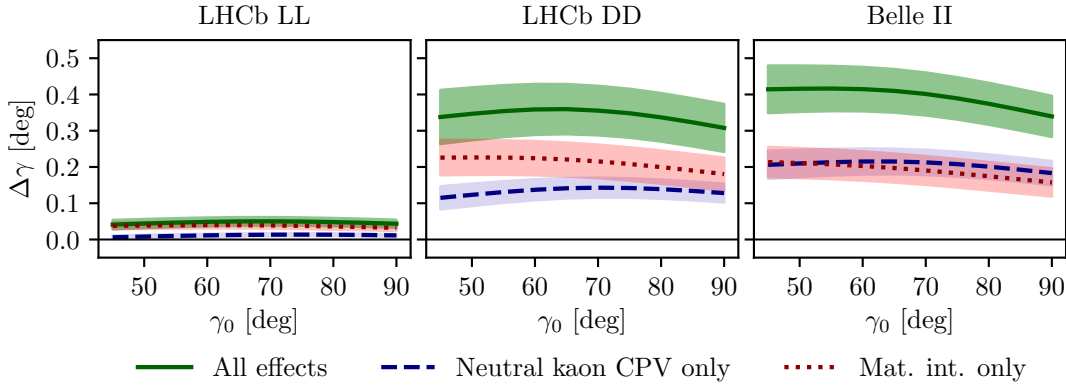


Figure 4.6: The bias $\Delta\gamma$ as a function of input γ_0 for (left) the LL LHCb category, (centre) the DD LHCb category, and (right) Belle II. The bias is calculated due to (blue, dashed line) neutral kaon CP violation alone, (red, dotted line) material interaction alone, and (green line) both effects. The shaded region shows the estimated 1σ uncertainty band.

4.3.6 Results

The obtained bias $\Delta\gamma$ is shown as a function of input γ^0 for the various experimental conditions in Fig. 4.6. The calculations are made using $(r_B^0, \delta_B^0) = (0.1, 130^\circ)$, approximately equal to the physics parameters relevant for $B^\pm \rightarrow DK^\pm$ decays [?, ?]. The bias does not vary significantly with γ^0 in the plotted range, which includes the world average value of direct γ measurements as well as the values obtained in full unitarity-triangle fits [?, ?, ?], and for all cases, the bias is found to be below 0.5° , corresponding to relative biases of about half a percent. Thus the biases are of $O(r\epsilon/r_B)$ as expected, given the arguments of Section 4.2.3. The contributions from the individual K_S^0 CPV and material interaction effects are also shown. It is seen that the neutral kaon CP violation and material interaction effects leads to approximately equal biases in all three cases.

Given the decay-time acceptance and momentum distribution for each experimental category, the mean life time, $\langle\tau\rangle$, of the reconstructed kaons can be calculated. In terms of the K_S^0 lifetime $\tau_{K_S^0} = (0.895 \pm 0.004) \times 10^{-11}$ s [?], $\langle\tau_{LL}\rangle \simeq 0.1\tau_{K_S^0}$ for the LHCb LL category, $\langle\tau_{DD}\rangle \simeq 0.8\tau_{K_S^0}$ for the LHCb DD category, and at Belle II $\langle\tau_{Belle\,II}\rangle \simeq \tau_{K_S^0}$. The difference in average kaon lifetime is reflected in the observed biases, which are found to be larger in the samples with longer lived kaons. The very small effect in the LL category is to be expected because the CP -violation effect due to K_S^0 not being CP -even is approximately cancelled by the CP -violation effect arising from $K_S^0 - K_L^0$ interference for kaons with decay times much smaller than $\tau_{K_S^0}$ [?].

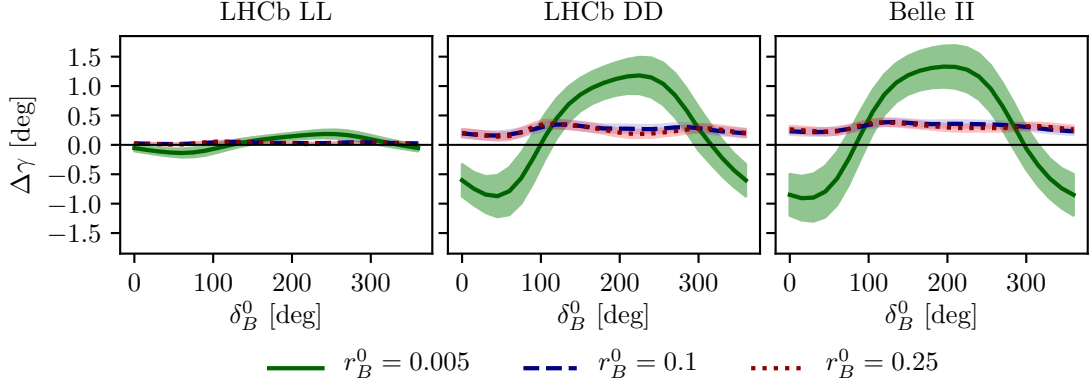


Figure 4.7: The bias $\Delta\gamma$ as a function of input δ_B for (left) the LL LHCb category, (centre) the DD LHCb category, and (right) Belle II. The bias is calculated for $\gamma = 75^\circ$ and (green line) $r_B = 0.005$, (blue, dashed line) $r_B = 0.1$, and (red, dotted line) $r_B = 0.25$. The shaded region shows the estimated 1σ uncertainty band.

1187 The uncertainty bands in Fig. 4.6 are calculated by repeating the study while
1188 varying some of the inputs. The model dependence of the predicted biases is
1189 probed by repeating the study using two other amplitude models as input for
1190 $A_1(s_{+-})$ and $A_2(s_{+-})$: the model published in Ref. [?] and the model included in
1191 EVTGEN [?]. hen defining $A_2(s_{+-})$ in terms of $A_1(s_{+-})$, there is an uncertainty
1192 due to the unknown (r_k, δ_k) parameters used to describe the $\pi\pi$ resonance terms.
1193 This uncertainty is assessed by making the study with several different random
1194 realisations of the parameter set. The studies are repeated while varying the time
1195 acceptances and material densities with $\pm 10\%$. There is an additional uncertainty
1196 due to the use of simulation samples generated with `RapidSim` to describe the kaon
1197 momentum distribution, in lieu of full detector simulations.

1198 There is also an uncertainty from the use of (c_i, s_i) as calculated using $A_1(s_{+-})$.
1199 It is to be expected that the measured values (\hat{c}_i, \hat{s}_i) from the CLEO collaboration
1200 differ by those calculated using $A_1^D(s_-, s_+)$ by terms of $O(\epsilon)$ due to neutral kaon
1201 CP violation, which is not taken into account in the measurement [?]. These
1202 corrections can be calculated via a procedure analogous to the one used to estimate
1203 the corrections on measurements of γ in this paper. However, as these corrections
1204 are much smaller than the experimental uncertainties in the measurement, they
1205 have not been studied further.

1206 For the purpose of this thesis, it is important to consider the bias in measurements
1207 that use $B^\pm \rightarrow D\pi^\pm$ decays as well, and other B decay modes can also be used in
1208 BPFGSZ measurements, such as $B^\pm \rightarrow D^*K^\pm$, $B^\pm \rightarrow DK^{*\pm}$, and $B^0 \rightarrow DK^{*0}$.
1209 For the purpose of the study presented here, the main difference between the decay

channels is that they have different values of r_B and δ_B . Figure 4.7 shows $\Delta\gamma$ as a function of input δ_B^0 , for $\gamma^0 = 75^\circ$ and three different values of r_B^0 . Aside from $r_B^0 = 0.1$, the results are shown for $r_B^0 = 0.005$, which corresponds to the expectation in $B^\pm \rightarrow D\pi^\pm$ decays [?] and $r_B^0 = 0.25$, which corresponds to $B^0 \rightarrow DK^{*0}$ decays [?, ?]. The most notable feature is that the biases are significantly larger in the $B^\pm \rightarrow D\pi^\pm$ case. This is expected: the r_B^0 dependent behaviour is governed by the relative importance of different $O(r\epsilon)$ correction terms to the phase-space distribution. There are terms of both $O(r_A\epsilon)$ and $O(r_B\epsilon)^3$, which lead to expected biases of size $O(r_A\epsilon/r_B)$ and $O(r_B\epsilon/r_B) = O(\epsilon)$, respectively, cf. the discussion of Section 4.2.3. In the $B^\pm \rightarrow D\pi^\pm$ case, the $O(r_A\epsilon)$ correction terms dominate because $r_A/r_B \simeq (0.05/0.005) = 10$. This explains the relatively large bias, as $|r_A\epsilon/r_B^{D\pi}| \simeq 4\%$. The bias is seen to be up to $\pm 1.5^\circ$, but only about $+0.2^\circ$ with the expected value of $\delta_B^{D\pi} \simeq 300^\circ$ [?, ?]. These biases are *much smaller* than the precision on γ that is obtainable in a $B^\pm \rightarrow D\pi^\pm$ analysis with current experimental yields, and do thus not pose a problem. In the $r_B^0 = 0.1$ and $r_B^0 = 0.25$ cases the $O(r_B\epsilon)$ correction terms dominate, and the biases are of $O(\epsilon)$, independent of the r_B^0 value. Therefore both cases have biases of similar size.

Further, it is clear that the biases depend on δ_B^0 and that the oscillation period of the δ_B dependence is different between the $r_B^0 = 0.005$ case and the $r_B^0 \in \{0.1, 0.25\}$ cases. It is to be expected that $\Delta\gamma$ oscillates as a function of δ_B^0 , because δ_B^0 enters the yield equations via $\cos(\delta_B^0 \pm \gamma)$ and $\sin(\delta_B^0 \pm \gamma)$ terms. As explained above, the $O(r_A\epsilon)$ terms dominate the $B^\pm \rightarrow D\pi^\pm$ bias, and these are independent of δ_B^0 . The $O(r_B\epsilon)$ terms, however, are important for the bias corrections for larger r_B values, and the terms include factors of $\cos(\delta_B^0 \pm \gamma)$ and $\sin(\delta_B^0 \pm \gamma)$. This explains the different bias dependence on δ_B^0 .

While the input value of $\gamma^0 = 75^\circ$ was chosen for these studies, there is minimal variation in the results if another value of γ^0 in the range $[60^\circ, 85^\circ]$ is used.

4.3.7 Coupled $B^\pm \rightarrow DK^\pm$ and $B^\pm \rightarrow D\pi^\pm$ measurements

The studies presented above have been extended on two accounts in order to assign a systematic uncertainty to the LHCb measurement presented in Chapter 5. Firstly, full LHCb simulation has been used to obtain the momentum distributions, as well as to fit a better description of the time acceptance and the reconstruction efficiency profile over the D -decay phase space. Secondly, the fit setup is modified

³There are similar terms of $O(r_A r_\chi)$ and $O(r_B r_\chi)$, but as ϵ and r_χ are of the same order of magnitude, these terms can be treated completely analogously to the $O(r_A\epsilon)$ and $O(r_B\epsilon)$ terms, and have been left out of the discussion for brevity.

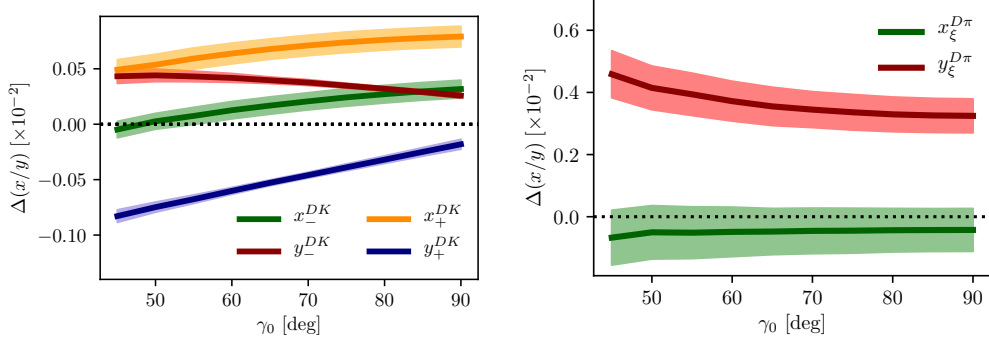


Figure 4.8: The bias on (left) the $B^\pm \rightarrow DK^\pm$ and (right) $B^\pm \rightarrow D\pi^\pm$ CP -violation observables in the LHCb DD category, evaluated in bias studies with inputs based on full LHCb simulation, calculated as a function of input γ_0 .

to correspond to the experimental approach described in Section 2.4 and Chapter 5: the signal yields are calculated for both the $B^\pm \rightarrow DK^\pm$ and $B^\pm \rightarrow D\pi^\pm$ channels, and fitted in a combined fit to obtain $(x_{\pm}^{DK}, y_{\pm}^{DK}, x_{\xi}^{D\pi}, y_{\xi}^{D\pi})$, where the F_i parameters are allowed to float in the fit. The biases obtained for each observable are shown in Fig. 4.8, evaluated using the time-acceptance, momentum distribution, and material budget relevant for the DD category (since the effect in the LL category is much smaller). As will be clear in Chapter 5, these biases are all significantly smaller than the corresponding statistical uncertainties. Thus, the effects of neutral kaon CP violation and material interactions contribute a manageable systematic uncertainty in current BPGGSZ measurements, even if the $B^\pm \rightarrow D\pi^\pm$ channel is promoted to a signal channel.

As the statistical uncertainty becomes comparable with the bias effects described in this chapter, the systematic uncertainty should be assigned by a more accurate study, incorporating the traversed material on a track-by-track basis in full detector simulation. Such a detailed calculations can also be used to apply a bias correction if desired.

4.4 Concluding remarks

The analysis presented in this chapter has shown the expected impact of neutral kaon CP violation and material interaction on current BPGGSZ measurements to be small compared to the statistical uncertainties; first by simple order-of-magnitude estimates and then by a detailed calculation of the expected effect in LHCb and Belle II.

While the calculations were made for the case of $D \rightarrow K_S^0 \pi^+ \pi^-$ decays, the BPGGSZ approach can of course also be applied in other D -decay final states,

such as $D \rightarrow K_S^0 K^+ K^-$ and $D \rightarrow K_S^0 \pi^+ \pi^- \pi^0$. The biases on measurements of γ based the D decay phase-space distributions should be of similar size in these decay channels. The impact on γ measurements based on the phase-space-integrated yield asymmetry can be expected to be tens of degrees for the $D \rightarrow K_S^0 K^+ K^-$ channel, where the yield asymmetry is expected to be around 2 %, for the reasons explained in Section 4.2.3. The $D \rightarrow K_S^0 \pi^+ \pi^- \pi^0$ decay, however, is dominantly CP -odd [?], and the bias in measurements based on the total asymmetry is therefore expected to be $O(\epsilon/r_B)$, ie. a few degrees [?]. More precise calculations of the biases would require a repeat of the study included here, with relevant amplitude models and binning schemes in place.

The chapter focuses on the model-independent, binned approach that is the subject of the thesis. However, the underlying mechanism that determines the scale of the bias, namely that the phase-space *distribution* of signal decays is unaffected at $\mathcal{O}(\epsilon)$ and $\mathcal{O}(r_\chi)$, is independent on the exact measurement approach. Therefore it is expected that amplitude-model-based measurements and measurements made with new unbinned methods such as those in Ref [?] will be similarly biased if kaon CP violation and regeneration are not accounted for.

5

1284

1285

1286

A BPGBGSZ measurement of γ with $B^\pm \rightarrow Dh^\pm$ decays

1287 This chapter describes a model-independent BPGBGSZ measurement of γ with
1288 $B^\pm \rightarrow DK^\pm$ and $B^\pm \rightarrow D\pi^\pm$ decays where $D \rightarrow K_S^0\pi^+\pi^-$ and $D \rightarrow K_S^0K^+K^-$,
1289 commonly denoted $B^\pm \rightarrow D(\rightarrow K_S^0h^+h^-)h'^\pm$ decays. The measurement is made
1290 with the full LHCb data set collected during Run 1 and 2 of the LHC, corresponding
1291 to an integrated luminosity of about 9 fb^{-1} . The analysis is under review for
1292 publication in the Journal of High Energy Physics at the time of writing [?]
1293 (one can hope).

1294 5.1 Candidate reconstruction and selection

1295 The $B^\pm \rightarrow D(\rightarrow K_S^0h^+h^-)h'^\pm$ candidates are constructed during the offline *stripping*
1296 stage described in Section 3.3.3. The candidates are defined by first combining
1297 tracks to form a $K_S^0 \rightarrow \pi^+\pi^-$ vertex, then a $D \rightarrow K_S^0h^+h^-$ vertex, and finally
1298 the $B^\pm \rightarrow Dh'^\pm$ candidate. Each final state track is required to satisfy certain
1299 momentum thresholds and track-quality requirements, and to be separated from all
1300 primary interaction vertices. Each decay vertex is required to satisfy a fit-quality
1301 threshold and to be separated from the primary vertex. Momentum thresholds
1302 are applied to the composite particles and they are required to have reconstructed
1303 invariant masses close to their known masses¹ except that the B candidate is
1304 required to have a reconstructed invariant mass in the interval $4750\text{--}7000\text{ MeV}/c^2$.

¹The exact mass window depends on the particle type and reconstruction category; narrower mass windows are applied at a later stage, as described below.

1305 The B candidate is required to satisfy $\chi^2_{\text{IP}} < 25$, where χ^2_{IP} is the difference in χ^2
 1306 value of the primary vertex fit, when the vertex is formed with- and without the B
 1307 candidate. As the final *stripping* stage, a multivariate algorithm is applied to the
 1308 formed B candidate to reduce the amount of random track combinations, denoted
 1309 combinatorial background, even further than the aforementioned requirements.

1310 Two data categories are defined, depending the tracks used to form the K_S^0
 1311 candidate: the LL category where both pions are long tracks, and DD category where
 1312 both pions are downstream tracks, using the track classifications of Section 3.2.

1313 Each candidate is re-analysed with the `DecayTreeFitter` (DTF) frame work [?],
 1314 where a simultaneous fit of the full decay chain is made with a number of constraints
 1315 applied: the momenta of the composite D and K_S^0 particles are required to form
 1316 invariant masses exactly equal to the known particle masses [?], and the momentum
 1317 of the B candidate is required to point in the direction defined by the B decay
 1318 vertex and the primary vertex. This refit results in improved resolution of the
 1319 invariant masses of the composite particles and, very importantly, of the Dalitz
 1320 coordinates in the D -decay phase space. It also ensures that all candidates fall in the
 1321 kinematically allowed region of the D -decay phase space. Unless otherwise specified,
 1322 all results in this chapter are based on the refitted track momenta; for reasons
 1323 explained below, some studies have to be based on parameters that are obtained
 1324 without the constraints described above, or with only a subset of them applied.

1325 Following the stripping stage, the further selection of signal candidates is
 1326 performed in three steps: an initial set of requirements that remove a large fraction
 1327 of candidates that are very likely to be background and veto a number of specific
 1328 backgrounds, the application of a multivariate analysis algorithm designed to allow
 1329 for filtering combinatorial background, and finally a set of particle-identification
 1330 requirements. The requirements are summarised in Table 5.1, and each step is
 1331 described in detail in the following sections.

1332 5.1.1 Initial requirements

1333 At the hardware trigger level, it is required that a particle associated with the signal
 1334 decay triggered the hadronic level-0 trigger (Trigger on Signal, or TOS), or that
 1335 the level-0 trigger decision was caused by a particle that is not associated with the
 1336 signal decay (Trigger Independent of Signal, or TIS). The inclusion of the latter
 1337 category increases the data sample about 50 %. At the software trigger level,

1338 Before any processing of the data, a loose preselection is applied to remove
 1339 obvious background candidates. The reconstructed D (K_S^0) mass is required to
 1340 be within 25 (15) MeV/ c^2 of the known values [?]. The *companion* particle, the

Table 5.1: Summary of requirements applied to data. The base requirements are applied to all data samples before training or applying the BDT.

Base requirements		
Variable	Cut	Comment
Bachelor momentum, p	$< 100 \text{ GeV}/c$	
Bachelor has RICH	<i>true</i>	
K^\pm in D decay: momentum, p	$< 100 \text{ GeV}/c$	In $D \rightarrow K_S^0 K^+ K^-$
K^\pm in D decay: have RICH	<i>true</i>	In $D \rightarrow K_S^0 K^+ K^-$
DecayTreeFit converged	<i>true</i>	
D mass	$m_{D^0} \in m_{D^0}^{PDG} \pm 25 \text{ MeV}/c^2$	From DTF with constrained K_S^0 mass
K_S^0 mass	$m_{K_S^0} \in m_{K_S^0}^{PDG} \pm 15 \text{ MeV}/c^2$	From DTF with constrained D^0 mass

Background suppressing requirements		
Variable	Cut	Comment
K_S^0 flight distance χ^2	> 49	for LL only
$\Delta z_{\text{significance}}^{DB}$	> 0.5	for all candidates

PID requirements		
Channel	Cut	Comment
$B^\pm \rightarrow DK^\pm$	PIDK > 4	for bachelor
$B^\pm \rightarrow D\pi^\pm$	PIDK < 4	for bachelor
$B^\pm \rightarrow Dh^\pm$	IsMuon = 0	for bachelor
$B^\pm \rightarrow D(\rightarrow K_S^0 \pi^+ \pi^-)h^\pm$	PIDe < 0 & IsMuon = 0	for charged D decay products
$B^\pm \rightarrow D(\rightarrow K_S^0 K^+ K^-)h^\pm$	PIDK > -5 & IsMuon = 0	for charged D decay products

BDT requirements		
Channel	Cut	Comment
Run 1, DD	> 0.6	
Others	> 0.8	

1341 pion or kaon produced in the $B^\pm \rightarrow Dh^\pm$ decay, is required to have associated
 1342 RICH information and a momentum less than $100 \text{ GeV}/c$; this ensures good particle-
 1343 identification performance. Finally, all of the DTF fits of the full decay chain
 1344 are required to have converged properly.

1345 Two additional requirements are made at this stage in order to suppress specific
 1346 backgrounds. In order to suppress decays of the type $B^\pm \rightarrow K_S^0 h^+ h^- h'^\pm$ with
 1347 no intermediate D meson, so called *charmless* decays, it is required that the
 1348 significance of the z -separation of the D^0 decay vertex and the B^\pm decay vertex
 1349 is above 0.5. The significance of the z -separation of the D^0 decay vertex and
 1350 the B^\pm decay vertex is defined as

$$\Delta z_{\text{significance}}^{D-B} = \frac{z_{vtx}^D - z_{vtx}^B}{\sqrt{\sigma^2(z_{vtx}^D) + \sigma^2(z_{vtx}^B)}}. \quad (5.1)$$

1351 This source of background described further in section 5.3.1. In order to suppress
 1352 a background from $D \rightarrow 4\pi$ and $D \rightarrow \pi\pi KK$ decays, it is required that the K_S^0

1353 flight distance χ_{FD}^2 is greater than 49, where

$$\chi_{\text{FD}}^2 = \left(\frac{\Delta r}{\sigma(\Delta r)} \right)^2, \quad (5.2)$$

1354 and Δr is the measured flight distance of the K_S^0 meson. This background is
1355 described in further detail in section 5.3.2.

1356 5.1.2 Boosted decision tree

1357 A Gradient Boosted Decision Tree [?] (abbreviated BDT in the following) is
1358 applied to classify each candidate on a scale from -1 to $+1$ as signal-like ($+1$)
1359 or combinatorial-background-like (-1), based on the values of a number of input
1360 parameters for candidate in question. The BDT is implemented in the TMVA
1361 frame work [?, ?].

1362 A boosted decision tree classifier consists of a number of sequentially trained
1363 decision trees, each of which classify events as either signal or background. Each tree
1364 bases the decision on an individual subset of variables, out of an overall set of input
1365 variables. At each training step, the input events are weighted when training a new
1366 tree, so that events that the already-trained trees classify incorrectly are given a
1367 higher weight; this is denoted boosting. The term *gradient boosting* denotes a specific
1368 weight calculation scheme [?]. The final score is the average over all decision trees.

1369 The full set of input variables are given in Table 5.2. It includes the momenta
1370 of particles in the decay; a number of geometric parameters such a absolute and
1371 relative vertex positions, and distances of closest approach between tracks; χ_{IP}^2
1372 values for a number of particles in the decay chain; the χ^2 per degree of freedom
1373 of the DTF refit; DIRA values, which denote the angle between the fitted particle
1374 momenta and the vector spanned by it's production ad decay vertices; and finally
1375 an isolation variable, defined as

$$A_{pt} = \frac{p_T(B) - \sum p_T(\text{other})}{p_T(B) + \sum p_T(\text{other})} \quad (5.3)$$

1376 where the sum is over all other tracks in a cone around the B -candidate. The cone
1377 is defined as being within a circle with a radius of 1.5 units around the B candidate
1378 in the $(\eta, \phi_{\text{azim}})$ -plane. This variable is highly efficient in rejecting combinatorial
1379 background. Two algorithms are trained, one for the LL category of K_S^0 mesons and
1380 one for the DD category, because some input parameters relate to the K_S^0 meson
1381 and have very different distributions between the two categories.

Table 5.2: Input parameter set used in BDTG trained to separate signal and combinatorial background, sorted according to importance in LL BDT.

Variable name	Importance LL/DD (Rank in DD)	Description
$\log(1-Ks_{\text{DIRA}}_{\text{BPV}})$	7.2 % / 3.5 % (16)	$\log \cos \theta_{\text{DIRA}}$ for K_S^0
$\log(Bu_{\text{RHO}}_{\text{BPV}})$	5.7 % / 5.5 % (5)	Radial distance of B vertex to beam line
$\log(Bach_{\text{PT}})$	5.2 % / 6.9 % (1)	p_T of the bachelor particle
$\log(1-D0_{\text{DIRA}}_{\text{BPV}})$	4.9 % / 5.8 % (4)	$\log \cos \theta_{\text{DIRA}}$ for D
$\log(1-Bu_{\text{DIRA}}_{\text{BPV}})$	4.9 % / 6.4 % (3)	$\log \cos \theta_{\text{DIRA}}$ for B^\pm
$\log(D0_{\text{RHO}}_{\text{BPV}})$	4.8 % / 5.3 % (6)	Radial distance of D vertex to beam line
$Bu_{\text{PTASY_1.5}}$	4.7 % / 4.9 % (7)	Asymmetry parameters of B^\pm
$\log(D0_{\text{PT}})$	4.7 % / 6.6 % (2)	p_T of the D meson
$\log(Bu_{\text{constDOKSPV_CHI2NDOF}})$	4.2 % / 4.5 % (9)	$\chi^2/\text{d.o.f}$ of kinematical refit with DecayTreeFitter
$\log(Bu_{\text{FDCHI2_OWNPV}})$	3.9 % / 4.1 % (11)	Flight distance χ^2 of the B^\pm
$\log(\max_{\text{Ksh1h2_IPCHI2_OWNPV}})$	3.9 % / 3.0 % (20)	Largest χ^2_{IP} of the K_S^0 decay products
$\log(D0_{\text{IPCHI2_OWNPV}})$	3.8 % / 3.3 % (17)	χ^2_{IP} of the D
$\log(\min_{\text{Ksh1h2_IPCHI2_OWNPV}})$	3.7 % / 0.9 % (26)	Smallest χ^2_{IP} of the K_S^0 decay products
$\log(Bu_{\text{P}})$	3.7 % / 3.9 % (12)	p of the B^\pm meson
$\log(Bu_{\text{IPCHI2_OWNPV}})$	3.6 % / 4.6 % (8)	χ^2_{IP} of the B^\pm
Bu_{MAXDOCA}	3.6 % / 3.3 % (18)	"Distance of closest approach" for B^\pm vertex
$\log(Bach_{\text{IPCHI2_OWNPV}})$	3.3 % / 4.3 % (10)	χ^2_{IP} of the bachelor particle
$\log(Bu_{\text{PT}})$	3.3 % / 3.7 % (14)	p_T of the B^\pm meson
$\log(\max_{\text{h1h2_IPCHI2_OWNPV}})$	3.1 % / 3.8 % (13)	Largest χ^2_{IP} of the D decay products
$\log(\min_{\text{h1h2_IPCHI2_OWNPV}})$	3.0 % / 3.4 % (19)	Smallest χ^2_{IP} of the D decay products
$\log(Ks_{\text{VTXCHI2DOF}})$	2.9 % / 2.3 % (21)	χ^2 of vertex fit for K_S^0
$D0_{\text{MAXDOCA}}$	2.9 % / 1.0 % (25)	"Distance of closest approach" for D vertex
$\log(D0_{\text{VTXCHI2DOF}})$	2.7 % / 1.6 % (24)	χ^2 of vertex fit for D
$\log(D0_{\text{P}})$	2.7 % / 1.8 % (22)	p of the D meson
$\log(Bach_{\text{P}})$	2.2 % / 3.6 % (15)	p of the bachelor particle
$\log(Bu_{\text{VTXCHI2DOF}})$	1.8 % / 1.7 % (23)	χ^2 of vertex fit for B^\pm

The BDTs are trained and tested with input samples representing typical signal and background decay candidates: a signal sample that consists of simulated $B^\pm \rightarrow D(\rightarrow K_S^0\pi^+\pi^-)\pi^\pm$ decays corresponding to the LHCb running conditions for the years 2012–2018, and a sample of combinatorial background candidates from real data, where the reconstructed invariant mass of the B meson is larger than 5800 MeV/ c^2 . The candidates in both samples were required to have passed the initial requirements described in the preceding section. The input-parameter distributions in the signal and background training samples are shown in Figs. 5.1 and 5.2. The signal and background samples are each split into two before the training stage: one sub sample, the training sample, is used to train the BDT, after which the trained algorithm is applied to the other sub sample, the test sample. The classifier is found to perform well on the test sample, not just the training sample, which ensures that it does not suffer significant overtraining. The BDT output distribution are shown for both test and training samples in Fig. 5.3, where it is clear that the classifier very effectively separates signal and background candidates.

Each candidate in data is classified using the BDT, and candidates that are assigned a score below some threshold value are discarded. The threshold values are chosen in a set of pseudo experiments, such that the expected sensitivity to γ is maximised. This is done by performing preliminary fits to the data set for a range of different BDT threshold values, then generating many pseudo data sets with the obtained yields, and applying the full fit and interpretation procedure described in Sections 5.4–5.7 to each data set. Thus, the expected uncertainty on γ is obtained for a range of threshold values. The procedure is applied independently for the LL and DD categories, as well as for the Run 1 and Run 2 data sets, because some parameter distributions differ slightly between the two runs. The optimal threshold values are found to be 0.8 in all situations, except for LL candidates in Run 1 where it is 0.6. This is illustrated in Fig. 5.4 where the results of the threshold scans are shown. The same classifier is applied to both $B^\pm \rightarrow D\pi^\pm$ and $B^\pm \rightarrow DK^\pm$ candidates, and both D final state categories. While the classifiers were trained using samples of $B^\pm \rightarrow D(\rightarrow K_S^0\pi^+\pi^-)\pi^\pm$ simulation and data, the decays are similar enough that no significant improvement in performance was obtained when considering a more elaborate setup. Across all categories, the requirement on the BDT output is found to remove approximately 98 % of the combinatorial background, while being approximately 93 % efficient on signal.

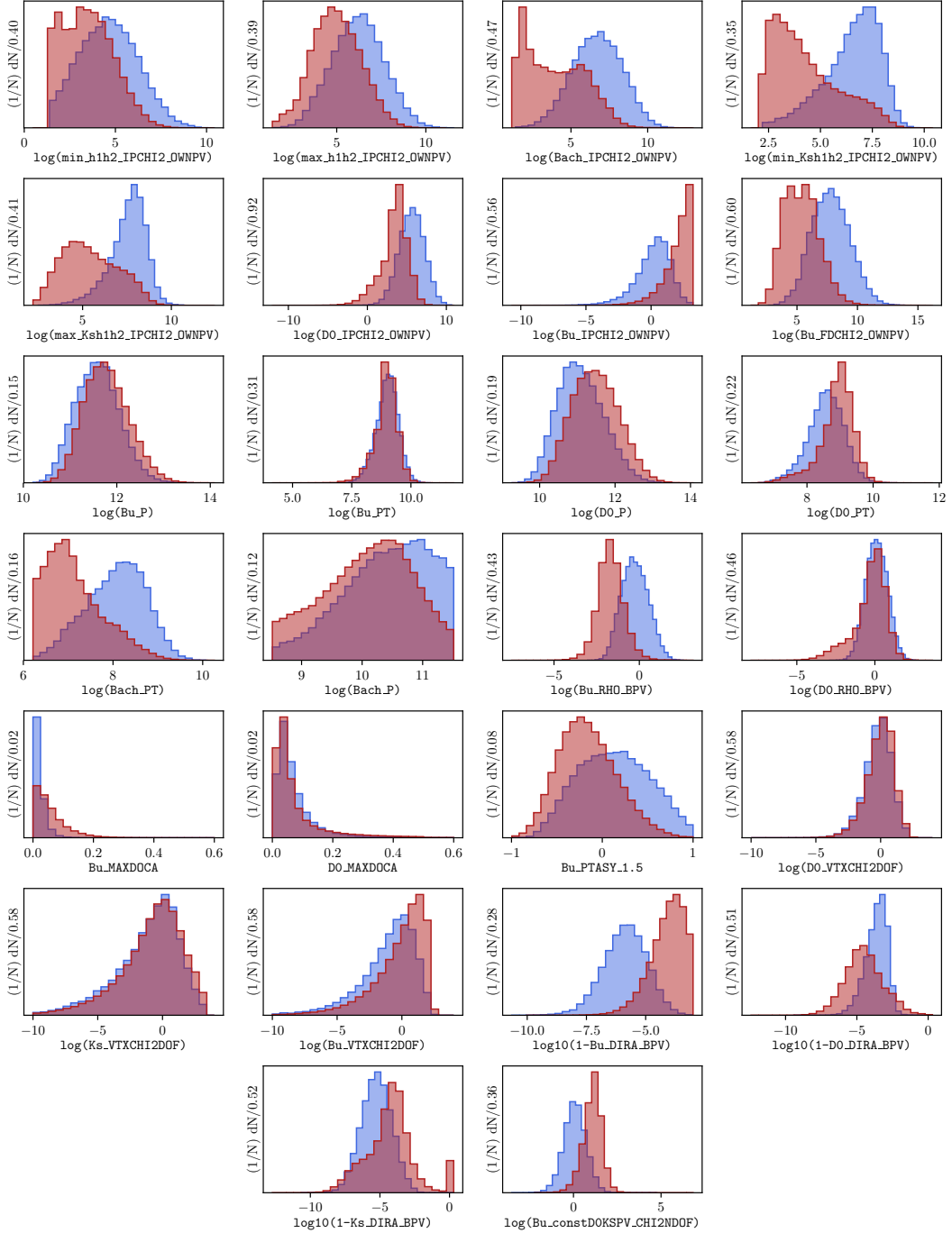


Figure 5.1: Distribution of input parameters in the LL training samples of (blue) signal decays from simulation and (red) background decays from the upper B sideband. The variable names described further in Table 5.2.

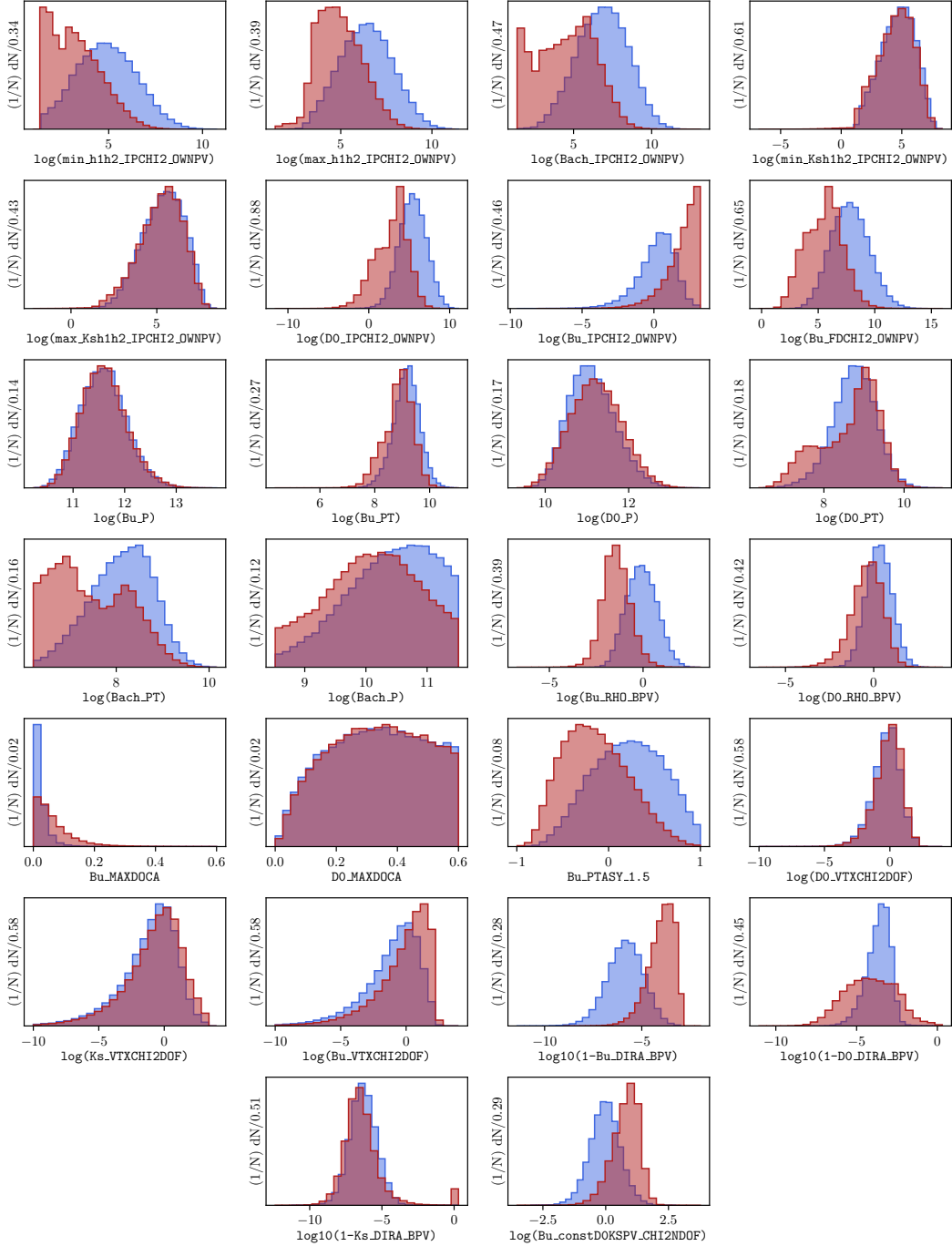


Figure 5.2: Distribution of input parameters in the DD training samples of (blue) signal decays from simulation and (red) background decays from the upper B sideband. The variable names described further in Table 5.2.

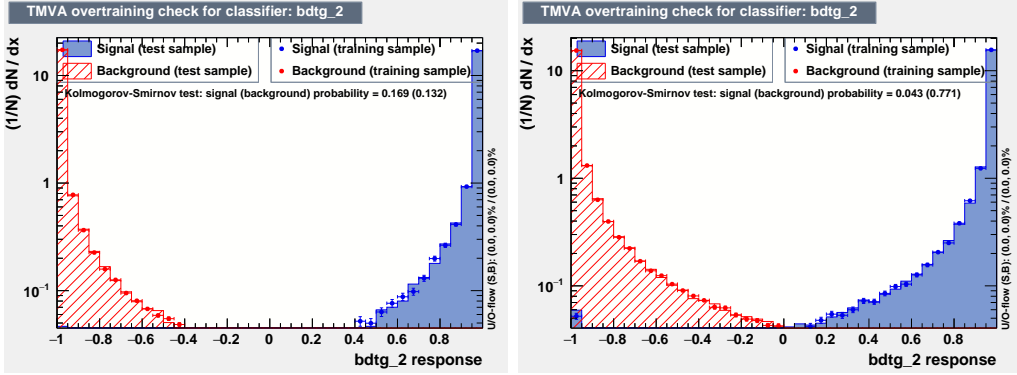


Figure 5.3: Distribution of BDT variable on test and training samples for (left) the LL and (right) the DD category, with logarithmic y -scale.

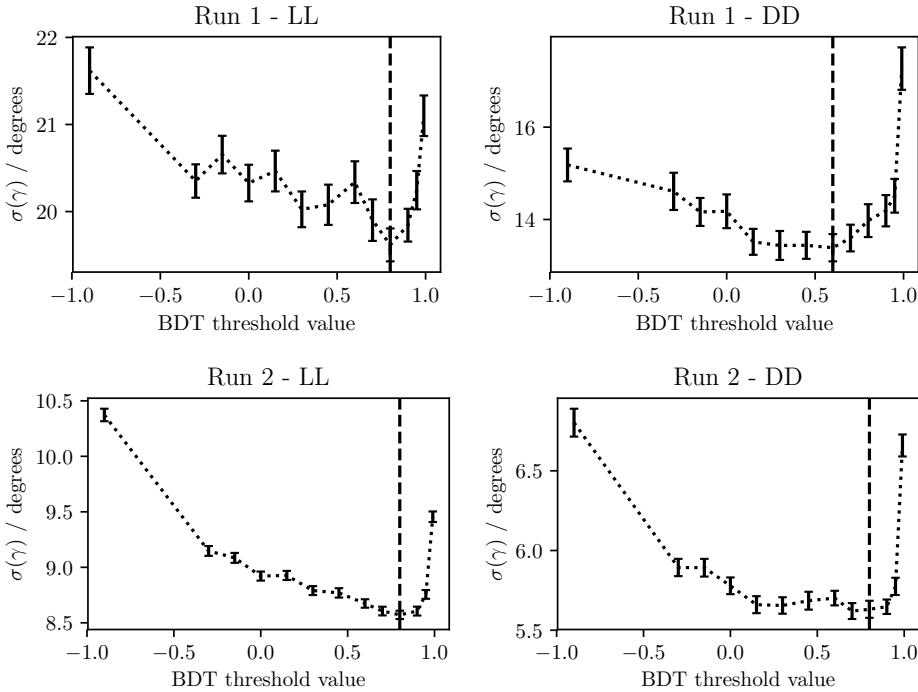


Figure 5.4: The mean uncertainty on γ in toy studies, performed with the signal and background yields corresponding to a given BDT requirement, using (top) the Run 1 and (bottom) Run 2 datasets, using only candidates in (left) the LL category and (right) the DD category. The dashed line shows the threshold value employed to discard background-like candidates in the selection.

5.1.3 Particle-identification requirements

- 1416 A PID requirement is made to separate $B^\pm \rightarrow DK^\pm$ and $B^\pm \rightarrow D\pi^\pm$ candidates in
- 1417 the data sample, by requiring that the PIDK of the companion particle satisfies
- 1418 $PIDK < 4$ for $B^\pm \rightarrow D\pi^\pm$ candidates and $PIDK > 4$ for $B^\pm \rightarrow DK^\pm$ candidates.
- 1419 The PIDK variable was defined in Section 3.1.3. This ensures that any given
- 1420 candidates is selected into only one of these samples.

1422 Further to the requirement on the companion, PID requirements are made to
1423 suppress semi-leptonic backgrounds as well as decays where a final state particle
1424 decays in flight, and a loose PID requirement is made in the $D \rightarrow K_S^0 K^+ K^-$
1425 channels where it leads to a higher signal purity:

- 1426 • the companion particle is required to satisfy `IsMuon` = 0.
- 1427 • For the $B \rightarrow D(\rightarrow K_S^0 \pi^+ \pi^-) h^\pm$ samples it is require that the charged pion
1428 track from the D decay with opposite charge to the companion satisfies
1429 $PIDe < 0 \& IsMuon = 0$, and for the other charged pion that `IsMuon` = 0.
- 1430 • For the $B \rightarrow D(\rightarrow K_S^0 K^+ K^-) h^\pm$ samples it is required that the charged kaon
1431 tracks from the D decay have RICH information, a momentum less than 100
1432 GeV/c and $PIDK > -5 \& IsMuon = 0$.

1433 These backgrounds are described in Section 5.3.3.

1434 5.1.4 Final requirements

1435 For a small fraction of candidates in the final sample, it is the case that two
1436 or more candidates originate in the same pp collision. In order to make sure
1437 that all candidates are completely independent, a single, arbitrary candidate from
1438 each pp collision is kept for these collisions, and the other candidates discarded.
1439 This requirements results in the removal of less than 0.7% of candidates in
1440 each data category.

1441 Furthermore, the D mass used to define the binning schemes described in Ref. [?]
1442 differs slightly from the mass used in the DTF refit. Therefore a few of the decays are
1443 reconstructed with Dalitz coordinates outside the allowed kinematic region. Because
1444 this problem only concerns a handful of candidates, they are simply discarded.

1445 5.1.5 Selected candidates

1446 In total, about 47,000 $B^\pm \rightarrow DK^\pm$ candidates and 400,000 $B^\pm \rightarrow D\pi^\pm$ candidates
1447 are selected, as summarised in Table 5.3. An example of the B mass distribution in
1448 one of the data categories is shown in Fig. 5.5; it is clear that a significant number
1449 of these candidates are background decays. The Dalitz plots for candidates in the
1450 signal region where $m_B \in [5249, 5309] \text{ MeV}/c^2$ are shown in Fig. 5.6 and 5.7. Due to
1451 the large yields in the full Run 1 and 2 LHCb data set, the asymmetries between
1452 the B^+ and B^- distributions are visible to the eye in the $B^\pm \rightarrow DK^\pm$ plots.

Table 5.3: Final candidate yield in each data category after the full selection has been applied, including removing candidates outside the region $m_B \in [5080, 5800] \text{ MeV}/c^2$.

B Decay	D final state	K_S^0 type	Run 1	Run 2	Total
$B^\pm \rightarrow DK^\pm$	$K_S^0\pi^+\pi^-$	LL	2275	10525	12800
		DD	5097	23508	28605
	$K_S^0K^+K^-$	LL	383	1610	1993
		DD	772	3397	4169
$B^\pm \rightarrow D\pi^\pm$	$K_S^0\pi^+\pi^-$	LL	18209	90509	108718
		DD	40167	205807	245974
	$K_S^0K^+K^-$	LL	2879	13757	16636
		DD	6033	29790	35823

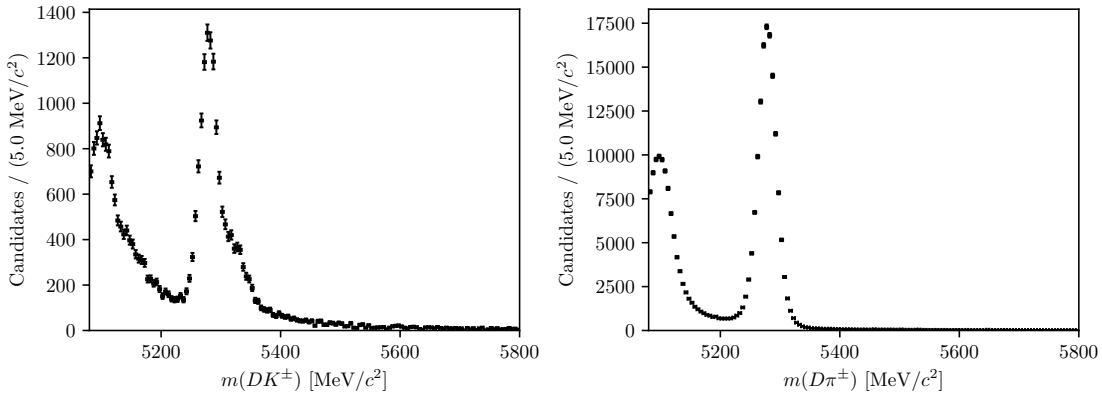


Figure 5.5: The spectrum of m_B in the (left) $B^\pm \rightarrow DK^\pm$ and (right) $B^\pm \rightarrow D\pi^\pm$ samples where $D \rightarrow K_S^0\pi^+\pi^-$ and the K_S^0 meson is reconstructed in the DD category, after the full selection has been applied.

1453 5.2 Signal selection efficiencies

1454 The efficiency of each step of the selection on signal decays can be investigated using
 1455 simulated decays. In the $B^\pm \rightarrow D\pi^\pm$ channel, only decays that were placed in
 1456 the "test" sample when training the BDT are used, in order to avoid overesti-
 1457 mating the efficiency.

1458 In general, the total selection efficiency up until the PID requirements, including
 1459 the offline stage and the effect of the geometrical LHCb acceptance, is about 1
 1460 permille, slightly higher for $B^\pm \rightarrow DK^\pm$ than $B^\pm \rightarrow D\pi^\pm$ decays, and slightly
 1461 higher for $D \rightarrow K_S^0K^+K^-$ than $D \rightarrow K_S^0\pi^+\pi^-$ decays. The PID requirements are
 1462 investigated separately in Section 5.2.1 below, using samples of calibration data.
 1463 The overall selection efficiency does not impact the measurement at all, because
 1464 the observables of interest are sensitive *only* to the distribution of decays over the
 1465 Dalitz plot (except, of course, in the sense that a higher signal efficiency is desirable).

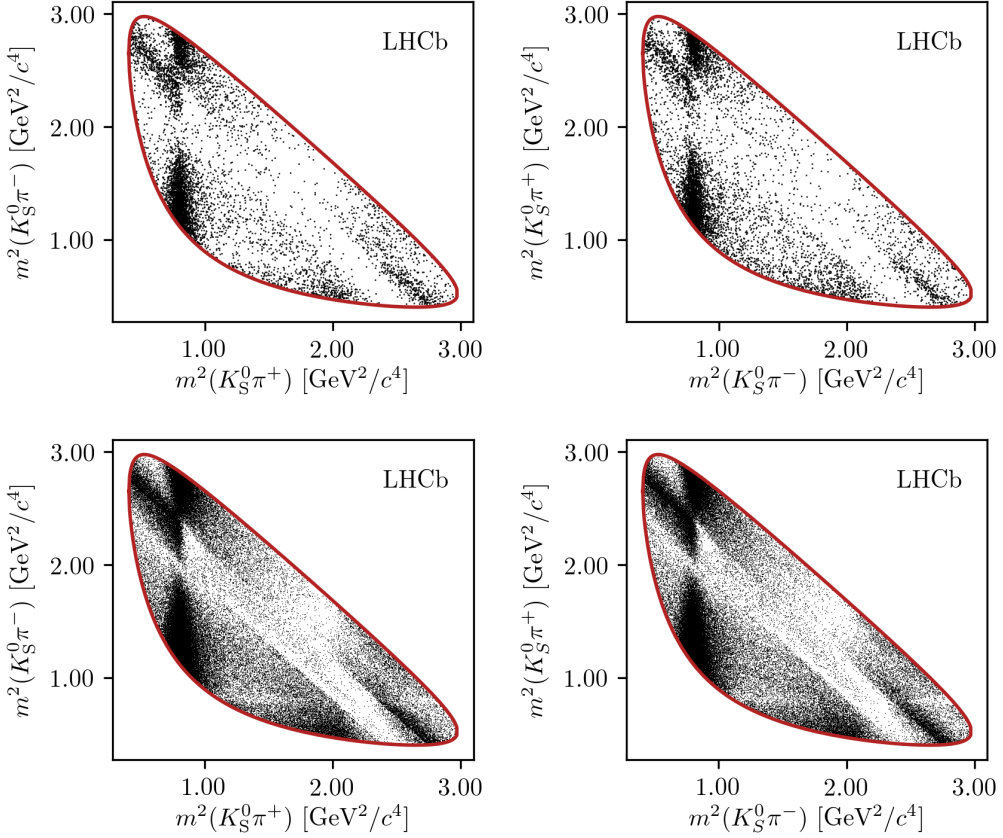


Figure 5.6: Dalitz plots of (left) $B^+ \rightarrow Dh^+$ and (right) $B^- \rightarrow Dh^-$ candidates in the signal region, in the (top) $B^\pm \rightarrow DK^\pm$ and (bottom) $B^\pm \rightarrow D\pi^\pm$ channels where $D \rightarrow K_S^0 \pi^+ \pi^-$. The LL and DD categories have been combined.

because it leads to larger signal yields). Likewise, it makes no difference that the overall selection efficiencies differ slightly between $B^\pm \rightarrow DK^\pm$ and $B^\pm \rightarrow D\pi^\pm$ decays, as long as the efficiency profile over the Dalitz plot is identical between the two decay channels. This is confirmed separately in Section 5.2.2 below.

The efficiencies of each individual selection step are shown in Fig. 5.8, obtained using simulated $B^\pm \rightarrow D\pi^\pm$ decays. The main reason that some signal decays do not survive the base requirement is the $p_{\text{companion}} < 100 \text{ GeV}/c$ requirement, which is in place to ensure that the PID performance for the companion is good. For decays with $p_{\text{companion}} > 100 \text{ GeV}/c$, only about 60 % of $B^\pm \rightarrow DK^\pm$ decays survive the subsequent $PIDK > 4$ requirement and the cross-feed from misidentified $B^\pm \rightarrow D\pi^\pm$ decays is 50 % larger than in the current selection. Thus, loosening this requirement leads to little statistical gain, while leading to larger systematic effects from the crossfeed background.

An equivalent plot for the combinatorial background is shown in Fig. 5.9, using $B^\pm \rightarrow D(\rightarrow K_S^0 \pi^+ \pi^-)\pi^\pm$ candidates in data with a reconstructed B mass

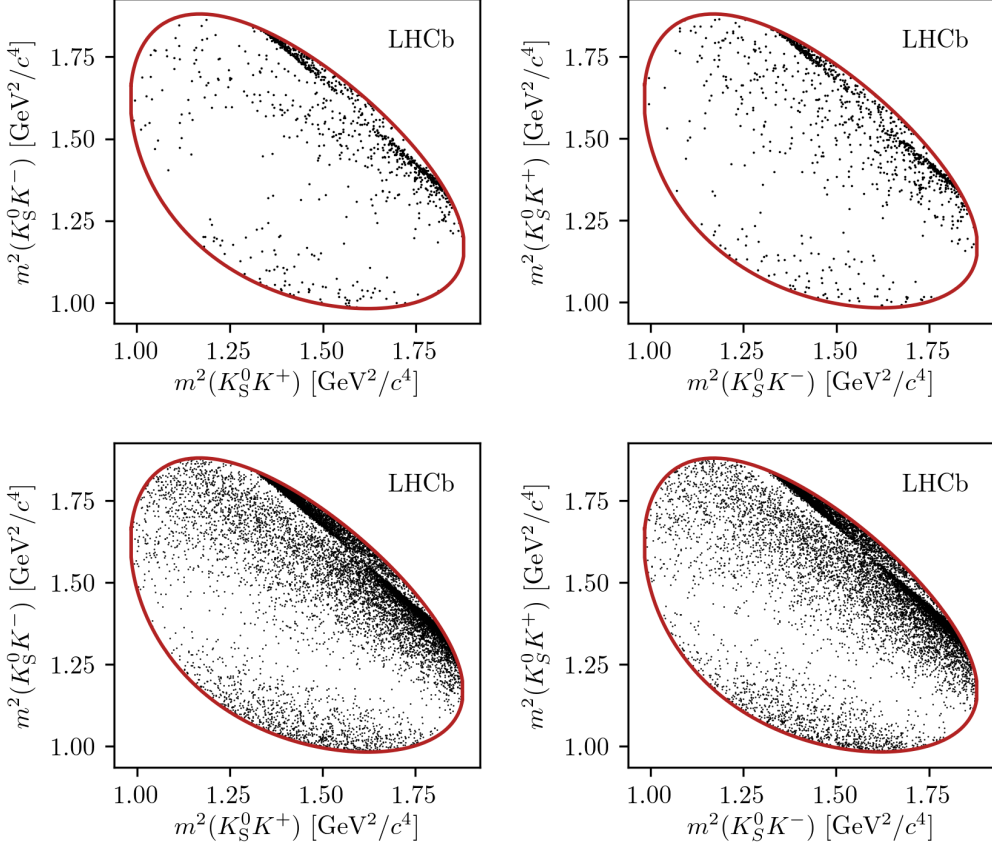


Figure 5.7: Dalitz plots of (left) $B^+ \rightarrow Dh^+$ and (right) $B^- \rightarrow Dh^-$ candidates in the signal region, in the (top) $B^\pm \rightarrow DK^\pm$ and (bottom) $B^\pm \rightarrow D\pi^\pm$ channels where $D \rightarrow K_S^0 K^+ K^-$. The LL and DD categories have been combined.

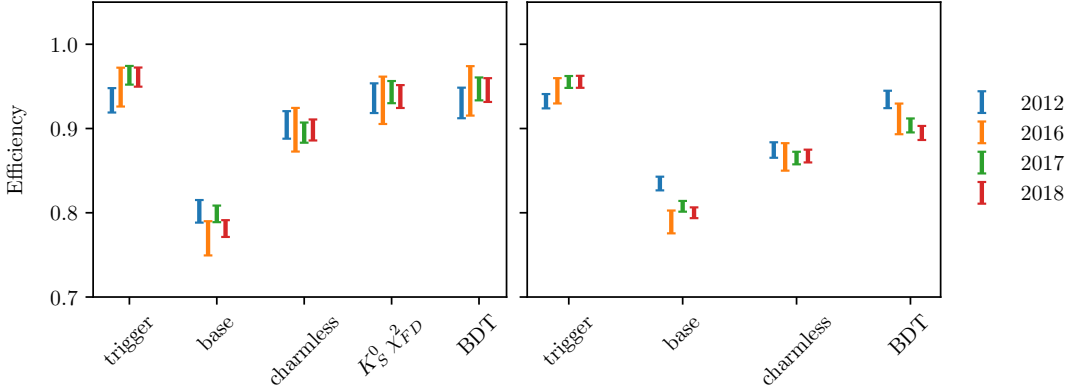


Figure 5.8: The efficiency of each selection step in samples of simulated $B^\pm \rightarrow D(\rightarrow K_S^0 \pi^+ \pi^-) \pi^\pm$ signal decays in the (left) LL and (right) DD categories. The selection steps are applied on top of each other, from left to right on the horizontal axis. The samples are split by year.

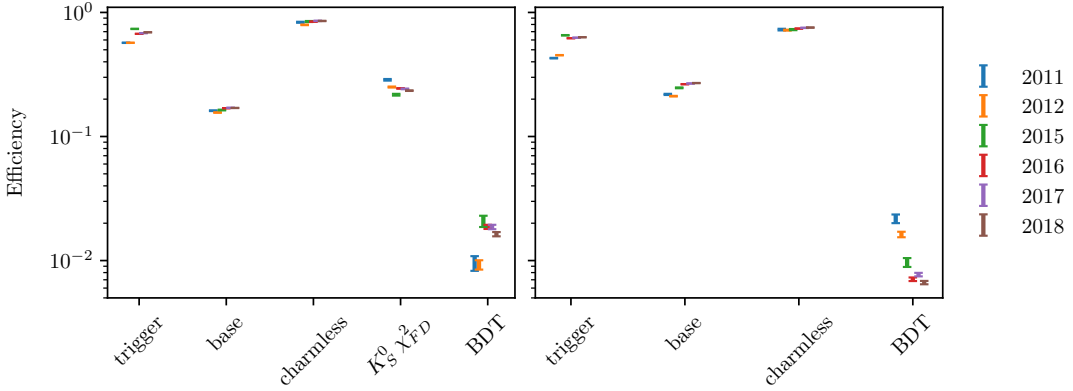


Figure 5.9: The efficiency of each selection step in samples of $B^\pm \rightarrow D(\rightarrow K_S^0 \pi^+ \pi^-) \pi^\pm$ candidates in data where the reconstructed B mass is above $5600 \text{ MeV}/c^2$, meaning the candidates stem from combinatorial background. The efficiency is shown for candidates in the (left) LL and (right) DD categories. The selection steps are applied on top of each other, from left to right on the horizontal axis. The samples are split by year. Notice the logarithmic scale on the vertical axis.

above $5600 \text{ MeV}/c^2$; it can be seen that the BDT is extremely efficient at rejection combinatorial background, but that the base requirements and the requirement on the K_S^0 flight distance also remove a decent amount of background.

5.2.1 Efficiency of the PID requirements

The efficiencies of the PID requirements on the companion enter the yield parameterisations of the mass fits in Section 5.4 and 5.5 and must therefore be known. They are determined using samples of calibration data selected without relying on PID variables, as implemented in the `PIDCalib` frame work [?]. Reasonably pure samples of pion and kaon tracks are obtained from $D^0 \rightarrow K^-\pi^+$ decays, where the D meson originates in a $D^{*+} \rightarrow D^0\pi^+$ decay and can therefore be flavour tagged. The remaining background is subtracted via the `sPlot` [?] procedure, based on a two-dimensional fit of the $m(K^-\pi^+)$ and $m(D^0\pi^+) - m(D^0)$ distributions. The obtained weights are employed to calculate the average efficiency of the requirement on `PIDK` for a number of bins in the momentum and pseudorapidity of the calibration tracks, and the number of charged tracks in the detector, thus constructing a three-dimensional efficiency lookup table. The procedure is carried out for each PID requirement, companion species, data-taking year, track charge, and magnet polarity. Based on these tables, expected PID efficiencies for the $B^\pm \rightarrow D\pi^\pm$ and $B^\pm \rightarrow DK^\pm$ signal decays are calculated that take the kinematical distribution and detector occupancy in the BPGGSZ data samples into account, by using the high-purity sample of $B^\pm \rightarrow D\pi^\pm$ candidates in the signal region as a reference. The dominating

Table 5.4: PID efficiencies obtained with the `PIDCalib` tool. The uncertainty incorporates statistical uncertainty due to the size of the reference sample, the systematic uncertainty due to the choice of binning scheme in `PIDCalib`, and a systematic uncertainty due to the `sWeight` calculation in `PIDCalib` of 0.1 %.

Efficiency	Particle	D final state	$\varepsilon_{\text{PID}} (\%)$	
			LL	DD
Run I and II				
Correct ID	Kaon	$D \rightarrow K_S^0 \pi^+ \pi^-$	86.74 ± 0.13	86.90 ± 0.22
		$D \rightarrow K_S^0 K^+ K^-$	86.22 ± 0.26	86.56 ± 0.30
	Pion	$D \rightarrow K_S^0 \pi^+ \pi^-$	97.11 ± 0.11	97.17 ± 0.13
		$D \rightarrow K_S^0 K^+ K^-$	97.07 ± 0.11	97.16 ± 0.14

uncertainty on the efficiencies is statistical in nature, due to the finite size of the reference sample. In addition, systematic uncertainties are included due to the `sPlot` procedure, estimated at 0.1 % [?], and due to the choice of binning scheme, estimated by repeating the procedure using a number of alternative binning schemes. The final efficiency estimates are shown in Table 5.4, including all sources of uncertainty.

5.2.2 Efficiency profile over the Dalitz plot

The studies above share the F_i parameters between the $B \rightarrow D\pi$ and $B \rightarrow DK$ channels. This is reasonable, since the phase-space dependence of the reconstruction efficiency is expected to be very similar between the two decays, given the similar kinematics. This assumption is verified in large simulation samples that were generated for the 2015+16 analysis [?] (described in detail in section ??). The full selection is applied to the samples. The $B \rightarrow D\pi$ sample LL (DD) sample has about 50,000 (130,000) decays, and the $B \rightarrow DK$ samples LL (DD)² sample has 44,000 (112,000) decays. For $B \rightarrow D\pi$ this is about 80 % of the number of decays in the full Run 1+2 data sample, and for $B \rightarrow DK$ this is a factor of about 9 more decays than in the data sample. The decays were simulated with an equal decay probability across the D -decay phase space, so that any non-uniform distribution of reconstructed decays is completely determined by a phase-space dependent reconstruction and selection efficiency. Therefore the assumption that the phase-space dependence is identical between the $B \rightarrow D\pi$ and $B \rightarrow DK$ channels is verified by seeing if the Dalitz coordinates are distributed differently between the $B \rightarrow D\pi$ and $B \rightarrow DK$ MC samples.

²LL and DD denote two data categories, split by the track types for the pion candidates used to form the K_S^0 candidate. See Section ??.

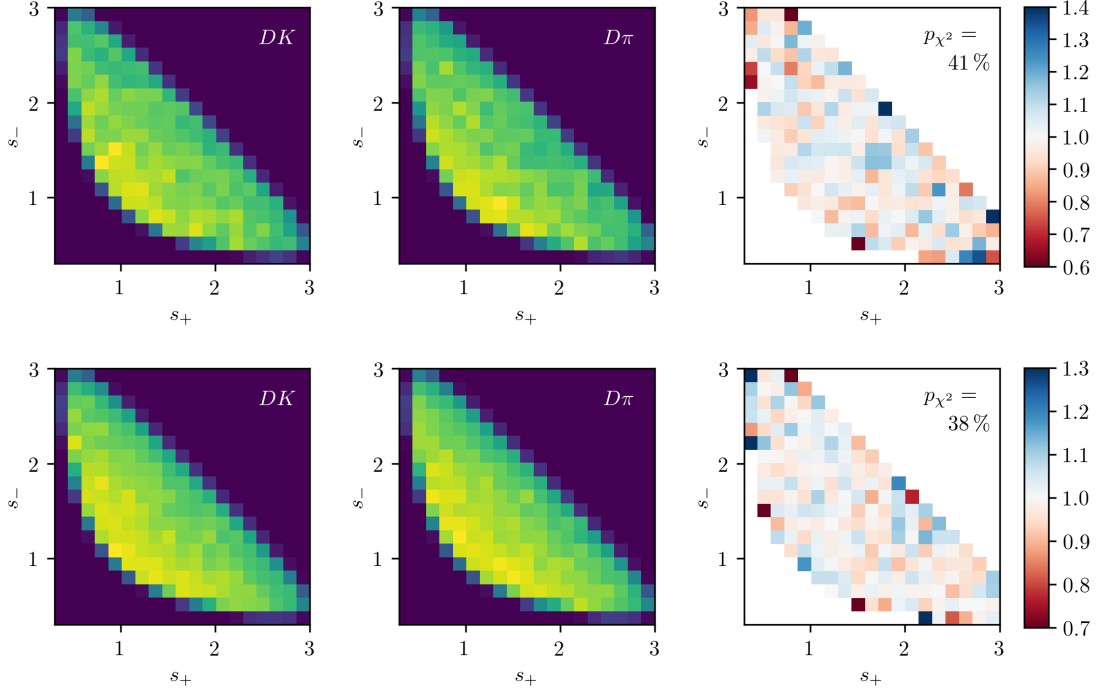


Figure 5.10: The (s_+, s_-) distribution in simulated samples of (left) $B \rightarrow DK$ decays and (center) $B \rightarrow D\pi$ decays where $D \rightarrow K_S^0 \pi^+ \pi^-$, as well as (right) the ratio between the two histograms (corrected for differences in sample sizes). The plots are shown for candidates in the (top) LL and (bottom) DD categories. The p values are the results of χ^2 compatibility tests between the two histograms.

This is investigated with two statistical tests. The first is a χ^2 comparison of 2D histograms of the distribution of $m^2(K_S^0 \pi^+)$ and $m^2(K_S^0 \pi^-)$ in the different $B \rightarrow D\pi$ and $B \rightarrow DK$ channels. These histograms, and the ratio between them, is shown in Fig. ??, along with the p -values from the χ^2 tests. It can be seen that in all cases the probability of obtaining the two histograms assuming that they share the same underlying distribution has a reasonable value, and there is no clear trend in the ratio plots. The second test is a Kolmogorov-Smirnov test of the compatibility of the one-dimensional distributions of $m^2(K_S^0 \pi^+)$, $m^2(K_S^0 \pi^-)$, $m^2(\pi^+ \pi^-)$, and $m^2(K_S^0 \pi^+) - m^2(K_S^0 \pi^-)$. These distributions and the corresponding p -values are shown in Fig. 5.12 and 5.13. Again, all the p values are reasonable. Therefore it is concluded that there are no statistically significant differences between the phase-space dependence of the reconstruction and selection efficiency between the $B \rightarrow D\pi$ and $B \rightarrow DK$ channels with these statistics. Because the simulation samples have approximately the same amount of decays as data (or significantly more in the $B \rightarrow DK$ case), any potential differences will be negligible with current statistics. Thus sharing the F_i parameters between the $B \rightarrow D\pi$ and $B \rightarrow DK$ channels is viable, and no efficiency correction is necessary.

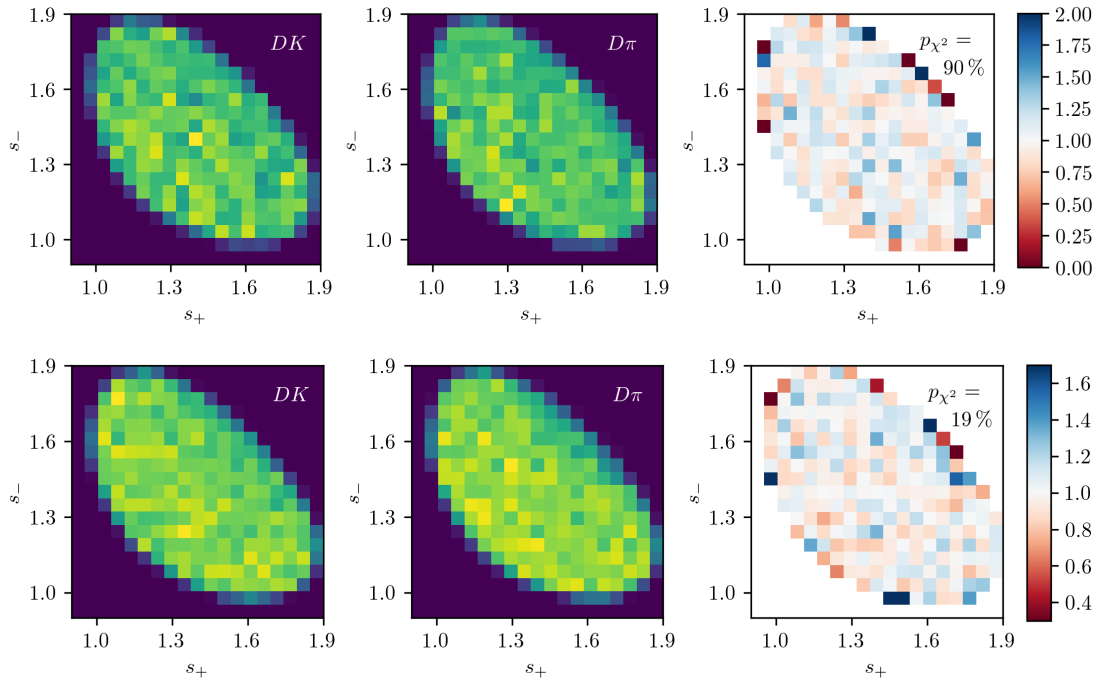


Figure 5.11: The (s_+, s_-) distribution in simulated samples of (left) $B \rightarrow DK$ decays and (center) $B \rightarrow D\pi$ decays where $D \rightarrow K_S^0 K^+ K^-$, as well as (right) the ratio between the two histograms (corrected for differences in sample sizes). The plots are shown for candidates in the (top) LL and (bottom) DD categories. The p values are the results of χ^2 compatibility tests between the two histograms.

1541 5.3 Background studies

1542 A wide range of backgrounds can potentially pollute the sample of signal candidates.
 1543 The backgrounds group into three categories depending on how they are treated
 1544 in the analysis:

- 1545 • Backgrounds that can be effectively removed in the selection
- 1546 • Backgrounds that are only present at a level where the impact on the
 1547 measurement result is small, and which do therefore not have to be modelled
- 1548 • Backgrounds that are present at a level where they have to be modelled in
 1549 the fit to data, and cannot effectively be rejected further in the selection

1550 The latter category comprises of combinatorial background, which remains present
 1551 at a non-negligible level after the application of the BDT described in Section 5.1.2;
 1552 contributions from a number of partly reconstructed $B \rightarrow Dh^\pm X$ decays, where
 1553 X denotes a pion or photon that is not included in the reconstructed decay, and
 1554 which can only be separated from signal decays by their $m(Dh)$ distribution; and

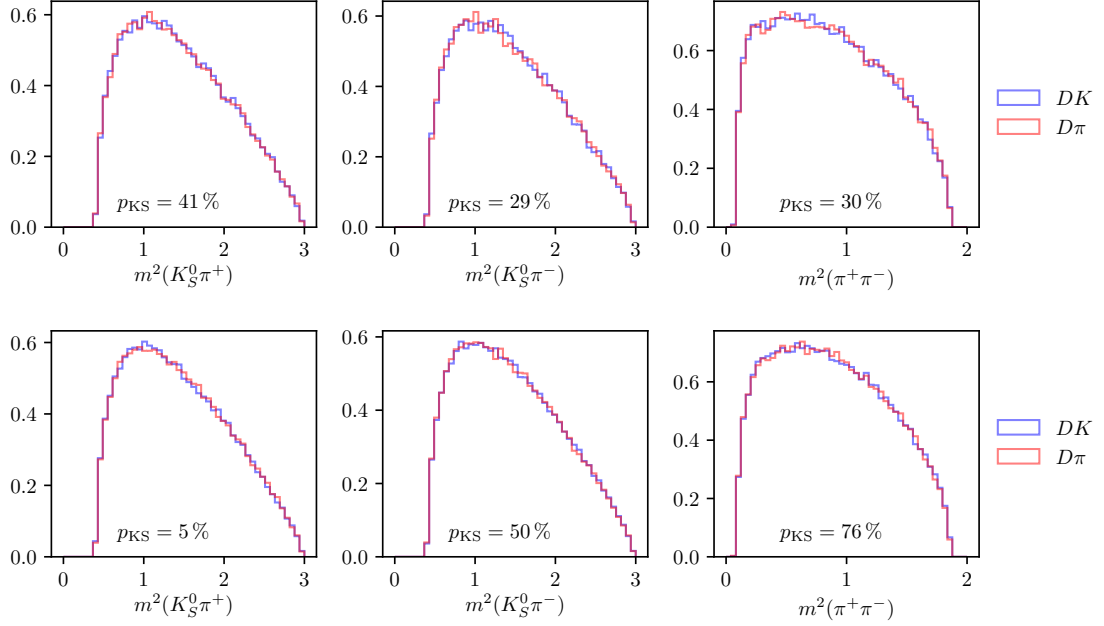


Figure 5.12: One-dimensional distributions of $m^2(K_S^0\pi^+)$, $m^2(K_S^0\pi^-)$, and $m^2(\pi^+\pi^-)$ in simulated (blue) $B^\pm \rightarrow DK^\pm$ and (red) $B^\pm \rightarrow D\pi^\pm$ decays where $D \rightarrow K_S^0\pi^+\pi^-$ in the (top) LL and (bottom) DD categories. The p values are the results of Kolmogorov-Smirnov compatibility tests between the distributions.

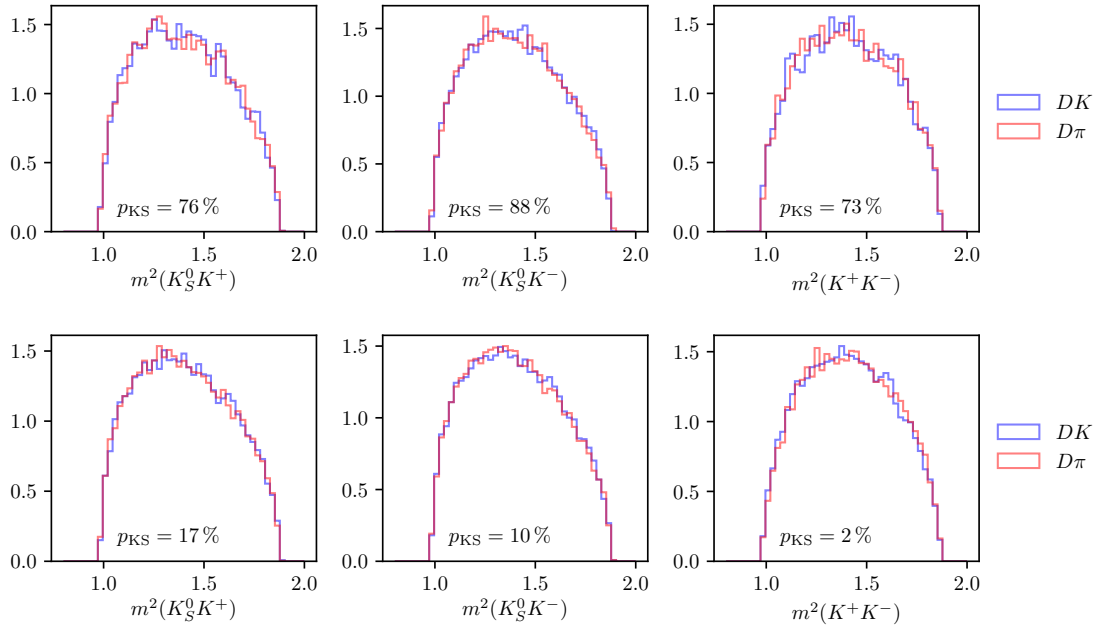


Figure 5.13: One-dimensional distributions of $m^2(K_S^0K^+)$, $m^2(K_S^0K^-)$, and $m^2(\pi^+\pi^-)$ in simulated (blue) $B^\pm \rightarrow DK^\pm$ and (red) $B^\pm \rightarrow D\pi^\pm$ decays where $D \rightarrow K_S^0K^+K^-$ in the (top) LL and (bottom) DD categories. The p values are the results of Kolmogorov-Smirnov compatibility tests between the distributions.

1555 finally $B^\pm \rightarrow D\pi^\pm$ decays that are categorised as $B^\pm \rightarrow DK^\pm$ decays in the particle-
1556 identification step and vice-versa. These background sources are described in detail
1557 in Section 5.4. This section focuses on backgrounds that led to specific requirements
1558 in the selection or proved to be small enough to not merit special treatment.

1559 5.3.1 Charmless decays

1560 There is potentially a so-called *charmless* background present in data, consisting
1561 of $B^\pm \rightarrow K_S^0 h^+ h^- h^\pm$ decays. These have the same final state as the signal decay,
1562 but no intermediate D meson. Because all final state particles are reconstructed,
1563 this background peaks in the B mass spectrum. This background is suppressed
1564 by requiring the reconstructed B and D decay vertices to be separated in the
1565 z direction; specifically by requiring that $\Delta z_{\text{significance}}^{D-B} > 0.5$, where $\Delta z_{\text{significance}}^{D-B}$
1566 was defined in Eq. (5.1). The remaining background level can be investigated
1567 by investigating the D mass sidebands.

1568 However, the use of the DecayTreeFitter χ^2 as an input variable in the BDT
1569 removes essentially all of the D (and K_S^0) sideband, due to the mass constraints
1570 in the decay chain fit. Therefore separate BDT's are trained for LL and DD
1571 candidates without the χ^2 as an input variable, and used when selecting candidates
1572 for the background studies presented in this section, and the following. In a similar
1573 manner, all mass window requirements are made on the *default* reconstructed
1574 masses, obtained with no use of DecayTreeFitter. The overlap of the two sets of
1575 selected candidates in the signal B -mass window is above 95 %.

1576 The reconstructed B mass spectrum is shown for $B^\pm \rightarrow D\pi^\pm$ candidates in the
1577 D sidebands in Fig. 5.14, both before and after making a requirement on $\Delta z_{\text{significance}}^{D-B}$.
1578 A peak is clearly visible, the size of which is reduced by the requirement. This peak
1579 is partly due to a contribution from $B^\pm \rightarrow K_S^0 \pi^+ \pi^- \pi^\pm$ decays ($B^\pm \rightarrow K_S^0 K^+ K^- \pi^\pm$
1580 decays) in the $D \rightarrow K_S^0 \pi^+ \pi^-$ ($D \rightarrow K_S^0 K^+ K^-$) channel, and partly due to real
1581 signal decays that leak into the D sidebands. The number of real signal decays can
1582 be calculated from the yield obtained in the fit of Section 5.4, and the reconstructed
1583 m_D distribution in simulated signal decays. Subtracting this contribution, it is
1584 estimated that approximately 450 (200) charmless decays are present in the $K_S^0 \pi^+ \pi^-$
1585 ($K_S^0 K^+ K^-$) data samples. In similar fashion, Fig. 5.15 shows the m_B spectra for
1586 $B^\pm \rightarrow DK^\pm$ candidates in the D sidebands. In these plots, the peaks are at
1587 m_B values that are lower (higher) than the B mass in the $K_S^0 \pi^+ \pi^-$ ($K_S^0 K^+ K^-$)
1588 categories, because they stem from real $B^\pm \rightarrow K_S^0 K^+ K^- \pi^\pm$ decays where a kaon is
1589 mis-reconstructed as a pion or a pion is misreconstructed as a kaon, respectively.
1590 The total contribution of charmless decays in the $B^\pm \rightarrow DK^\pm$ data samples is

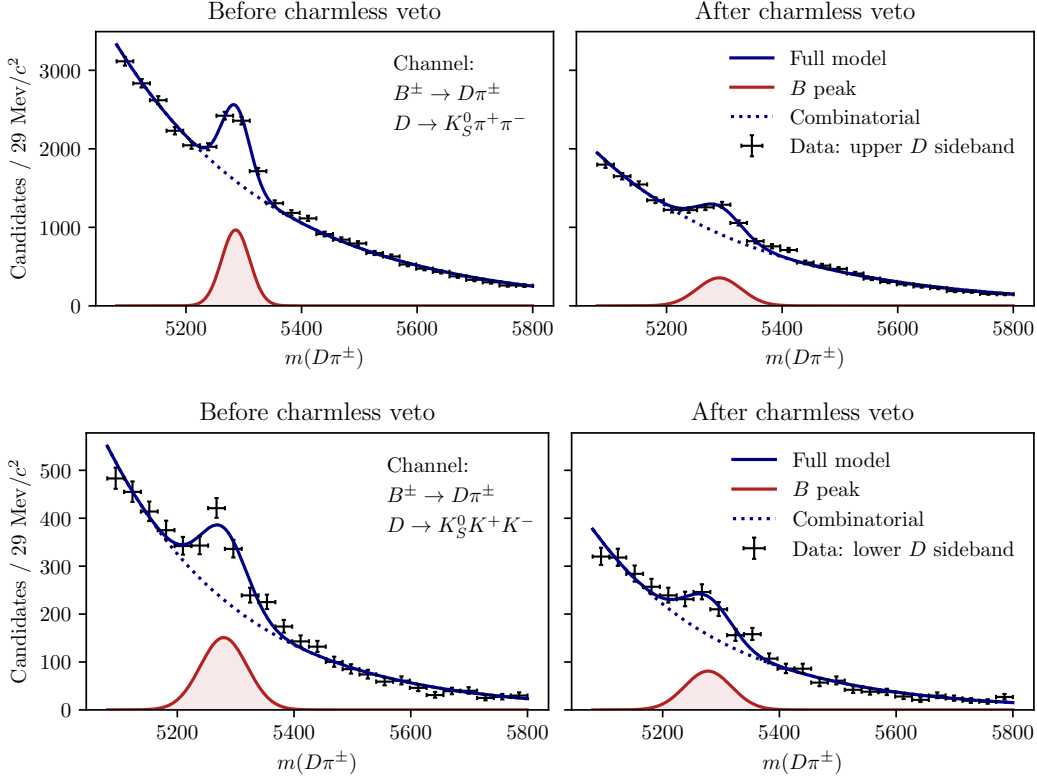


Figure 5.14: The B mass distribution of (top) $B^\pm \rightarrow D(\rightarrow K_S^0 \pi^+ \pi^-)\pi^\pm$ and (bottom) $B^\pm \rightarrow D(\rightarrow K_S^0 K^+ K^-)\pi^\pm$ candidates reconstructed in both the LL and DD categories, residing in the upper D mass sideband $m_D \in [1910, 1960] \text{ MeV}/c^2$ for $D \rightarrow K_S^0 \pi^+ \pi^-$ and in the lower sideband $m_D \in [1910, 1960] \text{ MeV}/c^2$ for $D \rightarrow K_S^0 K^+ K^-$, with (left) no requirement on $\Delta z_{\text{significance}}^{BD}$ and (right) after a requirement of $\Delta z_{\text{significance}}^{BD} > 0.5$.

estimated to be about 200 decays. As described further in Section 5.6.11, the presence of a charmless background at these levels has a negligible impact on the measurement results.

5.3.2 Background from four-body D decays

A similar potential background is from real $B^\pm \rightarrow Dh^\pm$ decays where the D meson decays directly to the $\pi^+\pi^-h^+h^-$ final state, without an intermediate K_S^0 meson. This background can be investigated by looking for a peak in the B mass spectrum for candidates in the K_S^0 sideband, as illustrated in Fig. 5.16. The figure shows the spectrum in the final data sample, illustrating the significant effect of making the requirement on the K_S^0 flight distance that was discussed in Section 5.1.1. The BDT that does *not* rely on the DTF χ^2 has been used to suppress combinatorial background. The remaining peak after requiring $\chi_{\text{FD}}^2 > 49$ is completely accounted for by real signal decays that leak into the K_S^0 sideband.

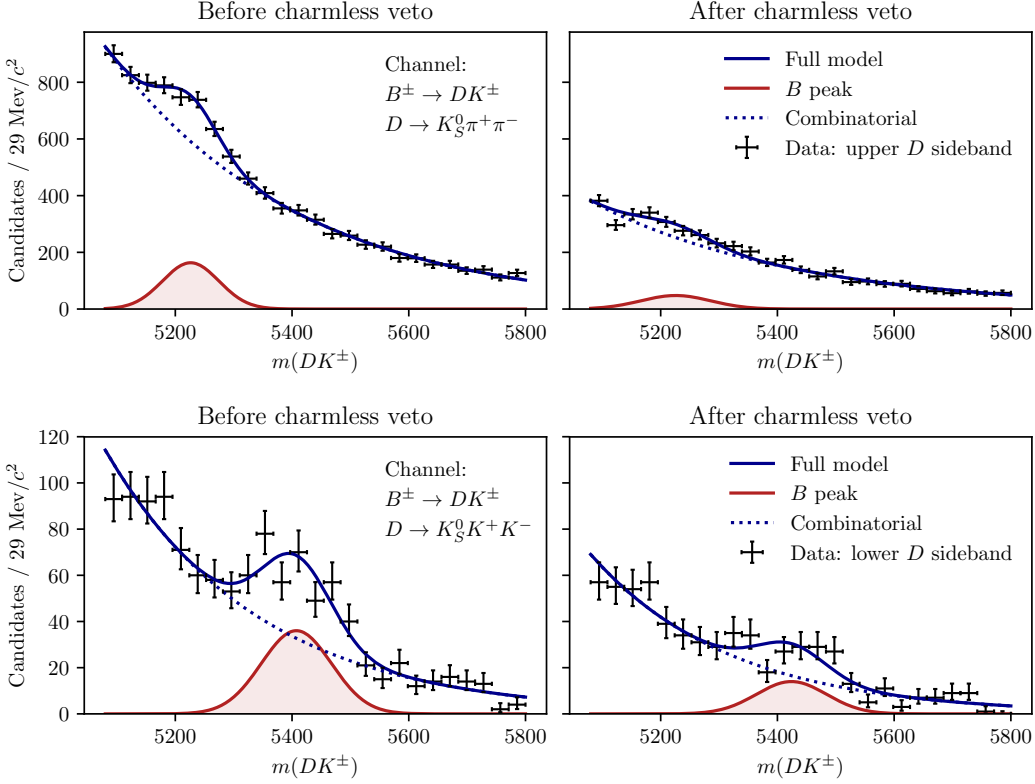


Figure 5.15: The B mass distribution of (top) $B^\pm \rightarrow D(\rightarrow K_S^0 \pi^+ \pi^-)K^\pm$ and (bottom) $B^\pm \rightarrow D(\rightarrow K_S^0 K^+ K^-)K^\pm$ candidates reconstructed in both the LL and DD categories, residing in the upper D mass sideband $m_D \in [1910, 1960] \text{ MeV}/c^2$ for $D \rightarrow K_S^0 \pi^+ \pi^-$ and in the lower sideband $m_D \in [1910, 1960] \text{ MeV}/c^2$ for $D \rightarrow K_S^0 K^+ K^-$, with (left) no requirement on $\Delta z_{\text{significance}}^{BD}$ and (right) after a requirement of $\Delta z_{\text{significance}}^{BD} > 0.5$.

1604 5.3.3 Semi-leptonic backgrounds

1605 The data sample has a minor background from $B \rightarrow D\mu\nu_\mu X$ decays, visible
 1606 in the B mass spectrum when the companion is required to satisfy `isMuon=1`.
 1607 This is shown in Fig. 5.17 for both the $B^\pm \rightarrow DK^\pm$ and $B^\pm \rightarrow D\pi^\pm$ channels
 1608 where $D \rightarrow K_S^0 \pi^+ \pi^-$. The B mass spectra for simulated $B^\pm \rightarrow D\mu^\pm\nu_\mu$ decays
 1609 reconstructed in each category are also shown, from simulation samples produced via
 1610 `RapidSim`. The background is very efficiently vetoed by requiring `IsMuon=0` on the
 1611 companion. This requirement removes approximately 85 % of the background decays,
 1612 as estimated using the `PIDCalib` calibration samples and the (p, p_T) distribution
 1613 for the muon in the `RapidSim` samples. The fraction of signal candidates for
 1614 which the companion satisfies `IsMuon=1` in simulated signal samples is $\leq 0.9\%$
 1615 so the impact on signal yield is small.

1616 The analogous $B \rightarrow D e \nu_e X$ background is investigated by inspecting the B
 1617 mass spectra after making requirements on `PIDE` for the companion candidate, but

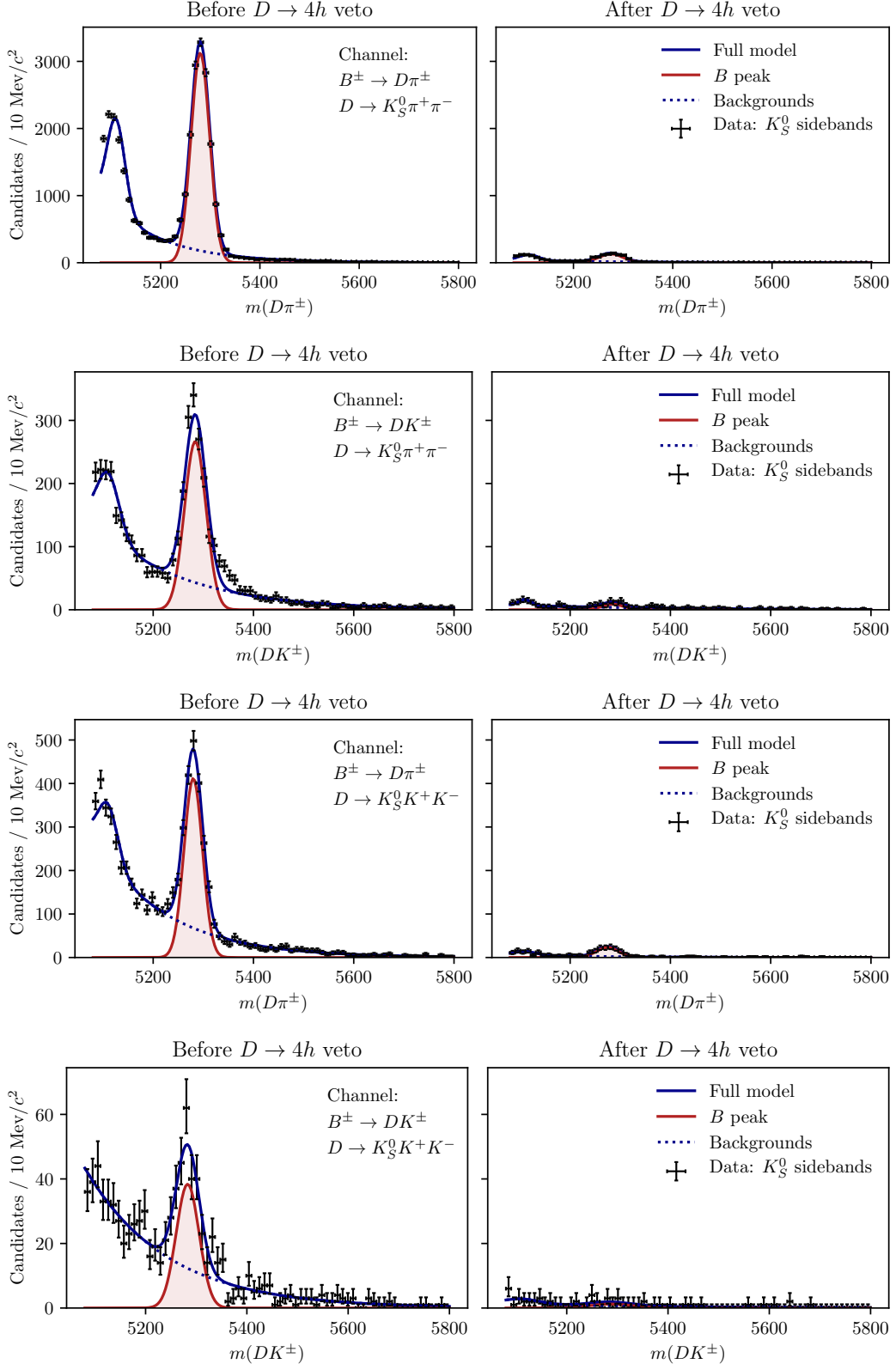


Figure 5.16: The B mass spectrum in the K_S^0 sideband where $m_{K_S^0} \in [467, 482] \text{ MeV}/c^2$ or $m_{K_S^0} \in [512, 527] \text{ MeV}/c^2$ (left) without a requirement on the K_S^0 flight distance significance, and (right) after the requirement implemented in the analysis.

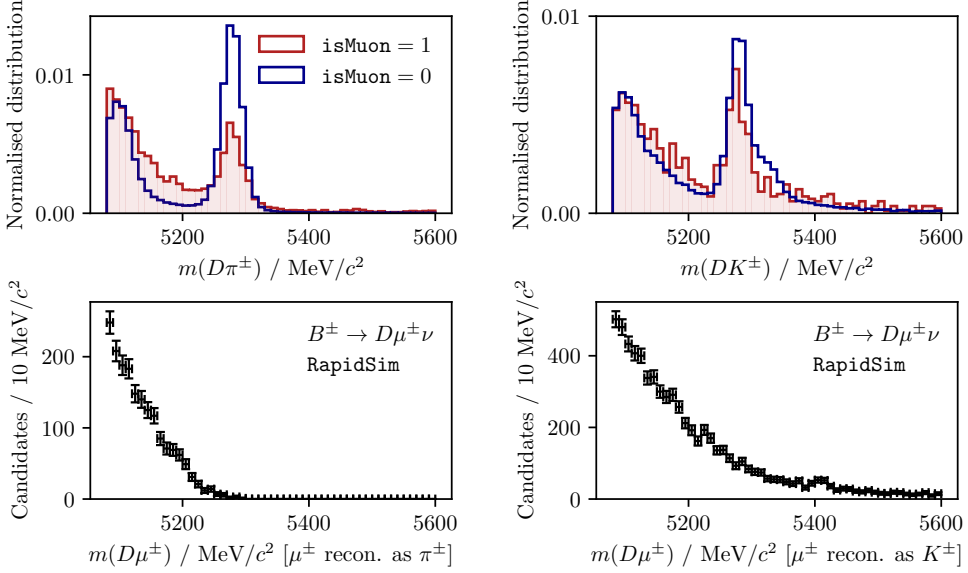


Figure 5.17: (Top) The m_B spectra in data split by the value of `Bach_isMuon` for (left) the $D\pi^\pm$ and (right) the DK^\pm samples where $D \rightarrow K_S^0 \pi^+ \pi^-$. The two histograms are normalised independently, so that the distributions can be compared. The fractions candidates in data (with $m_B \in [5080, 5800] \text{ MeV}/c^2$) that satisfy `Bach_isMuon=1` are 1.6% and 1.8% for the $D\pi^\pm$ and DK^\pm channels respectively. (Bottom) the `RapidSim` mass spectra for $B^\pm \rightarrow D^0 \mu^\pm \nu_\mu$ decays reconstructed in the (left) $D\pi^\pm$ and (right) DK^\pm categories.

a presence of the semi-leptonic background in data is not visible and no electron
veto is applied to the companion.

Background from semi-leptonic D decays

There is a potential background from real $B^\pm \rightarrow Dh^\pm$ decays where the D meson decays semi-leptonically: $D^0 \rightarrow K_S^0 \pi^- \ell^+ \nu_\ell$. This background is particularly dangerous because its peaks at the B mass, when the D -mass requirement is applied and it is reconstructed in the $D \rightarrow K_S^0 \pi^+ \pi^-$ category. This is illustrated in Fig. 5.18 using `RapidSim` samples of $B^\pm \rightarrow D(\rightarrow K^{*-}(X)(\rightarrow K_S^0 \pi^-) \ell^+ \nu_\ell) h^\pm$ decays for $X = 892, 1430, 1680$. The expected background yields relative to signal can be estimated by applying the B and D mass cuts to decays in the `RapidSim` samples, and using the relative branching ratios. Only the $D^0 \rightarrow K^{*-}(892) \ell \nu_\ell$ branching fractions have been measured [?], but there is no reason to expect that higher K^* resonances should not contribute. To estimate their potential contribution,

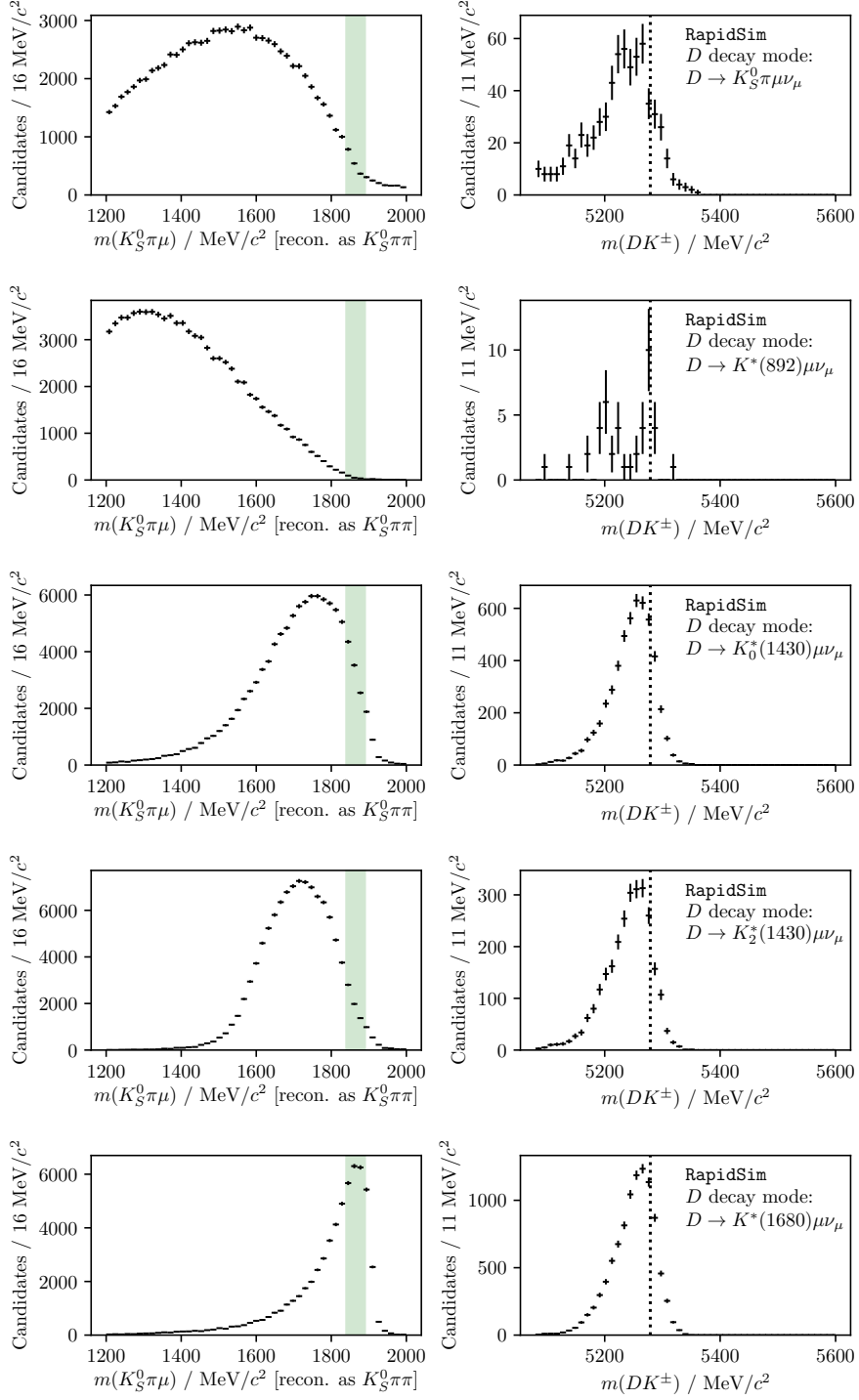


Figure 5.18: The reconstructed (left) $m(K_S^0\pi^+\pi^-)$ and (right) $m(Dh)$ distributions in RapidSim samples of $B^\pm \rightarrow DK^\pm$ decays where $D^0 \rightarrow K_S^0\pi^-\mu^+\nu_\mu$. The top plot is for PHSP decays, and the following plots show the distribution where the $K_S^0\pi^-$ originate in the resonances $K^{*-}(892)$, $K^{*-}_0(1430)$, $K^{*-}_2(1430)$, and $K^{*-}(1680)$. The shapes for the $D^0 \rightarrow K_S^0\pi^-e^+\nu_e$ case are almost identical.

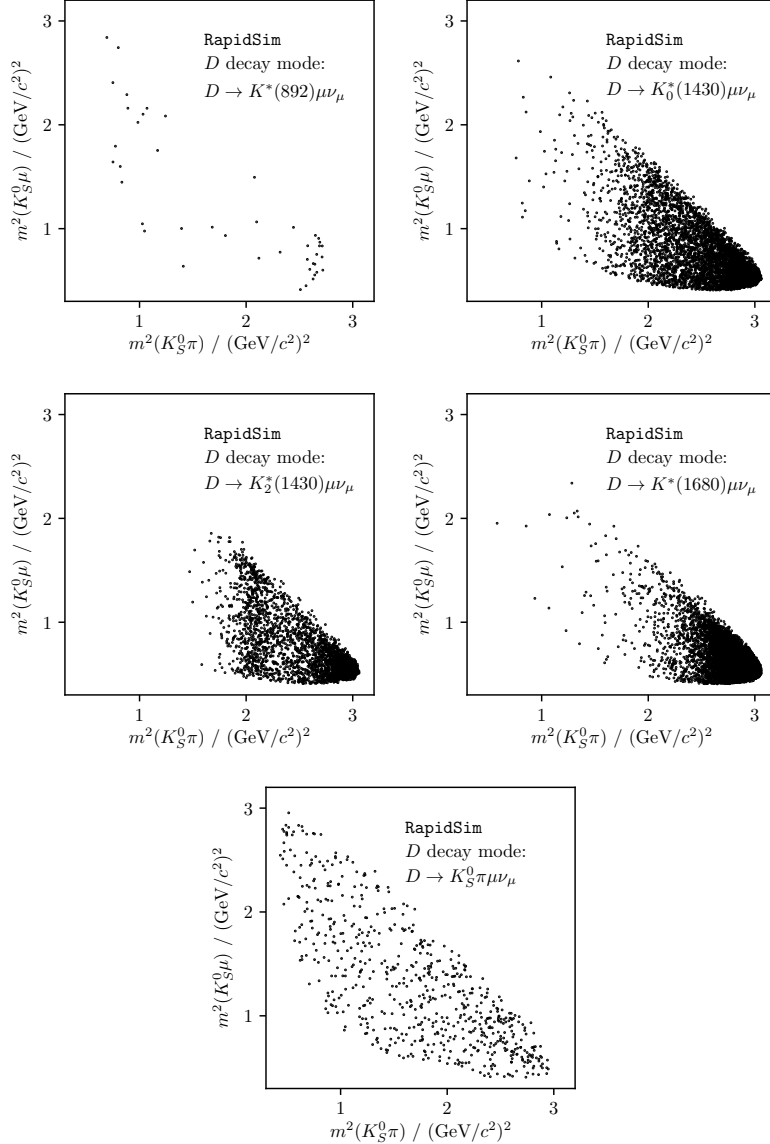


Figure 5.19: Dalitz distribution for $D \rightarrow K_S^0 \pi^- \mu \nu_\mu$ decays in RapidSim, where the $K_S^0 \pi^-$ originate in the resonances $K^{*-}(892)$, $K^{*-}_0(1430)$, $K^{*-}_2(1430)$, and $K^{*-}(1680)$, as well as for a flat PHSP distribution.

the branching ratios are approximated by

$$\text{BR}[D^0 \rightarrow K^{*-}(X)(\rightarrow K_S^0 \pi^-) \ell \nu_\ell] \simeq \frac{\text{BR}[D^0 \rightarrow K^{*-}(X)(\rightarrow K_S^0 \pi^-) \pi^+]}{\text{BR}[D^0 \rightarrow K^{*-}(892)(\rightarrow K_S^0 \pi^-) \pi^+]} \text{BR}[D^0 \rightarrow K^{*-}(892)(\rightarrow K_S^0 \pi^-) \ell \nu_\ell]$$

because all the relevant $D^0 \rightarrow K^{*-}(\rightarrow K_S^0 \pi^-) \pi^+$ branching fractions are known [?]. The efficiencies and branching ratios relative to the signal channel are given in Table 5.5. It is clear that the higher K^* resonances are important: the smaller branching ratios are compensated for by a higher selection efficiency, due to the

Table 5.5: The selection efficiencies of $B^\pm \rightarrow DK^\pm$ decays where $D^0 \rightarrow K_S^0\pi^-\ell^+\nu_\ell$ when reconstructed in the $D \rightarrow K_S^0\pi^+\pi^-$ mode in RapidSim relative to the signal selection efficiencies, for a number of decay modes: PHSP as well as resonant production where the $K_S^0\pi^-$ pair originates in one of several K^* resonances. The relative branching ratios are also shown, calculated as explained in the main text, as well as the predicted relative yields.

Mode	$\epsilon_{bkg}/\epsilon_{signal}$ (%)	$\Gamma_{bkg}/\Gamma_{signal}$ (%)	N_{bkg}/N_{signal} (%)
$D \rightarrow K_S^0\pi^-\mu^+\nu_\mu$ (PHSP)	0.92 ± 0.05	18.3 ± 14.8	0.17 ± 0.14
$D \rightarrow (K_S^0\pi^-)_{K^{*-}(892)}\mu^+\nu_\mu$	0.06 ± 0.01	22.3 ± 3.2	0.013 ± 0.003
$D \rightarrow (K_S^0\pi^-)_{K_0^{*-}(1430)}\mu^+\nu_\mu$	7.3 ± 0.1	3.7 ± 0.8	0.27 ± 0.06
$D \rightarrow (K_S^0\pi^-)_{K_2^{*-}(1430)}\mu^+\nu_\mu$	3.7 ± 0.1	0.5 ± 0.3	0.02 ± 0.01
$D \rightarrow (K_S^0\pi^-)_{K^{*-}(1680)}\mu^+\nu_\mu$	24.4 ± 0.3	0.6 ± 0.5	0.15 ± 0.12
$D \rightarrow K_S^0\pi^-e^+\nu_e$ (PHSP)	0.53 ± 0.02	20.8 ± 16.3	0.11 ± 0.09
$D \rightarrow (K_S^0\pi^-)_{K^{*-}(892)}e^+\nu_e$	0.15 ± 0.02	25.6 ± 2.5	0.04 ± 0.01
$D \rightarrow (K_S^0\pi^-)_{K_0^{*-}(1430)}e^+\nu_e$	6.3 ± 0.1	4.2 ± 0.8	0.26 ± 0.05
$D \rightarrow (K_S^0\pi^-)_{K_2^{*-}(1430)}e^+\nu_e$	4.12 ± 0.08	0.5 ± 0.3	0.02 ± 0.01
$D \rightarrow (K_S^0\pi^-)_{K^{*-}(1680)}e^+\nu_e$	10.0 ± 0.2	0.7 ± 0.5	0.07 ± 0.05
Total	-	-	1.1 ± 0.4

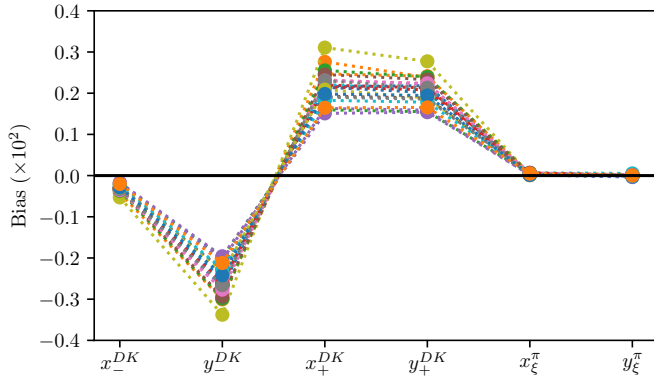


Figure 5.20: Estimated biases on the measured observables due to the presence of $D \rightarrow K_S^0\pi\ell\nu_\ell$ backgrounds, calculated while varying efficiencies and branching ratios within uncertainties.

1636 smaller phase-space of the missed neutrino. The total background yield is 1.1 %
 1637 of the signal yield in both the $B^\pm \rightarrow D\pi^\pm$ and $B^\pm \rightarrow DK^\pm$ channels. However,
 1638 there will be an additional contribution in the $B^\pm \rightarrow DK^\pm$ channel from real
 1639 $B^\pm \rightarrow D\pi^\pm$ decays with semi-leptonic D decays and a mis-identification of the
 1640 companion. This background also peaks, and the yield is approximately 0.4 %
 1641 of the $B^\pm \rightarrow DK^\pm$ signal yield.

1642 The potential impact from the presence of the background is estimated by

- 1643 1. calculating the expected $B^\pm \rightarrow D\pi^\pm$ and $B^\pm \rightarrow DK^\pm$ yields in each bin for
 1644 physics parameters similar to the world average values
- 1645 2. then calculating the background bin yields in each bin, using the relative
 1646 branching fractions and efficiencies described above and taking the bin-
 1647 distribution from the RapidSim samples. The RapidSim samples are produced
 1648 using the `ISGW2` model in `EvtGen` [?], yielding the Dalitz distributions in
 1649 Fig. 5.19.
- 1650 3. adding the signal and background yields, and fitting the new $B^\pm \rightarrow D\pi^\pm$ and
 1651 $B^\pm \rightarrow DK^\pm$ yields back with the default signal-yield expressions (including a
 1652 fit of the F_i parameters)

1653 The obtained biases are shown in Fig. 5.20, where they are calculated a number
 1654 of times, each time varying the efficiencies within statistical uncertainties and the
 1655 relevant branching fractions within the measurement uncertainties. The systematic
 1656 uncertainty due to the unknown branching fractions and the use of RapidSim in
 1657 lieu of full simulation is not included, but is of course significant. Nevertheless
 1658 it is clear that the potential biases are significant compared to the size of the
 1659 systematic uncertainties of the analysis presented in Section 5.6. Therefore the
 1660 backgrounds are vetoed by requiring `IsMuon=0` and `PIDe < 0` on the pions from
 1661 the D -decay with opposite charge to the bachelor in the $D \rightarrow K_S^0 \pi^+ \pi^-$ channel.
 1662 This requirement removes 88 % of the muonic background and 99 % of the electron
 1663 background, according to PID efficiencies obtained via the `PIDCalib` package,
 1664 using the (p, p_T) distribution for the muon/electron in the RapidSim samples. The
 1665 survival rate for signal decays in full simulation is 94 %, so the impact on the
 1666 obtainable precision is only about 3 %. A systematic uncertainty is assigned to
 1667 account for the potential remaining background.

1668 In the $D \rightarrow K_S^0 K^+ K^-$ channel an analogous study shows the relative yields
 1669 to be similar. The selection efficiencies are higher, as are the relative branching
 1670 ratios due to the lower $D \rightarrow K_S^0 K^+ K^-$ branching fraction, but in this mode the
 1671 $\text{PIDK} > -5$ requirement placed on the pion and lepton remove approximately 90 %
 1672 of the background, leaving the relative rate similar to in $D \rightarrow K_S^0 \pi^+ \pi^-$. However,
 1673 importantly, *the background is not peaking*, as shown in Fig. 5.21. The presence
 1674 of a percent-level, *non-peaking* background in the $D \rightarrow K_S^0 K^+ K^-$ channel is safe
 1675 to ignore and thus no veto is applied in the $D \rightarrow K_S^0 K^+ K^-$ channel.

1676 The muon-veto for the semi-leptonic background does remove some signal
 1677 decays, where an original pion or kaon results in hits in the muon detectors. A

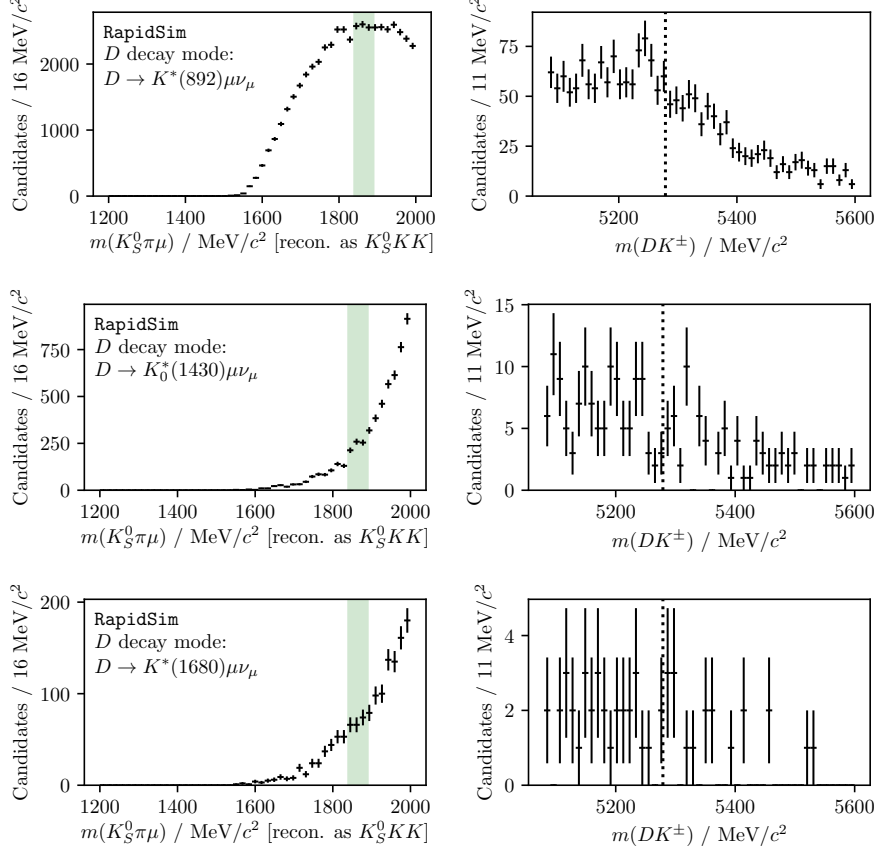


Figure 5.21: The reconstructed (left) $m(K_S^0 K^+ K^-)$ and (right) $m(Dh)$ distributions in RapidSim samples of $B^\pm \rightarrow DK^\pm$ decays where $D^0 \rightarrow K_S^0 \pi^- \mu^+ \nu_\mu$, where the $K_S^0 \pi^-$ originate in (top to bottom) the resonances $K^{*-}(892)$, $K^{*-}_0(1430)$, and $K^{*-}(1680)$. The shapes for the $D^0 \rightarrow K_S^0 \pi^- e^+ \nu_e$ case are almost identical.

1678 significant contribution is from particles that decay in flight. The track quality
 1679 of these decays is worse than for nominal decays, which affects the resolution on
 1680 the reconstructed Dalitz coordinates. In simulated signal decays the standard
 1681 deviation of $\Delta m_\pm^2 = m_{reco}^2(K_S^0 \pi^\pm) - m_{TRUE}^2(K_S^0 \pi^\pm)$ is 50 % larger for decays where
 1682 one of the D -decay products has `IsMuon=1` than in decays where this is not the
 1683 case. This can lead to systematic biases on the observables, as described further in
 1684 Section ???. The overall effect is small, as evidenced by the systematic uncertainty
 1685 described in that section; nevertheless this fact motivates removing decay-in-flight
 1686 decays of the D -decay products. Therefore it is also required that `IsMuon=0` for
 1687 the D -decay pion with the same charge as the companion in the $D \rightarrow K_S^0 \pi^+ \pi^-$
 1688 channels, and on the D -decay kaons in the $D \rightarrow K_S^0 K^+ K^-$ channels. This veto
 1689 removes about 2 % of signal candidates in simulation that survive the lepton vetoes
 1690 described in the previous sections.

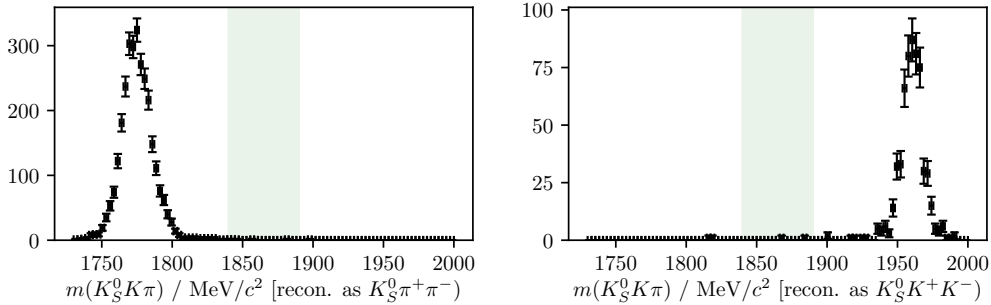


Figure 5.22: Simulated samples of $B^\pm \rightarrow D(\rightarrow K_S^0 K\pi)K^\pm$ decays reconstructed in the (left) $D \rightarrow K_S^0 \pi^+ \pi^-$ and (right) $D \rightarrow K_S^0 K^+ K^-$ channels, combining the LL and DD categories. The D -mass region included in the selection of signal decays is illustrated with the green band. The plots in the $B^\pm \rightarrow DK^\pm$ channels look almost identical.

1691 5.3.4 Cross-feed from other $D \rightarrow K_S^0 h^+ h^-$ decays

1692 Misidentification of a D decay product can lead to background from cross-feed be-
 1693 tween the $B^\pm \rightarrow D(\rightarrow K_S^0 \pi^+ \pi^-)h^\pm$ and $B^\pm \rightarrow D(\rightarrow K_S^0 K^+ K^-)h^\pm$ signal channels,
 1694 or cross-feed from $B^\pm \rightarrow D(\rightarrow K_S^0 K\pi)h^\pm$ decays into either of the signal channels.
 1695 However, this background is very highly suppressed by the employed requirement
 1696 on the D mass. This is illustrated in Fig. 5.22, where the D mass distribution in
 1697 samples of simulated $B^\pm \rightarrow D(\rightarrow K_S^0 K\pi)K^\pm$ decays are shown, when reconstructed
 1698 as $D \rightarrow K_S^0 \pi^+ \pi^-$ and $D \rightarrow K_S^0 K^+ K^-$ decays. Essentially no decays that fall in
 1699 the selected D mass window survive the full selection. Therefore this background
 1700 is not considered further. Neither is the background due to cross-feed between
 1701 $B^\pm \rightarrow D(\rightarrow K_S^0 \pi^+ \pi^-)h^\pm$ and $B^\pm \rightarrow D(\rightarrow K_S^0 K^+ K^-)h^\pm$, since it involves two
 1702 misidentified particles, and therefore will result in reconstructed D masses even
 1703 further away from the selected mass window. A very loose PID requirement on the
 1704 charged D decay products is nonetheless included in the $D \rightarrow K_S^0 K^+ K^-$ channel,
 1705 because it helps reduce the level of combinatorial background.

1706 5.3.5 Swapped-track backgrounds

1707 A possible peaking background stems from real $B \rightarrow DhX$ decays with the same
 1708 final state tracks as in the signal case, but where some tracks are mis-assigned in the
 1709 reconstruction. Examples are $B^\pm \rightarrow (K_S^0 h^+ h^-)_D h^\pm$ decays where the companion
 1710 and a D -decay product track are swapped, or $B^\pm \rightarrow (K^- \pi^+)_D K_S^0 h^\pm$ decays, where
 1711 the K_S^0 is assigned to the D decay and the real companion is swapped with the
 1712 D -decay product of the same charge. The signature of this background type is
 1713 a peak at the D mass, when the invariant mass corresponding to the companion

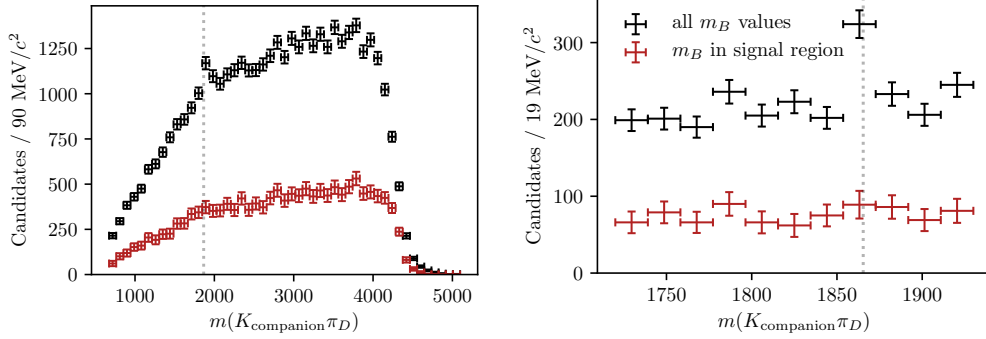


Figure 5.23: Invariant mass spectrum of the $m^2(K^\pm\pi^\mp)$ combination in the $B^\pm \rightarrow (K_S^0\pi^+\pi^-)K^\pm$ data sample for (black) all candidates and (red) candidates for which $m_B \in m_B^{PDG} \pm 30 \text{ MeV}/c^2$. The LL and DD categories are combined. The only difference between the left and right plots is the $m(K\pi)$ mass range on the horizontal axis. The dotted line indicated the known D mass [?].

track and some subset of the D -decay tracks is formed. The presence of the background has been investigated by forming all such combinations, for all data categories, after the full selection has been applied. Only in a single channel is a peak visible: the $B^\pm \rightarrow (K_S^0\pi^+\pi^-)K^\pm$ channel, where $m(K^\pm\pi^\pm)$ has a peak, as shown in Fig. 5.23. Thus, a background is present from the favoured two-body D decay $B^\pm \rightarrow (K^\pm\pi^\mp)_D K_S^0\pi^\pm$, where the K^\mp is reconstructed as the companion, and the pions assigned to the D decay.

Is not favourable to veto this background, because a requirement on the invariant mass of a track combination that includes the companion track would impact the Dalitz-plot acceptance differently in the DK^\pm and $D\pi^\pm$ channels. Thus it would break a fundamental underlying feature of the measurement: the identical selection efficiency profile between these modes. However, the yield excess in the $m(K_{\text{companion}}^\pm\pi^\mp_D)$ range around m_D , attributed to the background, corresponds to only about 0.5 % of the signal yield. A background at this level does not lead to a limiting systematic uncertainty on the measurement, as described in Section ??.

5.4 Signal and background mass shapes

The measurement employs *extended maximum-likelihood fits* [?] to the $m(Dh^\pm)$ distribution of signal candidates to determine the observables of interest. The analysis implements a two-step fit procedure: first the data samples are analysed without separating the candidates by B charge or Dalitz bin, in order to determine appropriate parametrisations of the $m(Dh^\pm)$ distribution of the signal and relevant background components. The parameterisations are then kept fixed in a subsequent

1736 fit of the observables of interest, where the candidates are split by B charge
1737 and Dalitz bin. This section describes the first step, whereas the latter fit is
1738 the subject of Section 5.5.

1739 In both steps, the candidates are split in 8 categories depending on whether
1740 the companion is categorised as a kaon or pion, whether the K_S^0 meson is in the
1741 LL or DD category, and by whether the D meson is reconstructed in the $K_S^0\pi^+\pi^-$
1742 or $K_S^0K^+K^-$ final state. In the remained of this text, these categories are indexed
1743 with the letter c . For each category, c , the expected number of observed decays
1744 at a given B mass, $F^c(m)$, is given by the sum of a signal contribution and a
1745 number of background distributions

$$F^c(m|\theta) = N_s^c(\theta)f_s^c(m|\theta) + \sum_b N_b^c(\theta)f_b^c(m|\theta), \quad (5.4)$$

1746 where θ denotes a set of parameters that describe the mass shapes and expected
1747 yields, in which some parameters are shared between categories. The distributions
1748 $f_{s/b}^c$ are normalised to integrate to unity, and the expected signal (background)
1749 yields are denoted N_s^c (N_b^c). A total, normalised distribution can then be defined

$$f^c(m|\theta) = \frac{1}{N_{\text{tot}}^c(\theta)}F^c(m|\theta), \quad N_{\text{tot}}^c(\theta) = N_s^c(\theta) + \sum_b N_b^c(\theta). \quad (5.5)$$

1750 Given a set of N_{observed}^c measured B masses, $\{m_i^c\}$, in a given category, the extended
1751 log-likelihood function is defined

$$\ln \mathcal{L}_c(\theta|\{m_i^c\}) \equiv \sum_i \ln f^c(m_i^c|\theta) + \ln \text{Poisson}(N_{\text{tot}}^c(\theta), N_{\text{observed}}^c) \quad (5.6)$$

1752 In a simultaneous fit the total, negative log-likelihood is $-\ln \mathcal{L} = -\sum_c \mathcal{L}_c$, and
1753 this function can be minimised to find the maximum-likelihood estimates of the
1754 parameters in θ , as well as their confidence regions and correlation coefficients.
1755 This is handled with the `RooFit` package [?].

1756 Apart from signal decays, the fit includes components that describe combinatorial
1757 background, backgrounds from decays where a companion pion is misidentified
1758 as a kaon or vice versa, and partially reconstructed backgrounds. Each of these
1759 components are described in detail in the following, before the results of the
1760 first-stage fit are presented in Section 5.4.5.

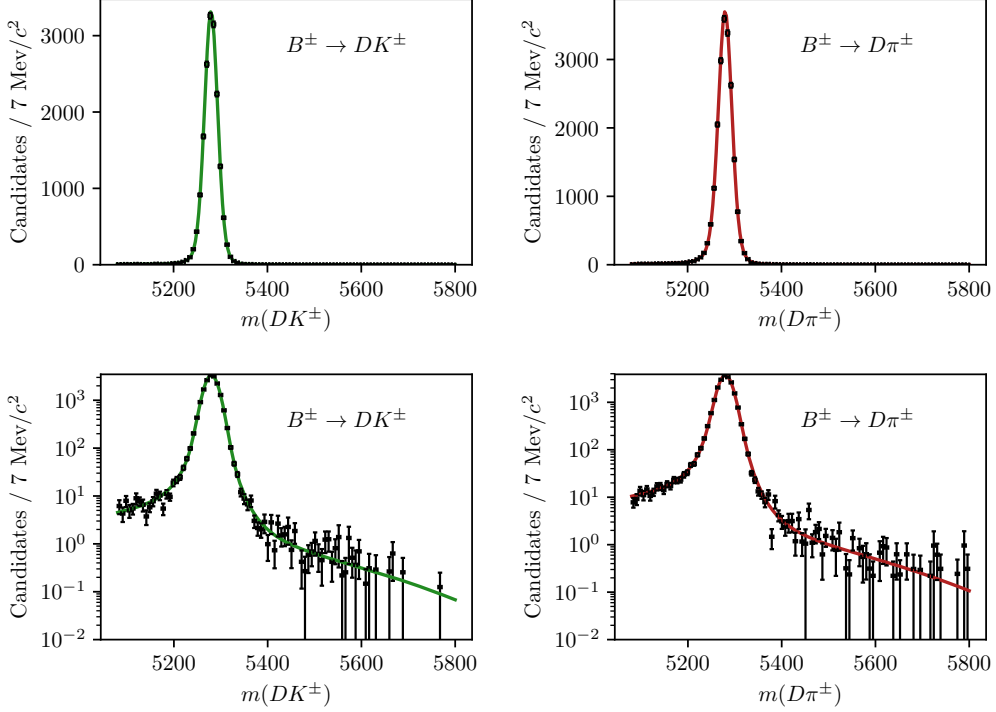


Figure 5.24: Fit projection of the signal shape to simulated $B^\pm \rightarrow D(\rightarrow K_S^0\pi^+\pi^-)h^\pm$ samples reconstructed in the LL category. (Left) shows DK shapes, and (right) shows $D\pi$ shapes. The shapes are shown with both linear and logarithmic y -axis scales.

5.4.1 Signal decays

The signal component is modelled with a sum of a Gaussian density function, $f_G(m|m_B, \sigma)$, and a modified Gaussian distribution with the parameterisation

$$f_C(m|m_B, \sigma, \alpha_L, \alpha_R, \beta) \propto \begin{cases} \exp \left[\frac{-\Delta m^2(1+\beta\Delta m^2)}{2\sigma^2 + \alpha_L \Delta m^2} \right], & \Delta m = m - m_B < 0 \\ \exp \left[\frac{-\Delta m^2(1+\beta\Delta m^2)}{2\sigma^2 + \alpha_R \Delta m^2} \right], & \Delta m = m - m_B > 0, \end{cases} \quad (5.7)$$

which is Gaussian when $\Delta m^2 \ll \sigma^2/\alpha_{L/R}$ or $\Delta m^2 \gg \beta^{-1}$ (with widths of σ and $\sqrt{\alpha_{L/R}/\beta}$ respectively), with an exponential-like transition that is able to model the effect of the experimental resolution of LHCb very well. For the case $\beta = 0$ the shape is denoted the *Cruijff* shape; however, in this case it tends to a uniform distribution for large Δm^2 values, and cannot model the tails of the signal distribution well. Thus, the full density function is

$$f_s(m|m_B, \sigma, \alpha_L, \alpha_R, \beta) = k_C f_C(m|m_B, \sigma, \alpha_L, \alpha_R, \beta) + (1 - k_C) f_G(m|m_B, \sigma). \quad (5.8)$$

The tail parameters $(\alpha_{L/R}, \beta)$ and the constant k_C are determined in fits to simulated signal decays that have passed the full selection. The parameters are shared

1772 between the $K_S^0\pi^+\pi^-$ and $K_S^0K^+K^-$ channels, but otherwise independent in the
 1773 fit categories. An example of a fit to simulated $B^\pm \rightarrow D(\rightarrow K_S^0\pi^+\pi^-)h^\pm$ decays
 1774 is given in Fig. 5.24. The resolution parameters σ are determined in the fit to
 1775 actual data. Separate parameters are determined in the LL and DD categories,
 1776 because the LL category has a better resolution on the K_S^0 momentum, and
 1777 therefore a narrow peak in reconstructed B mass. Likewise, separate resolution
 1778 parameters are used for $B^\pm \rightarrow D\pi^\pm$ and $B^\pm \rightarrow DK^\pm$ decays, because the smaller
 1779 Q value in the latter case leads to smaller momenta of the decay products, and
 1780 a correspondingly better resolution.

1781 The signal yields are determined independently in each $B^\pm \rightarrow D\pi^\pm$ category.
 1782 The yields in the $B^\pm \rightarrow DK^\pm$ categories are then parameterised in terms of a single
 1783 yield-ratio $\mathcal{R}_{K/\pi}$, and ϵ^c , the corresponding selection efficiency for a given category

$$N_{DK^\pm}^c = \mathcal{R}_{K/\pi} \times N_{D\pi^\pm}^c \times \frac{\epsilon_{DK^\pm}^c}{\epsilon_{D\pi^\pm}^c}. \quad (5.9)$$

1784 The selection efficiency is obtained in simulation, except for the PID efficiencies
 1785 which are obtained in calibration data as described in Section 5.1.3. The parameter
 1786 $\mathcal{R}_{K/\pi}$ is shared between all categories, and corresponds to the branching ratio
 1787 between $B^\pm \rightarrow DK^\pm$ and $B^\pm \rightarrow D\pi^\pm$ decays. Therefore, it can be compared to
 1788 the branching ratio ratio measured in dedication measurements, which serves as
 1789 an important cross check of the efficiency determination.

1790 5.4.2 Cross-feed between $B^\pm \rightarrow Dh^\pm$ channels

1791 There is a cross-feed between the $B^\pm \rightarrow D\pi^\pm$ and $B^\pm \rightarrow DK^\pm$ channels, where real
 1792 $B^\pm \rightarrow D\pi^\pm$ decays are reconstructed as $B^\pm \rightarrow DK^\pm$ decays, or where $B^\pm \rightarrow DK^\pm$
 1793 decays are reconstructed as $B^\pm \rightarrow D\pi^\pm$ decays. Due to relative branching fractions
 1794 the former contribution is by far the most important, but both are modelled.

1795 The cross-feed shapes are obtained in a data-driven manner using the sPlot
 1796 method [?], and fixed in the fit to data. Separate shapes are determined for each
 1797 category, using the following steps:

- 1798 • The procedure is based on the reasonably pure $B^\pm \rightarrow D\pi^\pm$ sample obtained
 1799 when the full selection is applied. A simple mass fit is performed to the
 1800 invariant mass spectrum and the sPlot method [?] is used to obtain the
 1801 sWeights, w_s , for the signal component. The mass fit uses the same components
 1802 for signal, low mass shape, and combinatorial background as described in this
 1803 section.

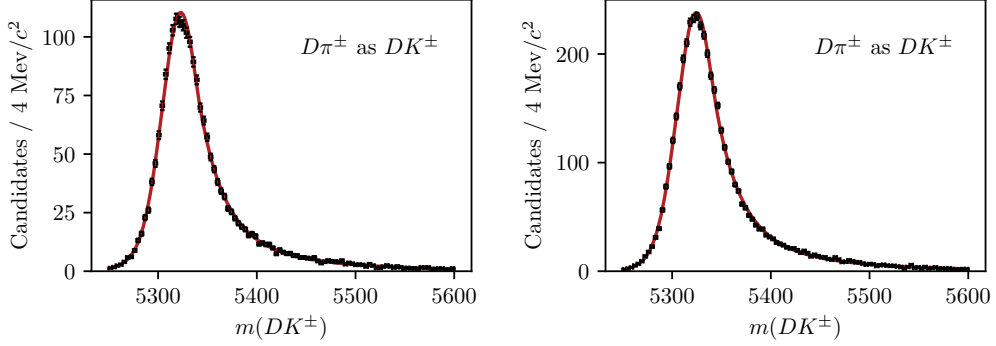


Figure 5.25: Fitted shape of the B^\pm invariant mass spectrum for $B^\pm \rightarrow D\pi^\pm$ decays misidentified as $B^\pm \rightarrow DK^\pm$ decays for (left) LL and (right) DD candidates in the $D \rightarrow K_S^0 \pi^+ \pi^-$ mode.

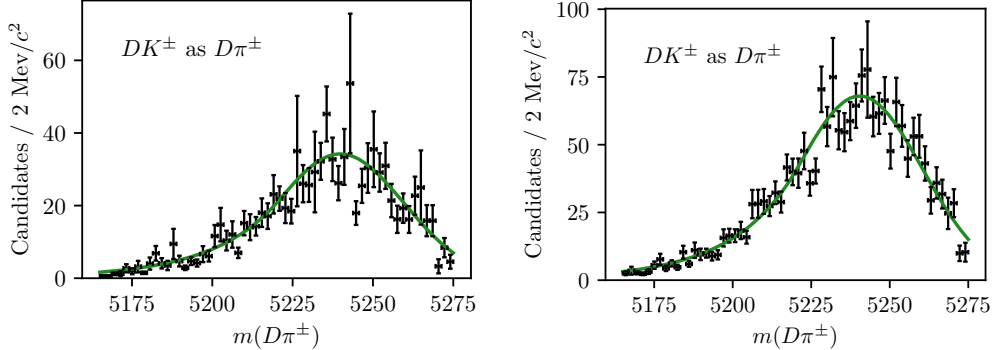


Figure 5.26: Fitted shape of the B^\pm invariant mass spectrum for $B^\pm \rightarrow DK^\pm$ decays misidentified as $B^\pm \rightarrow D\pi^\pm$ decays for (left) LL and (right) DD candidates in the $D \rightarrow K_S^0 \pi^+ \pi^-$ mode.

- 1804 • A set of weights are defined, based on the candidate-by-candidate PID
- 1805 efficiencies obtained as described in Section 5.1.3:
- 1806 – The extracted PID efficiencies of the $\text{PIDK} < 4$ cut $\epsilon_{D\pi \rightarrow D\pi}(p, \eta, n_{\text{tracks}})$
- 1807 are used to reverse-weight the $B^\pm \rightarrow D\pi^\pm$ sample, in order to obtain the
- 1808 bachelor kinematic distributions before the $\text{PIDK} < 4$ cut is applied.
- 1809 – The extracted PID efficiencies of the $\text{PIDK} > 4$ cut $\epsilon_{D\pi \rightarrow DK}(p, \eta, n_{\text{tracks}})$
- 1810 are used to obtain the bachelor kinematic distribution of the $B^\pm \rightarrow D\pi^\pm$
- 1811 candidates mis-identified as $B^\pm \rightarrow DK^\pm$.
- 1812 • The raw distribution of the invariant mass of B^\pm particles with a misidentified
- 1813 bachelor, m_B^{mis-ID} , is produced by also doing the DecayTreeFit kinematic refit
- 1814 while swapping the companion mass hypothesis of each $B^\pm \rightarrow D\pi^\pm$ candidate
- 1815 to a kaon hypothesis.

- 1816 • Each candidate is reweighted by the overall weight $w = w_s^{cand.}/\epsilon_{D\pi \rightarrow D\pi}^{cand.} \cdot$
 1817 $\epsilon_{D\pi \rightarrow DK}^{cand.}$, and the reweighed m_B^{mis-ID} distribution is fitted to obtain the cross-
 1818 feed mass distribution function.

1819 The distributions are modelled with a sum of two Crystal Ball density functions,
 1820 each defined by the parameterisation [?]

$$f_{CB}(m, \mu, \sigma, \alpha, n) \propto \begin{cases} \exp \left[-\frac{1}{2} \left(\frac{m-\mu}{\sigma} \right)^2 \right] & \text{if } (m-\mu)/\sigma > -\alpha \\ A \left(B - \frac{m-\mu}{\sigma} \right)^{-n} & \text{otherwise,} \end{cases} \quad (5.10)$$

1821 where $\alpha > 0$, and

$$A = \left(\frac{n}{\alpha} \right)^n \exp[-\alpha^2/2], \quad B = \frac{n}{\alpha} - \alpha. \quad (5.11)$$

1822 The obtained m_B^{mis-ID} spectrum and obtained mass shape is given in Fig. 5.25
 1823 for the $D \rightarrow K_S^0 \pi^+ \pi^-$ category; the $D \rightarrow K_S^0 K^+ K^-$ shapes are very similar. An
 1824 analogous procedure is used to obtain the mass distribution of $B^\pm \rightarrow DK^\pm$ decays
 1825 reconstructed in the $B^\pm \rightarrow D\pi^\pm$ category. In the first stage where sPlots are
 1826 extracted by a fit to the $B^\pm \rightarrow DK^\pm$ mass spectrum, the cross-feed component
 1827 determined as described above is included. An example of one of the resulting
 1828 shapes is given in Fig. 5.26

1829 The yield of cross-feed from $B^\pm \rightarrow D\pi^\pm$ decays in a given $B^\pm \rightarrow DK^\pm$ category
 1830 is parameterised in terms of the yield of correctly identified $B^\pm \rightarrow D\pi^\pm$ decays and
 1831 the mis-identification probability extracted from calibration samples as described
 1832 in Section 5.1.3. Denoting the rate at which a pion is reconstructed as a kaon
 1833 by $\epsilon_{\pi \rightarrow K}^c$ in a given category, c , the yield is

$$N_{\pi \rightarrow K}^c = N_{D\pi^\pm}^c \frac{\epsilon_{\pi \rightarrow K}^c}{1 - \epsilon_{\pi \rightarrow K}^c}, \quad (5.12)$$

1834 with an analogous definition of the yield of the cross-feed component from
 1835 $B^\pm \rightarrow DK^\pm$ decays in the $B^\pm \rightarrow D\pi^\pm$ spectrum.

1836 5.4.3 Partially reconstructed backgrounds

1837 A number of background candidates stem from partly reconstructed B decays of the
 1838 type $B \rightarrow DhX$, where X denotes a photon or a pion that is not reconstructed. It
 1839 is not possible to reject these decays in the selection, due to the similarity to signal
 1840 decays. However, the missing momentum results in reconstructed B masses below
 1841 the actual B mass, and the backgrounds are also denoted *lowmass* backgrounds.
 1842 These mass distributions are modelled with analytic shapes, derived based on two

principles. Firstly, the kinematic endpoints of the distributions are fully defined by the particle masses in the decay. Secondly, the angular distribution of the missing particle has a one-to-one relation to the missing momentum, and therefore to the reconstructed B mass. Depending on the spin-parity of the particles and resonances involved in the decay, two different mass distributions arise.

In B decays where the missing particle is a scalar that is produced in the decay of a vector resonance (eg. $B^\pm \rightarrow D^{*0}(\rightarrow D^0\pi^0)\pi^\pm$ decays where the π^0 is not reconstructed), the $m(D^0\pi^\pm)$ distribution has a double-peak structure. The D^{*0} helicity angle θ is defined as the angle between the π^0 momentum vector in the D^{*0} rest frame and the D^{*0} boost vector in the B rest frame. The helicity of D^{*0} means that the π^0 will travel predominantly in the direction where $\theta = 0$ or $\theta = \pi$. When $\theta = 0$ the fraction of momentum carried by the missing π^0 is lower, leading to a higher reconstructed $m(D^0\pi^\pm)$. When $\theta = \pi$ the converse occurs. The resulting B mass distribution is a parabola $f_{\text{HORNS}}^0(m)$ peaking near both kinematic endpoints a and b

$$f_{\text{HORNS}}^0(m) = \begin{cases} (m - \frac{a+b}{2})^2, & \text{if } a < m < b \\ 0, & \text{otherwise.} \end{cases} \quad (5.13)$$

Due to the double-peaking structure, and the fact that was developed by Paolo Gandini for the two-body ADS/GLW analyses [], this shape is denoted a *HORNSdini* shape when convolved with a resolution function as described below.

The second relevant decay situation is where the missing particle is a vector, again produced via the intermediate decay of a vector resonance (eg. $B^\pm \rightarrow D^{*0}(\rightarrow D^0\gamma)\pi^\pm$ decays where the photon is not reconstructed). In this case, the spin-parity of the photon (1^-) means that it will decay preferentially in the $\theta = \frac{\pi}{2}$ or $\theta = \frac{3\pi}{2}$ directions, and so a double-peak structure is not seen. In this case the parabolic distribution $f_{\text{HILL}}^0(m)$ with kinematic endpoints a, b has negative curvature and can be described by

$$f_{\text{HILL}}^0(m) = \begin{cases} -(m - a)(m - b), & \text{if } a < m < b \\ 0, & \text{otherwise.} \end{cases} \quad (5.14)$$

Resolution effects mean that the parabolic shapes must be convolved with a resolution function, chosen to be a sum of two Gaussians. For a single Gaussian shape $f_G(x|\mu, \sigma)$ with mean μ and width σ , the double Gaussian is expressed as

$$f_{DG}(x) = f_G(x|\mu, \sigma) + k_G f_G(x|\mu, R_\sigma \sigma). \quad (5.15)$$

where σ is the width of the first Gaussian, and k_G is the relative fractions between the two Gaussians and R_σ is their relative widths. Further, selection effects can

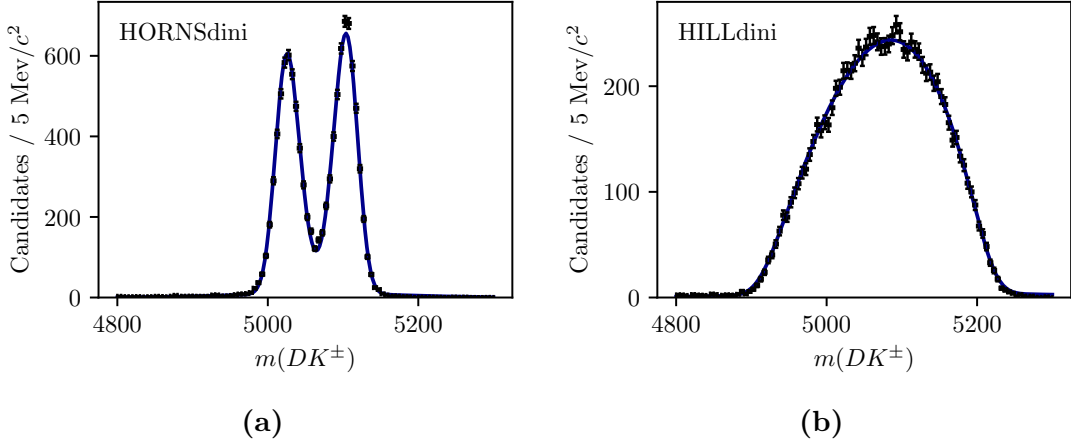


Figure 5.27: Examples of (a) the *HORNSdini* distribution fit to simulated $B^\pm \rightarrow (D^{*0} \rightarrow D^0[\pi^0])K^\pm$ decays, and (b) the *HILLSdini* distribution fit to simulated $B^\pm \rightarrow (D^{*0} \rightarrow D^0[\gamma])K^\pm$ decays. The fits in this figure are made to illustrate the features of each shape, but do not enter the actual fit to data.

distort the horns shape such that one of the peaks is higher than the other. This is
 taken into account by introducing a linear polynomial with slope parameter ξ . As
 $\xi \rightarrow 0$, the left hand peak decreases in size relative to the right hand peak. The
 resulting $HORNSdini$ and $HILLdini$ distributions are therefore

$$f_{\text{HORNS/HILL}}(m) = \int_a^b dx f_{\text{HORNS/HILL}}^0(x) f_{DG}(m|x, \sigma, k_G, R_\sigma) \left(\frac{1-\xi}{b-a}x + \frac{b\xi - a}{b-a} \right). \quad (5.16)$$

¹⁸⁷⁶ Examples of the shapes are given in Fig. 5.27. These shapes are used to fit all
¹⁸⁷⁷ partially reconstructed backgrounds, as described in the following section.

1878 Determination of the partially reconstructed background distributions

¹⁸⁷⁹ In both the $B^\pm \rightarrow DK^\pm$ and $B^\pm \rightarrow D\pi^\pm$ categories, components are included to
¹⁸⁸⁰ describe contributions from the partially reconstructed decays (where the particle
¹⁸⁸¹ in square brackets is not reconstructed)

- $B^\pm \rightarrow (D^{*0} \rightarrow D^0[\pi^0])h^\pm$, described using a *HORNSdini* distribution
 - $B^\pm \rightarrow (D^{*0} \rightarrow D^0[\gamma])h^\pm$: described using a *HILLdini* distribution
 - $B^0 \rightarrow (D^{*\pm} \rightarrow D^0[\pi^\pm])h^\mp$: described using a *HORNSdini* distribution
 - $B^{\pm(0)} \rightarrow D^0 h^\pm [\pi^{0(\mp)}]$: described using a *HORNSdini* distribution

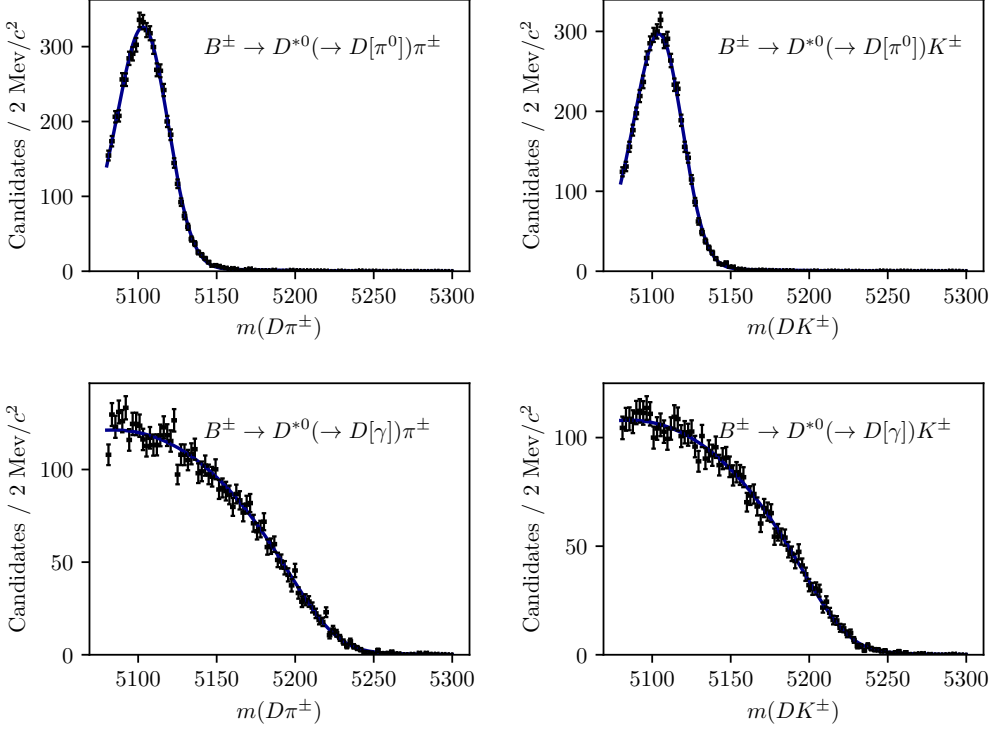


Figure 5.28: Fit projection of the fit to (top) simulated $B^+ \rightarrow D^{*0}(\rightarrow D^0[\pi^0])h^\pm$ decays and (bottom) simulated $B^+ \rightarrow D^{*0}(\rightarrow D^0[\gamma])h^\pm$ decays, all reconstructed in the DD category. Both the (left) DK and (right) $D\pi$ shapes are shown.

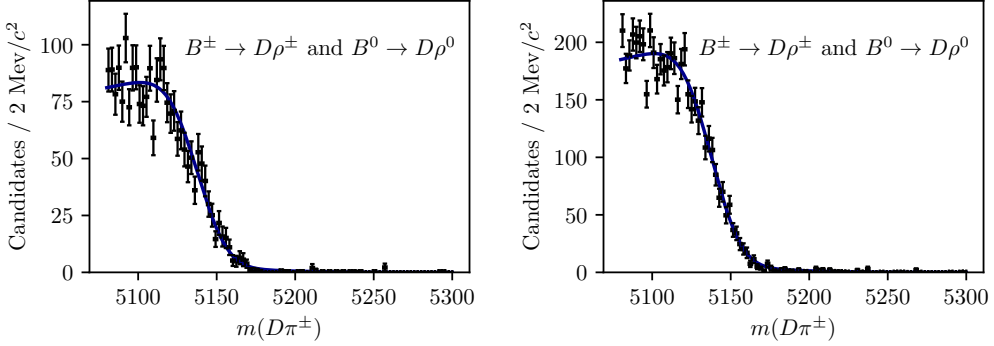


Figure 5.29: Projections of the fit to simulated $B^\pm \rightarrow D\rho^\pm$ and $B^0 \rightarrow D\rho^0$ samples reconstructed as $B^\pm \rightarrow D\pi^\pm$ decays for the (left) LL and (right) DD categories.

1886 The mass distributions of all the $B \rightarrow D^*h^\pm$ contributions are obtained from
 1887 fits to samples of full LHCb simulation. Examples of these fits are shown in
 1888 Fig. 5.28. All shape parameters are kept fixed in the fit to data, except for the
 1889 parameter σ of the resolution function in Eq. (5.15) which is allowed to obtain
 1890 the value preferred by data.

1891 The mass distribution of $B^{\pm(0)} \rightarrow D^0 h^\pm [\pi^{0(\mp)}]$ decays reconstructed in the

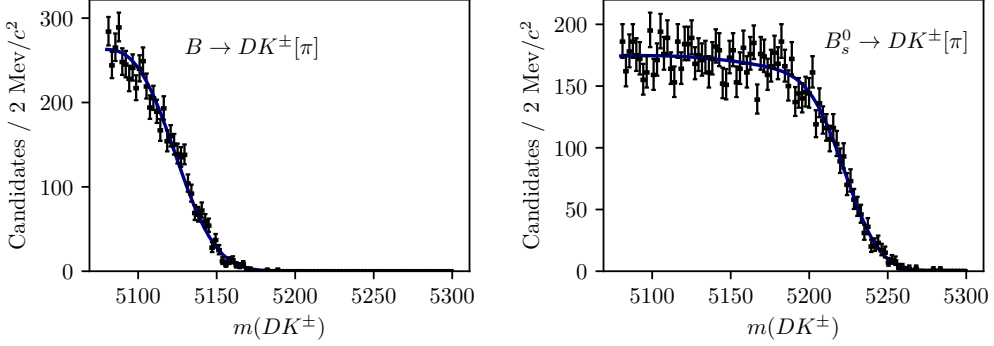


Figure 5.30: Fit projection for the fit used to obtain a shape for the partly reconstructed background from (left) $B \rightarrow DK\pi$ decays and (right) $B_s^0 \rightarrow D K^\pm[\pi]$ decays where a pion is not reconstructed.

1892 $B^\pm \rightarrow D\pi^\pm$ categories is obtained from full LHCb simulation samples of $B^\pm \rightarrow D^0\rho^\pm$
1893 and $B^0 \rightarrow D^0\rho^0$ decays. The shapes were compared to those predicted by an
1894 amplitude model for $B^0 \rightarrow D^0 \rightarrow \pi^\pm\pi^\mp$ decays developed by LHCb [?], but found
1895 to be very similar for the $m(D\pi^\pm)$ range relevant to this analysis. The obtained
1896 shapes are shown in Fig. 5.29.

1897 The mass distribution of $B^{\pm(0)} \rightarrow D^0 K^\pm[\pi^{0(\mp)}]$ decays reconstructed in the
1898 $B^\pm \rightarrow DK^\pm$ categories, on the other hand, is obtained from a sample of signal
1899 decays, generated via a amplitude model for $B^0 \rightarrow D^0 \rightarrow K^\pm\pi^\mp$ decays developed
1900 by LHCb [?] and smeared to take the LHCb resolution into account. This follows
1901 an approach developed in the context of a GLW analysis based on partially recon-
1902 structed decays made within LHCb [?]. The obtained shape is shown in Fig. 5.30.

1903 The background yields of these backgrounds are parameterised in terms of
1904 one total yield parameter, accounting for all partially reconstructed B^\pm and
1905 B^0 decays, and a number of parameters that describe the relative rates of the
1906 different contributions. In the $B^\pm \rightarrow D\pi^\pm$ channels, the relative rates of the
1907 $B^\pm \rightarrow (D^{*0} \rightarrow D^0[\pi^0])h^\pm$ and $B^0 \rightarrow (D^{*\pm} \rightarrow D^0[\pi^\pm])h^\mp$ backgrounds are fixed
1908 from the known branching fractions, and relative selection efficiencies in simulation.
1909 These backgrounds have almost identical mass distributions and it is not possible to
1910 determine the ratio in the fit to data. The relative yield of $B^\pm \rightarrow D^*(\rightarrow D^0[\gamma])\pi^\pm$
1911 compared to the $B \rightarrow D^*(\rightarrow D^0[\pi])\pi^\pm$ is denoted $f_{D^*\gamma}^{D\pi}$ and is floated in the fit to
1912 data, as is the relative yield of $B \rightarrow D^0\pi^\pm[\pi]$ decays compared to the $B \rightarrow D^*\pi$
1913 modes, denoted $f_{D\pi\pi}^{D\pi}$. In the $B^\pm \rightarrow DK^\pm$ channels, all the relative background
1914 rates are fixed via known branching fractions and relative selection efficiencies; this
1915 is necessary to obtain a stable fit, due to the lower yields.

In the $B^\pm \rightarrow DK^\pm$ categories, an additional partially reconstructed background is considered from $B_s^0 \rightarrow \bar{D}^0[\pi^+]K^-$ (an conjugate) decays. The mass shape is obtained from simulated decays, generated using an amplitude model published by LHCb [?] and smeared to account for the experimental resolution. The obtained shape is shown in Fig. 5.30. The yield of this background component is fixed relative to the signal yields in the corresponding $B^\pm \rightarrow D\pi^\pm$ category, taking the relative branching ratios and hadronisation factors into account.

In the $B^\pm \rightarrow DK^\pm$ channels there is a contribution from partially reconstructed $B \rightarrow D^*\pi^\pm X$ decays where the companion pion is misidentified as a kaon. The reverse contribution is negligible due to the relative branching fractions, and the fact that it is mostly shifted below the mass range of the fit. These are modelled using analytic, empirical mass distributions (essentially sums of a number of regular *HORNs/HILLdini* distributions), with parameters that are determined in fits to simulated $B \rightarrow D^*\pi^\pm$ and $B \rightarrow D\rho$ decays where the pion is reconstructed with the kaon mass hypothesis. The shapes are fixed in the fit to data.

1931

1932 Partially reconstructed backgrounds that are not modelled

1933 It was considered whether a background from $\Lambda_b^0 \rightarrow D^0p\pi^-$ decays where a pion
 1934 is not reconstructed, and the proton is misidentified as the companion, can be
 1935 expected to contribute significantly. This has been investigated in full LHCb
 1936 simulation samples, for the D final state $K_S^0\pi^+\pi^-$. Taking into account the selection
 1937 efficiencies, branching fractions, and hadronisation fraction of this background, the
 1938 expected relative yield of the Λ_b^0 background compared to signal of 0.03 % in the
 1939 $B^\pm \rightarrow D\pi^\pm$ channel, which is completely negligible. In the $B^\pm \rightarrow DK^\pm$ channel,
 1940 total of about 200 decays are expected, combined for the LL and DD categories.
 1941 However, most of these lie at B masses smaller than the signal peak, and their impact
 1942 is small. Therefore it is not necessary to model the background in the nominal fit;
 1943 a systematic uncertainty is assigned that accounts for the small potential impact.

1944 In the analogous case of $\Lambda_b^0 \rightarrow D^0pK^-$ decays, the missing energy of the non-
 1945 reconstructed kaon results in a reconstructed B mass below the fit range.

1946 It has also been investigated whether a background from $\Lambda_b^0 \rightarrow \Lambda_c^+\pi^-$ or $\Lambda_b^0 \rightarrow$
 1947 $\Lambda_c^+K^-$ decays can be expected, where $\Lambda_c^+ \rightarrow pK_S^0\pi^+\pi^-$, a pion is missed and the
 1948 proton is misidentified as a pion or kaon from the D decay. Since no PID requirement
 1949 is made on the D decay products in the $D \rightarrow K_S^0\pi^+\pi^-$ channels, and only a loose
 1950 one for $D \rightarrow K_S^0K^+K^-$, this is possible in principle. In practice, the background is
 1951 sufficiently suppressed from the applied D mass requirement to have no significant
 1952 impact, and is therefore not modelled. A systematic uncertainty is assigned that
 1953 accounts for any potential impact on the measurement due to this choice.

1954 5.4.4 Combinatorial background

1955 The combinatorial background is modelled with an exponentially falling density
 1956 function, where both the yield and exponential slope are determined independently
 1957 for each category. This shape is found to model the combinatorial well in all
 1958 categories, most evident in the high- m_B regions where this background dominates.

1959 5.4.5 Fit results

1960 The fit range is chosen to be $m_B \in [5080, 5800] \text{ MeV}/c^2$. The low end of this
 1961 interval includes the high-mass peak of the double-peak structure in the partially
 1962 reconstructed background, which helps the fit constrain the relative contributions of
 1963 backgrounds in the lowmass regions. A number of additional backgrounds exist at
 1964 even lower m_B values, thus extending the fit range to lower masses would necessitates
 1965 an extended model, but not benefit the description of the signal region. The high
 1966 end of the interval includes enough combinatorial background to allow the fit to
 1967 determine the exponential slope parameter accurately.

1968 A large number of pseudoexperiments are carried out to verify that the fit
 1969 procedure is self-consistent, in which toy data sets are generated according to
 1970 the expected B mass distributions, and then fitted. None of the parameters
 1971 obtained in the fit exhibit a mean bias different from zero. For most parameters
 1972 the uncertainties are well estimated. This is the case for the signal yields, and
 1973 the $DK^\pm\text{-}D\pi^\pm$ yield ratio \mathcal{R} , as evidenced by the pull plots in Fig. 5.31. The
 1974 fit underestimates the uncertainty by 10-20 % for some of the parameters related
 1975 to the partly reconstructed backgrounds, as shown in Fig. 5.32, but this is taken
 1976 into account when the uncertainties are propagated to the observables in the
 1977 second-stage fit, as described in Section 5.6.3.

1978 The projections of the fit to data are shown in Figs. 5.33 and 5.34, for the
 1979 $D \rightarrow K_S^0\pi^+\pi^-$ and $D \rightarrow K_S^0K^+K^-$ data sets, respectively. The obtained yields for
 1980 each fit component are given in Table 5.6. The total yield of $B^\pm \rightarrow D\pi^\pm$ decays is
 1981 approximately 230,000 across all channels. The obtained value of the yield ratio is
 1982 $\mathcal{R}_{K/\pi} = (7.7 \pm 0.1) \%$, corresponding to a total $B^\pm \rightarrow DK^\pm$ yield of 16,500, of which
 1983 about 14,300 pass the PID requirement and are reconstructed in the $B^\pm \rightarrow DK^\pm$
 1984 category. This value of \mathcal{R} is in excellent agreement with expectation from the
 1985 known branching fractions [?], which predict $\mathcal{R}_{K/\pi}^{\text{PDG}} = (7.8 \pm 0.3) \%$.³ The shape
 1986 parameters determined in the fit to data are summarised in Table 5.7.

³While it would seem this measurement thus determines the yield ratio $\mathcal{R}_{K/\pi}$ with a much better precision than the current world average uncertainty, that is because the result quoted here does not include any systematic uncertainties; it is only included to serve as a, successfully passed, cross check.

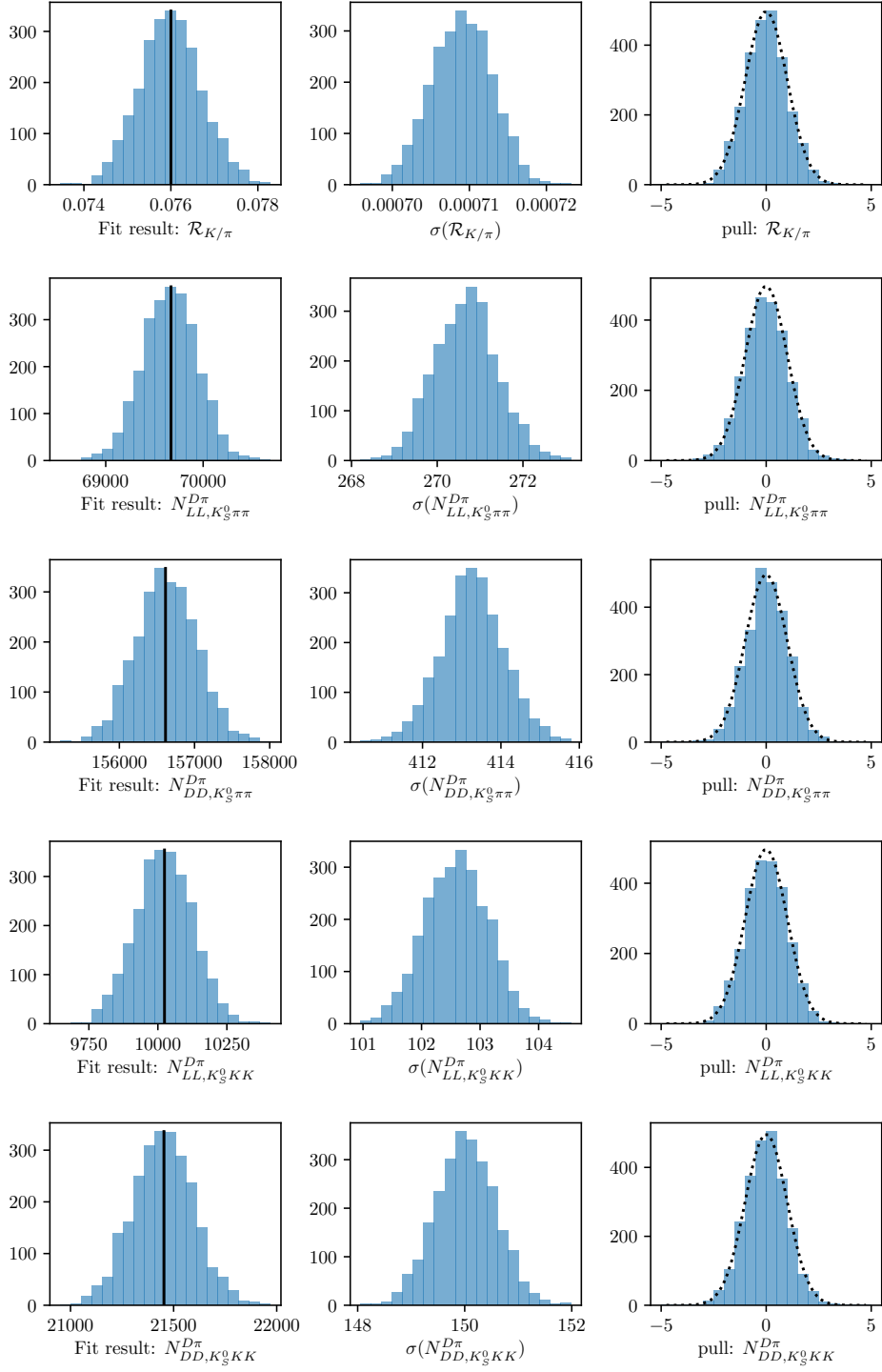


Figure 5.31: The (left) fitted value, (centre) estimated statistical uncertainty, and (right) pull plots for the signal yield parameters, as obtained in a number of pseudo experiments. The black line on the left shows the value used to generate the pseudo data sets; the dotted line on the right shows a Gaussian distribution with mean equal to zero and a standard deviation equal to unity.

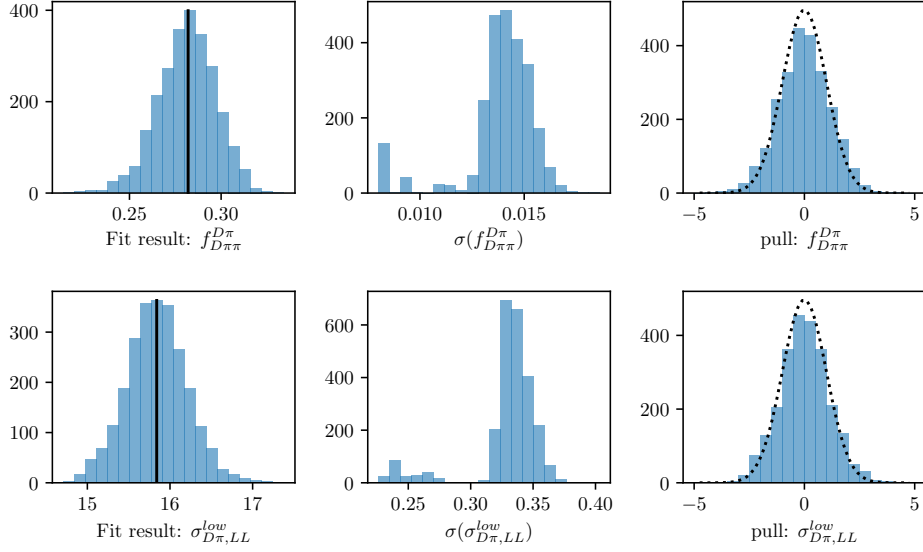


Figure 5.32: The (left) fitted value, (centre) estimated statistical uncertainty, and (right) pulls obtained in a number of pseudo experiments for two examples of parameters relating to the partially reconstructed backgrounds, where the uncertainties are slightly underestimated on average. The standard deviation of the pull distributions is approximately 1.15 in both cases.

Table 5.6: Fitted total candidate yields. The quoted signal yields are for the number of candidates that survive the respective PID cut, whereas the DK^\pm - $D\pi^\pm$ ratio is corrected for PID and selection efficiencies so that it corresponds to the branching ratio.

Component	LL	DD
Signal		
$B^\pm \rightarrow D(\rightarrow K_S^0\pi^+\pi^-)\pi^\pm$	$61,573 \pm 254$	$139,080 \pm 389$
$B^\pm \rightarrow D(\rightarrow K_S^0K^+K^-)\pi^\pm$	$9,160 \pm 98$	$19,910 \pm 144$
$R_{K/\pi} = n(DK)/n(D\pi)$ (%)	7.72 ± 0.08	
Combinatorial		
$B^\pm \rightarrow D(\rightarrow K_S^0\pi^+\pi^-)\pi^\pm$	$3,479 \pm 198$	$9,928 \pm 376$
$B^\pm \rightarrow D(\rightarrow K_S^0K^+K^-)\pi^\pm$	$1,103 \pm 94$	$2,545 \pm 155$
$B^\pm \rightarrow D(\rightarrow K_S^0\pi^+\pi^-)K^\pm$	$1,826 \pm 107$	$3,987 \pm 177$
$B^\pm \rightarrow D(\rightarrow K_S^0K^+K^-)K^\pm$	380 ± 39	655 ± 58
Part. Reco.		
$B^\pm \rightarrow D(\rightarrow K_S^0\pi^+\pi^-)\pi^\pm$	$43,004 \pm 242$	$95,452 \pm 403$
$B^\pm \rightarrow D(\rightarrow K_S^0K^+K^-)\pi^\pm$	$6,247 \pm 99$	$13,241 \pm 157$
$R_{K/\pi}^{low} = n_{low}(DK)/n_{low}(D\pi)$ (%)	6.65 ± 0.12	

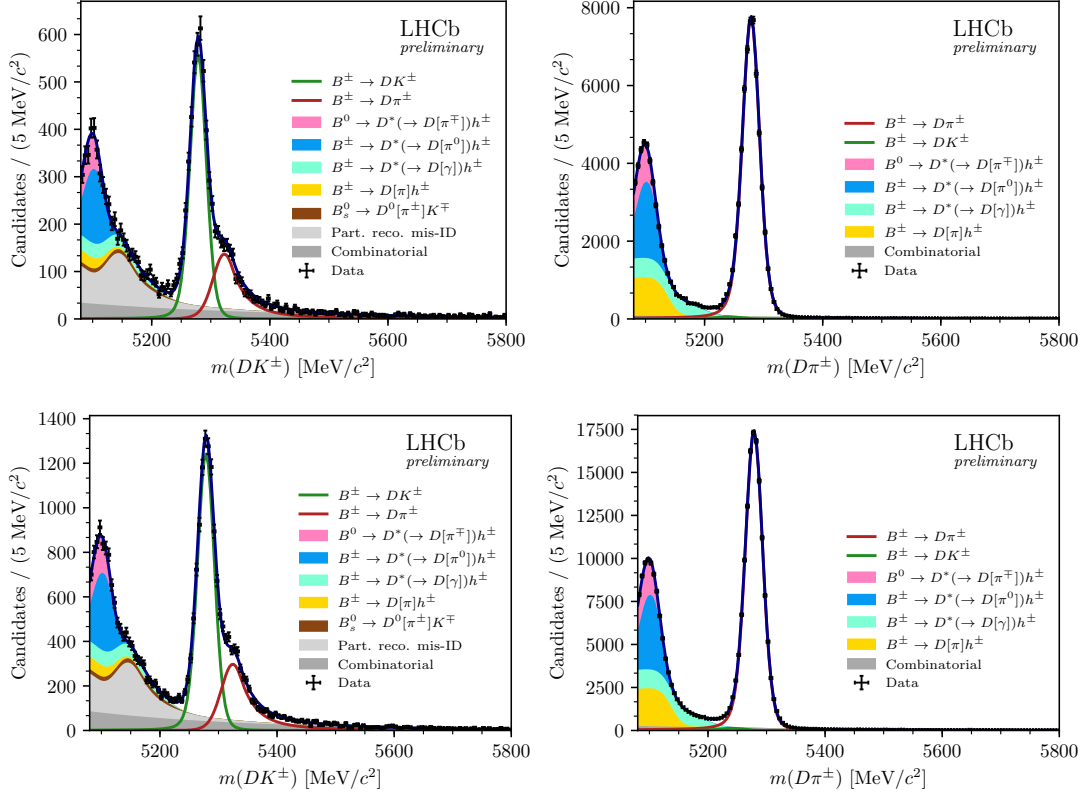


Figure 5.33: The invariant mass distribution for the (left) $B^\pm \rightarrow DK^\pm$ channel and (right) $B^\pm \rightarrow D\pi^\pm$ channel, where $D \rightarrow K_S^0\pi^+\pi^-$ and the K_S^0 is in the (top) LL and (bottom) the DD categories. The particle within square brackets in the legend denotes the particle that has not been reconstructed.

1987 5.5 Measurement of the CP-violation observables

1988 The section describes the second fit stage, in which the CP -violation observables
 1989 of interest are determined. Compared to the first fit stage, the candidates are
 1990 further split by B charge, and by the assigned Dalitz bin number, making for a
 1991 total of 160 categories. Another extended maximum-likelihood fit is carried out,
 1992 in which shape parameters of all signal and background components are fixed to
 1993 those determined in the first fit stage, and thus all floating parameters relate to
 1994 the signal and background yields. The signal yields are expressed in terms of the
 1995 observables of interest, $(x_{\pm}^{DK}, y_{\pm}^{DK}, x_{\xi}^{D\pi}, y_{\xi}^{D\pi})$, allowing the fit to determine their
 1996 optimal values. The details of the fit setup are summarised in the following section,
 1997 before the results are presented in Section 5.5.2, and a wide range of consistency
 1998 checks are described in Section 5.5.3.

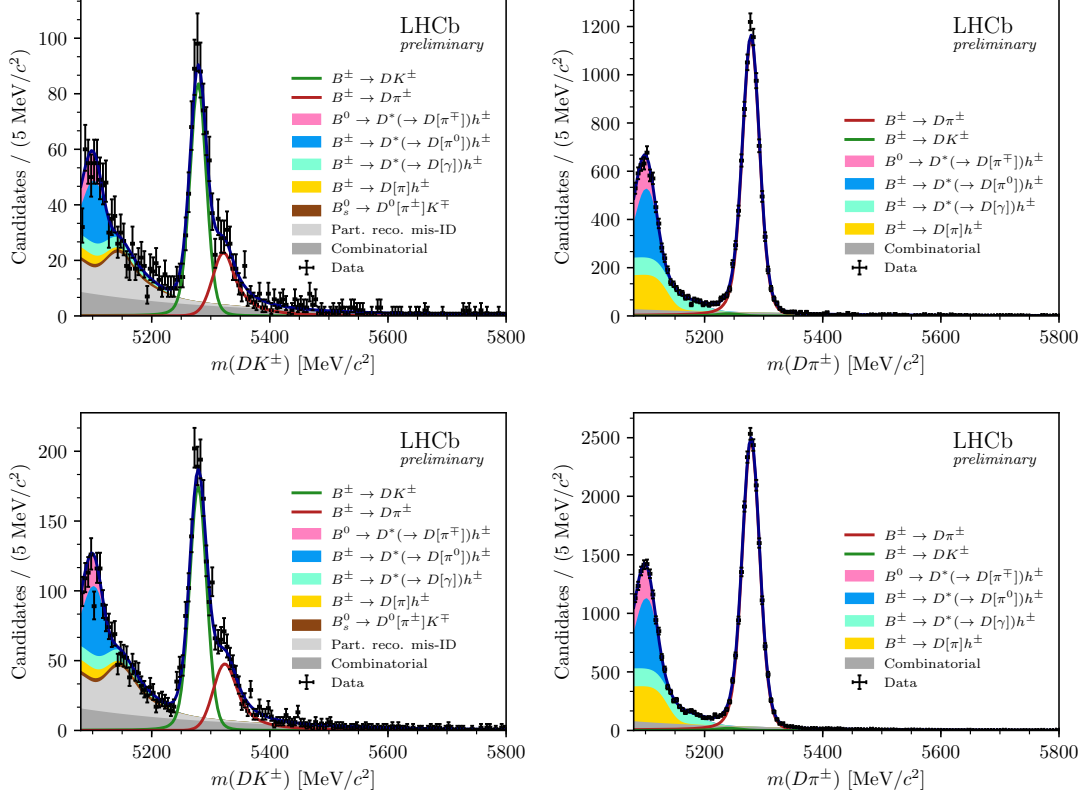


Figure 5.34: The invariant mass distribution for the (left) $B^\pm \rightarrow DK^\pm$ channel and (right) $B^\pm \rightarrow D\pi^\pm$ channel, where $D \rightarrow K_S^0 K^+ K^-$ and the K_S^0 is in the (top) LL and (bottom) the DD categories. The particle within square brackets in the legend denotes the particle that has not been reconstructed.

1999 5.5.1 Fit setup

2000 The signal yields in each bin (in a given category) are defined using the equations
 2001 of Chapter 2, in order to allow for the determination of the $(x_\pm^{DK}, y_\pm^{DK}, x_\xi^{D\pi}, y_\xi^{D\pi})$
 2002 observables. In practice, a set of variables are defined

$$Y_{c,i}^- = F_{c,-i} + [(x_-^c)^2 + (y_-^c)^2]F_{c,-i} + 2\sqrt{F_{c,i}F_{c,-i}}(c_i^c x_-^c + s_i^c y_-^c), \quad (5.17)$$

$$Y_{c,i}^+ = F_{c,-i} + [(x_+^c)^2 + (y_+^c)^2]F_{c,-i} + 2\sqrt{F_{c,i}F_{c,-i}}(c_i^c x_+^c - s_i^c y_+^c), \quad (5.18)$$

2003 for each data category, c , in terms of which the bin yields that enter the like-
 2004 lihood are given by

$$N_{c,i}^\pm = \frac{Y_{c,i}^\pm}{\sum_j Y_{c,j}^\pm} \times N_{c,\text{total}}^\pm. \quad (5.19)$$

2005 This parameterisation is essentially identical to the expressions in Section 2.4,
 2006 slightly modified so that the phase-space-integrated yields of B^+ and B^- decays

Table 5.7: Fitted parameter values.

	LL	DD
$\sigma_{D\pi}$ (MeV/c ²)	14.27 ± 0.05	14.58 ± 0.04
σ_{DK} (MeV/c ²)	13.61 ± 0.24	14.19 ± 0.17
μ (MeV/c ²)		5278.60 ± 0.04
Combinatorial Slopes		
Decay mode	Slope ($10 \times 10^{-3} GeV^{-1}c^2$)	
$B^\pm \rightarrow D(\rightarrow K_S^0\pi^+\pi^-)\pi^\pm$	-3.1 ± 0.2	-4.0 ± 0.1
$B^\pm \rightarrow D(\rightarrow K_S^0K^+K^-)\pi^\pm$	-4.1 ± 0.4	-5.5 ± 0.3
$B^\pm \rightarrow D(\rightarrow K_S^0\pi^+\pi^-)K^\pm$	-3.2 ± 0.2	-3.9 ± 0.2
$B^\pm \rightarrow D(\rightarrow K_S^0K^+K^-)K^\pm$	-4.2 ± 0.4	-4.3 ± 0.4
Part. Reco.		
$\sigma_{D\pi}^{low}$ (MeV/c ²)	13.73 ± 0.33	13.78 ± 0.28
$f_{D\pi\pi}^{D\pi}$		0.268 ± 0.013
$f_{D^*\gamma}^{D\pi}$		0.317 ± 0.005

in a given category are determined directly, in lieu of the normalisation constants h^\pm of that section. A single set of four parameters, $(x_-^{DK}, y_-^{DK}, x_+^{DK}, y_+^{DK})$, are shared between *all* $B^\pm \rightarrow DK^\pm$ categories; they enter the expressions of Eq. (5.17) directly, and are thus determined in the fit. In the $B^\pm \rightarrow D\pi^\pm$ categories, the four corresponding parameters, $(x_-^{D\pi}, y_-^{D\pi}, x_+^{D\pi}, y_+^{D\pi})$, are parameterised in terms of (x_\pm^{DK}, y_\pm^{DK}) and the addition two observables $(x_\xi^{D\pi}, y_\xi^{D\pi})$, as detailed in Section 2.4.

The strong-phase parameters (c_i, s_i) are fixed in the fit to data. In the $D \rightarrow K_S^0\pi^+\pi^-$ categories, the combined CLEO [?] and BESIII [?] measurement results are used, as reported in Ref. [?]. In the $D \rightarrow K_S^0K^+K^-$ categories, the results reported by the CLEO collaboration in Ref. [?] are used. The experimental uncertainty on these measurements is propagated to the measured *CP*-violation observables as part of the systematic uncertainties in Section ??.

The F_i parameters are determined in the fit. Separate parameter sets are determined for the LL and DD categories because the acceptance profile over the Dalitz plot differs between them. The F_i are, however, shared between the $B^\pm \rightarrow DK^\pm$ and $B^\pm \rightarrow D\pi^\pm$ categories; the small difference in the D momentum spectrum between the channels does not lead to a detectable difference in the acceptance profiles. This is a crucial assumption of the method, shown to be true using large samples of simulated decays in Section ??.

Because the F_i

2026 are subject to the constraint that $\sum_{i=-\mathcal{N}}^{\mathcal{N}} F_i^c = 1$, it is beneficial to introduce
 2027 a reparameterisation in the likelihood function. The F_i are re-expressed in terms
 2028 of a set of recursive fractions

$$\mathcal{R}_i = \begin{cases} F_i & , \quad i = -\mathcal{N} \\ F_i / (\sum_{j \geq i} F_j) & , \quad -\mathcal{N} < i < +\mathcal{N} \end{cases} , \quad (5.20)$$

2029 for which the constraint is much simpler, namely that each \mathcal{R}_i lies in the interval
 2030 $[0, 1]$. This results in much better convergence behaviour in the minimisation
 2031 of the negative log likelihood.

2032 The yield of combinatorial background decays is determined independently in
 2033 each bin. A single, overall bin yield of partially reconstructed background from B^\pm
 2034 and B^0 decays is determined in each of the 160 categories; the relative contribution
 2035 from each individual background is fixed from the results of the first-stage fit,
 2036 corrected for the different fit region (a systematic uncertainty is assigned due to this
 2037 choice). In the $B^\pm \rightarrow DK^\pm$ channels, the bin yields of the partially reconstructed
 2038 background from $B_s^0 \rightarrow \bar{D}^0[\pi^+]K^-$ decays are expressed via the F_i , exploiting that
 2039 a positive companion particle is always produced along with a \bar{D}^0 meson (and vice
 2040 versa). The overall yield is fixed from the results of the first stage fit. Finally,
 2041 the yield of the $D\pi^\pm \leftrightarrow DK^\pm$ cross-feed components in each bin are determined
 2042 via the obtained yield of correctly identified decays in the corresponding bin, and
 2043 the known PID efficiencies. This is true for both fully and partially reconstructed
 2044 decays, although only a $D\pi^\pm \rightarrow DK^\pm$ component is included in the latter case.

2045 The fit range is decreased to $m_B \in [5150, 5800] \text{ MeV}/c^2$. The information from
 2046 candidates with lower reconstructed B masses was useful in determining the relative
 2047 rates and free mass shape parameters of the partially reconstructed background
 2048 components in the first-stage fit; however, with these fixed in the second-stage
 2049 fit, this is no longer the case. Furthermore, the setup assumes that the shape of
 2050 the partially reconstructed background is identical across the Dalitz bins. This
 2051 assumption is not perfectly true, but the impact is minimal when the lower limit
 2052 of the fit range is taken to be $5150 \text{ MeV}/c^2$.

2053 Self-consistency check

2054 In order to establish the fit stability and investigate a potential bias, a series of
 2055 pseudoexperiments are run, in which toy datasets are generated using the model,
 2056 and then fitted back. The total yields are taken from the first-stage fit. The signal
 2057 yields are distributed between Dalitz bins using input physics parameters that
 2058 approximately equal the values obtained in Section 5.5.2 from the results of the fit

Table 5.8: Mean biases and pulls for the observables of interest in the final, binned fit, obtained in a large number of pseudoexperiments.

Parameter	Name in code	Mean bias ($\times 10^{-2}$)	Mean pull	Pull width
x_-^{DK}	A_xm_dk	-0.018 ± 0.022	-0.01 ± 0.02	1.01 ± 0.02
y_-^{DK}	A_ym_dk	-0.014 ± 0.026	-0.00 ± 0.02	0.99 ± 0.02
x_+^{DK}	A_xp_dk	-0.018 ± 0.022	-0.01 ± 0.02	1.00 ± 0.02
y_+^{DK}	A_yp_dk	-0.016 ± 0.028	0.01 ± 0.02	1.00 ± 0.02
$x_\xi^{D\pi}$	A_Re_xi_dpi	0.029 ± 0.052	0.06 ± 0.02	1.00 ± 0.02
$y_\xi^{D\pi}$	A_Im_xi_dpi	0.000 ± 0.060	0.01 ± 0.02	1.00 ± 0.02

to data. The F_i parameters are taken from a fit to data. The partly reconstructed background is distributed as " D^0 -like", ie. in the B^\pm channels $N_i^\pm \propto F_{\mp i}$, except for the B_s^0 background, which is " \bar{D}^0 -like" ($N_i^\pm \propto F_{\pm i}$). The combinatorial background includes real D mesons paired with a random bachelor, as well as fake D mesons that are themselves made up of random tracks. The former is distributed as 50/50 D^0 -like and \bar{D}^0 -like in the toy generation, whereas the latter is assumed to be evenly distributed over the Dalitz plot (ie. the bin yield is proportional to the bin area).

A set of 2000 pseudoexperiments has been run, out of which 98.8% converged properly. The pull plots for the observables of interest are shown in Figs. 5.35 and 5.36; the mean biases and pulls are summarised in Table 5.8. No biases are statistically significant, and the uncertainties are seen to be well estimated.

5.5.2 Main results

The values and statistical uncertainties of observables obtained in the fit are

$$\begin{aligned} x_-^{DK} &= (-5.68 \pm 0.96) \times 10^{-2}, & y_-^{DK} &= (-6.55 \pm 1.14) \times 10^{-2}, \\ x_+^{DK} &= (-9.30 \pm 0.98) \times 10^{-2}, & y_+^{DK} &= (-1.25 \pm 1.23) \times 10^{-2}, \\ x_\xi^{D\pi} &= (-5.47 \pm 1.99) \times 10^{-2}, & y_\xi^{D\pi} &= (0.71 \pm 2.33) \times 10^{-2}. \end{aligned} \quad (5.21)$$

The statistical correlation matrix for the observables is given in Table 5.9. The 2D log-likelihood profile for the observables is shown in Fig. 5.37.

The full set of fit projections in all 160 categories is included in Appendix A. While the CP asymmetry of the phase-space integrated yield is small, this is not the case for all individual bin-pairs. This is shown in Fig. 5.38 where, as an example, the fit projections for the $B^+ \rightarrow DK^+$ decays in bin +2 and the $B^- \rightarrow DK^-$ decays in bin -2 of the $D \rightarrow K_S^0 \pi^+ \pi^-$ Dalitz plot are compared. The presence of CP violation is clearly visible.

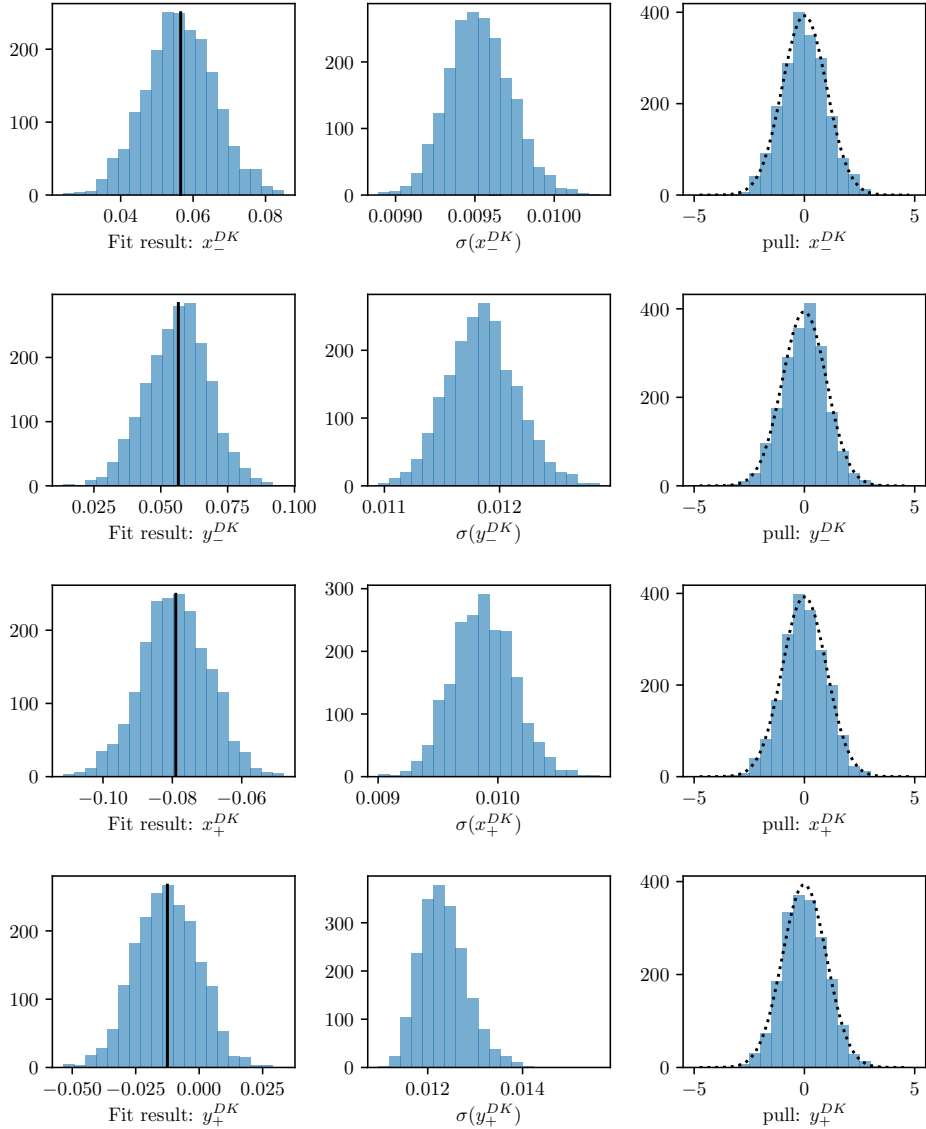


Figure 5.35: The (left) fitted value, (centre) estimated statistical uncertainty, and (right) pulls for the $B^\pm \rightarrow DK^\pm$ observables, as obtained in a number of pseudo experiments. The black line on the left shows the value used to generate the pseudo data sets; the dotted line on the right shows a Gaussian distribution with mean equal to zero and a standard deviation equal to unity.

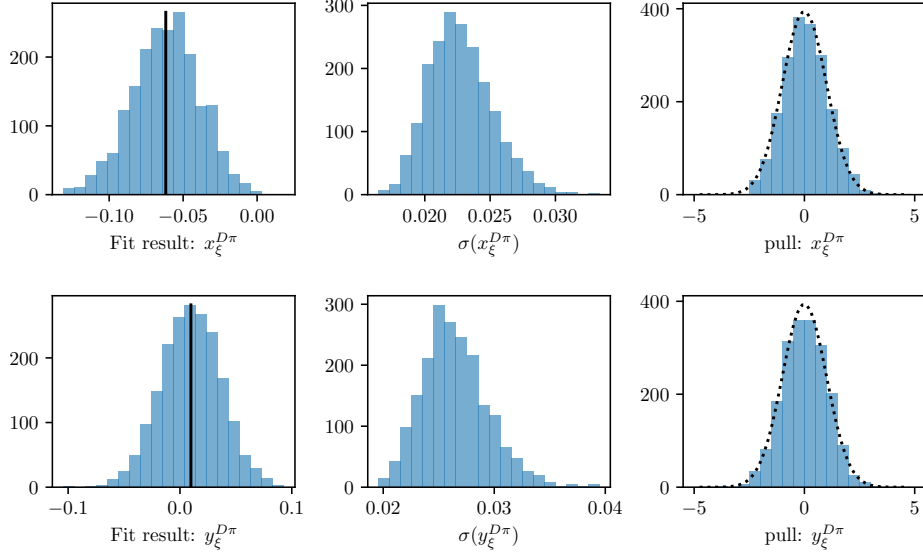


Figure 5.36: The (left) fitted value, (centre) estimated statistical uncertainty, and (right) pulls for the $B^\pm \rightarrow D\pi^\pm$ observables, as obtained in a number of pseudo experiments. The black line on the left shows the value used to generate the pseudo data sets; the dotted line on the right shows a Gaussian distribution with mean equal to zero and a standard deviation equal to unity.

Table 5.9: Statistical uncertainties and correlation matrix for the fit to data.

Uncertainty ($\times 10^{-2}$)						
	$x_-^{DK\pm}$	$y_-^{DK\pm}$	$x_+^{DK\pm}$	$y_+^{DK\pm}$	$x_\xi^{D\pi^\pm}$	$y_\xi^{D\pi^\pm}$
σ	0.96	1.14	0.96	1.20	1.99	2.34

Correlations						
	$x_-^{DK\pm}$	$y_-^{DK\pm}$	$x_+^{DK\pm}$	$y_+^{DK\pm}$	$x_\xi^{D\pi^\pm}$	$y_\xi^{D\pi^\pm}$
$x_-^{DK\pm}$	1.000	-0.125	-0.013	0.019	0.028	-0.165
$y_-^{DK\pm}$		1.000	-0.011	-0.009	0.105	0.030
$x_+^{DK\pm}$			1.000	0.088	-0.099	0.038
$y_+^{DK\pm}$				1.000	-0.076	-0.141
$x_\xi^{D\pi^\pm}$					1.000	0.146
$y_\xi^{D\pi^\pm}$						1.000

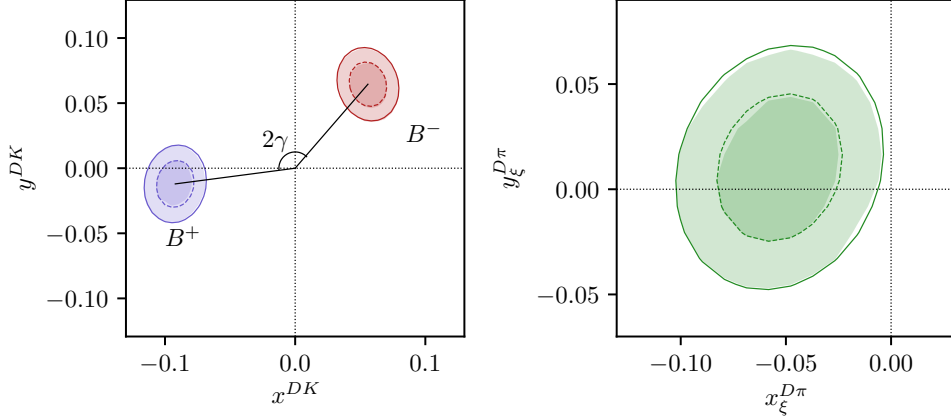


Figure 5.37: The 68 % and 95 % confidence regions for the fitted observables. The lines show the regions estimated from the covariance matrix returned by the default fit. The shaded areas are obtained in a likelihood scan, where the binned fit is run many times with all observables held at fixed values, scanning pairs of observables over the relevant ranges. The scan is made separately for the three pairs (x_{-}^{DK}, y_{-}^{DK}) , (x_{+}^{DK}, y_{+}^{DK}) , and $(x_{\xi}^{D\pi}, y_{\xi}^{D\pi})$, holding the four other parameters fixed at their default-fit central values during a given scan. Then the minimum log-likelihood is related to a χ^2 via $\mathcal{L}_{\min} = \frac{1}{2}\chi^2$ (discarding an irrelevant constant), and the confidence region limits placed at $\chi^2 = 2.30$ and $\chi^2 = 6.18$, yielding the relevant percentiles for a χ^2 distribution with 2 degrees of freedom.

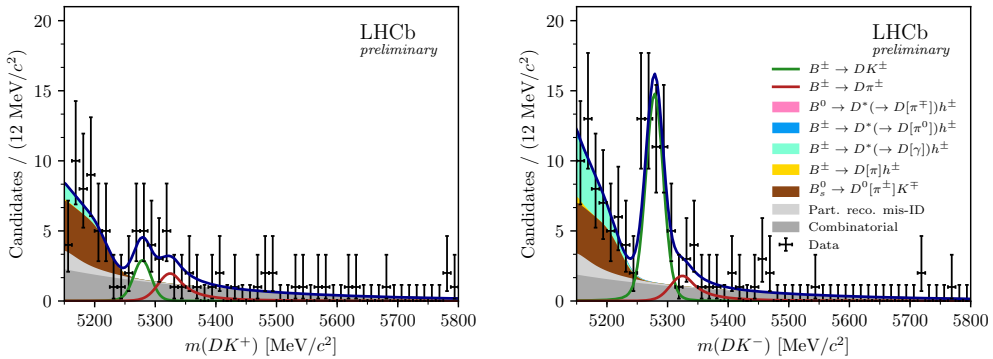


Figure 5.38: The invariant mass distribution for the (left) $B^+ \rightarrow DK^+$ candidates in bin -2 and (right) the $B^- \rightarrow DK^-$ candidates in bin +2, where $D \rightarrow K_S^0\pi^+\pi^-$ and the K_S^0 is reconstructed in the DD category.

2080 The obtained F_i parameter values are shown in Table 5.10. These parameters can
 2081 be useful in other BPGBS measurements made within the LHCb collaboration:
 2082 it is expected that the systematic uncertainty due to differences between the
 2083 Dalitz-plot acceptance profile in $B^\pm \rightarrow Dh^\pm$ decays and, say, $B \rightarrow D^*K$ or
 2084 $B \rightarrow DK^*$ decays is smaller than the systematic arising from extracting the
 2085 efficiency profile from simulated decays. Therefore, the obtain central values and

Table 5.10: The fitted F_i values including statistical uncertainties. The underlying \mathcal{R}_i values are given with both statistical and systematic uncertainties in Section ??.

F_i values: $D \rightarrow K_S^0 \pi^+ \pi^-$		
bin	LL	DD
-8	0.024 ± 0.001	0.024 ± 0.000
-7	0.127 ± 0.001	0.133 ± 0.001
-6	0.062 ± 0.001	0.056 ± 0.001
-5	0.046 ± 0.001	0.042 ± 0.001
-4	0.095 ± 0.001	0.095 ± 0.001
-3	0.160 ± 0.001	0.160 ± 0.001
-2	0.153 ± 0.001	0.153 ± 0.001
-1	0.095 ± 0.001	0.097 ± 0.001
1	0.022 ± 0.001	0.020 ± 0.000
2	0.005 ± 0.000	0.005 ± 0.000
3	0.004 ± 0.000	0.004 ± 0.000
4	0.055 ± 0.001	0.056 ± 0.001
5	0.027 ± 0.001	0.022 ± 0.000
6	0.004 ± 0.000	0.003 ± 0.000
7	0.055 ± 0.001	0.057 ± 0.001
8	0.067 ± 0.001	0.072 ± 0.001

F_i values: $D \rightarrow K_S^0 K^+ K^-$		
bin	LL	DD
-2	0.207 ± 0.004	0.202 ± 0.003
-1	0.222 ± 0.004	0.230 ± 0.003
1	0.290 ± 0.005	0.296 ± 0.003
2	0.281 ± 0.005	0.271 ± 0.003

uncertainties have been made public [?], including a set of systematic uncertainties discussed in Section 5.6.12.⁴

5.5.3 Cross checks

A series of cross checks are performed to verify that the fit to data is behaving as expected.

⁴In practice, it is the obtained \mathcal{R}_i values that are made public, related to the F_i parameters via Eq. (5.20).

2091 **Comparison to results of earlier analyses**

2092 It is confirmed that the results obtained in fits of the Run 1 or 2015+16 data
 2093 sets in isolation are compatible with the results obtained in the original LHCb
 2094 analyses of those data sets [?, ?]. In order to do so, the whole analysis procedure
 2095 is carried out using only the relevant subset of data, and the strong-phase inputs
 2096 from the CLEO collaboration are used in the fit. Two effects need to be taken
 2097 into account when comparing the central values.

2098 The overlap between the samples need to be taken into account. The overlap
 2099 is not 100 % due to changes in the candidate selection. The overlap between the
 2100 new selection and the data set of the original analysis of Run 1 data is about
 2101 70 %, whereas is it about 90 % for the 2015+16 data set. In order to determine the
 2102 expected difference between the observables fitted from data sets with significant
 2103 overlap, a large number of toy data sets were generated in sets of two, where
 2104 70 (90) % of decays were shared between the data sets. Both data sets were
 2105 fitted and the difference between the obtained central values for each observable
 2106 tabulated; the standard deviation of these distributions are used to calculate the
 2107 pulls between the old analysis results and the new fits to data. This check does
 2108 not take into account that the semi-leptonic PID cuts were introduced to remove a
 2109 potential peaking background, which may have had a small systematic effect on
 2110 the earlier measurement results. Thus the expected differences are likely to be
 2111 slightly underestimated and the check conservative.

2112 Furthermore, the F_i parameters were determined in a semi-leptonic control
 2113 channel in the earlier analyses. Therefore, the expected difference obtained above is
 2114 adjusted by adding the F_i -related systematic uncertainty of the original analysis
 2115 in quadrature, when comparing the old results to those in new fits to the Run 1
 2116 and 15+16 data sets. No further corrections have been made to the expected
 2117 differences, which effectively assumes all other systematic uncertainties to be 100 %
 2118 correlated. Also for this reason can the check be considered conservative. As can
 2119 be seen in Tables 5.11 and 5.12, neither the Run 1 and 2015+16 comparisons show
 2120 unreasonable differences in central values.

2121 **Directly fitting the signal yields**

2122 As a cross-check, the fit is run in an alternative mode, in which the signal yields of
 2123 each bin are independent parameters. The obtained yields are compared to those
 2124 predicted from the results of the default fit in Fig. 5.39. The yields are shown for
 2125 each "effective bin", where effective bin i is defined as bin $+i$ for B^+ decays and bin

Table 5.11: Comparison between the results on the Run 1 analysis [?] and the central values obtained when fitting the Run 1 dataset with the selection and fit setup described in this note. The pull is calculated using the 1σ expected difference, which takes the sample overlap and the systematic uncertainty on the F_i parameters in the previous analysis into account, but assumes all other systematic uncertainties to be perfectly correlated. The new fits are performed using the CLEO strong-phase inputs.

Observable	Run 1 result [?] (central value $\times 10^{-2}$)	New Fit (central value $\times 10^{-2}$)	Pull
x_-^{DK}	2.50	4.04	0.85
y_-^{DK}	7.50	9.14	1.02
x_+^{DK}	-7.70	-9.40	-0.91
y_+^{DK}	-2.20	0.80	1.77
<i>p</i> -value: 0.057			

Table 5.12: Comparison between the results on the 2015+16 analysis [?] and the central values obtained when fitting the 2015+16 dataset with the selection and fit setup described in this note. The pull is calculated using the 1σ expected difference, which takes the sample overlap and the systematic uncertainty on the F_i parameters in the previous analysis into account, but assumes all other systematic uncertainties to be perfectly correlated. The new fits are performed using the CLEO strong-phase inputs.

Observable	15+16 result [?] (central value $\times 10^{-2}$)	New Fit (central value $\times 10^{-2}$)	Pull
x_-^{DK}	9.00	8.36	-0.50
y_-^{DK}	2.10	1.16	-0.62
x_+^{DK}	-7.70	-8.58	-0.56
y_+^{DK}	-1.00	-2.82	-1.39
<i>p</i> -value: 0.239			

2126 $-i$ for B^- decays; in the CP symmetric case, these bins are expected to have equal
 2127 yields (modulo production and detection asymmetries). The agreement between the
 2128 two fit set-ups is seen to be excellent. The normalised yield asymmetries, defined as

$$A^i \equiv \frac{N_{-i}^- - N_i^+}{N_{-i}^- + N_i^+} \quad (5.22)$$

2129 are shown in Fig. 5.40 for all decay channels. Again, the agreement between
 2130 the nominal fit, and the alternative fit with independent yields is found to be
 2131 excellent. It is also clear how, in the case of $B^\pm \rightarrow DK^\pm$ decays, the asymmetry
 2132 is significantly different from zero for a number of bin pairs.

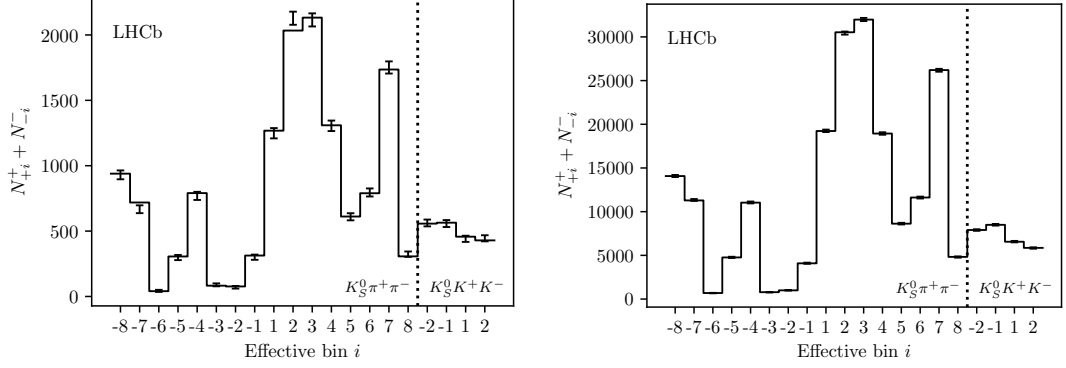


Figure 5.39: Comparison of (lines) the predicted yield given the determined CP observables and (error bars) the yield obtained in fits to data where each yield is an independent parameter. The yields are shown for (left) $B^\pm \rightarrow DK^\pm$ decays and (right) $B^\pm \rightarrow D\pi^\pm$ decays. The LL and DD categories have been combined, as has the B^+ and B^- yields for each effective Dalitz bin, defined as bin $+i$ for B^+ decays and bin $-i$ for B^- decays.

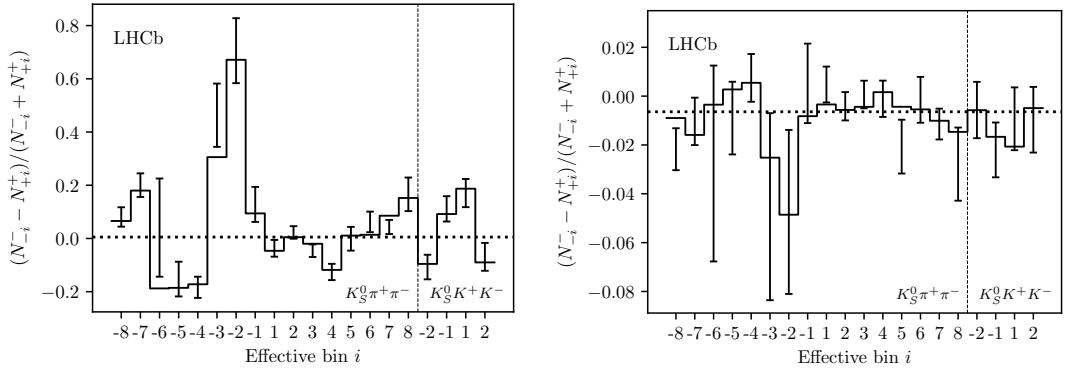


Figure 5.40: The bin-by-bin asymmetries $(N_{-i}^{-} - N_{+i}^{+})/(N_{-i}^{-} + N_{+i}^{+})$ for each Dalitz-plot bin number for (left) $B^\pm \rightarrow DK^\pm$ decays and (right) $B^\pm \rightarrow D\pi^\pm$ decays. The prediction from the central values of the CP -violation observables is shown with a solid line and the asymmetries obtained in fits with independent bin yields are shown with the error bars. The predicted asymmetries in a fit that does not allow for CP violation are shown with a dotted line.

2133 Fitting subsets of the data separately

2134 One cross check is carrying out, by determining the CP observables using a number
 2135 of independent sub samples of the data set separately. This is done for the
 2136 following following data splits

- 2137 • Fig. 5.41a shows the same plots, comparing the fits to the data set split by
 2138 K_S^0 track type.

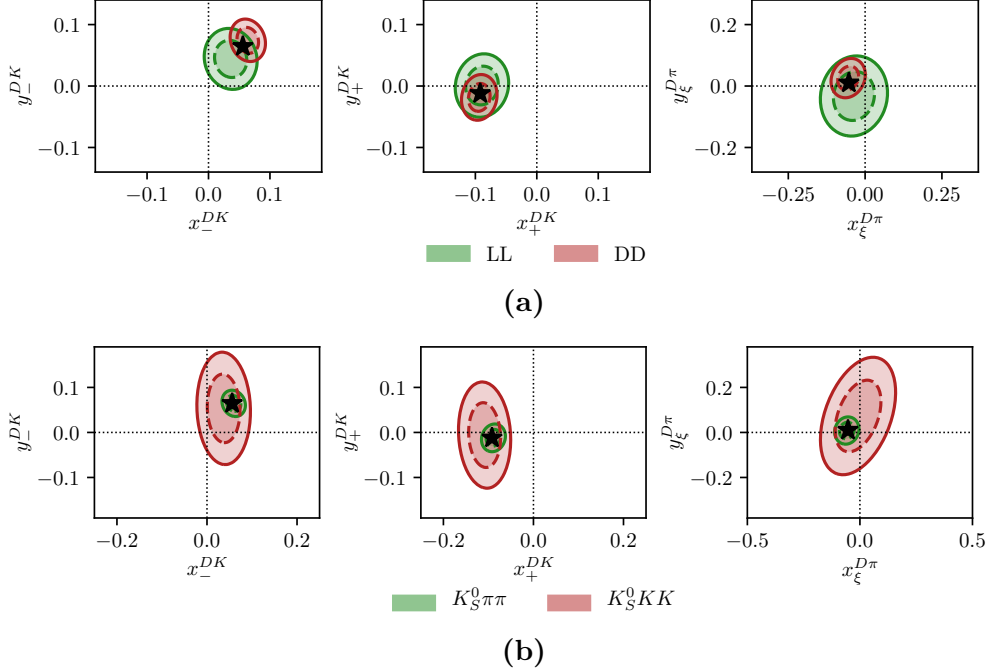


Figure 5.41: Comparison of the 68 % and 95 % confidence regions for (left) (x_{-}^{DK}, y_{-}^{DK}) , (centre) (x_{+}^{DK}, y_{+}^{DK}) , and (right) $(x_{\xi}^{D\pi}, y_{\xi}^{D\pi})$ obtained from fits to sub sets of the data set. The uncertainties are statistical only. The central values of the default fit are shown with a black star. The dataset is split by (a) LL and DD K_S^0 types and (b) D decay mode.

- Fig. 5.41b shows the same plots, comparing the fits to the data set split by whether the D meson decays to the $K_S^0\pi^+\pi^-$ or $K_S^0K^+K^-$ final state.
- Fig. 5.42a shows the two dimensional log likelihood contours for the observables for fits to the Run 1, 2015+16, 2017 and 2018 datasets separately
- Fig. 5.42b shows the same plots, comparing the fits to the data set split by whether the candidate event was triggered by one of the signal particles at the hardware level (TOS), or by another particle in the underlying event (TIS).
- Fig. 5.42c shows the same plots, comparing the fits to the data set split the magnet polarity during data taking.
- All figures show the Gaussian likelihood contours corresponding to the statistical uncertainties. There is good agreement between the results in all cases, given that in each cases the sub datasets are independent and therefore the statistical errors are uncorrelated.

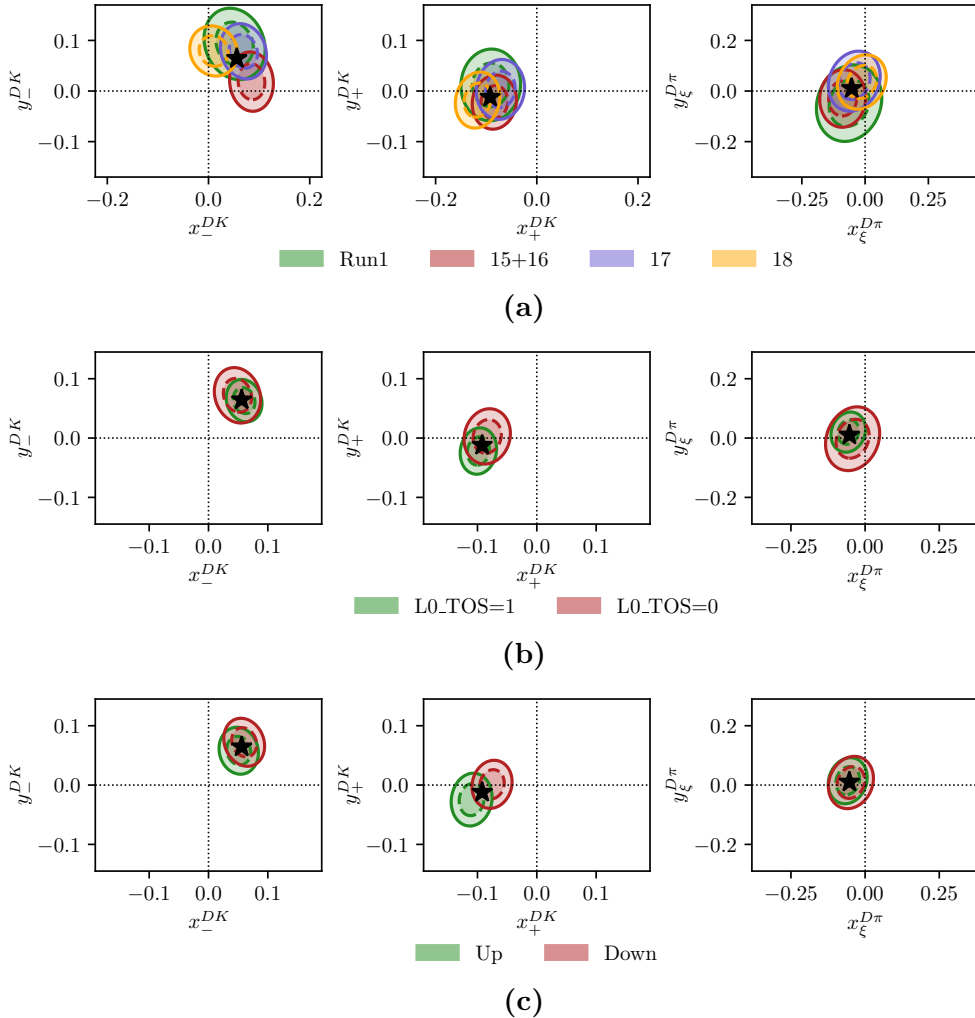


Figure 5.42: Comparison of the 68 % and 95 % confidence regions for (left) (x_-^{DK}, y_-^{DK}) , (centre) (x_+^{DK}, y_+^{DK}) , and (right) $(x_\xi^{D\pi}, y_\xi^{D\pi})$ obtained from fits to sub sets of the data set. The uncertainties are statistical only. The central values of the default fit are shown with a black star. The dataset is split by (a) data taking year, (b) trigger category, and (c) magnet polarity.

2152 Significantly reducing the $B^\pm \rightarrow D\pi^\pm$ to $B^\pm \rightarrow DK^\pm$ cross feed

2153 One of the dominant backgrounds in the signal region of the $B^\pm \rightarrow DK^\pm$ channel is
 2154 from partly reconstructed $B \rightarrow D\pi X$ decays where the bachelor pion is misidentified
 2155 as a kaon. The background mode is well described by the included shape component,
 2156 and included in all relevant systematic studies. Nevertheless, an additional cross
 2157 check is carried out to ensure that it is not having a significant effect on the fit: the
 2158 analysis is repeated with PID requirement of $\text{PID}_K > 12$ required to place a candidate
 2159 in the $B^\pm \rightarrow DK^\pm$ category, instead of $\text{PID}_K > 4$. With this requirement 99.7 %
 2160 of $B^\pm \rightarrow D\pi^\pm$ decays are correctly identified, making the cross-feed component

Table 5.13: Results of running the measurement with the default PIDK cut at 4 used to separate $B^\pm \rightarrow DK^\pm$ and $B^\pm \rightarrow D\pi^\pm$ candidates, as well as with an alternative PIK cut at 12, resulting in much lower cross-feed from misidentified $B^\pm \rightarrow D\pi^\pm$ decays. We also show the pulls, defined as $\Delta x / \sqrt{|\sigma_{PIDK>12}^2 - \sigma_{PIDK>4}^2|}$ as described in the main text body. The comparison was made before the BESIII measurement of the $D \rightarrow K_S^0 K^+ K^-$ strong-phase inputs became available; therefore the fits use the CLEO-only results [?] for this mode, which explains why the results quoted for $PIDK > 4$ differ slightly from the nominal fit results.

Parameter	PIDK > 4	PIDK > 12	$\sigma = \sqrt{\sigma_{PIDK>12}^2 - \sigma_{PIDK>4}^2}$	Pull
x_-^{DK}	5.59 ± 0.96	5.82 ± 1.01	0.30	0.77
y_-^{DK}	6.45 ± 1.14	6.86 ± 1.19	0.36	1.13
x_+^{DK}	-9.21 ± 0.96	-8.94 ± 1.01	0.30	0.93
y_+^{DK}	-1.21 ± 1.20	-0.94 ± 1.26	0.37	0.71
$x_\xi^{D\pi}$	-5.30 ± 1.99	-5.13 ± 2.02	0.32	0.52
$y_\xi^{D\pi}$	1.03 ± 2.34	1.71 ± 2.33	0.28	2.40

in the $B^\pm \rightarrow DK^\pm$ channels significantly smaller than in the default fit. This is clearly visible in Fig. 5.43, where the fit projections for the global fit of the $D \rightarrow K_S^0 \pi^+ \pi^-$ modes are shown. In return, the probability of correctly identifying a kaon companion drops to about 68–69 %, resulting in a smaller effective signal yield.

The measurement results are compared in Table 5.13, where the differences in central value are seen to be reasonably small. It is not trivial to determine whether the difference is statistically significant or not: the same candidates are analysed in both cases, the difference being that a number of candidates that are placed in the $B^\pm \rightarrow DK^\pm$ category in the nominal fit are placed in the $B^\pm \rightarrow D\pi^\pm$ category in the alternative fit. The uncertainty will not be 100 % correlated because signal events that move from the DK to $D\pi$ category are placed in a region with high background; however, this is somewhat compensated for by candidates that remain in the DK category gaining statistical power due to the increased purity. An estimate of the expected statistical fluctuation can be determined by taking the difference of the statistical uncertainties in quadrature. Using this estimate, the observed shifts are found to be consistent with statistical fluctuation, and thus there is no sign of the background from $D\pi^\pm \rightarrow DK^\pm$ cross-feed causing issues.

Compare results obtained with different strong-phase inputs

It is interesting to compare the results obtained with different strong-phase inputs. This is done in Fig. 5.44, where the default fit results are compared to those obtained if the CP fit is done with the CLEO-only inputs [?], and with the model

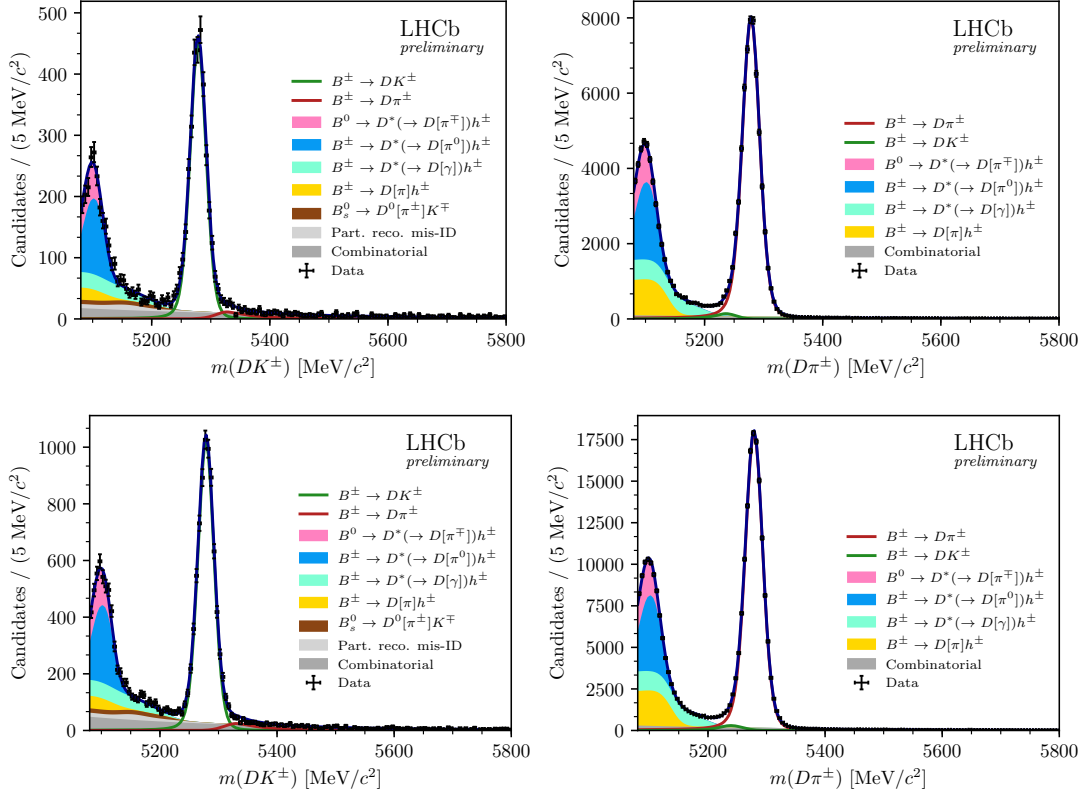


Figure 5.43: Fit projections for fits to the $D \rightarrow K_0^0 \pi^+ \pi^-$ candidates with a companion PIDK requirement at 12 instead of 4 used to split into (left) $B^\pm \rightarrow DK^\pm$ and (right) $B^\pm \rightarrow D\pi^\pm$ candidates, for the (top) LL and (bottom) DD categories.

2182 predictions from the 2018 Belle model [?] and the 2008 BaBar model [?]. For the
2183 measurements, only the strong-phase-related uncertainties are included in the plot,
2184 since the statistical uncertainties are correlated. All results are found to agree well.

2185 5.6 Systematic uncertainties

2186 The following sections cover the suite of systematic uncertainties on the measurement
2187 that has been considered. All uncertainties are summarised in Section 5.6.12.

2188 5.6.1 Strong phase uncertainties

2189 The observables x_\pm^{DK} , y_\pm^{DK} , $x_\xi^{D\pi}$ and $y_\xi^{D\pi}$ are extracted using the central values of c_i
2190 and s_i from the BESIII–CLEO combinations [?, ?, ?]. Subsequently, the measurement
2191 uncertainty on these inputs is propagated to the observables by performing a large
2192 set of fits to data, using alternative values of c_i and s_i . The new c_i and s_i values are
2193 obtained by smearing the central values by their measured statistical and systematic
2194 uncertainties while taking into account their correlations. The use of different c_i

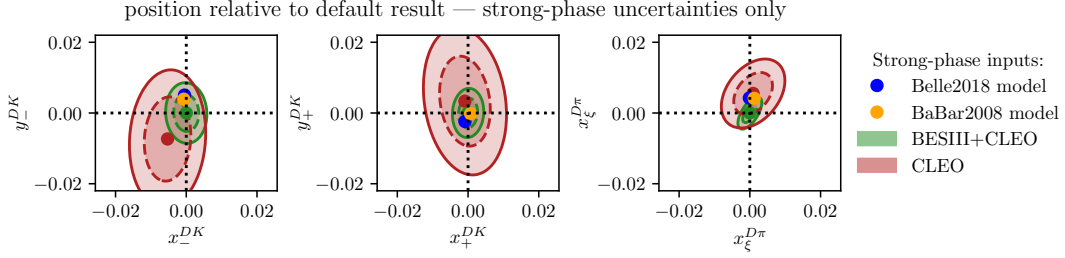


Figure 5.44: Fit results for (left) (x_-^{DK}, y_-^{DK}) , (centre) (x_+^{DK}, y_+^{DK}) , and (right) $(x_\xi^{D\pi}, y_\xi^{D\pi})$ depending on strong-phase inputs, shown relative to the default fit results. The included results are based on (green) the BESIII-CLEO combination, which is the default, (red) the CLEO-only results, (blue dot) the 2018 Belle model [?] and (orange dot) the 2008 BaBar model [?]. For the measurements, only strong-phase related uncertainties are included in the plotted confidence regions.

and s_i values changes the extracted x_\pm^{DK} , y_\pm^{DK} , $x_\xi^{D\pi}$ and $y_\xi^{D\pi}$ values. The width of the distributions of central values extracted from 1000 data fits are assigned as a systematic uncertainty. The distributions are shown in Fig. 5.45 and the assigned uncertainties are summarised in Table 5.14. The correlation matrix related to the strong-phase uncertainty can be obtained from the correlations observed between observables in the fits, and is also given in the table.

The set of (c_i, s_i) that was employed in this analysis will be used in a series of future BPGBGSZ measurements, both with additional B decay modes within the LHCb collaboration and by the Belle II collaboration. This introduces some correlation between the measurement results. In order to allow for an estimate of the degree of correlation by future analysts, the 1000 samples (c_i, s_i) values and the corresponding fit results for $(x_\pm^{DK}, y_\pm^{DK}, x_\xi^{D\pi}, y_\xi^{D\pi})$ have been made public as supplementary material to Ref. ??.

5.6.2 Efficiency-profile-related systematic uncertainties

The non-trivial efficiency profile over the Dalitz plot can have a range of effects, considered in the sections below.

The assumption that $\eta^{DK}(s_-, s_+) = \eta^{D\pi}(s_-, s_+)$

The assumption that $\eta^{DK}(s_-, s_+) = \eta^{D\pi}(s_-, s_+)$ as examined in detail in Section ???. It was found that with signal yields similar to those in the data set, no statistically significant difference between the efficiency profiles $\eta^{DK}(s_-, s_+)$ and $\eta^{D\pi}(s_-, s_+)$ was discernible, and no additional uncertainty due to this assumption is assigned.

Table 5.14: Systematic uncertainties and correlation matrix due to strong-phase inputs.

Uncertainty ($\times 10^{-2}$)						
	$x_-^{DK^\pm}$	$y_-^{DK^\pm}$	$x_+^{DK^\pm}$	$y_+^{DK^\pm}$	$x_\xi^{D\pi^\pm}$	$y_\xi^{D\pi^\pm}$
σ	0.23	0.35	0.18	0.28	0.14	0.18

Correlations						
	$x_-^{DK^\pm}$	$y_-^{DK^\pm}$	$x_+^{DK^\pm}$	$y_+^{DK^\pm}$	$x_\xi^{D\pi^\pm}$	$y_\xi^{D\pi^\pm}$
$x_-^{DK^\pm}$	1.000	-0.047	-0.490	0.322	0.189	0.144
$y_-^{DK^\pm}$		1.000	0.059	-0.237	-0.116	-0.117
$x_+^{DK^\pm}$			1.000	0.061	0.004	-0.139
$y_+^{DK^\pm}$				1.000	0.127	-0.199
$x_\xi^{D\pi^\pm}$					1.000	0.638
$y_\xi^{D\pi^\pm}$						1.000

2216 The assumption that $\eta(s_-, s_+) = \eta(s_+, s_-)$

2217 The measurement is sensitive to effects that break the assumption $\eta(s_-, s_+) =$
 2218 $\eta(s_+, s_-)$. Such a breakdown would mean that opposite points on the Dalitz plot
 2219 have different efficiencies and can only arise through a charge detection asymmetry
 2220 (e.g. that it is more likely to detect a K^+ in the detector rather than a K^-).⁵

2221 The potential size of such an asymmetry can be studied in simulation
 2222 where the D decay has a uniform distribution over the allowed phase space; in such
 2223 simulated samples, it would manifest itself as an observation of different fractional
 2224 yields of B^- decays in bin i and B^+ decays in bin $-i$. This effect has been looked for
 2225 using the large samples of $B^\pm \rightarrow D\pi^\pm$ decays that were generated for the analysis
 2226 of 2015 and 2016 data. The study is performed using the rectangular binning
 2227 schemes shown in Fig. 5.46, because this scheme results in bin yields that are
 2228 more sensitive to effects that vary smoothly over phase space. The comparison
 2229 plots are shown in Fig. 5.47, where it can be seen that the p values for the
 2230 hypothesis that there is no asymmetry all take on reasonable values. Hence no
 2231 further systematic uncertainty is considered.

2232 Effect of phase-space efficiency profile on c_i and s_i

2233 As discussed in Section 2.4 there is a small bias, because the c_i and s_i values
 2234 that are used correspond to the definition

⁵Note that the measurement is insensitive to any asymmetry in the reconstruction of the companion track.

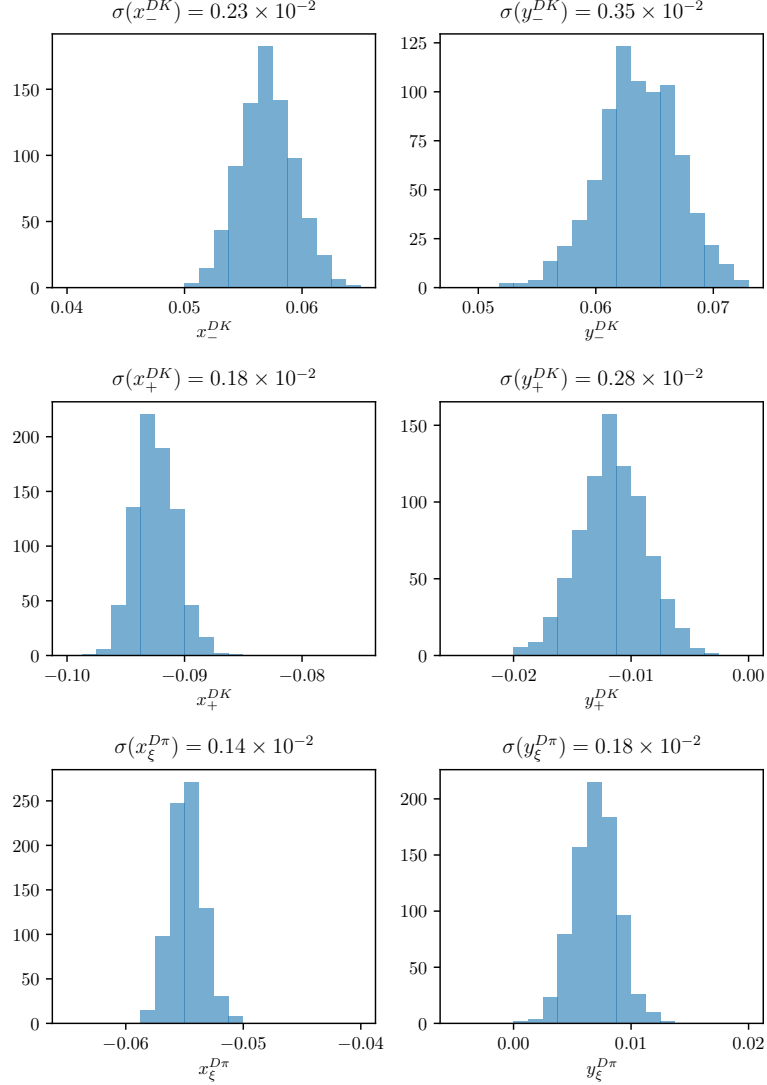


Figure 5.45: Spread of central values for the fitted observables when the input c_i and s_i from the BESIII+CLEO combination are varied according to their uncertainties and correlations.

$$c_i = \frac{\int_i ds^2 |A_S^D(s_{-+})| |A_S^D(s_{+-})| \cos[\Delta\delta_D(s_{-+})]}{\sqrt{\int_i ds^2 |A_S^D(s_{-+})|^2} \sqrt{\int_i ds^2 |A_S^D(s_{+-})|^2}}, \quad (\text{and equivalent for } s_i,) \quad (5.23)$$

whereas the non-flat efficiency profile in LHCb, $\eta(s_-, s_+) \equiv \eta(s_{-+})$, means that the appropriate c_i' and s_i' entering the exact yield expressions are

$$c_i^{\text{eff}} = \frac{\int_i ds^2 \eta(s_{-+}) |A_S^D(s_{-+})| |A_S^D(s_{+-})| \cos[\Delta\delta_D(s_{-+})]}{\sqrt{\int_i ds^2 |A_S^D(s_{-+})|^2} \sqrt{\int_i ds^2 |A_S^D(s_{+-})|^2}}, \quad (\text{and equivalent for } s_i^{\text{eff}}.) \quad (5.24)$$

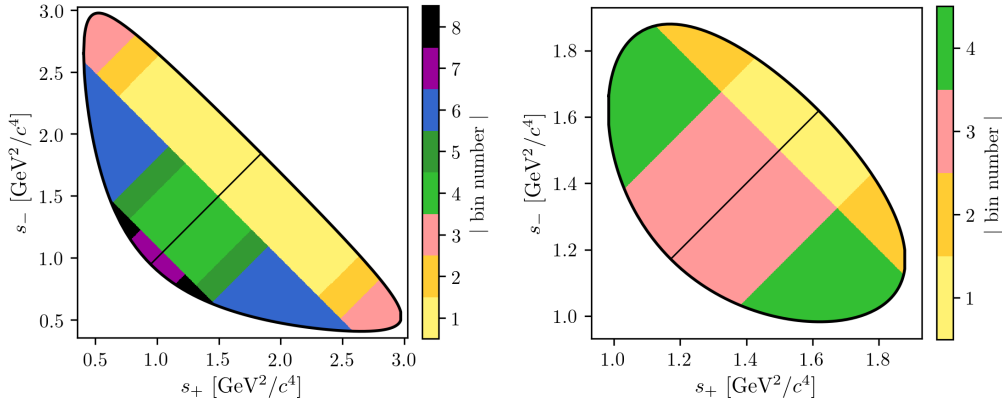


Figure 5.46: The rectangular binning schemes used to group candidates in (left) the $D \rightarrow K_S^0\pi^+\pi^-$ and (right) the $D \rightarrow K_S^0K^+K^-$ categories in a number of systematic uncertainty studies.

2237 The shifts $\Delta c_i = c_i^{\text{eff}} - c_i$, $\Delta s_i = s_i^{\text{eff}} - s_i$ can be estimated using the efficiency
 2238 profile in simulation and the latest amplitude models: the 2018 Belle model [?] for $D \rightarrow K_S^0\pi^+\pi^-$ and the 2010 BaBar model [?] for $D \rightarrow K_S^0K^+K^-$. The strong-
 2239 phase parameters are first calculated assuming a uniform reconstruction efficiency
 2240 over phase space according to Eq. (5.23), obtaining a set of values $\{c_i^{\text{model}}, s_i^{\text{model}}\}$.
 2241 Then, an alternative set is calculated, $\{c_i^{\text{eff}}, s_i^{\text{eff}}\}$, using the same model, and the
 2242 reconstruction efficiency profile found in full LHCb simulation. The results, as well
 2243 as their differences, are tabulated in Tables 5.15 and 5.16. The LHCb reconstruction
 2244 efficiency at a given point in phase-space is taken to be proportional to the yield
 2245 in simulation, as the simulated decays were generated with a uniform distribution
 2246 over phase space. The efficiency is averaged over the LL and DD categories
 2247 in the calculation.

2249 A systematic uncertainty due to employing the measured c_i and s_i directly
 2250 in the fit is assigned by generating a large number of toy data sets where the
 2251 signal yields are calculated using $(c_i^{\text{eff}}, s_i^{\text{eff}})$, and then fitting the data sets using
 2252 $(c_i^{\text{model}}, s_i^{\text{model}})$. The mean bias of each observable in these toys is assigned as the
 2253 systematic uncertainty, and is determined to be 0.1×10^{-2} or less for all observables.
 2254 The smallness of the effect is the reason no effort is made to correct the c_i and
 2255 s_i values in the nominal measurement.

2256 5.6.3 Mass shapes

2257 A number of uncertainties relate to the mass distributions that enter the fit model.
 2258 Each is described in detail the sections below.

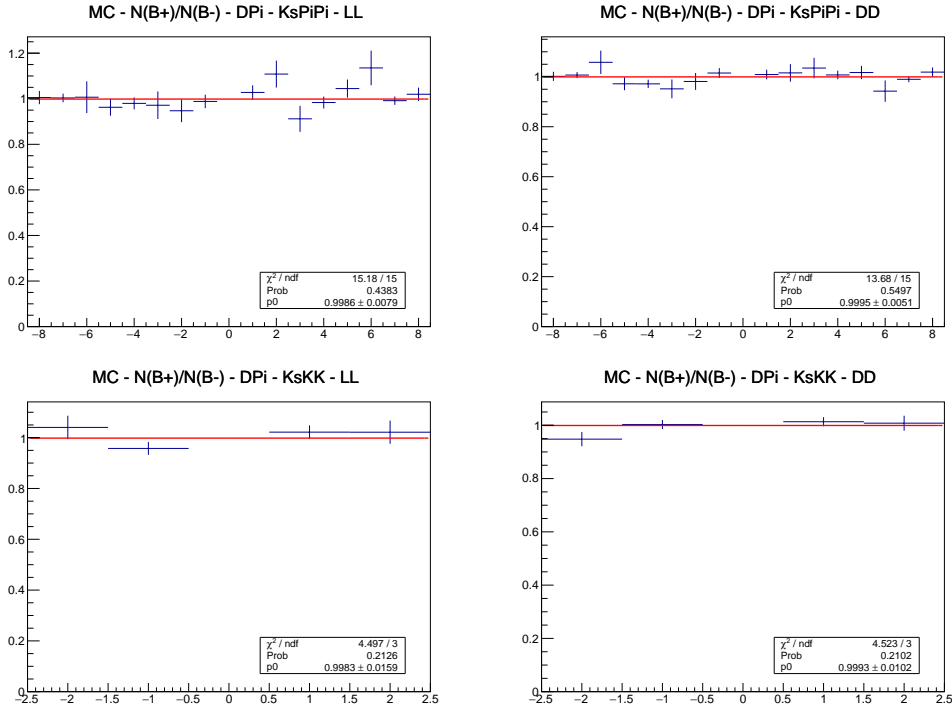


Figure 5.47: Comparison of the ratio of B^- decays reconstructed in bin $+i$ to B^+ decays reconstructed in bin $-i$ for simulated $B^\pm \rightarrow D\pi^\pm$ decays where (top) $D \rightarrow K_S^0\pi^+\pi^-$ and (bottom) $D \rightarrow K_S^0K^+K^-$, also split into (left) the LL and (right) the DD categories. Calculated p values for the hypothesis that the ratio is flat are also shown, all of them being at least 20 %.

2259 Determination of shape parameters

2260 The statistical uncertainties on the shape parameters that are obtained in fits
 2261 to simulated decays and in the first stage fit to data need to be propagated to
 2262 the uncertainty on the obtained parameters. This is done via a bootstrapping
 2263 procedure, repeating these steps many times:

- 2264 • Each of the data sets used determine parameters of the signal, crossfeed, and
 2265 lowmass shapes that are fixed in the first-stage fit to data of Section 5.4 are
 2266 re-sampled with replacement, drawing a number of events equal to the original
 2267 data-set size. These are from simulation for signal and lowmass shapes, and
 2268 real data for the crossfeed shapes. All of the shapes are fit again, on the
 2269 re-sampled data sets.
- 2270 • The real dataset is re-sampled with replacement, drawing a number of events
 2271 equal to the original data-set size. Then, the first-stage fit of Section 5.4 is
 2272 repeated with the shapes obtained as described above, obtaining values for
 2273 the remaining shape parameters.

Table 5.15: The c_i and s_i values for $D \rightarrow K_S^0 \pi^+ \pi^-$ decays calculated via the 2018 Belle model [?] in two cases: assuming a uniform reconstruction efficiency over phase space, denoted $(c/s)_i^{\text{model}}$, and including the LHCb efficiency profile as obtained in simulation, averaged for LL and DD, denoted $(c/s)_i^{\text{eff}}$. The change due to including the efficiency is also tabulated.

Bin	c_i^{model}	c_i^{eff}	Δc_i	s_i^{model}	s_i^{eff}	Δs_i
1	-0.027	-0.007	0.019	0.812	0.794	-0.018
2	0.837	0.859	0.022	0.164	0.152	-0.012
3	0.163	0.163	-0.000	0.872	0.880	0.008
4	-0.914	-0.915	-0.001	0.076	0.082	0.006
5	-0.149	-0.170	-0.021	-0.856	-0.854	0.002
6	0.373	0.362	-0.011	-0.782	-0.805	-0.023
7	0.863	0.862	-0.000	-0.203	-0.202	0.002
8	0.860	0.862	0.002	0.330	0.336	0.006

Table 5.16: The c_i and s_i values for $D \rightarrow K_S^0 K^+ K^-$ decays calculated via the 2010 BaBar model [?] in two cases: assuming a uniform reconstruction efficiency over phase space, denoted $(c/s)_i^{\text{model}}$, and including the LHCb efficiency profile as obtained in simulation, averaged for LL and DD, denoted $(c/s)_i^{\text{eff}}$. The change due to including the efficiency is also tabulated.

Bin	c_i^{model}	c_i^{eff}	Δc_i	s_i^{model}	s_i^{eff}	Δs_i
1	0.738	0.735	-0.002	0.266	0.263	-0.003
2	-0.697	-0.744	-0.046	0.332	0.329	-0.003

- 2274 • Finally, the CP fit is repeated using the shape parameters determined in the
 2275 preceding steps, but *without* re-sampling the dataset (to avoid a statistical
 2276 spread in the obtained central values that is independent of the shape
 2277 parameters).

2278 The uncertainty on each observable is taken to be the standard deviation of the
 2279 set of central values obtained as described above. This procedure propagates
 2280 the statistical uncertainty on the fixed parameters to the observables, in a way
 2281 that takes correlations into account, and which does not rely on the uncertainty
 2282 estimates in the preliminary fits being accurate. The uncertainties are less than
 2283 0.1×10^{-2} for all DK^\pm observables, in line with earlier analyses, and less than
 2284 0.2×10^{-2} for all $D\pi^\pm$ observables.

2285 A potential bias arises due the use of sWeights when obtaining the mass
 2286 distribution of decays where a $\pi \leftrightarrow K$ misidentification has taken place. This
 2287 is because the $m_{\text{swap}}(Dh^\pm)$ mass that is calculated while assuming a swapped
 2288 companion hypothesis and the nominal $m_{\text{default}}(Dh^\pm)$ mass are correlated (it

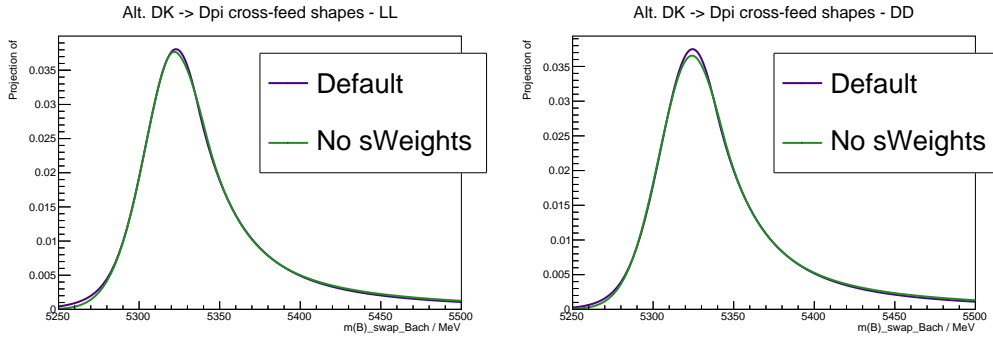


Figure 5.48: Comparison of the default and no-sWeights alternative shape for the $D\pi \rightarrow DK$ cross-feed component in the (left) LL and (right) DD categories where $D \rightarrow K_S^0\pi^+\pi^-$. The binned fit obtains essentially the same central values for the CP -violation observables, independently of which shape is used.

is always the case that $m_{\text{swap}} > m_{\text{default}}$ for a $\pi \rightarrow K$ misidentification ,for example). Thus, the assumptions of the sPlot method are not satisfied [?]. The correlation coefficient in the signal region is about 20% for simulated signal decays. In order to assess the potential impact, an alternative mass distribution for $(B^\pm \rightarrow D\pi^\pm) \rightarrow (B^\pm \rightarrow DK^\pm)$ cross-feed is derived that does not rely on sWeights. Instead of fitting $B^\pm \rightarrow D\pi^\pm$ sample in the whole fit range and assigning sWeights before recalculating the B mass under the kaon companion hypothesis, the shape is obtained using $B^\pm \rightarrow D\pi^\pm$ candidates in the signal region. This is possible because the $B^\pm \rightarrow D\pi^\pm$ sample is very pure. The shapes are compared in Fig. 5.48 and are seen to be almost identical. Thus the sWeights do successfully subtract the contribution of combinatorial and partially reconstructed backgrounds in the default setup. The impact on the obtained CP -violation observables of using one or the other shape in the fits is negligible, and no further systematic uncertainty is assigned due to this effect.

Using the same mass shapes in all Dalitz bins

The mass shapes obtained the first-stage fit where all Dalitz bins are combined, are used in each individual bin of the subsequent binned fit. However, there could be some variation in the shape over the D -decay phase space, due to correlations between the phase-space coordinates and particle kinematics. The potential effect is investigated in pseudoexperiments, where toy data sets are generated with alternative signal, crossfeed, and combinatorial-background shapes that are allowed to differ between bins, and fitted with the default shapes. The partially reconstructed background is treated in a separate study, because further physics effects contribute to bin-by-bin variation, as described in the following section.

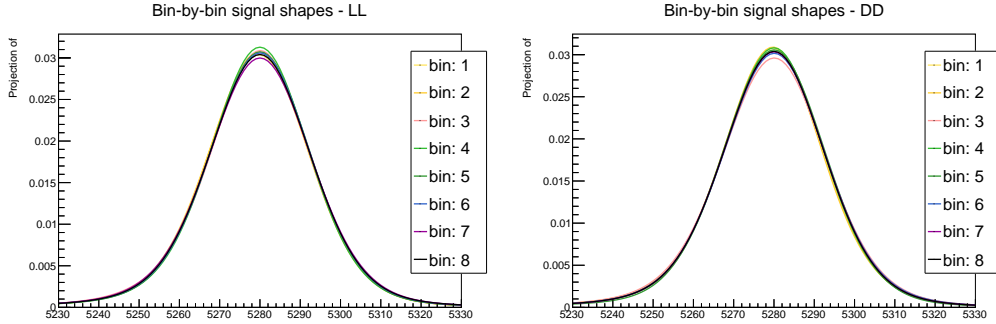


Figure 5.49: Signal shapes obtained in MC for individual Dalitz bins in the optimal binning scheme, for (left) LL and (right) DD candidates in the $B^\pm \rightarrow D(\rightarrow K_S^0\pi^+\pi^-)\pi^\pm$ category.

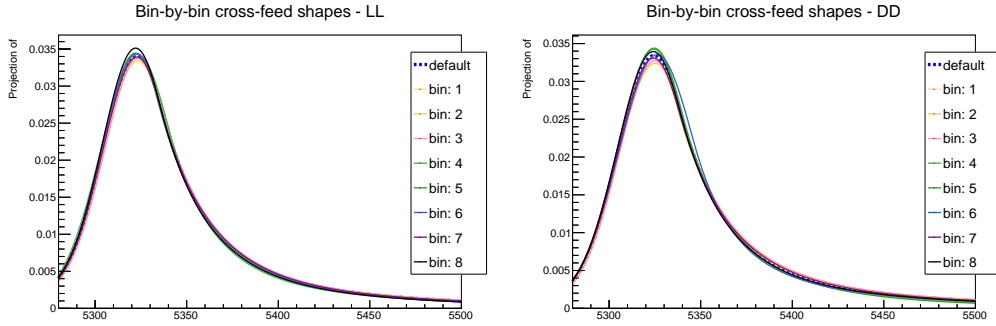


Figure 5.50: Mass shapes for $D\pi \rightarrow DK$ cross feed obtained for individual Dalitz bins in the optimal binning scheme, for (left) LL and (right) DD candidates in the $D \rightarrow K_S^0\pi^+\pi^-$ category.

2313 The alternative signal and cross-feed mass shapes are fitted independently in
2314 each bin, following identical procedures to those outlined in Sections 5.4.1 and 5.4.2.
2315 Examples of the obtained shapes are compared in Figs. 5.49 and 5.50.

2316 The shape of the combinatorial background can also vary over the D decay
2317 phase-space; for example will the relative amount of fake D candidates versus real
2318 D decays paired with a random bachelor certainly depend on the real D decay
2319 amplitude for a given phase-space region. The effect is investigated in the high
2320 B -mass sideband $m_B \in [5600, 6500]$ MeV/ c^2 , in which the $m(Dh^\pm)$ distribution is
2321 fitted with a single exponential distribution, in bins of the Dalitz plot. The fits
2322 combine B^+ and B^- candidates and merge bins $+i$ and $-i$, and are carried out
2323 for both the *optimal* binning scheme of Fig. 2.7 (on page 21) and a *rectangular*
2324 binning scheme, shown in Fig. 5.46, which better captures continuous trends over
2325 the Dalitz plot. The study is done for $D \rightarrow K_S^0\pi^+\pi^-$ only due to available statistics.
2326 The DD category of $B^\pm \rightarrow D\pi^\pm$ decays has the largest statistics and shows the
2327 largest variation, and the fitted slopes for this channel are shown in Fig. 5.51. Two

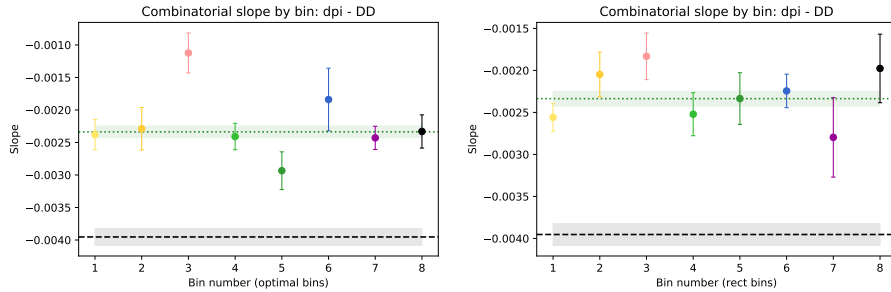


Figure 5.51: Plot of (dots) combinatorial slope in the high B mass background for each bin in the (left) the optimal binning scheme and (right) the rectangular binning scheme, for the DD $B^\pm \rightarrow D(\rightarrow K_S^0\pi^+\pi^-)\pi^\pm$ category. The slope when all bins are combined (green, dashed line) is also shown, and compared with (black dashed line) the slope in the default fit region.

effects are visible: 1) there is some variation in the slope as a function of the Dalitz bin, especially visible for the rectangular scheme, and 2) the exponential slope is larger in general in the high B -mass sideband. The latter effect does not pose a problem, since the employed exponential is found to provide an excellent fit in the default fit region. It does however need to be taken into account when deriving alternative, bin-dependent combinatorial slopes relevant for the default fit region. In order to do so, the alternative slope for bin i is defined

$$\alpha_{\text{default-range}}^i = \frac{\alpha_{\text{high-}m_B}^i}{\alpha_{\text{high-}m_B}^{\text{all-}DP}} \times \alpha_{\text{default-range}}^{\text{all-}DP}, \quad (5.25)$$

and used when generating the combinatorial-background component of the toy data sets for the study.

The average bias obtained for each observable in the ensemble of pseudo-experiments is assigned as a systematic uncertainty, found to be about 0.1×10^{-2} for each observable.

Ignoring physics effects in the lowmass background

In the CP fit, the same relative fractions of partly reconstructed B^\pm and B^0 backgrounds are used in each bin, as determined in the first-stage fit described in Section 5.4 (whereas the partly reconstructed $B_s^0 \rightarrow \bar{D}^0[\pi^+]K^-$ background is treated separately). However the distribution over the Dalitz plot depends on whether the partly reconstructed decays occur via an intermediate D^0 meson, a \bar{D}^0 meson, or and admixture of both. Consider a decay reconstructed as $B^- \rightarrow DK^-$ but which is actually a partially-reconstructed background. There are then four types of background that should be considered:

- Decays in which the D -meson in the true decay is a D^0 -meson. An example of this is $B^- \rightarrow D^{*0}(D^0\pi^0)\pi^-$ for which the π^0 from the D^{*0} decay is missed and the π^- is misidentified as the companion K^- . These are denoted ' D^0 -like'.⁶
- Decays in which the D -meson in the true decay is a \bar{D}^0 -meson. An example of this is $B_s^0 \rightarrow \bar{D}^0\pi^+K^-$ for which the π^+ is missed and the K^- is reconstructed as the companion K^- . These are denoted ' \bar{D}^0 -like'.
- Decays in which the D meson in the true decay can be either flavour, and both D flavours contribute to the decay amplitude. An example of this is $B^- \rightarrow D^*K^-$ for which the total decay amplitude into a D final state has contributions from both D^{*0} (decaying to D^0) and \bar{D}^{*0} (decaying to \bar{D}^0). The relative amplitude magnitude and phase between the two possible B decays are denoted $r_B^{D^*}$ and $\delta_B^{D^*}$ respectively. These are denoted ' r_B -like'.
- Decays that can be reconstructed as both D^0 - and \bar{D}^0 -like but where there is no quantum-mechanical interference. An example is $\bar{B}^0 \rightarrow D^0\pi^+\pi^-$ decays where either the π^+ or π^- can be reconstructed as the bachelor. These are denoted 50/50 D^0 -like and \bar{D}^0 -like.

For $B^+ \rightarrow DK^+$ decays everything is CP conjugated. The Dalitz-plot distribution for each of these cases is:

- D^0 decays (' D^0 -like')

$$\begin{aligned} N_{\pm i}(B^-) &\propto F_{\pm i} \\ N_{\pm i}(B^+) &\propto F_{\mp i} \end{aligned} \tag{5.26}$$

- \bar{D}^0 decays (' \bar{D}^0 -like'):

$$\begin{aligned} N_{\pm i}(B^-) &\propto F_{\mp i} \\ N_{\pm i}(B^+) &\propto F_{\pm i} \end{aligned} \tag{5.27}$$

- Decays with a quantum-mechanical admixture of D^0 and \bar{D}^0 (' r_B -like'):

$$\begin{aligned} N_{\pm i}(B^-) &\propto F_{\pm i} + (r_B^*)^2 F_{\mp i} + 2\sqrt{F_{+i}F_{-i}}[x_{-}^*c_{\pm i} + y_{-}^*s_{\pm i}] \\ N_{\pm i}(B^+) &\propto F_{\mp i} + (r_B^*)^2 F_{\pm i} + 2\sqrt{F_{+i}F_{-i}}[x_{+}^*c_{\pm i} - y_{+}^*s_{\pm i}] \end{aligned} \tag{5.28}$$

where (x_{\pm}^*, y_{\pm}^*) are defined analogously to the standard $B^\pm \rightarrow DK^\pm$ case.

⁶The naming convention is defined in terms of the D present in candidates reconstructed as B^- decays. For the charge conjugate case this decay would of course happen via a \bar{D}^0 , but is still denoted D^0 -like.

- 2371 • 50/50 D^0 -like and \bar{D}^0 -like:

$$\begin{aligned} N_{\pm i}(B^-) &\propto F_{\pm i} + F_{\mp i} \\ N_{\pm i}(B^+) &\propto F_{\pm i} + F_{\mp i} \end{aligned} \quad (5.29)$$

2372 The use of a single background shape across all bins may therefore introduce biases
 2373 because, if an admixture of these backgrounds is present, such a shape has no
 2374 sensitivity to bin-to-bin variations.

2375 In the $D\pi$ channel, the dominant backgrounds are all D^0 -like ($\bar{B}^0 \rightarrow D^{*-}\pi^0$,
 2376 $B^- \rightarrow D^0\rho^-$, $B^- \rightarrow D^{*0}\pi^-$). There is a small contribution from $\bar{B}^0 \rightarrow D^0\rho(\rightarrow$
 2377 $\pi^+\pi^-)$ decays where either the π^+ or π^- from the ρ^0 decay can be assigned as the
 2378 bachelor, and thus this background is 50/50 D^0 -like and \bar{D}^0 -like. The background
 2379 only corresponds to about 0.5 % of the total partially reconstructed background and
 2380 thus the impact is small. Nevertheless it is considered in the study described below.

2381 In the DK channel all categories of background appear. In the mass region
 2382 of the CP fit approximately 75.5% of backgrounds are D^0 -like ($\bar{B}^0 \rightarrow D^{*-}K^-$,
 2383 mis-identified $B^- \rightarrow D^{*0}\pi^-$, and mis-identified $B^- \rightarrow D^0\rho^-$), 7.5 % are \bar{D}^0 -like
 2384 ($B_s^0 \rightarrow \bar{D}^0\pi^+K^-$), 1% is 50/50 D^0 - \bar{D}^0 -like (mis-identified $B^0 \rightarrow D\rho^0$), and 16% are
 2385 r_B -like ($B^- \rightarrow D^*K^-$, $B^0 \rightarrow DK^{*0}$, and $B^- \rightarrow DK^{*-}$).

2386 In order to estimate the bias due to ignoring this effect, a large number of toy
 2387 data sets are generated using the default low mass shapes and total yields from
 2388 the first-stage fit in Section 5.4, but distributing each of them individually over
 2389 the Dalitz-bins according to Eqs. (5.26)-(5.28). When calculating the distribution
 2390 of $B^+ \rightarrow D^{*0}K^+$ decays over the Dalitz plot, the values [?]

$$r_B^{D^*} = 0.191 \quad \delta_B^{D^*} = 331.6^\circ \quad (5.30)$$

2391 are used. When calculating the distribution of $B^+ \rightarrow D^0K^{*+}$ decays over the
 2392 Dalitz plot the values [?]

$$r_B^{K^*} = 0.092 \quad \delta_B^{K^*} = 40^\circ. \quad (5.31)$$

2393 are used. The toy data sets are then fit with the default set up, and the observed
 2394 mean bias assigned as the corresponding uncertainty. The corresponding uncer-
 2395 tainties were found to be about 0.1×10^{-2} for all uncertainties. The variation in
 2396 the shapes is rather small in the mass range included in the fit, which explains
 2397 the small impact.

2398 If the B_s^0 background is *not* treated separately in the default fit, but instead
 2399 included in a single lowmass background shape along with the B^0 and B^\pm contribu-
 2400 tions, the systematic uncertainty is an order of magnitude larger when evaluated
 2401 as described above, and would be a dominating systematic. This motivates the
 2402 separate treatment of the B_s^0 background.

2403 5.6.4 CP violation and material interaction of the K_S^0

2404 A systematic uncertainty due to CP -violation effects and material interaction of
 2405 the K_S^0 is assigned using the results obtained in Section 4.3.7. In that section,
 2406 the expected bias on all observables in a combined $B^\pm \rightarrow Dh^\pm$ measurement
 2407 was evaluated for the detector geometry and particle kinematics of the LHCb
 2408 experiment. The calculation was made for $(r_B^{DK^\pm/D\pi^\pm}, \delta_B^{DK^\pm/D\pi^\pm})$ values close to
 2409 the world averages, and a number of γ values; the results were summarised in Fig. 4.8.
 2410 The systematic uncertainty is taken to be the largest absolute bias observed for each
 2411 parameter in the study. The largest uncertainty (on $y_\xi^{D\pi}$ where it is 0.46×10^{-2}) is
 2412 still an order of magnitude smaller than the statistical uncertainty.

2413 5.6.5 Impact of D mixing

2414 The effect of D -mixing is not accounted for in the measurement, which leads to
 2415 a small bias. Earlier studies have shown this to lead to a sub-degree bias on
 2416 measurements of γ in $B^\pm \rightarrow DK^\pm$ decays, in the case where the F_i parameters
 2417 are determined experimentally under the same experimental conditions as the γ
 2418 measurement [?]. A number of pseudoexperiments are carried out to verify that this
 2419 is also the case for the combined DK^\pm – $D\pi^\pm$ setup employed in the thesis. They
 2420 are performed following the same procedure described in Section 5.6.4 for the case
 2421 of K_S^0 CP violation. The yields are calculated while taking D mixing into account,
 2422 using the mixing parameter values $x = (0.39_{-0.12}^{+0.11})\%$ and $y = (0.65_{-0.07}^{+0.06})\%$ [?],
 2423 and then fitted back assuming no D mixing. The biases are found to be small, as
 2424 expected, all of them smaller than 0.05×10^{-2} . The largest relative biases are on
 2425 the $B^\pm \rightarrow D\pi^\pm$ parameters, but even for those the relative effect is less than 2%.
 2426 In agreement with Ref. [?], it is found that the biases increase with an order of
 2427 magnitude if the F_i parameters are fixed to the expected values with no D -mixing,
 2428 instead of being determined as part of the fit.

2429 5.6.6 PID efficiencies

2430 The uncertainty related to PID efficiencies is assessed by repeating the full two-stage
 2431 fit procedure a number of times, each time varying the PID efficiencies within
 2432 the uncertainties. The used uncertainty includes both a statistical and systematic
 2433 component, as described in detail in Section 5.1.3. The standard deviations of
 2434 the central values obtained for each observable are assigned as the systematic
 2435 uncertainty. The uncertainties come out below 0.1×10^{-2} for all observables.

2436 **5.6.7 Dalitz-coordinate resolution**

2437 There is a small systematic uncertainty related to Dalitz-plot-bin migration, where
2438 the non-perfect resolution on the momentum measurement means that a candidate
2439 is assigned to a different bin than it truly belongs to. This leads to non-negligible
2440 net migration between bins that share a border in a region of phase space where
2441 the amplitude varies rapidly. However, since the F_i are measured in the data
2442 set, all leading order effects of migration are inherently taken into account. The
2443 measurement is only sensitive to differences in migration between the DK^\pm and
2444 $D\pi^\pm$ channels and the effect is small.

2445 The systematic uncertainty due to this effect is assigned using pseudoexperiments.
2446 The study is made for the $D \rightarrow K_S^0 \pi^+ \pi^-$ mode only, which is sufficient since it
2447 completely dominates the overall sensitivity.

- 2448 1. Signal $B^\pm \rightarrow DK^\pm$ and $B^\pm \rightarrow D\pi^\pm$ decays are generated continuously over
2449 phase space, according to the expected distribution obtained with the latest
2450 amplitude model from the Belle collaboration [], assuming values of γ and
2451 $(r_B^{DK^\pm/D\pi^\pm}, \delta_B^{DK^\pm/D\pi^\pm})$ close to the current world averages.
- 2452 2. The Dalitz coordinates of each candidate are then smeared using the experi-
2453 ment resolution obtained in simulation. This is described further below.
- 2454 3. Finally, the generated candidates are binned and fitted back using the default
2455 setup.

2456 The resolution is obtained via simulation, by comparing the reconstructed
2457 phase-space coordinates with those calculated from the true momenta in samples of
2458 simulated $D \rightarrow K_S^0 \pi^+ \pi^-$ decays. As can be seen in Fig. 5.52, the resolution is found
2459 to vary over phase space and the distribution of shifts has significant exponential
2460 tails. In order to take both effects into account, the smearing is done by shifting each
2461 generated decay with a realised coordinate shift in full simulation, for a simulated
2462 decay that took place at approximately the same place in the Dalitz plot. The
2463 shift is multiplied with 120 % to take into account that the resolution is generally
2464 better in simulation than data. If the shift results in Dalitz coordinates outside the
2465 kinematically allowed region, a different shift is applied randomly instead.

2466 The average bias seen in the pseudoexperiments is assigned as the systematic
2467 uncertainty. The uncertainties come out at about $(0.1 - 0.2) \times 10^{-2}$ for all parameters.
2468 It is noted that for all four DK^\pm parameters the bias is towards a smaller value
2469 of r_B^{DK} ; this is to be expected, as bin migration washes out the asymmetries in
2470 different areas of the Dalitz plot.

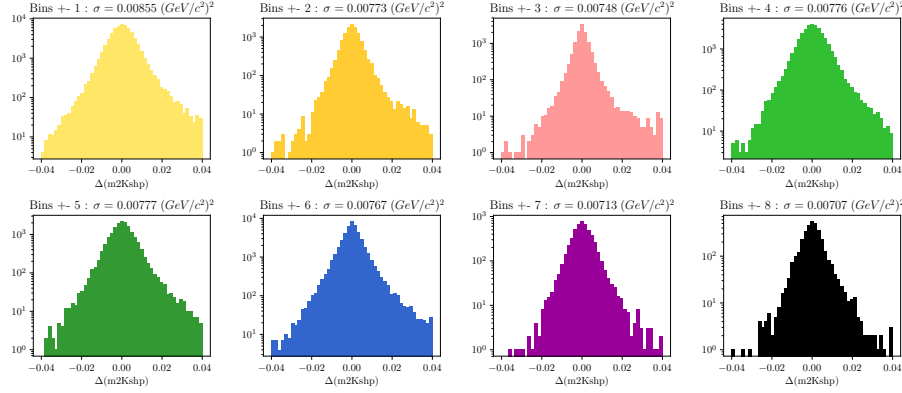


Figure 5.52: Distribution of the biases $\Delta(m^2) = m_{true}^2 - m_{reconstructed}^2$ in simulation for $m^2(K_S^0\pi^+)$ in bins of the rectangular binning scheme of Fig. 5.46.

5.6.8 The fixed yield fractions

A number of relative yields are fixed from efficiencies in simulation and branching fractions. In the DK^\pm modes, this is the case for all the relative yields of the partially reconstructed backgrounds, including partially reconstructed $B \rightarrow D\pi[X]$ decays where the pion is misidentified as a kaon, and the yield of the $B_s^0 \rightarrow DK\pi$ background relative to the $B \rightarrow D\pi$ yield. In the $B^\pm \rightarrow D\pi^\pm$ channel, the only fixed yield ratio is that of the partially reconstructed $B^\pm \rightarrow D^{*0}(\rightarrow D\pi^0)\pi^\pm$ and $B^0 \rightarrow D^{*\mp}(\rightarrow D\pi^\mp)\pi^\pm$ modes. The uncertainty on the observables due to uncertainties on these fixed fractions is assessed by repeating the two-stage fit procedure many times, each time shifting the yield ratios randomly within their uncertainties. The uncertainty on each observable is taken to be the standard deviation of the set of central values obtained in these fits. These are all smaller than 0.1×10^{-2} .

5.6.9 Systematic uncertainty due to backgrounds that are not modelled in fit

There are a number of backgrounds that are expected to be present at a small level, but which are not modelled in the fits to data because their impact on the fit results is minimal. Instead, a systematic uncertainty is assigned. Each contribution is described in the following sections and the related systematic uncertainties are summarised in Table 5.17.

Background from Λ_b decays

This section considers the possible impact of the two potential backgrounds from Λ_b^0 decays described in Section 5.4.3: $\Lambda_b^0 \rightarrow D^0 p\pi^-$ decays where the pion is not

Table 5.17: Summary of systematic uncertainties due to backgrounds that are potentially present with a small yield, but not included in the mass fit.

All uncertainties are quoted with implicit: $\times 10^{-2}$						
Mode	$\sigma(x_-^{DK^\pm})$	$\sigma(y_-^{DK^\pm})$	$\sigma(x_+^{DK^\pm})$	$\sigma(y_+^{DK^\pm})$	$\sigma(x_\xi^{D\pi^\pm})$	$\sigma(y_\xi^{D\pi^\pm})$
Λ_b^0 backgrounds	0.04	0.05	0.04	0.06	0.08	0.13
$B \rightarrow D\mu\nu X$	0.04	0.07	0.04	0.05	0.10	0.11
$B^\pm \rightarrow D(\rightarrow K_S^0\pi\mu\nu)h^\pm$	0.00	0.03	0.02	0.02	0.00	0.00
Swapped tracks	0.10	0.13	0.12	0.08	0.00	0.01
Total	0.11	0.16	0.13	0.12	0.08	0.13

2493 included the candidate reconstruction and the proton assigned as the companion, and
 2494 $\Lambda_b^0 \rightarrow \Lambda_c^+(\rightarrow pK_S^0\pi^+\pi^-)\pi^-$ decays where a pion in the Λ_c^+ decay is not reconstructed
 2495 and the proton reconstructed as one of the D decay products. The impact of not
 2496 including these in the default fit is assessed by generating toy data sets where the
 2497 backgrounds are included in the generation step, which are then fitted back with
 2498 default model. The former background is distributed over the Dalitz plot as \bar{D}^0 -like,
 2499 cf. the terminology of Section 5.6.3, since a positive bachelor is produced along
 2500 with a D^0 meson. The latter is also distributed as \bar{D}^0 -like in the study; the exact
 2501 distribution is unknown, but a \bar{D}^0 -like background is likely to have the largest
 2502 effect and thus this is a conservative choice. The total yields are taken relative to
 2503 the signal yields, using the yield ratios discussed in Section 5.4.3. The $m(Dh^\pm)$
 2504 distributions are obtained using simulated samples, produced with **RapidSim**. The
 2505 mean biases come out to be less than 0.1×10^{-2} for each CP -violation observable,
 2506 which is assigned as a systematic uncertainty.

2507 Semi-leptonic backgrounds

2508 The impact of remnant $B \rightarrow D\mu\nu_\mu$ decays after requiring `isMuon=0` on the bachelor
 2509 is assessed in pseudoexperiments. Toy datasets are generated where the background
 2510 is added in the generation step, which are then fitted with the default model. The
 2511 background yield relative to signal and the mass shape are obtained from a sample
 2512 of fully simulated decays for conditions corresponding to the run conditions in
 2513 2012. The obtained bias in the toys is assigned as the systematic uncertainties:
 2514 it is below 0.1×10^{-2} for all parameters.

2515 The systematic uncertainty relating to the presence of $D^0 \rightarrow K_S^0\pi^-\mu^+\nu_\mu$ is
 2516 estimated by repeating the bias studies of Section 5.3.3, but scaling the background
 2517 yields to 10 % to take into account the lepton veto on the D decay products. All
 2518 biases are less than 0.05×10^{-2} in this case.

2519 **Swapped tracks**

2520 There is a peaking background present from $B^\pm \rightarrow D(\rightarrow K^\mp\pi^\pm)K_S^0\pi^\pm$ decays where
 2521 the kaon is reconstructed as the companion and the K_S^0 is assigned to the D decay.
 2522 The yield of this background is determined to be 0.5 % of the signal yield in the
 2523 $B^\pm \rightarrow DK^\pm$ channel in Section 5.3.5. The potential impact from the presence
 2524 of the background is estimated by

- 2525 1. Calculating the expected $B^\pm \rightarrow D\pi^\pm$ and $B^\pm \rightarrow DK^\pm$ signal yields in each
 2526 bin for physics parameters similar to the world average values.
 - 2527 2. Then calculating the background bin yields in each $B^\pm \rightarrow DK^\pm$ bin, using
 2528 a total yield equal to 0.5 % of the signal yield, and the bin distribution
 2529 from simulated samples of $B^\pm \rightarrow D(\rightarrow K^\mp\pi^\pm)K_S^0\pi^\pm$ decays, produced via
 2530 `RapidSim`. The study is carried out for multiple simulated samples, including
 2531 decays where the $K_S^0\pi$ pair in the B decay originate in different K^* resonances
 2532 (generated with `EvtGen` and the proper resonance-spin models), as well as B
 2533 decays that are evenly distributed over the allowed phase space.
 - 2534 3. For each sample, the signal and background yields are added, and the new
 2535 $B^\pm \rightarrow D\pi^\pm$ and $B^\pm \rightarrow DK^\pm$ yields are fitted back with the default signal-
 2536 yield expressions (including a fit of the F_i parameters).
- 2537 For each parameter, the most significant bias seen across the different `RapidSim`
 2538 samples is taken as the related systematic uncertainty. The uncertainty is below
 2539 0.15×10^{-2} for all parameters.

2540 **5.6.10 Bias correction**

2541 In the default sensitivity study, the bias was found to be compatible with zero.
 2542 However, the size of a potential bias can vary depending on the input parame-
 2543 ters. The size of the bias has been investigated with alternate input values of
 2544 ($\gamma, r_B^{DK^\pm}, \delta_B^{DK^\pm}, r_B^{D\pi^\pm}, \delta_B^{D\pi^\pm}$), obtaining the results in Table 5.18. A systematic
 2545 uncertainty due to a potential, small bias is calculated as the difference between
 2546 the maximum and minimum bias for a given parameter. The uncertainty assigned
 2547 in this way is very small in general, and less than 0.1×10^{-2} for all parameters.

Table 5.18: Biases observed with alternative input parameters and the systematic uncertainty assigned for the bias correction. All numbers are quoted with an implicit $\times 10^{-2}$.

Input ($\gamma, r_B^{DK^\pm}, \delta_B^{DK^\pm}, r_B^{D\pi^\pm}, \delta_B^{D\pi^\pm}$)	$x_-^{DK^\pm}$	$y_-^{DK^\pm}$	$x_+^{DK^\pm}$	$y_+^{DK^\pm}$	$x_\xi^{D\pi^\pm}$	$y_\xi^{D\pi^\pm}$
(72, 0.080, 117, 0.005, 288)	-0.02	-0.01	-0.02	-0.02	0.03	0.00
(75, 0.100, 130, 0.005, 300)	-0.03	-0.04	-0.00	0.02	0.01	-0.03
(82, 0.112, 144, 0.005, 330)	0.00	-0.01	0.00	0.03	-0.03	0.02
(71, 0.099, 129, 0.005, 300)	-0.02	-0.04	-0.00	-0.00	0.05	-0.00
Syst. uncertainty	0.04	0.03	0.02	0.04	0.09	0.05

2548 5.6.11 Charmless backgrounds

2549 As discussed in Section 5.3.1, a small number of charmless background decays
 2550 survive the D flight distance cut. In this section the systematic uncertainty related
 2551 to those is assessed, in a series of pseudoexperiments. Toy datasets are generated,
 2552 where a charmless background component is included, using the yields and shapes
 2553 obtained in the studies of Section 5.3.1. The Dalitz-bin distribution is obtained
 2554 by repeating the fits of that section for each bin individually. These datasets are
 2555 subsequently fitted back using the default model, which does not include a charmless
 2556 component. No statistically significant bias is observed.

2557 The study described above does not allow for charge-asymmetries in the charmless
 2558 backgrounds, in terms of overall yields and phase-space distributions. These
 2559 asymmetries are likely to be present, due to large local CP -violation in regions
 2560 of phase space in B^\pm decays to hadrons []. The yields in the data-driven studies
 2561 of Section 5.3.1 are not large enough to assess asymmetries, let alone asymmetric
 2562 bin distributions with any degree of statistical precision. Instead, an extreme-case
 2563 scenario is investigated, where *all* the charmless background is added to either the B^+
 2564 or B^- data sample in generation. In both cases, no statistically significant biases are
 2565 observed, and it is concluded that the impact of charmless background is negligible.

2566 5.6.12 Summary of systematic uncertainties

2567 The complete set of included systematic uncertainties are summarised in Table 5.19.
 2568 It can be seen that the measurement is statistically limited. The correlation matrix
 2569 pertaining to the LHCb related systematics is given in Table 5.20. For studies where
 2570 the systematic uncertainty is obtained by repeating fits to data multiple times while
 2571 varying some input, the correlation matrix from the correlations of the fitted central
 2572 values. For studies that are based on generating a large number of toy datasets and

Table 5.19: Overview of all sources of uncertainty on the measurement.

Source	All uncertainties are quoted with implicit: $\times 10^{-2}$					
	$\sigma(x_-^{DK^\pm})$	$\sigma(y_-^{DK^\pm})$	$\sigma(x_+^{DK^\pm})$	$\sigma(y_+^{DK^\pm})$	$\sigma(x_\xi^{D\pi^\pm})$	$\sigma(y_\xi^{D\pi^\pm})$
Statistical	0.96	1.14	0.96	1.20	1.99	2.34
Strong-Phase inputs	0.23	0.35	0.18	0.28	0.14	0.18
Efficiency correction of (c_i, s_i)	0.11	0.05	0.05	0.10	0.08	0.09
Mass-shape parameters	0.05	0.08	0.03	0.08	0.16	0.17
Mass-shape bin dependence	0.05	0.07	0.04	0.08	0.07	0.09
Lowmass physics effects	0.04	0.10	0.15	0.05	0.10	0.09
CP violation of K_S^0	0.03	0.04	0.08	0.08	0.09	0.46
D mixing	0.04	0.01	0.00	0.02	0.02	0.01
PID efficiencies	0.03	0.03	0.01	0.05	0.02	0.02
Fixed yield ratios	0.05	0.06	0.03	0.06	0.02	0.02
Dalitz-bin migration	0.04	0.08	0.08	0.11	0.18	0.10
Bias correction	0.04	0.03	0.02	0.04	0.09	0.05
Small backgrounds	0.11	0.16	0.13	0.12	0.08	0.13
Total LHCb systematic	0.20	0.25	0.24	0.26	0.32	0.54
Total systematic	0.31	0.43	0.30	0.38	0.35	0.57

Table 5.20: Total LHCb-related systematic uncertainties and their correlation matrix.

Uncertainty ($\times 10^{-2}$)						
	$x_-^{DK^\pm}$	$y_-^{DK^\pm}$	$x_+^{DK^\pm}$	$y_+^{DK^\pm}$	$x_\xi^{D\pi^\pm}$	$y_\xi^{D\pi^\pm}$
σ	0.20	0.25	0.24	0.26	0.32	0.54
Correlations						
	$x_-^{DK^\pm}$	$y_-^{DK^\pm}$	$x_+^{DK^\pm}$	$y_+^{DK^\pm}$	$x_\xi^{D\pi^\pm}$	$y_\xi^{D\pi^\pm}$
$x_-^{DK^\pm}$	1.000	0.864	0.734	0.897	0.349	0.318
$y_-^{DK^\pm}$		1.000	0.874	0.903	0.408	0.362
$x_+^{DK^\pm}$			1.000	0.771	0.563	0.447
$y_+^{DK^\pm}$				1.000	0.507	0.451
$x_\xi^{D\pi^\pm}$					1.000	0.484
$y_\xi^{D\pi^\pm}$						1.000

2573 determining the average bias, the correlation of a systematic on two observables
2574 is taken to be +100 % if the biases are in the same direction, and -100 % if they
2575 are in opposite directions. The total systematic correlation matrix, including both
2576 LHCb-related systematics and that of the strong-phase inputs, is given in Table 5.21.

2577 The studies described in this section also allow for an estimate of the systematic
2578 uncertainties on the \mathcal{R}_i parameters of Eq. (5.20) or, equivalently the F_i parameters,
2579 in a completely analogous manner to how the uncertainty on the CP -violation
2580 observables was assigned. In all cases, however, the systematic uncertainty is found
2581 to be much smaller than the statistical uncertainties that were given in Table 5.10.

Table 5.21: Total systematic uncertainties and their correlation matrix, including contributions due to strong-phase inputs as well as LHCb-related uncertainties.

Uncertainty ($\times 10^{-2}$)						
	$x_-^{DK\pm}$	$y_-^{DK\pm}$	$x_+^{DK\pm}$	$y_+^{DK\pm}$	$x_\xi^{D\pi\pm}$	$y_\xi^{D\pi\pm}$
σ	0.31	0.43	0.30	0.38	0.35	0.57

Correlations						
	$x_-^{DK\pm}$	$y_-^{DK\pm}$	$x_+^{DK\pm}$	$y_+^{DK\pm}$	$x_\xi^{D\pi\pm}$	$y_\xi^{D\pi\pm}$
$x_-^{DK\pm}$	1.000	0.301	0.156	0.576	0.265	0.231
$y_-^{DK\pm}$		1.000	0.437	0.218	0.183	0.170
$x_+^{DK\pm}$			1.000	0.445	0.414	0.310
$y_+^{DK\pm}$				1.000	0.353	0.243
$x_\xi^{D\pi\pm}$					1.000	0.502
$y_\xi^{D\pi\pm}$						1.000

2582 The central values, statistical, and systematic uncertainties of the \mathcal{R}_i parameters
 2583 have been made public in Ref. [?] because they can be employed in future LHCb
 2584 measurements, as discussed in Section 5.5.2.

2585 5.7 Obtained constraints on γ

2586 The measured values of $(x_\pm^{DK}, y_\pm^{DK}, x_\xi^{D\pi}, y_\xi^{D\pi})$ can be used to put constraints on the
 2587 possible values of the CKM angle γ and the hadronic nuisance parameters $r_B^{DK\pm}$,
 2588 $\delta_B^{DK\pm}$, $r_B^{D\pi\pm}$, and $\delta_B^{D\pi\pm}$. This is handled using the `gammacombo` package, which is
 2589 also used to combine all measurements of γ made by the LHCb collaboration [].

2590 5.7.1 Statistical approach

2591 The optimal central values determined in a maximum likelihood fit. The set of
 2592 all observables for which a measurement has been made is denoted A , and the set
 2593 of underlying physics parameters is denoted θ . The physics parameters of course
 2594 determine the probability density function of measurement results of A , $f(A|\theta)$.
 2595 Given a specific set of measurement results, A_{obs} , a likelihood function is defined

$$\mathcal{L}(\theta|A_{\text{obs}}) = f(A_{\text{obs}}|\theta) \quad (5.32)$$

2596 and the estimate of θ is the set of parameters that maximize the likelihood

$$\hat{\theta} = \arg \max_{\theta} \mathcal{L}(\theta|A_{\text{obs}}). \quad (5.33)$$

2597 In practice, a χ^2 function is defined

$$\chi^2(\theta|A_{\text{obs}}) = -2 \ln \mathcal{L}(\theta|A_{\text{obs}}) \quad (5.34)$$

2598 and minimized instead. In the specific case where the likelihood profile is Gaussian,
2599 it is given by the simple expression

$$\chi^2(\theta|A_{\text{obs}}) = (A_{\text{obs}} - A(\theta))^T \Sigma_{A_{\text{obs}}}^{-1} (A_{\text{obs}} - A(\theta)) + c, \quad (5.35)$$

2600 where $\Sigma_{A_{\text{obs}}}$ is the covariance matrix for the measured observables, $A(\theta)$ denotes the
2601 value of the observables expressed in terms of the underlying physics parameters,
2602 and c is a constant that is independent of θ . In the specific case considered here

$$\begin{aligned} A &= (x_-^{DK}, y_-^{DK}, x_+^{DK}, y_+^{DK}, x_\xi^{D\pi}, y_\xi^{D\pi}) \\ \theta &= (\gamma, r_B^{DK\pm}, \delta_B^{DK\pm}, r_B^{D\pi\pm}, \delta_B^{D\pi\pm}). \end{aligned} \quad (5.36)$$

2603 The likelihood scan presented in Section ?? proved that the Gaussian expression
2604 in Eq. (5.35) provides an excellent description of the likelihood profile of the
2605 measurement, when $\Sigma_{A_{\text{obs}}}$ is taken to be the covariance matrix obtained in that
2606 section. Thus, the χ^2 function defined in Eq. (5.35) is minimised to determine
2607 the best estimate of γ .

2608 Two different methods are employed to construct confidence regions for the
2609 observables of interest, known within the `gammacombo` framework as the PROB and
2610 PLUGIN methods. Both methods aim to construct confidence regions for some
2611 subset, ϕ , of the full parameter set θ . The remaining parameters, dubbed nuisance
2612 parameters below, are denoted $\eta = \theta \setminus \phi$. In practice, ϕ most often denotes a single
2613 parameter, and of special interest is of course the case where $\phi = \gamma$. Both methods
2614 aim to solve the problem that due to the number of parameters in θ (six in the case
2615 considered here, but up to X in the latest LHCb combination []), it is not feasible
2616 to derive the confidence regions from a full-fledged Neumann construction []. Under
2617 assumptions discussed below, the methods achieve reasonable coverage nonetheless,
2618 ie. had the measurement been repeated many times, the confidence region is
2619 expected to cover the true parameter(s) with a probability at least at large as
2620 the quoted confidence level (CL), independently of the true parameter value. The
2621 presentation follows the `gammacombo` manual [].

2622 The PROB method is a simple profile-likelihood method. The minimum value
2623 of the χ^2 function is denoted $\chi^2_{\min} \equiv \chi^2(\hat{\theta}|A_{\text{obs}})$. To evaluate the CL for a specific
2624 value (set of values) of ϕ_0 , the χ^2 function is again minimised, this time under

the constraint that $\phi = \phi_0$, resulting in a new minimum $\hat{\theta}' = (\phi_0, \hat{\eta}')$. In the approximation that all likelihoods are exactly Gaussian, the variable

$$\Delta\chi^2(\phi_0|A_{\text{obs}}) = \chi^2(\hat{\theta}'|A_{\text{obs}}) - \chi^2_{\min} \quad (5.37)$$

follows a χ^2 distribution with n degrees of freedom, where n is the number of parameters in ϕ [?]. This can be used to evaluate CL at that point as

$$CL(\phi_0|A_{\text{obs}}) = F_n(\Delta\chi^2(\phi_0|A_{\text{obs}})) \quad (5.38)$$

where F_n is the cumulative distribution function of a χ^2 distribution with n degrees of freedom. The method takes its colloquial name from the fact that this function is named `Prob` in the `ROOT` package. Confidence regions can be defined by scanning the values of ϕ_0 over a region of interest. These confidence regions assume that the estimates $\hat{\theta}$ follow a Gaussian distribution centred on the true values, which is generally the case for maximum likelihood estimates in large samples []; in other cases they may not have good coverage properties. Given the Gaussian shape obtained in the likelihood scan of Section ?? the confidence regions are likely to be well behaved in the case considered here.

However, for the purpose of comparing to the combination of several LHCb measurements in Section 5.5.3 below, the `PLUGIN` method is necessary. It foregoes the assumption that $\Delta\chi^2$ follows a χ^2 distribution, and instead estimates the distribution in a bootstrapping scheme. The procedure is as follows: the values of $\hat{\theta}$, $\hat{\theta}'$, and $\Delta\chi^2(\phi_0|A_{\text{obs}})$ are determined as described above; then the following steps are carried out a number, N_{toys} , of times

- 2644 1. Generate a "toy" result, A_{toy}^i , following the distribution $f(A|\hat{\theta}')$
- 2645 2. Determine $\Delta\chi^2(\phi_0|A_{\text{toy}}^i)$ by minimising the χ^2 function for the results A_{toy}^i twice, once where all parameters in θ are free, and once where $\phi = \phi_0$ is enforced

2648 Then the CL is defined by

$$CL(\phi_0) = 1 - \frac{N(\Delta\chi^2(\phi_0|A_{\text{obs}}) < \Delta\chi^2(\phi_0|A_{\text{toy}}^i))}{N_{\text{toys}}} \quad (5.39)$$

2649 The method is described in Ref. [?], based on the hybrid resampling method presented in [?, ?]. While the coverage properties are not proven, evidence is presented 2650 in terms of asymptotic results and simulation studies in those references. The 2651 coverage properties have also been investigated in relation to LHCb combinations, 2652 and the intervals were found to perform well in most cases [].

2654 **5.7.2 Interpretation results**

2655 The central values and confidence regions obtained for the physics parameters are

$$\begin{aligned} \gamma &= (68.7^{+5.2}_{-5.1})^\circ, \\ r_B^{DK^\pm} &= 0.0904^{+0.0077}_{-0.0075}, \\ \delta_B^{DK^\pm} &= (118.3^{+5.5}_{-5.6})^\circ, \\ r_B^{D\pi^\pm} &= 0.0050^{+0.0017}_{-0.0017}, \\ \delta_B^{D\pi^\pm} &= (291^{+24}_{-26})^\circ, \end{aligned} \quad (5.40)$$

2656 where the quoted uncertainties are obtained via the **PLUGIN** method. The one-
2657 dimensional CL plots are shown in Fig. 5.53. It is also clear that the **PROB** and
2658 **PLUGIN** confidence regions agree well; this is expected given the Gaussian likelihood.
2659 A series of two-dimensional confidence regions are shown in Fig. 5.54, where it
2660 can be seen that the observables define a single solution for γ as expected. It
2661 is worth noticing that the uncertainty of this measurement alone is on par with
2662 the current world average, due to the increased data sample, and the significant
2663 reduction of systematic uncertainties due to the new measurement strategy and
2664 updated inputs from BESIII.

2665 The contribution to the uncertainty on γ from each of the statistical, strong-
2666 phase-related, and LHCb-related uncertainties in isolation can be estimated by
2667 repeating the interpretation while only including subsets of the uncertainties on
2668 the input parameters. Such studies have been performed using the **PROB** method.
2669 Running with statistical uncertainties only yields an uncertainty on γ of 5.05° .
2670 Including only the statistical and LHCb-related systematic uncertainties yields an
2671 uncertainty on γ of 5.08° , suggesting that the LHCb-related systematics contribute
2672 an uncertainty of 0.6° . This is a reduction compared to earlier analyses, where
2673 the contribution was about 2° . A significant contribution to the improvement is
2674 the efficiency-related systematic that has been avoided by promoting $B^\pm \rightarrow D\pi^\pm$
2675 to a signal channel. Including only the statistical and the strong-phase-related
2676 uncertainties leads to an uncertainty on γ of 5.09° , showing the strong-phase-related
2677 uncertainty to be 0.6° , somewhat lower than the expectation of 1.2° presented in
2678 Ref. [?]. This is partly because the uncertainty estimate of that paper does not
2679 take into account the use of the $D \rightarrow K_S^0 K^+ K^-$ channel, and partly because the
2680 uncertainty estimate depends on the specific central values.

2681 The obtained statistical uncertainty on γ is in excellent agreement with the
2682 expectation from pseudoexperiments. The interpretation procedure outlined above
2683 has been performed for each of the pseudoexperiments performed to establish the

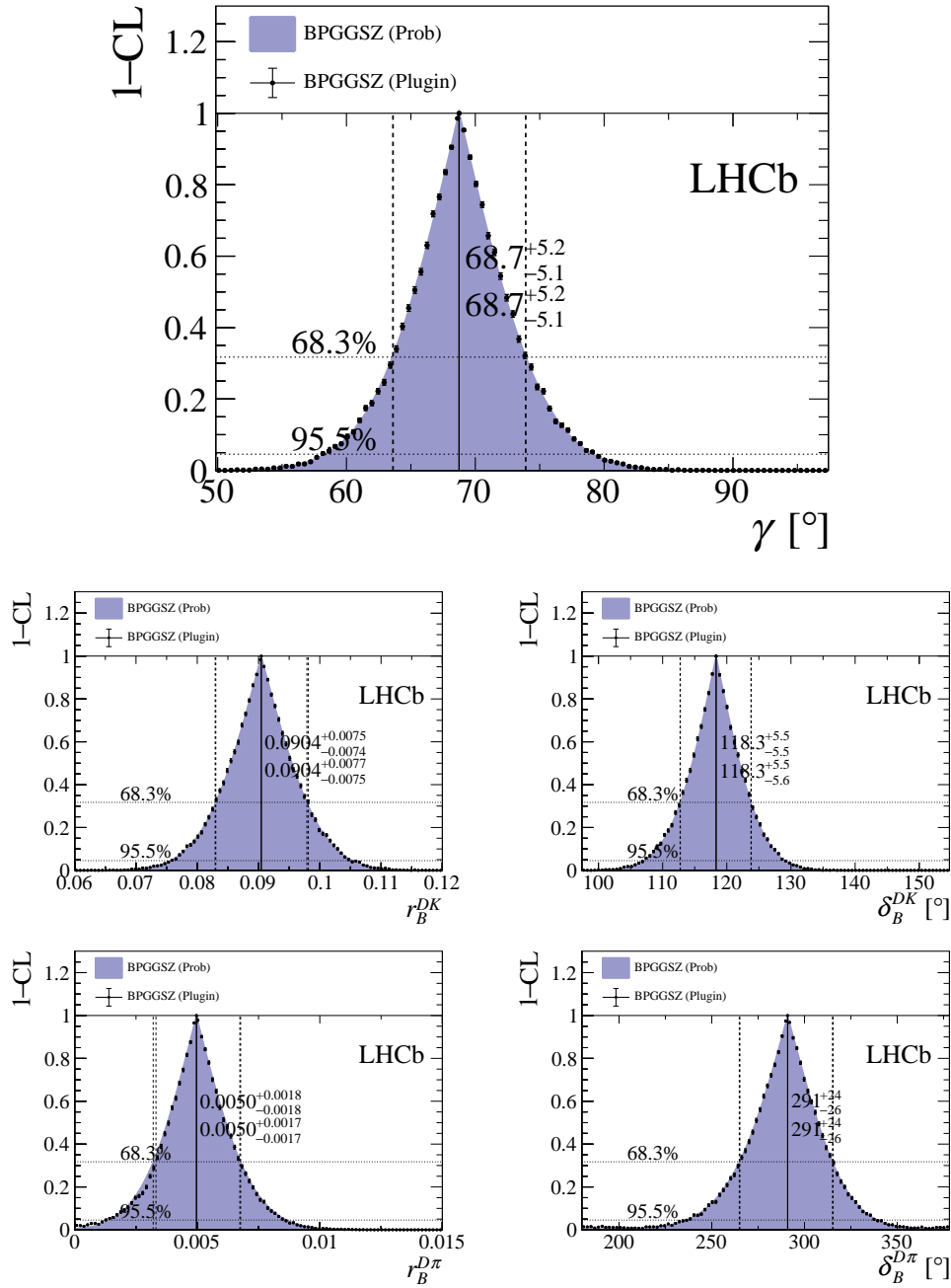


Figure 5.53: Confidence levels for the physics parameters of interest. The solutions are written on the plots, where the top number is given with PROB uncertainties and the bottom number with PLUGIN uncertainties.

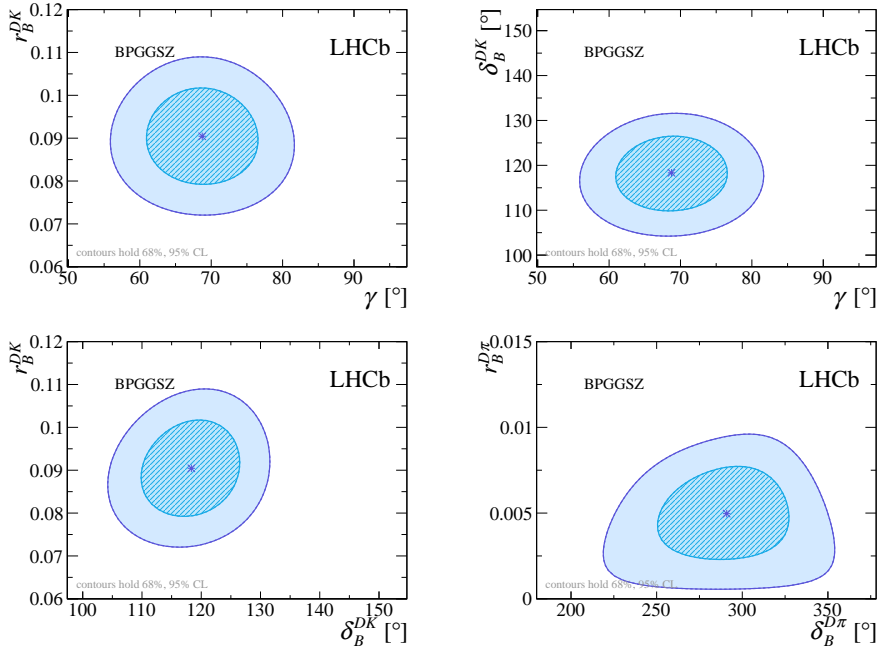


Figure 5.54: The 68 % and 95 % confidence regions for combinations of the physics parameters of interest, as obtained from the results of this measurement. The regions are calculated via the PROB method of `gammacombo`.

feasibility of the CP fit in Section 5.5.1 (including only statistical uncertainties on the observables) and the central 90 % interval of the obtained uncertainties is $[4.4^\circ, 6.0^\circ]$. Similar studies have been carried out where no background decays are included in the generated toy data sets. In this case, the precision on γ is improved by about 30 %.

5.7.3 Compatibility with other measurements

It is worth comparing the obtained constraints on the physics parameters with the information available from other measurements, made at the B factories and by the LHCb collaboration using other decay channels. This comparison is made for γ and the hadronic parameters in the $B^\pm \rightarrow DK^\pm$ decay in Fig. 5.55, comparing to the results of the combinations of γ measurements by the Belle [?] and BaBar [?] collaborations presented in 2013, and the 2018 combination of LHCb results [?]. For this purpose, the LHCb combination is re-performed, removing the input from earlier BPGBGSZ measurements that use $B^\pm \rightarrow DK^\pm$ decays, because they were made using data that is re-analysed in the present thesis; thus they need to be excluded to make the results that are compared independent. The combination employs the same statistical method outlined above, with the exception that the likelihood now depends on observables measured in a number of different analyses. The included measurements are summarised in Table ???. It can be seen in Fig. 5.55

Figure 5.55: Caption here

2702 that the results obtained in this thesis agree well with the Belle and BaBar results,
2703 but are in some tension with the 2018 LHCb combination.

2704 The level of compatibility can be quantified by calculating the three-dimensional
2705 χ^2 of the BPGGSZ results and those of the LHCb combination (without the earlier
2706 BPGGSZ measurements), with respect to the best fit values of $(\gamma, r_B^{DK^\pm}, \delta_B^{DK^\pm})$
2707 when all measurements are combined. The two-dimensional confidence regions
2708 obtained in these three cases are compared in Fig. 5.56, where the tension in $r_B^{DK^\pm}$
2709 and $\delta_B^{DK^\pm}$ is visible again. The calculation is based on the PLUGIN uncertainties; for
2710 the LHCb combination these uncertainty estimates are slightly larger than the ones
2711 obtained via the PROB method. One obtains $\chi^2 = \chi_{GGSZ}^2 + \chi_{LHCb}^2 = 0.7 + 9.1 = 9.8$,
2712 which for 3 degrees of freedom correspond to a p -value of 2 %, or a 2.3σ deviation.
2713 However, this tension is expected to be reduced when other measurements in the
2714 LHCb combination are updated to include results based on the full Run 1 and 2 data
2715 set. The most important update is that of the two-body ADS/GLW measurement
2716 in $B^\pm \rightarrow DK^\pm$ decays because that measurement, and the BPGGSZ measurement
2717 presented in this thesis, have the largest impact in the combination.

2718 The latest LHCb combination in which $B^\pm \rightarrow D\pi^\pm$ parameters were determined
2719 is from 2016 [?]. Two solutions existed for $(r_B^{D\pi^\pm}, \delta_B^{D\pi^\pm})$ which made the interpreta-
2720 tion problematic. As can be seen in Fig. 5.57 the measurement presented in this
2721 thesis picks out one of these solutions, with which it is in excellent agreement. This
2722 solution agrees with the theoretically expected value of $r_B^{D\pi^\pm} \sim 0.005$ [?]. Thus, the
2723 inclusion of the results presented here are expected to lead to a much less problematic
2724 inclusion of results from the $B^\pm \rightarrow D\pi^\pm$ channel in future LHCb combinations.

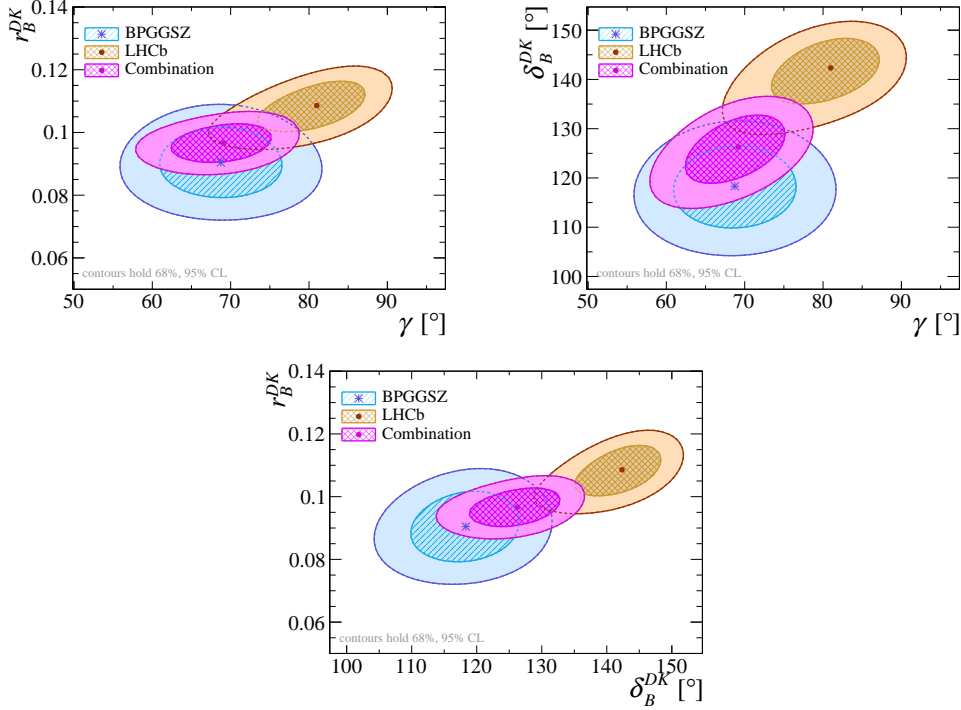


Figure 5.56: The 68 % and 95 % confidence regions for $(\gamma, r_B^{DK\pm})$, $(\gamma, \delta_B^{DK\pm})$, and $(\delta_B^{DK\pm}, r_B^{DK\pm})$ for this measurement, the 2018 LHCb combination [?] where the two-body ADS/GLW results have been updated to those from Ref. [?], and the combination thereof, calculated via the PROB method of `gammacombo`.

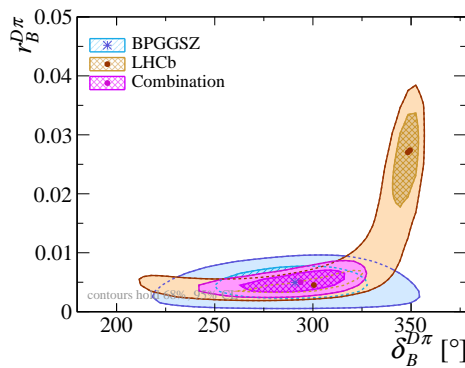


Figure 5.57: The 68 % and 95 % confidence regions for $(\delta_B^{D\pi\pm}, r_B^{D\pi\pm})$ obtained from the results of this measurement, in the 2016 LHCb combination [?], and the combination thereof, calculated via the PROB method of `gammacombo`.

Table 5.22: List of the LHCb measurements used in the combination that the results obtained in the present thesis is compared to. These correspond to the 2018 LHCb combination [?], except that the earlier BPGBS results made with $B^\pm \rightarrow DK^\pm$ decays have not been included in the comparison. In the method column, TD stands for "time-dependent".

B decay	D decay	Method	Ref.	Data set
$B^+ \rightarrow DK^+$	$D \rightarrow h^+h^-$	GLW	[?]	2011-16
$B^+ \rightarrow DK^+$	$D \rightarrow h^+h^-$	ADS	[?]	2011-12
$B^+ \rightarrow DK^+$	$D \rightarrow h^+\pi^-\pi^+\pi^-$	GLW/ADS	[?]	2011-12
$B^+ \rightarrow DK^+$	$D \rightarrow h^+h^-\pi^0$	GLW/ADS	[?]	2011-12
$B^+ \rightarrow DK^+$	$D \rightarrow K_S^0 K^+ \pi^-$	GLS	[?]	2011-12
$B^+ \rightarrow D^*K^+$	$D \rightarrow h^+h^-$	GLW	[?]	2011-16
$B^+ \rightarrow DK^{*+}$	$D \rightarrow h^+h^-$	GLW/ADS	[?]	2011-16
$B^+ \rightarrow DK^{*+}$	$D \rightarrow h^+\pi^-\pi^+\pi^-$	GLW/ADS	[?]	2011-16
$B^+ \rightarrow DK^+\pi^+\pi^-$	$D \rightarrow h^+h^-$	GLW/ADS	[?]	2011-12
$B^0 \rightarrow DK^{*0}$	$D \rightarrow K^+\pi^-$	ADS	[?]	2011-12
$B^0 \rightarrow DK^+\pi^-$	$D \rightarrow h^+h^-$	GLW-Dalitz	[?]	2011-12
$B^0 \rightarrow DK^{*0}$	$D \rightarrow K_S^0 \pi^+\pi^-$	BPGBS	[?]	2011-12
$B_s^0 \rightarrow D_s^\mp K^\pm$	$D_s^+ \rightarrow h^+h^-\pi^+$	TD	[?]	2011-12
$B^0 \rightarrow D^\mp\pi^\pm$	$D^+ \rightarrow K^+\pi^-\pi^+$	TD	[?]	2011-12
Measurements included in Ref. [?] but not in the present comparison				
$B^+ \rightarrow DK^+$	$D \rightarrow K_S^0 h^+h^-$	BPGBS	[?]	2011-12
$B^+ \rightarrow DK^+$	$D \rightarrow K_S^0 h^+h^-$	BPGBS	[?]	2015-16

6

2725

2726

Conclusions

2727 Say something clever

Appendices

A

2729

2730

Projections of main fit to data